Southampton Oceanography Centre
UNIVERSITY OF SOUTHAMPTON AND NATURAL ENVIRONMENT RESEARCH COUNCIL

University of Southampton

Algal Motility in Variable Turbulence

PhD Dissertation

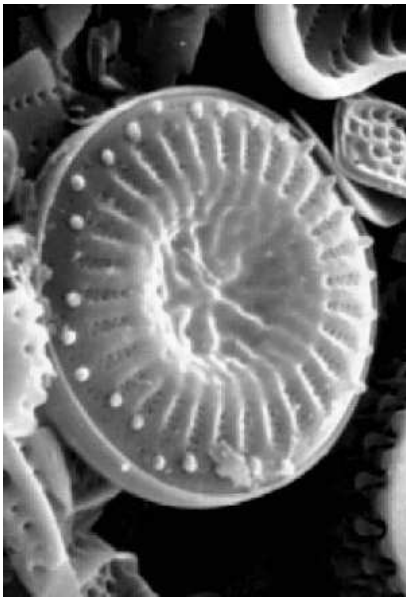

submitted by

Oliver N. Ross

to the Graduate School of the Southampton Oceanography Centre in partial fulfillment of the requirements for the degree of Doctor of Philosophy

July 2004

Southampton
Oceanography Centre
UNIVERSITY OF SOUTHAMPTON AND
NATURAL ENVIRONMENT RESEARCH COUNCIL

Graduate School of the Southampton Oceanography Centre

This PhD dissertation by

Oliver N. Ross

has been produced under the supervision of the following persons

Supervisors

Dr. Jonathan Sharples and Dr. Mike Lucas

Chair of Advisory Panel

Prof. Martin Palmer

Members of Advisory Panel

Prof. Kelvin J. Richards and Dr. David Smeed

I hereby declare that no part of this thesis has been submitted for a degree to the University of Southampton, or any other University, at any time previously. The material included is the work of the author, except where expressly stated.

Southampton 14 July 2004, Oliver Ross

University of Southampton

Abstract

Faculty of Engineering, Science and Mathematics
School of Ocean & Earth Sciences

Doctor of Philosophy

Algal Motility in Variable Turbulence

by Oliver N. Ross

This project is broadly concerned with the interactions between phytoplankton and turbulence, in particular addressing the question of how motility and sinking of phytoplankton cells are affected by the turbulent fluctuations of water around them. These issues are addressed through a coupled 1D physical-biological Lagrangian model with space- and time-variable turbulence. With this individual-based approach it was possible to investigate the direct effects of turbulent intensity on the swimming success. Different swimming strategies could be examined that were driven by either environmental or physiological cues. The individual light histories of the cells provided information on issues related to photo-inhibition and -acclimation and thus general productivity.

During the model development stage, several issues arose which had not been addressed in the oceanographic literature. These resulted in some novel contributions to the field of marine Lagrangian modelling. The model is applied to three different case studies: the partially mixed estuary of Southampton Water where the tides produce periods of strong but episodic vertical mixing; a stratified but tidally energetic shelf sea where observations often show the predominance of motile species at the base of the thermocline; and a freshwater lake where artificial mixing has been used to control toxic bloom events.

The results from the estuarine study showed that although the tidal mixing is generally too strong for motility to be effective, it is the periodic absence of turbulence that the motile cells are able to utilise which resulted in a much increased light availability throughout the springs-neaps cycle, and hence an increased potential for growth. Investigations on the relationship between photo-acclimation and turbulent mixing pointed towards the existence of an acclimation number which could be used to derive the turbulent intensity from the vertical heterogeneity of a suitably chosen physiological parameter.

In the stratified shelf sea study, motility resulted in a clear competitive advantage over neutrally buoyant cells as it permitted the motile species to intercept the weak upward nitrate flux across the thermocline ahead of the competition, while maintaining a depth that provided them with sufficient light to photosynthesise.

The lake study showed how artificial mixing could disrupt the vertical migratory rhythms of *Microcystis aeruginosa* and resulted in significantly decreased growth. The results pointed towards the existence of a critical turbulence threshold for *Microcystis* but due to the lack of an empirical growth formulation that was suitable for this Lagrangian approach, this last result is of more speculative nature.

Overall, it could be shown how motility enables the cells to access various environmental niches peculiar to the individual habitat. In all studied scenarios, motility led to an increase of the crucial resource that was determinant of the species competition.

Acknowledgements

Many people have contributed to the work presented in this thesis. My first acknowledgements must go to my supervisor, Dr. Jonathan Sharples, who not only introduced me to this exciting area of research but also provided me with continual support, active input and encouragement throughout these past four years.

Many big thanks go to Dr. Joanna Waniek and Cesar Ribeiro for the many interesting discussions about Southampton Water providing useful information and insights. I would also like to thank Cesar and my other office mate James Harle as we had an excellent time together in office 564/12 over these past four years.

The study of Lake Nieuwe Meer would have been impossible without the active collaboration between our group and the Aquatic Microbiology group of Prof. Jef Huisman from the University of Amsterdam. In particular I would like to thank Jutta Passarge for her patient answers to all my questions regarding *Microcystis* and Lake Nieuwe Meer.

Thanks go also to our collaborators from the IMPRESS project, and in particular Beth Scott, for providing a stimulating scientific experience which was very interdisciplinary and therefore educational. My participation in two cruises provided me with some interesting experiences and the data have been useful for the setup of the shelf sea model. I would therefore like to acknowledge the crews of RV Clupea and RV Pelagia. This research was funded through the European IMPRESS project, EU project code Q5RS-2000-30864.

My thanks also go to Neil Jenkinson and Dave Spanner, the SOC computer magicians, who provided first aid during numerous hardware failures.

Finally I would like to thank all the friends I made here in Southampton for an excellent time together and my parents for their continual support over many years.

Contents

List of Figures

List of Tables

List of Key Symbols

Variables

d_c	*Microcystis* colony diameter	p. 127
E	Turbulent kinetic energy (TKE)	Eq. (1.6)
g	Acceleration due to gravity	Eq. (1.19)
h	Mixed layer depth	Eq. (1.32)
I	Light intensity	Eq. (2.24)
I_0	Light intensity at midday	Eq. (2.24)
I_b	Light inhibition threshold for phytoplankton	p. 20
I_c	Light compensation point for phytoplankton	p. 20
$I_{d/l}$	Dark-/light acclimatised saturation onset irradiance	Eq. (2.26)
$K_{x,y,z}$	Turbulent eddy diffusivity in the x,y,z direction	Eq. (1.17)
k_{bg}	Background light attenuation coefficient	Eq. (2.25)
k_m	Cell specific light absorption coeffient	Eq. (2.25)
k_s	Light attenuation coefficient due to self-shading	Eq. (2.25)
k_t	Total light attenuation coefficient	Eq. (2.24)
ℓ	Turbulent length scale ($L > \ell > \eta$)	p. 9
L	Turbulent macro (integral) length scale	Eq. (1.4)
N	Brunt-Väisälä frequency	Eq. (1.32)
$N_{x,y,z,h}$	Turbulent eddy viscosity in the x,y,z,horizontal direction	Eq. (1.15)
$\mathscr{P}$	Peclet number	Eq. (1.37)
$P^{d/l}$	Light dependent fully dark-/light acclimatised production	Eq. (2.26)
$P_m^{d/l}$	Maximum fully dark-/light acclimatised production	Eq. (2.26)
Q	Cellular nutrient-to-carbon ratio	Eq. (4.1)
q	Turbulent velocity scale (equiv. to u')	p. 15
Q_{max}	Cellular maximum nutrient storage quota	Eq. (4.1)
Q_{min}	Cellular nutrient subsistence quota	Eq. (4.1)
$\Re$	Reynolds number	Eq. (1.1)
r	Cellular metabolic respiration rate (inclusive of grazing)	p. 56
Rf	Flux Richardson number	Eq. (1.21)
Ri	Gradient Richardson number	Eq. (1.22)
Δt	Model time step	Eq. (2.15)
U	Macroscopic velocity	Eq. (1.2)
u	Fluctuating (turbulent) component of U	Eq. (1.2)
u'	Turbulent intensity (rms of u)	Eq. (1.3)
w	Particle sinking/swimming velocity	Eq. (1.37)
X	Local inhibition parameter (based on ambient light)	Eq. (2.27)
Y	Cellular inhibition status (based on light history)	Eq. (2.28)
$\tilde{z}$	Vertical distance from a boundary	Eq. (2.10)

Greek Letters

ε	TKE dissipation	Eq. (1.4)

$\Delta\Gamma_{\mathrm{lp}}$	Net glucose accumulation/depletion over the light period	Eq. (5.2)
Γ	Cellular glucose concentration	Eq. (5.1)
Γ	Turbulent Prandtl or Schmidt number	Eq. (1.18)
η	Kolmogoroff microscale	Eq. (1.5)
κ_N	Half saturation nutrient concentration	Eq. (4.1)
μ	Specific growth rate	Eq. (5.2)
ν	Kinematic viscosity	Eq. (1.1)
ϱ	Density	Eq. (1.8)
τ	Reynolds stesses	Eq. (1.13)
τ_a	Cellular photo-acclimation time scale	Eq. (2.28)
τ_m	Turbulent mixing time scale	Eq. (1.37)
τ_s	Particle sinking/swimming time scale	Eq. (1.37)
ξ	Scaling factor relating k_s to k_m through the biomass	Eq. (2.25)

Abbreviations

ABP	Associated British Ports	p. 66
ADCP	Acoustic Doppler Current Profiler	p. 65
BML	Bottom Mixed Layer	p. 45
DNS	Direct Numerical Simulation (of turbulence)	p. 12
HCS	(nutrient) Half Saturation Concentration	p. 112
HWS	High Water Stand	p. 66
LES	Large Eddy Simulation (of turbulence)	p. 12
NTS	Neap Tide Scenario	p. 73
PAR	Photosynthetically Active Radiation	p. 18
PDF	Probability Density Function	p. 48
SCM	Subsurface Chlorophyll Maximum	p. 23
SML	Surface Mixed Layer	p. 20
STS	Spring Tide Scenario	p. 73
TCS	Turbulence Closure Scheme	p. 41
TKE	Turbulent Kinetic Energy	p. 8
w/sNTS	weak/strong Neap Tide Scenario	p. 73
w/sSTS	weak/strong Spring Tide Scenario	p. 73

Introduction

Despite the name of our planet, most of it is not dry land but covered by vast expanses of water. The oceans account for over two thirds of the earth's surface and provide a habitat whose size is many times greater than that provided by land and freshwater combined. The first life forms are believed to have originated in the ancient oceans and some of the habitats found today (hydrothermal vents, cold seeps) still resemble those prehistoric conditions.

To study this diversity, the field of oceanographic research draws upon many of the principle natural sciences, such as physics, biology, chemistry, geology, and mathematics, and applies them to the marine environment. Compared to these classical sciences, the field of oceanographic research is relatively young, however, and despite the high level of sophistication reached, many of the processes in our oceans are still not fully understood. We often have to resort to empirical relationships for lack of a consistent theory that accurately describes them. This is mainly due to the many unknowns that govern these processes, which operate on a vast range of spatial and temporal scales. Further complication is added by the difficulty in accessing and measuring the variables involved. Until recently, ship based observations provided the only source of oceanographic data. The inherent problem with this approach is that it can only provide spot measurements, both in space and time, of a highly dynamic and heterogeneous environment. The more recent advent of satellites and remote sensing techniques opened up great opportunities and provided a major step forward as it became possible for the first time to capture snapshots of the ocean on a global scale. In comparison with atmospheric research, oceanography still lacks a technique to remotely probe the depths of the ocean, however, as water, unlike the atmosphere, is much less transparent to electromagnetic and acoustic waves which are the classic remote sensing tools. Satellites can probe only the skin of the ocean while the depths are still only accessible through ships and submersibles. Numerical modelling has provided a valuable addition to complement the difficult to obtain observational data. The constantly increasing speed of modern computers permitted ever more sophisticated models which could eventually encompass a great range of time and space scales. One of the major difficulties in oceanographic research is its observational, rather than experimental, nature. In the ocean it is rarely possible to carry out a manipulative experiment designed to test a specific hypothesis[1]. Instead oceanographic observations tend to comprise a series of correlations around which a causative framework has to be formed. Without being able to manipulate

[1] Note that some manipulative experiments are possible on small scales such as iron fertilisation or mesocosm studies which form but a subset of oceanography, however.

the environment, however, it is often difficult to choose between several apparently plausible solutions. For oceanographers the capability of numerical modelling is critical in plugging this experimental gap, with models providing a means to manipulate a virtual environment. A model can only ever be an approximation to limited subsets of all environmental processes and interactions. The problem, therefore, becomes one of knowing how realistic a model is in its parameterisation of the environment, and how far the interpretation of the model results can be trusted against the model's inherent limitations. In the present work, this numerical modelling approach is applied to an actively developing area of marine research that attempts to bridge the gap between the two traditionally separate realms of marine biology and physical oceanography. The recognition of the close connections between the marine biosphere and its physical environment has created an exciting field of research which synthesises both traditional sciences into the study of bio-physical interactions.

The interactions which represent the focus of this project are those between marine phytoplankton and turbulence. Phytoplankton are the dominant plants in the ocean converting inorganic materials (such as nitrate or phosphate) into organic compounds (e.g. lipids or proteins) by the process of photosynthesis. This primary production process is of paramount importance as it initiates the oceanic food chain that reaches through all trophic levels. Their role as one of the main global fixers of carbon dioxide has also been recognised in climate research as any changes in primary productivity are likely to impact on the atmospheric carbon dioxide content and thus the climatic development on the planet. Globally the marine primary producers are estimated to fix about 40-50% of the total 10^{11} tonnes of carbon fixed each year by all marine and terrestrial plants. Compared to terrestrial primary producers, the production exhibits several important differences. Typical turnover times for carbon in the terrestrial system are of the order of years (i.e. the growth of large forests), while in the ocean the turnover time is dominated by the cycles of marine primary producers operating on time scales of days to weeks. Compared to the ocean the terrestrial producers live in an environment where access to light and nutrients is more stable as both resources are available at the earth's surface. Oceanic primary producers on the other hand have evolved to live in a turbulent fluid environment, where there is often a large spatial separation between the sunlight (at the sea surface) and the required inorganic nutrients (typically greatest several 10s of metres below the surface, and often completely absent in the surface water[2]). An understanding of the underlying physical processes governing marine primary production is an essential component of understanding both our climate (via their effect on CO_2) and the sustainability of our demands for marine food supplies (via their fuelling of the rest of the marine food chain).

Phytoplankton have evolved to live in a turbulent, fluid environment. Phytoplankton motility is thought to represent one of those adaptations to the spatial separation of light and nutrients. While the plankton are drifting organisms (literally "wanderers") in the ocean, some species are capable of self-propelled locomotion. It is the interaction between this motility and the turbulent fluctuations of the surrounding water and the effect of these interactions on the

[2]Note that some species (e.g. *trichodesmium*) can fix atmospheric N_2, and nutrients can be high at the surface in regions that are influenced by freshwater run-off and upwelling

primary production, which will receive particular attention in this thesis.

Most of the earlier research in this area was restricted to very simplified representations of the physical environment neglecting its spatial (e.g. Woods and Onken, 1982) and temporal (e.g. Lizon et al., 1998) heterogeneity. The lower available resources in computing power also meant that most of the earlier research had to treat phytoplankton as clouds of particles rather than individuals (e.g. Lewis et al., 1984*a*).

In this context, the present thesis presents a rather novel approach of using a Lagrangian representation of phytoplankton in combination with a realistic representation of turbulence (that accounts both for the spatial and temporal heterogeneity of turbulence) coupled with a biological model that describes the individual growth responses to light and nutrients.

Chapter 1 gives an outline of the underlying theory that the remainder of this thesis will draw upon. It summarises the relevant issues of turbulence with respect to modelling approaches, and its interaction with small particles. A range of topics related to primary production, phytoplankton biology and morphology are discussed paying particular attention to the aspect of motility. Chapter 2 explains the basic components of the computer model that are common to all later experiments. The model development draws on work from outside the oceanographic literature, particularly work within meteorology, where it can be argued that large-scale convective motions that dominate meteorological turbulence has forced an earlier appreciation of Lagrangian modelling. Model development in this project has also had to solve some particular problems specific to the marine environment and primary producers. In chapters 3 to 5 the model is applied to three different case studies: a partially mixed estuary, a stratified but tidally energetic shelf sea, and an artificially mixed freshwater lake. These examples represent a wide range of environmental conditions where motile phytoplankton are found, and the model is used as an investigative tool to assess the advantage that motility confers on phytoplankton compared to neutral buoyancy. Chapter 6 presents the conclusions of this study by summarising the achievements and shortcomings of the model, and pointing the direction of future work stemming from this project. Additional material that is relevant to Chapters 3 and 5 is provided in the Appendix.

Chapter 1

General Background

This project is broadly concerned with the interactions between phytoplankton and turbulence, in particular addressing the question of how motility and sinking of phytoplankton cells are affected by the turbulent fluctuations of water around them. This first chapter will introduce some of the physical and biological concepts that are relevant to the understanding of these issues. The concepts are presented mostly in a descriptive manner because a full analytical treatment, especially for turbulence, would be beyond the scope of this study. Derivations of the equations used are provided only if they are relevant for the understanding and are otherwise referenced.

Section 1.1 deals with the scales of fluid motion and turbulence in the ocean in the context of typical phytoplankton sizes and motion. The necessary physical framework for the present study is provided with Section 1.2 which describes the physics of turbulence, diffusion, mixing and stability. Section 1.3 introduces the biological concepts of photosynthetic primary production in various geographical regimes, resolving the growth dependencies on light and nutrients. The biological and morphological adaptations of phytoplankton to their physical environment are described in Section 1.4 focussing primarily on diatoms and dinoflagellates as two common and well studied representatives of non-motile and motile phytoplankton groups. Section 1.5 discusses the effects of turbulence on phytoplankton at the microscale both in terms of motility and metabolism (e.g. photo-acclimation). The Eulerian and Lagrangian modelling approaches are compared in Section 1.7 paying particular attention to the movement of individual particles and the coupling of the particle movement with the turbulent flow. The project objectives are summarised in Section 1.8.

1.1 Scales in the Ocean

The physical and biological processes in the ocean operate on a wide range of length and time scales. For many oceanographic applications the only measure available is often an order of magnitude estimate of a length scale (e.g. for turbulence) or time scale (e.g. for mixing) that is used to describe a physical processes which cannot be resolved analytically or measured

accurately. This section will therefore describe some of the scales that are relevant to the present work.

1.1.1 Length Scales

For the physical processes, the length scales range from the width of an ocean basin, which is of the order of 10^7 m (e.g. large scale ocean circulation), down to the Kolmogoroff microscale (size of the smallest turbulent eddies, see Section 1.2) which is of the order 10^{-3} m. For primary production, the relevant length scales range from 100 m (depth of mixed layer/euphotic zone) down to the millimetre scale (molecular diffusion, interaction with turbulence) while marine phytoplankton can be as small as 10^{-6} m (Table 1.1).

TABLE 1.1: Size categories for phytoplankton (after Sieburth et al., 1978).

Femtoplankton	0.02 - 0.2 μm
Picoplankton	0.2 - 2 μm
Nanoplankton	2 - 20 μm
Microplankton	20 - 200 μm
Macroplankton	200 - 2000 μm
Megaplankton	$>$ 2000 μm

The size of the plankters becomes important if one wishes to understand how small scale interactions take place and how the cells are affected by their physical environment. One of the main foci of this study is the motility of the cells and how the cells are able to use it to their advantage in a highly turbulent and viscous environment. A useful quantity to consider in this context is the Reynolds number $\Re$:

$$\Re = \frac{\text{inertial forces}}{\text{viscous forces}} = \frac{u\,l}{\nu} \tag{1.1}$$

where u represents a characteristic swimming velocity, l is a characteristic length (of the organism) and ν is the kinematic viscosity of the fluid (typically $\nu \approx 10^{-6}\ \mathrm{m^2\,s^{-1}}$ for sea water). If we neglect the influence of body shape and consider the example of a small fish with $l = 10$ cm, $u = 1\ \mathrm{m\,s^{-1}}$ we obtain $\Re \approx 10^5$. The inertial forces thus dominate in this animal's world. An averaged size phytoplankton, on the other hand, has $l = 50\ \mu$m, $u = 0.1\ \mathrm{mm\,s^{-1}}$ and thus $\Re \approx 10^{-3}$ which means that the viscous forces are about 1000 times bigger than the inertial forces. Purcell (1977) compared this with humans trying to swim in molasses. The morphological adaptations of the phytoplankton to this viscous environment will be discussed in Section 1.4.2. Empirically, swimming velocity increases with body length and thus $\Re$ increases with body length. From a large range of empirical data Okubo (1987) obtained $\Re = 1.4 \cdot 10^6 \cdot l^{1.86}$ which yields $\Re = 1$ for $l \approx 500\ \mu$m (Fig. 1.1). Most of the members of the planktonic community are smaller than 100 μm and have therefore Reynolds numbers well below unity.

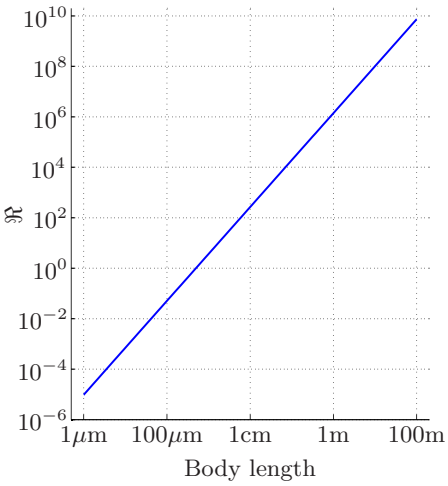

Figure 1.1: Relating the Reynolds number to the body length of biological organisms (after Okubo, 1987).

1.1.2 Time Scales

Generally speaking, the time scale of a physical or biological process increases or decreases in direct proportion to the related length scale. One of the largest oceanic time scales is the time it takes for the thermohaline circulation to complete one cycle which may require up to 10 000 years. Large scale oceanic gyres have periods of several years and as we follow the energy cascade down to the smallest turbulent length scales, the associated time scales (eddy turnover times) become of the order of seconds. Similar patterns exist for the life times (e.g. eddy decay times) of these physical structures.

In the biological context, it is usually the large mammals that have life spans of around 100 years while smaller fish live only between 1-10 years. Further down the food chain, we find life spans for zoo- or phytoplankton of the order of weeks or days. Similar patterns are observed for the times it takes for these organisms to reproduce. Large mammals often carry their offspring for over one year before giving birth while phytoplankton doubling times are of the order of one day down to hours for small bacteria.

For the present work the relevant physical time scales range from the small eddy decay times of a few seconds to the springs-neaps period of over two weeks which influences the rhythm of turbulent mixing to which the phytoplankton cells are exposed. The biological time scales span a similar range of seconds to days. On the short time scales, the cell has to use its motility against the immediate turbulent mixing. It is only the long term effect, however, which determines whether this short term effort has been worthwhile, i.e. whether motility was useful for adjusting the cell's vertical position in the water column.

The turbulent mixing and diffusion time and length scales will be discussed as part of the following section.

1.2 Turbulent Mixing and Diffusion in the Ocean

Despite being one of the principle unsolved problems in physics, the concept of turbulence has become a familiar term in everyday language where it is often used as a synonym for mixing or agitation in general. Based on their observations, Taylor and von Kármán (1937) formulated a definition of turbulence stating that turbulence is generated if a fluid flows past a solid boundary or two layers of fluids of differing velocity flow over one another. Under certain conditions (i.e. high Reynolds numbers), this velocity shear can create instabilities in the laminar flow which then undergoes a transition to turbulent flow. Turbulent flows are highly individualistic but a number of common characteristics emerge that can be used to identify and distinguish them from other types of irregular flow: turbulent flow is irregular (random) both in time and space, three-dimensional, vortical (i.e. rotational), strongly non-linear, highly diffusive, and highly dissipative. It is these complex properties that make it a difficult task to understand and model turbulent processes. Due to the random nature of turbulence, one relies on the laws of probability to describe the development of averages of

certain quantities like temperature or velocity. As in the example of velocity, U, the turbulent fluctuations are often separated from the mean flow, $\overline{U}$, by writing:

$$U = \overline{U} + u \tag{1.2}$$

where u describes the turbulent fluctuations such that $\overline{u} = 0$. This notation is often referred to as the Reynolds decomposition. The intensity of the turbulence fluctuations is defined as the root-mean-square value

$$u' = \sqrt{\overline{u^2}} \tag{1.3}$$

The average values can be either time averages, if the flow field is steady, or space averages, if the flow is isotropic. In cases where the turbulence is neither isotropic nor steady, the averages have to be taken over a large number of experiments that have the same initial and boundary conditions (ensemble average). Part of the difficulty of turbulence already originates here, as there is no logical method to decide whether a motion is part of the mean flow or part of the turbulent fluctuations. The criterion of $\overline{u} = 0$ can assist in this decision but the problem remains of finding averaging times/lengths that are large enough to obtain this result, but at the same time small enough in comparison to the time/length scales of the large scale mean flow.

1.2.1 The Cascade Theory of Turbulence

In 1941 Kolmogoroff (1941) introduced the concept of the energy cascade. He imagined that turbulence is formed by eddies of many different sizes. Energy is supplied to the largest ones through external processes (boundaries, shear), and as they become unstable, they transfer their energy to smaller and smaller eddies. As long as the eddies are large, the transfer is practically inviscid and no energy is dissipated. As they become smaller, they finally reach an eddy size for which viscosity cannot be neglected anymore (called the Kolmogoroff micro scale η) and at this point the energy will begin to dissipate into heat. The cascade hypothesis assumes that the eddies become unstable within a time of the order of the turnover time. If L denotes the length scale of the largest eddies, this turnover time can be approximated by $T_L = L/u'$. The rate of energy transfer per units mass, ε [m^2 s^{-3}], is therefore proportional to u'^2 times the eddy frequency u'/L

$$\varepsilon \sim \frac{u'^3}{L} \tag{1.4}$$

If the turbulence is homogeneous, relation 1.4 holds for all inviscid energy transfers in the so-called inertial range, i.e. for length scales much greater than the Kolmogoroff scale. L is often called the integral length scale as it denotes the scale at which energy is fed into the system.

Due to its dissipative nature, turbulence requires a continuous supply of energy to make up for the viscous losses. As the turbulent kinetic energy (TKE) is passed down the energy cascade to smaller scales $\ell \ll L$, the time which viscosity would need to dampen the velocity fluctuations, $T_\nu = \ell^2/\nu$, becomes smaller as well. At some point, $T_\nu < T_\ell = \ell/u'$ and the energy begins

to dissipate before it can be passed down to even smaller scales. The Kolmogoroff scale η describes the length scale at which both times are equal, i.e.

$$\frac{\eta^2}{\nu} = \frac{\eta}{u'} \overset{\text{Eq. (1.4)}}{=} \frac{\eta}{(\varepsilon\eta)^{1/3}} \Rightarrow \eta = \left(\frac{\nu^3}{\varepsilon}\right)^{1/4} \tag{1.5}$$

The arguments leading to Eq. (1.4) and (1.5) are very much based on dimensional analysis and the exact implementations of these equations may vary for different applications. In the oceanographic literature, for example, the right-hand-side of the last equation in Eq. (1.5) is often multiplied by a factor of 2π, mainly for mathematical convenience but, as observations by Lazier and Mann (1989) indicate, $2\pi\ (\nu^3/\varepsilon)^{1/4}$ also represents a more realistic minimum length scale.

Analogous to the inertial range defined earlier, the length scales for which $\ell \sim \eta$ is called the dissipative range. For length scales in the inertial range that have $\ell < L$, the associated time scales decrease monotonically with eddy size. The smaller eddies are thus embedded in the larger ones and are in local equilibrium as they evolve much faster and dissipate before the 'host' eddy has changed appreciably. This is the theoretical justification for using homogeneous turbulence as a building bloc for many theoretical considerations. Over this pseudo-homogeneous range, the turbulent kinetic energy E [$\mathrm{m^3\ s^{-2}}$] contained in these eddies has been shown to obey a power law of the form

$$E = C\,\varepsilon^{2/3}k^{-5/3} \quad \text{for} \quad L^{-1} \ll k \ll \eta^{-1} \tag{1.6}$$

where k is the eddy wavenumber $k = 2\pi/\ell$ and $C \approx 1.5$ has been found to be a universal constant, valid for all turbulent flows. Note that E is independent of ν in this inertial range. Eq. (1.6) is generally referred to as *Kolmogoroff's* $k^{-5/3}$ *power law* (Fig. 1.2). If the Reynolds number is large, then $\eta \ll L$ and the inertial range is quite broad. Although most of the TKE is contained in the largest eddies which account for most of the diffusive transport, a

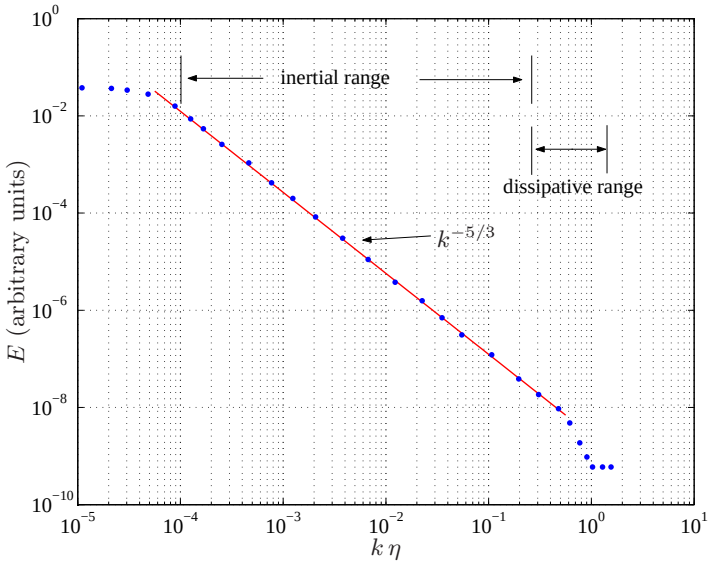

Figure 1.2: A typical wavenumber spectrum that would be observed in the ocean (redrawn after Kundu and Cohen, 2002, p. 521).

phytoplankton cell sits inside the smallest eddies whose characteristics are independent of the larger ones and thus of the source of turbulence.

For a scalar quantity such as temperature or a nutrient concentration, a more relevant length scale is the so-called Batchelor scale

$$L_B = \left(\frac{\nu D^2}{\varepsilon}\right)^{1/4} \tag{1.7}$$

where D is the molecular diffusion constant. The analysis of Batchelor (1959) showed that turbulent straining of the fluid causes a scalar property to be distributed in long thin lines that are parallel to the flow. The minimum size of these lines at which the steepening of the concentration gradient (through turbulent stretching) and smoothing (by diffusion) are in balance is given by Eq. (1.7). Their separation is usually large compared to L_B. Thus it can be assumed that at scales less than L_B, turbulent flows are not significantly different from laminar ones and consequently both velocity and scalar gradients are extremely small. Usually L_B is about 30 times smaller than the Kolmogoroff scale.

1.2.2 Analytical Methods

At any given moment, a turbulent flow will satisfy the Navier-Stokes equations:

$$\frac{\mathrm{D}\mathbf{U}}{\mathrm{D}t} = \underbrace{-\frac{1}{\varrho}\nabla P}_{\text{pressure}} + \underbrace{\nu\,\nabla^2\mathbf{U}}_{\text{friction}} + \text{other forces} \tag{1.8}$$

where contributions due to gravity and the Coriolis terms have been abbreviated as 'other forces' as they are of no concern here. $\mathbf{U} = (U, V, W)$ is the velocity vector, P the pressure, ϱ is the density, and ν the kinematic viscosity. Together with the continuity equation

$$\nabla\mathbf{U} = 0 \tag{1.9}$$

the Navier-Stokes equations form a closed system, meaning that there are four equations for the four unknowns U,V,W, and P. For a scalar property Φ, the corresponding equation to Eq. (1.8) is

$$\frac{\partial\Phi}{\partial t} + \mathbf{U}\nabla\Phi = \gamma\nabla^2\Phi \tag{1.10}$$

where γ is the molecular diffusion coefficient of Φ. The total derivative on the left hand side of Eq. (1.8) contains the non-linear terms, which for the x direction are

$$\frac{\mathrm{D}U}{\mathrm{D}t} \equiv \underbrace{\frac{\partial U}{\partial t}}_{\text{local change}} + \underbrace{U\frac{\partial U}{\partial x} + V\frac{\partial U}{\partial y} + W\frac{\partial U}{\partial z}}_{\text{non-linear advective terms}} \tag{1.11}$$

Under certain flow conditions (high Reynolds numbers) these terms produce instabilities which can eventually lead to the transition from laminar to turbulent flow. In such a case, the predictions using the Navier-Stokes equations would become worse as time progresses due to the error in determining the initial conditions (principle problem of any chaotic system). In

addition, the range of size and time scales makes it impossible to predict the flow in any detail with the present computing power. A common work-around for this problem, as in many chaotic systems, is to resort to statistical descriptions of the averages. This is achieved by inserting the Reynolds decomposition from Eq. (1.2) into Eq. (1.8) and building the average to obtain the averaged equations of motion for turbulent flow. Expanding out the total derivative, the x component of Eq. (1.8) becomes (see Kundu and Cohen (2002) p. 508 for a derivation):

$$\frac{\partial \overline{U}}{\partial t} + \overline{\mathbf{U}}\,\nabla\overline{U} + \frac{\partial(\overline{uu})}{\partial x} + \frac{\partial(\overline{uv})}{\partial y} + \frac{\partial(\overline{uw})}{\partial z} = -\frac{1}{\varrho}\,\nabla\overline{P} + \nu\,\nabla^2\overline{U} + \overline{\text{o.f.}} \tag{1.12}$$

The Reynolds decomposition produced thus three additional stress terms for each dimension (last three terms on the left hand side), the so-called Reynolds stresses which can be expressed in the Reynolds stress tensor

$$\underline{\underline{\tau}} = -\varrho \begin{pmatrix} \overline{u^2} & \overline{uv} & \overline{uw} \\ \overline{uv} & \overline{v^2} & \overline{vw} \\ \overline{uw} & \overline{vw} & \overline{w^2} \end{pmatrix} \tag{1.13}$$

The diagonal elements in Eq. (1.13) are the normal components due to pressure, the off-diagonal elements are the tangential or shear stresses (Fig. 1.3). In the case of completely isotropic turbulence, the off-diagonal elements vanish and $\overline{u^2} = \overline{v^2} = \overline{w^2}$. In analogy to Eq. (1.3) the turbulent kinetic energy (TKE) can be expressed as (per unit volume)

$$\text{TKE} = \frac{1}{2}(\tau_{xx} + \tau_{yy} + \tau_{zz}) = \frac{\varrho}{2}\,(\overline{u^2} + \overline{v^2} + \overline{w^2}) = \frac{\varrho}{2}\,\mathbf{u}'^2 \tag{1.14}$$

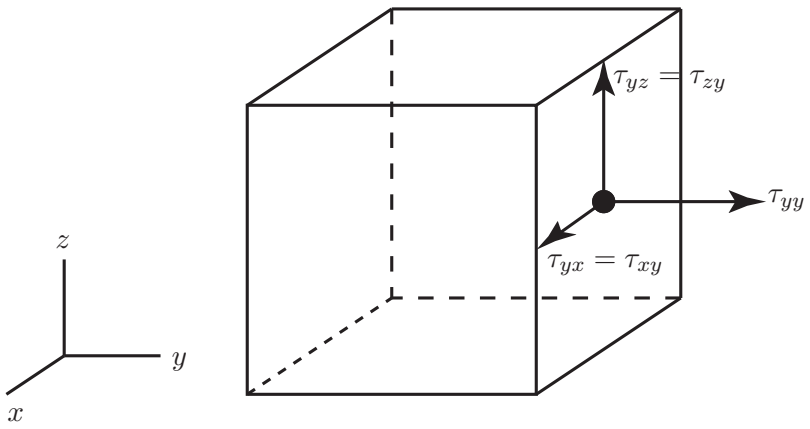

Figure 1.3: Illustration of the Reynolds stresses on a cubic fluid element.

Another way to interpret the Reynolds stresses is as the rate of mean momentum transfer by turbulent fluctuations per unit area. E.g. $\tau_{xy} = -\varrho\,\overline{uv}$ represents the average flux of v-momentum along the u-direction (and vice versa).

The main problem in calculating turbulent flows is the determination of these Reynolds stresses. A statistical analysis of the equations of motion always leads to the same problem that there are more unknowns than equations. This is called the *closure problem of turbulence* (see Section 1.2.5). A common way to accomplish the closure is by expressing the Reynolds stresses

in terms of the large-scale velocities, thereby reducing the number of unknowns to the original four. One of the most common and possibly most crude methods to deal with this problem dates back to 1877 when Boussinesq recognised that these macroscopic turbulence stresses resemble those produced by the molecular viscosity for laminar flow. He therefore introduced a 'turbulence' - or 'eddy viscosity' N to describe the transfer of momentum due to turbulent fluctuations (Rodi, 2000)

$$\frac{\tau_{xx}}{\varrho} = 2N_x\frac{\partial\overline{U}}{\partial x} \qquad \frac{\tau_{yy}}{\varrho} = 2N_y\frac{\partial\overline{V}}{\partial y} \qquad \frac{\tau_{zz}}{\varrho} = 2N_z\frac{\partial\overline{W}}{\partial z} \tag{1.15a}$$

$$\frac{\tau_{xy}}{\varrho} = N_y\left(\frac{\partial\overline{V}}{\partial x}+\frac{\partial\overline{U}}{\partial y}\right) \qquad \frac{\tau_{xz}}{\varrho} = N_z\frac{\partial\overline{U}}{\partial z}+N_x\frac{\partial\overline{W}}{\partial x} \qquad \frac{\tau_{yz}}{\varrho} = N_z\frac{\partial\overline{V}}{\partial z}+N_y\frac{\partial\overline{W}}{\partial y} \tag{1.15b}$$

In order to meet the symmetry requirements between τ_{xy} and τ_{yx}, etc., it is necessary to have a uniform eddy diffusivity in the horizontal, i.e. set $N_x = N_y =: N_h$. If N_h and N_z are assumed constant, the averaged Navier-Stokes equation [Eq. (1.12)] becomes

$$\frac{\mathrm{D}\overline{\mathbf{U}}}{\mathrm{D}t} = -\frac{1}{\varrho}\nabla\overline{P}+N_h\left(\frac{\partial^2}{\partial x^2}+\frac{\partial^2}{\partial y^2}\right)\overline{\mathbf{U}}+N_z\frac{\partial^2}{\partial z^2}\overline{\mathbf{U}}+\nu\nabla^2\overline{\mathbf{U}}+\overline{\text{o.f.}} \tag{1.16}$$

Applying the same method to the Navier-Stokes equation for a scalar [Eq. (1.10)] one obtains a 'turbulence' - or 'eddy diffusivity' K

$$-\overline{u\phi} = K_x\frac{\partial\overline{\Phi}}{\partial x} \qquad -\overline{v\phi} = K_y\frac{\partial\overline{\Phi}}{\partial y} \qquad -\overline{w\phi} = K_z\frac{\partial\overline{\Phi}}{\partial z} \tag{1.17}$$

K and N are related through the turbulent Prandtl or Schmidt number[1]

$$\Gamma = \frac{N}{K} \tag{1.18}$$

This phenomenological approach to turbulence attempts to parameterise the macroscopic properties of turbulent flow (i.e. its diffusive nature) without having to deal with all the small scale processes that occur in the turbulence. This approach makes crucial assumptions at a very early stage in the analysis thereby discarding any claim to accurately represent the turbulent flow. By doing so, it becomes impossible to calculate or derive N and K analytically. The significant failure of the analogy with molecular friction makes it even difficult to determine N and K empirically as they are heavily dependent on the flow characteristics. As Hinze (1975) points out, the concept of a scalar eddy viscosity or diffusivity is only of limited use to represent the actual turbulent motion as it fails to represent large scale transport by coherent turbulent eddy structures or the temporal or spatial intermittency, that is characteristic of turbulence. However, its strength lies in its simplicity as the equations become much easier to handle. This ease of use makes it a widely used approach in the marine community. Other parameterisations of turbulence such as direct numerical simulation (DNS) or large eddy simulation (LES) experiments are much more complicated and require large amounts of computing power (see Section 1.2.5).

[1] Prandtl number for heat transport, Schmidt number for mass transport.

1.2.3 Mechanisms of Mixing and Stability

Turbulence in the ocean is mainly generated by velocity shear. Some of the main mechanisms that produce shear stresses are tidal currents passing over the sea bed, wind blowing over the sea surface, or breaking internal waves. If the water column is stratified, the static stability hinders the vertical exchange of mass or momentum and leads to a dampening of the turbulence. In order to quantify the evolution of turbulence it is necessary to establish an equation that describes its sources and sinks. By multiplying the equation of motion for the turbulent fluctuations ($\partial \mathbf{u}/\partial t$) with $\mathbf{u}$ one obtains an equation for the kinetic energy budget of the turbulent flow (see Kundu and Cohen (2002); Rodi (2000) for a derivation). Ignoring the transport terms which only redistribute the TKE and aligning the x-direction with the direction of the mean flow, one obtains:

$$\frac{\partial E}{\partial t} = \underbrace{\overline{uw}\left(\frac{\partial \overline{U}}{\partial z}\right)}_{\text{shear production}} - \underbrace{\frac{g}{\varrho}\overline{\varrho w}}_{\text{work against buoyancy}} - \underbrace{\varepsilon}_{\text{dissipation}} \tag{1.19}$$

The gravity term (g is the acceleration due to gravity), which was written under 'other forces' in Eq. (1.8), has been included here. The Coriolis term drops out, as the Coriolis force is a pseudo-force only which 'acts' perpendicular to the flow, i.e. it does not alter the magnitude of the flow and has thus no influence on its kinetic energy. If the eddy-viscosity and -diffusivity simplification is used [Eq. (1.15) and Eq. (1.17)], Eq. (1.19) becomes

$$\frac{\partial E}{\partial t} = N_z \left(\frac{\partial \overline{U}}{\partial z}\right)^2 + K_z \frac{g}{\varrho}\frac{\partial \varrho}{\partial z} - \varepsilon \tag{1.20}$$

The first term on the right is the source term as it contains the amount of kinetic energy that the turbulence draws from the macroscopic flow. In most scenarios, the buoyancy term will be a sink of TKE as the static stability will produce $(\partial \varrho/\partial z) < 0$ and thus hinder any vertical transfers (note that $z = 0$ at the sea bed and increases upwards). The more stable the water column, the more turbulent energy is required for vertical transfers. Only during periods of convective instability can this term become a source of TKE. The last term in Eq. (1.20) represents the viscous losses at the Kolmogoroff scale.

In order to quantify the effects of stratification on the turbulent mixing, one may consider the ratio between the buoyant destruction to the shear production of TKE. Using Eq. (1.19) we obtain

$$\mathrm{Rf} = \frac{-(g/\varrho)\,\overline{w\varrho}}{-\overline{uw}\,(\partial \overline{U}/\partial z)} \tag{1.21}$$

This ratio is called the Flux Richardson number. For $\mathrm{Rf} > 1$ the buoyant destruction exceeds the production and the turbulence is decaying. Experiments have shown, however, that the critical value at which turbulence ceases to be self-supporting may be less than unity. Values in the literature for this critical value of Rf vary considerably. In the 1960's Miles (1961) and Howard (1961) found that $\mathrm{Rf} > 0.25$ represented a necessary although not sufficient condition for linear stability. For many years to come, this was taken as a basis for the argument that turbulence cannot exist for $\mathrm{Rf} > 0.25$. A more recent study that considered

the non-linear interactions as well (Abarbanel et al., 1984) derived the necessary and sufficient stability condition of $\mathrm{Rf} > 1$. Since then this result has been verified using both observational data (Martin, 1985; Strang and Fernando, 2001) and numerical results from direct numerical simulation (DNS) of turbulence (Gerz et al., 1989) and large eddy simulation (LES) (Wang et al., 1996) which all found that turbulence could persist up to $\mathrm{Rf} \approx 1$. This led to the recent introduction of higher critical Richardson numbers into more simple turbulence closure schemes (Burchard and Deleersnijder, 2001; Canuto et al., 2001) (see also the discussion in Section 1.2.5).

Replacing again the flux and stress terms with the eddy diffusivity and -viscosity delivers a ratio that is often used in observational oceanography as it is easier to measure: the gradient Richardson number

$$\mathrm{Ri} = \frac{(g/\varrho)(\partial\varrho/\partial z)}{(\partial\overline{U}/\partial z)^2} = \Gamma\,\mathrm{Rf} \tag{1.22}$$

where Γ is again the turbulent Prandtl or Schmidt number from Eq. (1.18). The numerator in Eq. (1.22) is the square of the Brunt-Väisälä or buoyancy frequency. In stratified fluids, generally $\Gamma > 1$ since internal waves can produce a vertical transfer of momentum but not of heat or mass. K_z is therefore reduced more than N_z. This is often the reason why turbulence can still persist even when $\mathrm{Ri} > 1$ as long as $\mathrm{Rf} < \mathrm{Rf}_c$. In neutral environments $N_z \approx K_z$ which is called the Reynolds analogy.

1.2.4 Molecular versus Turbulent Diffusion

Applying the above phenomenological approach to a constituent Φ (e.g. temperature), the flux F of Φ due to turbulent diffusion can be written (in one dimension) as

$$F = -K_z \frac{\mathrm{d}\Phi}{\mathrm{d}z} \tag{1.23}$$

The magnitude of K can span a wide range of values in the ocean that vary according to location and stratification. Due to the much larger horizontal length scales (the water depth limits the maximum length scale in the vertical) the eddy diffusivity is usually much larger in the horizontal than in the vertical. Values for the horizontal eddy diffusivity have been estimated to be of the order of $K_h = 500\,\mathrm{m^2\,s^{-1}}$ (Gargett, 1984) while K_z can range from about $10^{-6}\,\mathrm{m^2\,s^{-1}}$ in the depths of the ocean or in stratified lakes to about $1\,\mathrm{m^2\,s^{-1}}$ in places with strong tidal and wind induced turbulent mixing (Simpson et al., 1996). We can now define a mixing time scale

$$\tau_K = \frac{\ell^2}{K} \tag{1.24}$$

which gives an estimate of the time it takes turbulent diffusion to cover the distance ℓ. Using the above value of the horizontal eddy diffusivity and a length scale of $\ell = 1000\,\mathrm{m}$ we obtain $\tau_K = 0.5\mathrm{h}$. For transport in the vertical, using $K_z = 10^{-3}\mathrm{m^2\,s^{-1}}$ and $\ell = 10\mathrm{m}$ we get $\tau_K \approx 1$ d. These time scales can be compared to those for molecular diffusion. For temperature, the molecular diffusivity is about $\gamma_T = 1.5 \times 10^{-7}\,\mathrm{m^2\,s^{-1}}$, for mass the molecular diffusion is $\gamma_m = 1.5 \times 10^{-9}\,\mathrm{m^2\,s^{-1}}$. A temperature gradient that exists across a distance of 10 m would,

in the absence of turbulent diffusion, be able to persist for a time of about $\tau_{\gamma_T} \approx 21$ years. A salinity gradient across the same small distance would take a mind-boggling 2100 years before it was eroded by molecular diffusion. Without turbulent diffusion, the ocean would thus be a very heterogeneous place where gradients in temperature, salinity, etc, would be able to persist for a very long time. The ineffectiveness of molecular diffusion to transport a property effectively over a significant distance will be revisited in Section 1.5.1 in the context of the diffusion limitation of small phytoplankton.

1.2.5 Modelling Turbulence

Like turbulence itself, the modelling side of this subject is an area of active research which is reflected in the great abundance and variety of turbulence models in the literature. State of the art reviews exist with Rodi (2000) and Kantha and Clayson (2000) where several different models are described, or with Simpson et al. (1996) and Burchard and Bolding (2001) where the performance of various models is compared.

One of the best known early models of turbulence goes back to Prandtl (1925) and is generally referred to as the mixing length model. It employs the concepts of eddy viscosity and diffusivity, directly linking the eddy viscosity to the local gradient in the macroscopic velocity through the mixing length ℓ_m which has to be prescribed through physical reasoning or empirically: $N_z = \ell_m^2 |\partial \overline{U}/\partial z|$. The advent of computers and their steady increase in performance has led to a simultaneous increase in the complexity of the models. Energy-equation models appeared (one-equation models) which also required *ad hoc* assumptions about the length scale L. A good compromise between model complexity and efficiency is provided with the so-called two equation models which contain transport equations both for the energy and the length scale of turbulence.

Two Equation Models of Turbulence Closure

For dimensional reasons, the eddy viscosity is proportional to a velocity scale q and a length scale L that characterise the turbulent flow. Two-equation models therefore contain one transport equation for q (or often for the TKE instead, using the relation $E = q^2/2$) and a second equation for L (or a combination of L and E since the latter is known from the first equation). While the energy equation is generally of the form of Eq. (1.19) (see below), different approaches have been taken to obtain the length scale. These two approaches have developed into two separate and almost competing schools, using different styles of notation. One school employs the so-called k-ε models ($k \equiv E$ in the notation in this thesis) where the second equation describes the transport of the dissipation ε and the length scale is found through the relation $\varepsilon \propto E^{3/2}/L$ [Eq. (1.4)]. The second school uses equations for E and the product $E\,L$ and is based on two papers by Mellor and Yamada (1974) and Mellor and Yamada (1982). According to Rodi (1987), the arguments of the relative merits of the ε and EL equations are rather academic because both equations are fairly empirical and, with the

constants suitably adjusted, perform in a similar manner. It has been only recently, however, that cross-comparisons and attempts to unify the notation have been made (Burchard and Deleersnijder, 2001; Burchard and Bolding, 2001). These comparisons indeed confirmed the qualitative equivalence of both approaches, especially if the improved version of the Mellor-Yamada (MY) model by Galperin et al. (1988) is used which has been accepted to replace the original version (Mellor, 2001). The governing equations for both approaches are

energy equation

$$\textit{both:}\quad \frac{\mathrm{D}E}{\mathrm{D}t} = \frac{\partial}{\partial z}\left(K_q\frac{\partial E}{\partial z}\right) + N_z\left[\left(\frac{\partial \overline{U}}{\partial z}\right)^2 + \left(\frac{\partial \overline{V}}{\partial z}\right)^2\right] + K_z\frac{g}{\varrho}\frac{\partial \varrho}{\partial z} - \varepsilon \tag{1.25}$$

length scale equations

$$k\text{-}\varepsilon\text{:}\quad \frac{\mathrm{D}\varepsilon}{\mathrm{D}t} = \frac{\partial}{\partial z}\left(N_\varepsilon\frac{\partial \varepsilon}{\partial z}\right) + A_1\frac{\varepsilon}{E}\left\{N_z\left[\left(\frac{\partial \overline{U}}{\partial z}\right)^2 + \left(\frac{\partial \overline{V}}{\partial z}\right)^2\right] + A_2\,K_z\frac{g}{\varrho}\frac{\partial \varrho}{\partial z}\right\} - A_3\frac{\varepsilon^2}{E} \tag{1.26}$$

$$MY\text{:}\quad \frac{\mathrm{D}q^2\ell}{\mathrm{D}t} = \frac{\partial}{\partial z}\left(K_q\frac{\partial q^2\ell}{\partial z}\right) + B_1\,\ell\left\{N_z\left[\left(\frac{\partial \overline{U}}{\partial z}\right)^2 + \left(\frac{\partial \overline{V}}{\partial z}\right)^2\right] + B_2\,K_z\frac{g}{\varrho}\frac{\partial \varrho}{\partial z}\right\} - \ell\varepsilon W \tag{1.27}$$

$$\text{with}\qquad W = 1 + B_3\frac{\ell}{\kappa}\left(\frac{1}{z} + \frac{1}{|z-H|}\right)\qquad (0 < z < H) \tag{1.28}$$

In the MY scheme, W is a wall-proximity function which comes into force near the boundaries to achieve $\ell \approx \kappa z$ for $z \to 0$ and $z \to H$, where $\kappa = 0.41$ is von Kàrmàn's constant. The A_i and B_i are 'universal' empirical constants that can be determined from simple turbulent flows in the laboratory. N_ε and K_q are the diffusivities of ε and q respectively with $K_q = N_z/const$. Usually $const = 1$ and $K_q = N_z$. In both schemes, the eddy viscosity and diffusivity are found through relations of the form

$$N_z = c_\mu \ell q \qquad \text{and} \qquad K_z = c'_\mu \ell q \tag{1.29}$$

where c_μ and c'_μ are called stability or structure functions. Their choice depends on the Richardson number and combinations of the above empirical constants. The shape of these functions has been the subject of many studies (Galperin et al., 1988; Kantha and Clayson, 1994; Burchard and Baumert, 1995; D'Alessio et al., 1998; Canuto et al., 2001) which shows that entirely satisfying solutions have not been found yet and that they might never be found.

Known shortcomings of both models are:

- they mix insufficiently (Martin, 1985);
- they fail to represent non-local (i.e. macroscopic) processes (D'Alessio et al., 1998);
- they do not consider breaking waves [a parameterisation exists by Craig and Banner (1994) but has not yet been successfully implemented into these two-equation models (Burchard and Bolding, 2001)];

- they do not consider internal waves. Generally, internal waves are parameterised as background diffusivity in ocean models, but less arbitrary suggestions exist by Kantha and Clayson (1994) and Canuto et al. (2001).

More realistic (and thus more complex) models of turbulence have therefore been developed which are often used to calibrate these more simple representations. They are briefly described in what follows. A more detailed description of the particular k-ε model used in this study is provided in Section 2.1.2.

Large Eddy Simulation Models

This approach is based on the argument that most of the turbulent kinetic energy, and thus most of the turbulent transport, is in the largest turbulent eddies. As was discussed previously, at smaller scales, the turbulence becomes practically independent of the source, i.e. the shape and structure of the smaller eddies will be very similar for different types of turbulent flow. The idea behind the large eddy simulation (LES) is thus to simulate the large eddies at the integral scale explicitly and parameterise the smaller scales by approaches such as the inertial subrange of the turbulence spectrum (Section 1.2.1). This appears to work very well for convective boundary layers, like those in the atmosphere, as the dominant structures in these kinds of flows are large buoyant eddies. The models are less successful with shear-generated turbulence and in scenarios like the oceanic mixed layer, as the largest eddies tend to be quite small in these cases and an adequate resolution would require large amounts of computing power (Kantha and Clayson, 2000). Also near boundaries, the LES struggles as it cannot parameterise the length scales correctly. Nevertheless, in a field where experimental data are hard to come by, LES has provided useful information on the larger eddies that has been used to calibrate less complex models such as the two-equation models that were described in the previous paragraphs. A more detailed description of LES models can be found in Kantha and Clayson (2000).

Direct Numerical Simulation Models

Direct numerical simulation (DNS) models represent one further step up from LES in terms of complexity, as the DNS approach attempts to explicitly solve the Navier-Stokes equations for all scales from the Kolmogoroff micro-scale to the largest integral scale. This task is monumental and even with the most powerful computers, this method is currently not capable to simulate any large scale oceanographic or geophysical flow. The advantage of DNS models is that they manage to solve the Navier-Stokes equations without approximations thereby allowing to numerically calculate and thus elucidate certain properties of the flow that are difficult if not impossible to measure. These simulations often provide the only available data that can be used to better understand the turbulent processes and, as in the LES case, calibrate less complex models. Again a more detailed review of this subject can be found in Kantha and Clayson (2000).

1.3 Phytoplankton as Primary Producers

Having introduced some of the physical issues relevant to the present study, this section will turn the focus to the biology. The following paragraphs will give a short overview of the role of phytoplankton as primary producers in the world's oceans. The light- and nutrient dependence of growth as well as seasonal cycles in various geographical regimes are discussed. The morphological adaptations and biology of phytoplankton are discussed in Section 1.4.

Phytoplankton are the dominant plants in the ocean and through photosynthesis, they convert inorganic materials (such as nitrate or phosphate) into organic compounds (e.g. lipids or proteins). As primary producers, phytoplankton form the first link of the oceanic food chain that reaches through all trophic levels. In order to photosynthesise, phytoplankton require carbon dioxide, water and light energy to produce carbohydrates. Although a number of steps are involved, the main chemical reactions are usually summarised as

$$\underbrace{6\,CO_2}_{\text{carbon dioxide}} + \underbrace{6\,H_2O}_{\text{water}} \overset{\text{photosynthesis}}{\underset{\text{respiration}}{\rightleftharpoons}} \underbrace{C_6H_{12}O_6}_{\text{carbohydrate}} + \underbrace{6\,O_2}_{\text{oxygen}} \tag{1.30}$$

The process of photosynthesis itself occurs within the chloroplasts and is driven with the energy provided by the sun. The chloroplasts contain the photosynthetic pigments where the conversion from radiant to chemical energy takes place. The dominant pigment is chlorophyll *a* but there are also chlorophylls *b, c,* and *d* plus several accessory pigments (carotenes, xantophylls, and phycobilins) present in many species. Each of the above pigments is able to absorb light of wavelengths within the range of about 400-700 nm but each pigment shows a different absorption spectrum depending on the molecular structure and the required excitation energy. This range of wavelengths ($400 < \lambda < 700\,\text{nm}$) that can be utilised for photosynthesis is referred to as photosynthetically active radiation (PAR). As the process of light absorption is based on the quantum interpretation of light, the commonly used irradiance unit is the Einstein [E] which represents one mole of photons. For monochromatic radiation the conversion from this quantum based unit to the SI unit Joules is easily achieved by using Planck's relation

$$1\ \text{Einstein} \mathrel{\hat{=}} N_A h\nu\ \text{Joules} \tag{1.31}$$

where N_A is the number of photons in one mole ($6.023 \cdot 10^{23}$), h is Planck's constant ($6.626 \cdot 10^{-34}$ J s) and ν the frequency associated with the particular wavelength. For the entire PAR spectrum the conversion is less straightforward since there is a range of frequencies to convert and the amount of photons within the PAR range depends on the distribution of solar energy over this frequency range. For a wide range of marine waters, Morel and Smith (1974) found that the conversion factor between Einsteins and Joules varied no more than ±10% from the average of $1\,\text{J} \mathrel{\hat{\approx}} 4.16 \cdot 10^{-6}\,\text{E}$. This value has been widely accepted in the literature and will be used also in the present study.

1.3.1 Photosynthesis as a Function of the Incident Light

The rate of photosynthesis thus depends on the rate of capture of light quanta from within the PAR range. This is not a simple proportionality, however, as the amount of primary production also depends on how efficiently the photosynthetic apparatus can make use of the absorbed energy. This varies between species and also within one species depending on the physiological state of the cells. Light quanta may be collected by the pigments faster than the electron carriers and enzymes can make use of them. This is particularly true in high light intensities where the excess absorbed energy can inactivate the photosynthetic system and lead to photoinhibition (see Section 1.3.2).

The dependence of the photosynthetic production, P, on the available light, I, has been widely investigated. The so-called P/I curves usually result from ^{14}C incubation experiments where living phytoplankton cultures are inoculated with ^{14}C and split into sub-samples which are incubated simultaneously at different constant irradiances for a set time period (usually between one to several hours). The net carbon uptake by the cells is determined and divided by the incubation time to give an average rate of photosynthetic carbon production at each light intensity. The result is a plot of photosynthesis versus irradiance: the P/I curve. Apart from the ^{14}C method which yields the photosynthetic rate in units of mg C per mg chl a per time, other methods exist that measure primary production in terms of the produced oxygen or carbon dioxide [cf. Eq. (1.30)] in μmoles CO_2 or O_2 per mg chl a per time.

Much effort has gone into finding a functional description of the light dependence of P but the fact that P/I curves are in general not repeatable between experiments has been a major obstacle to advance in this field[2]. Nevertheless, the need to quantify primary production produced a variety of functional forms (e.g. Jassby and Platt, 1976) that are widely used in the marine community. Most of the functional forms share some common properties which will be discussed using the example curve from Fig. 1.4.

In the dark, the cells usually exhibit a net consumption of O_2 or liberation of CO_2 [see

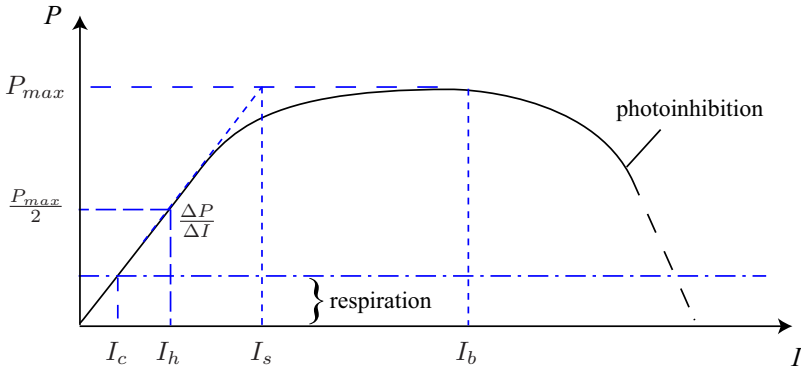

Figure 1.4: Typical shape of a P-I curve representing the response in phytoplankton production to light. The various marked irradiances are I_c = compensation point, I_h = half saturation point, I_s = saturation onset and I_b = inhibition threshold (see text).

[2]The sources of this variability will be further discussed in the context of photo-acclimation in Section 1.3.2.

Eq. (1.30)] as a result of cell respiration. As the light intensity is increased, photosynthetic production increases also but respiration will initially still be higher than production. At a certain compensation light intensity, I_c, the production will balance the respiration and beyond this point net positive photosynthesis is achieved. The typical behaviour is that P increases linearly with I up to a certain value. The slope of this initial linear increase is the quantum yield of the cell: $\alpha := \Delta P/\Delta I$. At some point, the graph begins to curve and eventually level off at the maximum photosynthetic rate P_{max}. By extrapolating the linear part of the curve one obtains the saturation onset irradiance I_s. With further increase in irradiance, P begins to decrease as photoinhibition sets in. The irradiance at which this decrease occurs is termed the inhibition threshold I_b (see also Section 2.3.2). The curve is often narrower than in the example shown and I_b may be quite close to I_s.

If we assume an exponential decrease of the irradiance with depth (see Section 2.3.1) then we can assign each of the above light intensities certain depths in the water column. The compensation light intensity, I_c, for example, becomes the compensation depth D_c, etc. Above the compensation depth, the cell will be a net producer of O_2, below D_c, the cell will consume O_2. Over the course of a day, a cell might be mixed above and below the compensation depth and thus experience an average light intensity I_D. The mixing depth over which I_D equals I_c is called the critical depth D_{cr} after Sverdrup (1953). At this depth, the total respiration, represented by the area of the rectangle *abdc* in Fig. 1.5, equals the total gross production which is represented by the area *ace*. If the depth of the surface mixed layer (SML) is above D_{cr}, the daily production of all cells in this water column is likely to exceed the respiration and one expects to see an increase in biomass. If the depth of the SML is below the critical depth the cells will receive a light dose that is on average below the compensation point and thus the number of cells in the water cannot increase. The shallowing of the SML above D_{cr} as the irradiance increases in spring each year has been recognised as one of the main mechanisms to initiate the spring bloom (see Section 1.3.4).

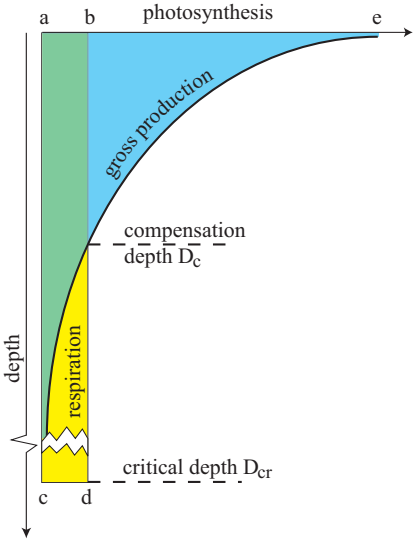

Figure 1.5: Illustrating the concepts of compensation and critical depth. See text for details.

1.3.2 Photo-acclimation

Phytoplankton live in highly dynamic environments. Their photosynthetic apparatus may be subject to significant stresses because of rapid changes or imbalances in irradiance and nutrient supply. As mentioned above, turbulence affects the light history of phytoplankton cells by moving them vertically up and down through the light gradient. In addition, they are exposed to more short term changes such as alternate focusing and defocusing of light by surface waves (Falkowski, 1984) or the passing of clouds. On longer time scales there is the diel

irradiance cycle of the sun and at the extreme end the variation caused by the passing of the seasons. Apart from the latter, a single generation may be exposed to the entire spectrum of this variability. As a result, the cells have developed mechanisms to acclimatise to their light environment. The kinetics of the different acclimation processes are very complex. They occur on several levels and time scales, ranging from seconds (e.g. dissipation of excess electrons through induction) over minutes (state transitions and changes in the number of Rubisco enzymes, i.e. the quantum yield α) to hours (changes in the chlorophyll to carbon ratio and thus P_{max}). An extensive body of literature exists on this topic (e.g. Marra, 1978*a*,*b*; Platt et al., 1980; Perry et al., 1981; Falkowski, 1983, 1984; Neale and Marra, 1985; Neale and Richerson, 1987; Cullen and Lewis, 1988; Geider et al., 1997; Lizon et al., 1998; MacIntyre et al., 2000). One often finds that the terms photo-adaptation and photo-acclimation are used interchangeably in the literature. This study will follow the recommended terminology by Falkowski and Raven (1997) who differentiate between the above mentioned short term *acclimation* processes and physiological *adaptations* which occur on longer time scales (through genetic modifications in the cells).

Due to the inherent difficulty of measuring vertical turbulent velocities and diffusivities in the ocean, it has been suggested (Marra, 1978*b*; Falkowski, 1983) that the recent light history of a cell could be used to derive information about the mixing intensity in the euphotic zone. This hypothesis was examined observationally by Lewis et al. (1984*b*) who measured the rates of turbulent kinetic energy (TKE) dissipation, ε, and compared them to the simultaneously measured maximum potential photosynthetic rate normalised to chlorophyll *a*, P_{max}. They found that at high TKE dissipation rates there was little variation in P_{max} with depth. On days when TKE dissipation was low, surface samples showed higher values of P_{max} which implies that these cells had enough time to adapt to the higher irradiance at the surface. Their results suggest that the dominant source of variation, responsible for the observed difference in physiological performance, is turbulence-induced fluctuations in light incident on the algal cell. They observed only few motile cells but suggested that motile cells could potentially resist the vertical displacement induced by turbulence. Using the swimming time scale τ_s from Eq. (1.37) and comparing it to the mixing time scale τ_m which they substitute as

$$\tau_m = \frac{h^2}{K} \approx \frac{4h^2}{\varepsilon} N^2 \tag{1.32}$$

where N is the Brunt-Väisälä frequency, they obtain a condition that relates the swimming velocity w to the TKE dissipation rate ε

$$\overline{w} \overset{!}{>} \frac{\varepsilon}{4hN^2} \tag{1.33}$$

This condition must be fulfilled in order for swimming to dominate over mixing. Lewis et al. (1984*b*) conclude by reiterating the hypothesis from Marra (1978*b*) and Falkowski (1983) that the rate of vertical mixing might be inferred from the vertical distribution of appropriate algal physiological indicators. This idea has also been investigated by Cullen and Lewis (1988) and Therriault et al. (1990), and more recently by Nagai et al. (2003) and Farmer and McNeil (1999). The latter authors employ neutrally buoyant floats to determine the vertical trajectories and light histories of suspended phytoplankton. They then use a photo-acclimation model

to draw conclusions about the diurnal variations of the subsurface production rates as a result of photo-acclimation. In the context of the present study, the inclusion of photo-acclimation in the biological model might prove crucial for trying to determine the real benefits of motility to the individual cell.

1.3.3 Nutrient Dependence of Photosynthesis

Apart from light, phytoplankton also require a variety of nutrients to perform photosynthesis. Some of which are abundant throughout the ocean (e.g. magnesium, calcium, potassium, sulphate, etc.), others can become limiting in certain situations (e.g. nitrogen, phosphate, silicate, iron, manganese). Often there is also a synergistic effect between nutrients. Some areas of the subarctic North Pacific, the Equatorial Pacific or Antarctic Ocean, for example, are characterised by high nitrate but low chlorophyll concentrations (so-called HNLC areas). The reason for the low phytoplankton biomass has been attributed to a lack of iron which is required by phytoplankton to utilise inorganic nitrogen (e.g. Martin et al., 1994; Falkowski, 1995).

The process in which phytoplankton convert inorganic nitrate and phosphate into carbohydrates and proteins can be abbreviated as

$$C_{106}N_{16}P \rightarrow \text{organic compounds} \tag{1.34}$$

Thus with one atom of nitrogen, the cell can metabolise about $106/16 \approx 6.6$ atoms of carbon. This C:N ratio is usually referred to as the Redfield ratio. For phosphate, the corresponding ratio is C:P=106. Each species has different requirements for each nutrient which allows for a great variety of phytoplankton to grow under certain environmental conditions.

The relative availability of nutrients for phytoplankton (particularly of nitrate and phosphorous which are most often present in limiting concentrations) can be used to classify aquatic environments. Regions that have low concentrations of essential nutrients, and therefore low primary productivity, are called oligotrophic (usually $< 0.1\,\mathrm{mg\,Chl\,m^{-3}}$). Much of the production in these areas is often maintained through recycled nutrients, mainly in the form of ammonia from excretion by plankton grazers. This type of production is usually termed regenerated production as opposed to new production which is based on nitrate. Regenerated production alone cannot maintain a certain population level due to the constant sedimentation loss of dead organisms and excretions from the euphotic zone. It is therefore necessary to also have a source of new nutrients which allows for new production to supplement regenerated production (see below). The ratio of new production to total production [termed f-ratio, (Eppley and Peterson, 1979)] is very important for estimates of global carbon budgets in climate models. On the other end of the scale there are eutrophic waters. They contain nutrients in high concentrations and high phytoplankton densities (usually 1-10 $\mathrm{mg\,Chl\,m^{-3}}$). In extreme cases, where an excessively high nutrient concentration is present (often due to anthropogenic sources) one speaks of hypertrophic environments. Intermediate waters are sometimes classified as mesotrophic.

1.3.4 Seasonal Cycles of Primary Production in the Surface Ocean

In the open ocean environment one can distinguish between several geographical regimes which each exhibit their own characteristic light, nutrient, and temperature structure. Near the equator, this structure is more or less static throughout the year whereas towards the poles these structures show a strong seasonal dependence. This section will give a brief general overview over the different seasonal cycles in these regimes.

Tropical Waters

The warm tropical waters such as the Equatorial Pacific are characterised by a permanent thermocline dividing the water column into a nutrient depleted (oligotrophic) surface and an nutrient richer bottom layer. This scenario is similar to a late summer scenario in temperate waters. The pycnocline acts as a stable barrier to vertical diffusion and thus nutrients from the sub-surface mixed layer diffuse only slowly into the SML. If the depth of the pycnocline is less than the euphotic depth, the pycnocline area will have sufficient light, nutrients and a high enough residence time for the phytoplankton cells (due to the reduced turbulent mixing) to form a population maximum, the so-called subsurface chlorophyll maximum (SCM) (see Section 4.1)[3]. This productive zone is bounded at the bottom by either low light or the edge of the pycnocline and at the top by low nutrients. In some tropical regions this picture does not apply, e.g. in the equatorial upwelling systems where the large scale vertical transport of nutrients from below supports very high primary and secondary production near the surface. According to Malone (1980) nano- and picoplankton account for more than 75 percent of phytoplankton biomass and 80 percent of primary productivity in oceanic waters where seasonal and geographical variations are small. Continental shelf and upwelling regions are characterised by a higher more variable biomass supporting a higher amount of microplankton.

The Subtropical Gyres and Large Eddies

The oligotrophic waters of the subtropical gyres cover more than 60% of the total ocean surface and contribute over 30% of the global marine carbon fixation (Maranon et al., 2003). These large structures provide some seasonality due to the increased winds in winter which can significantly deepen the SML and thus cease production and replenish the SML with nutrients. This small variability translates into large differences in primary production (Maranon et al., 2003). The subtropical gyres are driven by the trade winds and by the westerlies of the temperate regions while their subpolar counterparts depend on the polar easterlies. They consist of a narrow, swift-flowing western boundary current (e.g. the Gulf Stream for the gyre in the northern subtropical Atlantic), an eastward-flowing zonal current, a broad and slow-moving eastern boundary current, and a westward flowing zonal current. These swift moving boundary currents often shed large scale eddy structures which are able to persist for several months creating a self-contained mesoscale habitat. Two main patterns are present: in the

[3]Note that the SCM does not necessarily constitute the biomass maximum in the water column.

anti-cyclonic eddies, the surface water converges towards the centre of the eddy (due to the Coriolis force) resulting in a depression of the thermocline (warm core eddy). In this situation no new nutrients can come to the surface from below and production is highly nutrient limited. The opposite is true for cyclonic or cold core eddies, were the diverging flow of the surface water causes permanent upwelling of deep water at the centre of the eddy which provides a constant source of nutrients to the SML. Cyclonic eddies are therefore very productive.

Temperate Waters

Temperate waters show a strong seasonality in their annual production due to the pronounced changes in the physical forcing. In winter, increased wind mixing in combination with reduced solar heating (which causes convection) lead to a progressive deepening of the SML. This deepening of the mixed layer brings up more nutrients from below but as a result the phytoplankton cells also find themselves more often below the euphotic zone where they can no longer photosynthesise. At the end of winter, when surface warming increases again, the reverse process begins. The SML starts to shallow and as it surpasses the critical depth (cf. Fig. 1.5), the phytoplankton cells start to spend most of their time within the euphotic zone where they find high concentrations of nutrients due to the negligible consumption during the winter period. The result is an explosive increase in biomass in the surface mixed layer, which is termed the spring bloom. As the season progresses towards summer, the spring bloom begins to move poleward following the increasing irradiance levels. This period of intense growth is short lived, however, as the nutrients in the SML become depleted quickly. From about mid to late summer, the conditions become similar to the tropical regime (see above) where production is limited to what can be sustained by recycled nitrogen and the small amount that diffuses through the pycnocline. The species composition often shifts from a diatom dominated population to motile cells such as flagellates or coccolithophores. If these stably stratified conditions occur on the continental shelf, high production can often be observed near tidal mixing fronts, where a shallowing in the bathymetry causes the tidal mixing to push the isopycnals to the surface (Simpson and Hunter, 1974; Simpson and Bowers, 1981). The highest sustained production usually occurs on the more stable side of the front but can be high throughout the frontal region. As the wind mixing and surface cooling increase again towards the end of the year, more nutrients become entrained again in the SML and an autumn bloom may occur just before the SML deepens again below the critical depth.

In order to understand the challenges and issues faced by the various types of phytoplankton in these different environments, the following sections will give a brief overview of the biological and morphological adaptations they have developed to face these challenges.

1.4 Phytoplankton Biology and Morphology

There are over 20 000 species of marine phytoplankton in the world's oceans with new species being added continually. Most species belong to the nano- to microplanktonic size range

(Table 1.1) but some species are large enough to be collected in fine meshed nets. They differ greatly in shape, physiology and geographical distribution. Table 1.2 gives a summary of the major types. Due to this large variety, it is beyond the scope of this thesis to provide a complete review on the subject. As the focus is on motility and the advantage it provides over non-motile cells, this section will focus on two main representatives from each group: dinoflagellates for motile phytoplankton, and diatoms, as representatives for non-motile species.

TABLE 1.2: Overview of the major taxonomic groups of phytoplankton (adapted from Lalli and Parsons, 2002).

Common name	Area(s) of predominance	Common genera
Blue-green algae/bacteria	Tropical	Oscillatoria, Synechococcus
Red algae	Cold temperate	Rhodella
Cryptomonads	Coastal	Cryptomonas
Chrysomonads, Silicoflagellates	Coastal, Cold waters	Aureococcus, Dictyocha
Diatoms	All waters, esp. coastal	Coscinodiscus, Rhizosolenia
Chloromonads	Brackish	Heterosigma
Coccolithophorids, Prymnesiomonads	Oceanic, Coastal	Emiliania, Isochrysis
Euglenoids	Coastal	Eutreptiella
Prasinomonads	All waters	Tetrasalmis
Dinoflagellates	All waters, esp. warm	Ceratium, Gonyaulax

1.4.1 Diatoms

Diatoms are one of the most abundant groups and possibly the most studied phytoplankton group in the ocean. All diatoms are unicellular organisms that can have sizes from 2 μm to over 1000 μm (Lalli and Parsons, 2002). They possess an external skeleton made of silica which can account for between 4-50% of the dry weight of a cell. They thus require silicate to grow which can become limiting in some cases. They are able to multiply both by asexual division and sexual reproduction. Planktonic diatoms do not possess any locomotor structures and are thus immotile. It has been suggested, however, that their rapid growth (observed growth rates for diatoms can exceed 4 doublings per day, Malone et al., 1973) can cause an increase in buoyancy (e.g. Eppley et al., 1967) which might enable them to migrate upwards into the euphotic zone more quickly in periods of reduced mixing. Most diatoms, however, are negatively buoyant and therefore rely on high vertical mixing to keep them entrained in the euphotic zone. Some species also exhibit a variety of mechanisms which retard sinking such as having a small size in general or by forming long chains. In these chains water becomes

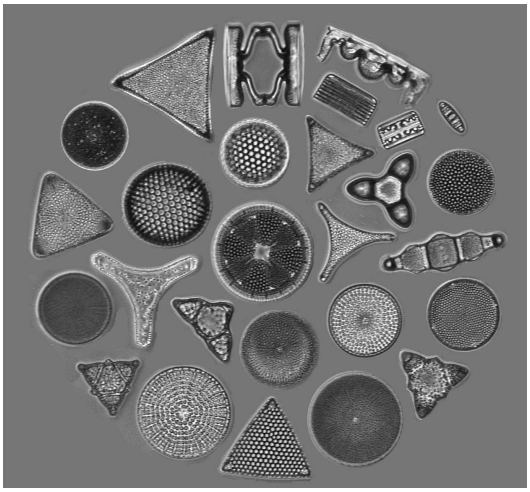

Figure 1.6: Composite image showing the variety of diatom shapes encountered in nature. (Image source: Plankton image database at http://botit.botany.wisc.edu/)

trapped in the gaps between the cells and this increased porosity leads to a lower effective density and thus retards the sinking. Cells that are able to become positively buoyant often show the opposite behaviour in that they form large spherical aggregates in order to bundle the buoyancy into a small a volume as possible to increase their potential velocity. These aggregates also face a lower risk of predation as their sheer size makes them difficult to ingest for zooplankton.

1.4.2 Dinoflagellates

The second most abundant phytoplankton group after diatoms are the dinoflagellates. They can exhibit characteristics of both plants (autotrophs) and animals (heterotrophs) with some species being mixotrophic. They can assume a variety of shapes ranging from the so-called *bladder type* (cf. top image in Fig. 1.7), in which the cells are greatly expanded in size, over the horned *branch type* (lower image in Fig. 1.7) to the elongated *ribbon type*. Their sizes range from 2 to 2,000 μm with the majority between 2 and 200 μm (Kamykowski et al., 1992). The collection edited by Taylor (1987) gives a good overview of the morphology and behaviour of dinoflagellates.

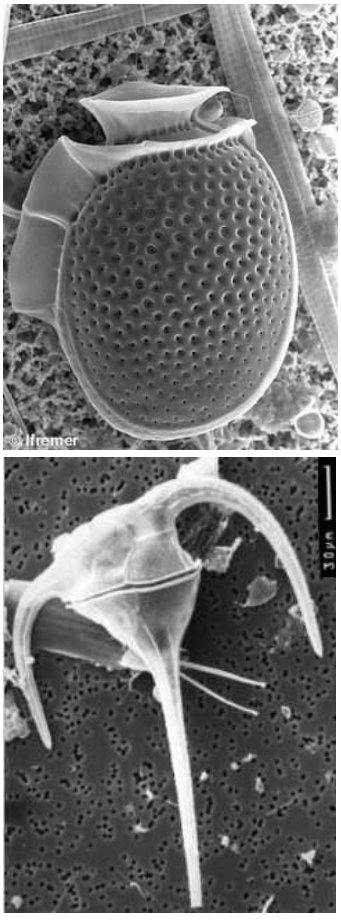

Figure 1.7: SEM images of *Dinophysis sp.* (top) and *Ceratium sp.*

Usually dinoflagellates are slightly more dense than seawater with $1.03 < \varrho_{cytoplasm} < 1.10\ \mathrm{g\,cm^{-3}}$ while $1.021 < \varrho_{seawater} < 1.028\ \mathrm{g\,cm^{-3}}$). Unlike diatoms, they possess two flagella and are thus capable of locomotion. Two configurations exist: the Desmohpyceae and the Dinophyceae. In the former configuration, the two flagella extend both from the anterior end of the cell (e.g. in *Prorocentrum sp.*). The majority of dinoflagellate species are part of the Dinophyceae, however, (e.g. *Dinophysis sp.*) where one flagellum extends from the posterior end of the cell and propels the organism forward, and the second is wrapped transversely around the cell allowing it to rotate about the main axis. The flagella are often covered in hairs, scales and swellings. The first two are believed to aid the swimming. The swellings are often involved in photoreception, providing the cell with a means to detect light from or towards which it may want to swim.

The flagella provide the cell with a highly specialised swimming mechanism that is particularly adapted to the specific environment of low Reynolds numbers (see Section 1.1). The flagella perform corkscrew-like rotations which, due to their non-periodicity, allow the cell to move forward in this viscous environment (Purcell, 1977). Another less common mechanism exists in ciliates (e.g. *Mesodinium sp.*) where the cell uses a 'flexible oar' (cilium) for locomotion. Absolute dinoflagellate swimming speeds range from less than $0.1\ \mathrm{mm\,s^{-1}}$ to over $0.6\ \mathrm{mm\,s^{-1}}$

(Kamykowski and McCollum, 1986; Levandowski and Kaneta, 1987) although some velocities above 1.4 mm s^{-1} are reported (Lombardi and Capon, 1971; Horstmann, 1980). The largest velocities are reached only by the largest organisms (see Section 1.1.1) whereas most nano- and small microplankton have swimming velocities below 0.3 mm s^{-1}.

Strong vertical mixing could overcome the swimming efforts of dinoflagellates and move them out of the euphotic zone as well as produce other detrimental effects (see Section 1.6). This might explain why diatoms and dinoflagellates are often found to be mutually exclusive in the environment. Diatoms, in general, are more 'robust' than dinoflagellates, they can grow faster (Smayda, 1997), they have lower respiration rates than dinoflagellates and therefore survive longer in the dark (approx. 8 days for dinoflagellates compared to approx. 40 days for diatoms) (Broekhuizen, 1999). What is thus the reason for their success considering that they have apparently been endowed with less favourable qualities? Many dinoflagellate species are capable of mixotrophy or are outright heterotrophs. The autotrophic species have generally lower light requirements than diatoms to achieve their maximum photosynthetic rate. Their slow growth rate enables them to adapt better to low light conditions and they are able to utilise low ambient nutrient concentrations, outcompeting diatoms in the oligotrophic waters of the tropics and many other nutrient limited regions of the world oceans. Some species produce allelochemicals to repel predators and competitors ('harmful algal blooms'), and last but maybe not least, they are much more motile than other algal taxa. This might help them realise population growth rates which are similar to those of diatoms (Broekhuizen, 1999).

1.5 Mechanisms and Potential Importance of Motility and Vertical Movement

Having established the presence of locomotory structures in phytoplankton, the question remains how the cells could possibly use this motility. Clearly, there can be no general answer to this question as the use is likely to depend strongly on the environmental conditions and physiological requirements of the cell. This section will provide a very general outline of some of the most relevant hypotheses brought forward to explain the benefits of cell motility.

1.5.1 The Boundary Layer Hypothesis

As mentioned in Section 1.3.3, all phytoplankton cells in the sea have a need to exchange molecules such as O_2, CO_2 or NH_3 with the environment. Since all solid boundaries in a liquid medium have associated with them a boundary layer in which water movement is reduced (due to the no-slip condition at the boundary) this layer will impede the nutrient uptake of the organisms by creating a small depleted layer around it (Munk and Riley, 1952). Turbulence is very ineffective in transporting nutrients towards such small organisms as the smallest length scales of turbulent eddies are of the order of several millimetres (e.g. Osborn, 1978; Oakey and Elliot, 1980). Small organisms must therefore rely on molecular diffusion to overcome the

nutrient gradient across the boundary layer (Csanady, 1986). It has been suggested that the organisms could also use their motility (be it sinking or swimming) to generate movement relative to the water and hence replenish the boundary layer with nutrients. Swimming is found in a variety of organisms that range from bacteria-size upward. Depending on the size, the motive for swimming must differ, however, since its effects differ significantly. For small cells in the 1-10 μm range, diffusion is about 100 times more effective in supplying nutrients than movement. This is often expressed as the Sherwood number:

$$S = \frac{\text{time for transport by diffusion}}{\text{time for transport by movement}} = \frac{L^2/D}{L/u} = \frac{Lu}{D} \approx 10^{-2} \text{ for } L \approx 1\,\mu\text{m} \qquad (1.35)$$

where L is the distance over which the nutrient is to be transported, u the water velocity and D the diffusion constant. Hence these small organisms are likely to use their motility to search for higher nutrient concentrations rather than to reduce the diffusion limitation. Although the relative swimming speed of phytoplankton decreases with size (from about 100 body lengths per second for the smallest nanoplankton to about 1 body length per second for megaplankton) the effectiveness of swimming to increase the nutrient uptake is greatly enhanced. Most published studies agree that locomotion can alleviate about 30% of the diffusion limitation for the larger species and less for organisms $< 100\,\mu$m (e.g. Gavis, 1976; Pasciak and Gavis, 1974; Sommer, 1988; Berg and Purcell, 1977; Purcell, 1977). Despite this appreciable increase in nutrient uptake, the conclusion reached was that swimming and sinking are not very effective in overcoming the diffusion limitation but might just be sufficient to give one species a competitive edge over another.

1.5.2 The Migration Hypothesis

Other suggestions brought forward to explain the use of motility are based on the so-called *phytoplankton dilemma* (e.g. Klausmeier and Lichtmann, 2001) which refers to the spatial separation of the two primary resources for phytoplankton growth: light is supplied from above whereas nutrients are often more abundant at depth (see also Section 4.1). It was therefore suggested that phytoplankters could use their motility to adapt their position in the water column to meet their requirements of either of the two resources. Some experimental studies seem to confirm a tendency of phytoplankton to migrate upward into the euphotic zone during day time (phototaxis) to photosynthesise and downward to lower regions in the water column at night time (geotaxis) where they find more nutrient-rich waters (Kamykowski, 1995; Levandowski and Kaneta, 1987; Margalef, 1978; Kamykowski and Zentara, 1977). According to Smayda (1997) they exhibit a metabolic coupling between daylight photosynthesis and nocturnal nutrient uptake (and storage). Passow (1991) found that apart from showing the above mentioned positive phototaxis, some species that were monitored over two 27 hour periods in the Baltic Sea also showed to use their motility to avoid light saturation, following an isolume of approximately 100 $\mu\text{E}\,\text{m}^{-2}\,\text{s}^{-1}$ (a value which very much depends on the light history of the cells). Kamykowski (1995) found that swimming speeds of dinoflagellates were enhanced by 20% in the presence of light intensities above 40 $\text{W}\,\text{m}^{-2}$, suggesting that ascents

aided by light may compensate for descents aided by cell sinking. Apart from this taxis-directed orientation, alternate migration patterns have been observed which suggest that there is also the possibility of the cell orienting itself according to its metabolic state (Kamykowski and Yamazaki, 1997) producing circadian rhythms which are out of phase with the daylight cycle. Broekhuizen (1999) argues that this migratory behaviour might only pay off for the fastest swimmers while slower species take longer for the trip and are therefore more prone to disruption by turbulence which could lead to starvation. This seems particularly true for stratified open ocean scenarios where the cell would have to cover tens of metres per day to oscillate between the lower (nutrient rich) and the upper (light rich) layers.

Yet a different migratory strategy was brought forward by Crawford and Purdie (1992). These authors monitored the vertical distribution of the planktonic, phototrophic ciliate *Mesodinium rubrum* over a tidal cycle in the macro-tidal estuary of Southampton Water on the southern coast of Great Britain (see Chapter 3). They found evidence for the cells to use their motility in order to avoid the high velocities near the surface which would flush them from the estuary when the ebb flow sets in. They use their phenomenal burst swimming speed of over $8\,\mathrm{mm\,s^{-1}}$ (Jonsson and Tiselius, 1990) to migrate to greater depths during the high water stand (see Section 3.1.1 for a description of the tides in Southampton Water) and resurface again at ebb tide. This migratory behaviour has been observed previously in other estuarine systems for some dinoflagellate species (Anderson and Stolzenbach, 1985).

1.5.3 The Turbulence Avoidance Hypothesis

Crawford and Purdie (1992) also claimed to recognise a general turbulence avoidance 'strategy' in the cells. The swimming behaviour of the particular species alternated between rapid "jumps" and periods of motionlessness. They argue that the frequency of the jumps increases as turbulence increases which would, without any directional response of the cell, lead to aggregations in more stable water. Although the cells are very small ($\oslash \approx$ 15-70 μm), dinoflagellates of similar sizes have been shown to be capable of detecting microscale fluid deformations down to turbulent length scales of the order of 33 μm which is the published threshold to stimulate dinoflagellate bioluminescence (Rohr et al., 1990). The capacity in phytoplankton for turbulence detection and avoidance seems thus possible.

1.5.4 Phytoplankton Sinking

The sedimentation loss of phytoplankton has been the subject of several studies (e.g. Sommer, 1984; Olesen, 1995; Visser et al., 1995*a*; Ruiz et al., 1996; Ruiz, 1996). It is relevant also for climate models as the sedimentation loss of cells is a measure for the atmospheric carbon export into the bottom mixed layer (e.g. Walsh, 1980). The buoyancy dependent sinking itself can be seen as another mechanism to vertically adjust one's position in the water column. For spherical particles with low Reynolds numbers, the sinking velocity can be calculated from the

Stokes Law

$$w = \frac{1}{18}\left[\frac{(\varrho_c - \varrho_f)\, g d^2}{\varrho_f \nu}\right] \tag{1.36}$$

where ν is the kinematic viscosity of water (typically $10^{-6}\ \mathrm{m^2\,s^{-1}}$ for sea water), g is the acceleration due to gravity, d the cell diameter and $\varrho_{c/f}$ the cell/fluid density. For particles whose shapes significantly deviate from that of a sphere, an effective diameter must be used to account for the increased friction of the water with the cells' non-spherical surface. Chain formation is an effective mechanism which is often used by negatively buoyant cells to reduce their effective density. Water becomes trapped in the gaps between the cells which increases their porosity and thus retards their sinking. Other cells like the cyanobacterium *Microcystis aeruginosa* for example, form large spherical colonies of 1000 cells and more. They possess gas vacuoles which provide them with positive buoyancy (see Section 5.2). By forming large spherical colonies they bundle their positive buoyancy into a geometry that provides the best surface-to-volume ratio (i.e. a sphere) thereby increasing the potential vertical velocities which allows them to cover greater distances. In general the sinking velocities are below the swimming velocities from Section 1.4.2 as the cells would otherwise quickly sink out of the euphotic zone. However, some of the larger diatoms can reach sinking velocities of up to $0.3\ \mathrm{mm\,s^{-1}}$.

Having a certain swimming or sinking velocity does not necessarily imply that the net vertical displacement of the cell is going to correspond to this velocity. The main problem for motile cells is that turbulent mixing may be strong enough in some cases to render any swimming efforts meaningless. The next section will therefore focus on the effects of turbulence, both on the motility and on the general cell physiology.

1.6 Phytoplankton and Turbulence

It is only recently, that turbulence has been accepted to the higher echelon of principal environmental variables that affect phytoplankton growth. It is now recognised to be of equal importance to some of the more traditional variables such as temperature, nutrient and light availability (e.g. Margalef, 1978; Lewis et al., 1984*b*; Berman and Shteinman, 1998; MacIntyre et al., 2000). In a stratified water column, for example, life in the surface mixed layer (SML) depends on the presence (or periodical occurrence) of turbulence to transport nutrients across the pycnocline. If the resupply of nutrients does not keep up with the consumption by phytoplankton, the SML becomes depleted, first of nutrients, and shortly after of phytoplankton (see Section 4.1). In the absence of turbulence, molecular diffusion would be the only mechanism to bring up nutrients from deeper water which would occur far too slowly to match the consumption (see Section 1.2.4).

It is important to distinguish between these macroscopic effects of turbulence and the microscopic effects that occur at the level of an individual cell. In terms of nutrient transport, turbulence has been shown to have only a small effect on the flux toward the individual organism (see Section 1.5.1). A different issue that is addressed in the present section is the degree to which turbulence affects the individual cell trajectories. Given the typical speeds, and the

observed turbulent velocity fluctuations, it is not clear how motility or sinking are impacted upon by turbulent mixing, and how this affects phytoplankton survival. It is often argued that the dominant species in stratified environments, for instance, tend to be dinoflagellates (e.g. Margalef, 1978; Smayda, 1997) due to their ability to position themselves at the nutricline. The magnitude of the swimming velocity can become crucial in these situations, however, since it not only determines the vertical distance a cell can cover over a diel cycle but also how well it can resist vertical mixing and maintain a deterministic swimming behaviour. Section 1.6.2 will summarise the more subtle effects that turbulence has on the cell metabolism (which can in turn affect the swimming behaviour).

1.6.1 Effect of Turbulence on Cell Trajectories

Karp-Boss et al. (2000) examined the success of phytoplankton re-orientation at various turbulent intensities. Due to the ambient velocity shear the phytoplankton cell will not only be subject to translatory displacements but also be rotated about an arbitrary axis. If the turbulence intensity is too high, they might be unable to re-orient themselves effectively and would therefore be unable to maintain a certain swimming direction. They pose the question of whether dinoflagellates could alter their swimming behaviour in response to the ambient shear field, in which case the resultant swimming behaviour could not be predicted by simply superimposing their swimming motion with the ambient flow field as has been done in previous studies (e.g. Yamazaki and Kamykowski, 1991; Kamykowski, 1995; Kamykowski et al., 1992). They conclude that if the time scale of re-orientation of the cells is shorter than the time scale of the smallest fluctuations in the turbulent flow, they might be able to re-orient effectively and maintain their swimming direction. Their experiments, using two different species of dinoflagellates, suggest that in natural conditions of weak to moderate turbulence the organisms are expected to be able to re-orient successfully. In stronger turbulence other mechanisms such as chain formation may be used to maintain a certain orientation of the organisms.

Kessler (1985) examined the passive orientation mechanism termed gyrotaxis. It is a purely physical process by which the orientation of a swimming cell in a velocity gradient is simply the result of compensating viscous and gravitational torques. This author was able to produce cell accumulations produced by a focusing of their swimming trajectories in a fluid jet.

One of the questions which remains unanswered is whether motility is still useful to a cell to adjust its vertical position in moderate to strong turbulence, or more precisely, whether there is something like a cut-off intensity of turbulence for the various swimming velocities above which deterministic directional swimming becomes impossible. Since it is difficult to answer this question at the level of an individual cell, a macroscopic quantity is often used in this context: the Peclet number $\mathscr{P}$

$$\mathscr{P} = \frac{\text{mixing time scale}}{\text{swimming or sinking time scale}} = \frac{\tau_m}{\tau_s} = \frac{h^2/K}{h/w} = \frac{w\,h}{K} \tag{1.37}$$

where K is the vertical eddy diffusivity, h a characteristic length (e.g. the depth of the surface mixed layer) and w the particle sinking or swimming velocity. It is usually argued that if

$\mathscr{P} \gg 1$, i.e. in cases where the mixing time scale is much larger than the swimming time scale, the cells will not be affected by turbulence and motility will win over mixing. If $\mathscr{P} \ll 1$, then the mixing timescale is much shorter and motility will have no or little effect on the particle's position.

In a modelling study by Ruiz et al. (1996), the authors attempt to quantify the sedimentation loss of phytoplankton cells from the surface mixed layer as a function of the turbulence intensity by superimposing the random turbulent motion onto the deterministic sinking (or swimming) behaviour of the cells. They show that for some species $\mathscr{P} \ll 1$ at any time, i.e. these species are not affected by turbulence at all, while other species which have $\mathscr{P} \approx 1$ might shift from a turbulence-sensitive state to a turbulence-insensitive state by modifying their sinking (swimming) velocities. As Visser (1997) rightly points out, however, these results only apply to water columns with isotropic turbulence which is not the case at the bottom of the surface mixed layer. If the turbulence is non-isotropic it is possible to define a localised Peclet number (see Section 3.3). However, in stratified scenarios the definition of the mixing depth becomes somewhat ambiguous since the vertical turbulent exchanges are hindered by the pycnocline.

1.6.2 Effect of Turbulence on Cell Metabolism

Strong turbulent mixing can disrupt the cellular clock, mitotic cycle (cell division) and alter nucleic acid concentrations (Berdalet and Estrada, 1993; Pollingher and Zemal, 1981; Estrada and Berdalet, 1998) and thus negatively affect the growth rate. It has also been observed that motile cells may suffer physical damage which can result in the loss of their longitudinal flagellum depriving them of their ability to swim forward. Such cells can only spin in place (Thomas and Gibson, 1990). In extreme cases, high shear rates can also induce cellular disintegration (Berdalet and Estrada, 1993). Turbulence can therefore negatively influence dinoflagellate growth by three mechanisms: physical damage, physiological impairment and behavioural modification. In these conditions the more robust but immotile diatoms are at an advantage since their residence time in the euphotic zone is increased. It should be noted, however, that the turbulent mixing in the above mentioned studies was created in a laboratory environment where the turbulence was usually produced by an oscillating grid. This method has fallen in disregard recently as the obtained results may suffer from the too high turbulence produced in the immediate environment of the grid which can induce the above described physical damage to the cells. The intensity of the grid generated turbulence in the above studies sometimes exceeded observed values in natural environments by over one order of magnitude.

1.7 Modelling Phytoplankton in a Lagrangian Framework

The concept of numerically tracking individual organisms through a turbulent aquatic environment is a powerful tool with which to investigate environmental processes and interactions between organisms and their physical environment. Section 1.7.1 compares the two fundamen-

tal approaches used in most marine models: the continuum based Eulerian and the individual based Lagrangian method. Section 1.7.2 examines to what degree the motion of a turbulent flow and a particle (e.g. plankton cell) may become decoupled, i.e. whether individual particles are able to follow the turbulent flow or whether adjustments need to be made when modelling their trajectories.

1.7.1 Lagrangian versus Eulerian Models

Until recently, it has been impossible to track a statistically significant number of individuals on a standard desktop computer, and most environmental processes have had to be treated statistically through ensemble averages, treating the organisms like a continuum property such as salinity or temperature. This Eulerian method has an inherent problem however, as Woods and Onken (1982) have pointed out: averaging non-linear equations before integration does not give the same results as averaging them after integration. While only the latter procedure is correct, the former is adopted, for example, in the Eulerian-continuum method of modelling primary production. Imagine a patch of phytoplankton in the surface mixed layer of the ocean for which we wish to calculate the primary production over 24 h. Using the Eulerian approach, we would proceed by applying the depth-averaged light intensity of the surface mixed layer to the entire particle ensemble and then integrate the growth function over time. The Lagrangian approach would first integrate over time, using the actual light history of each particle, and then we could build the ensemble average to evaluate the performance of the entire community. Only the latter procedure would yield the systematically correct results. Nevertheless, the Eulerian method has been used very successfully, since it is able to describe correctly some simpler properties of phytoplankton development and is computationally far cheaper than its Lagrangian counterpart. Due to the advent of high power computers, combinations of the Eulerian and Lagrangian method have emerged (e.g. Broekhuizen, 1999) where the nutrients and organic matter are described on a Eulerian grid and the phytoplankton cells are modelled using a Lagrangian approach.

Processes that rely on this Lagrangian approach range from primary production studies of planktonic cells, where the light history (photo-acclimation) or the motility of the individual is of crucial importance (e.g. Woods and Onken, 1982; Wolf and Woods, 1988; Barkmann and Woods, 1996; Kamykowski et al., 1996; Lizon et al., 1998), through sedimentation (e.g. Ruiz et al., 1996) and predator-prey encounter rates (e.g. Saiz et al., 2003), to trophic interactions (e.g. Metaxas, 2001).

Most of this earlier research was restricted to very simplified representations of the physical environment neglecting its spatial (e.g. Woods and Onken, 1982; Wolf and Woods, 1988) and temporal (e.g. Lizon et al., 1998) heterogeneity. The lower available resources in computing power also meant that phytoplankton were usually treated using the Eulerian continuum method rather than individuals (e.g. Lewis et al., 1984*a*).

Clearly, for the present study it is imperative to use the Lagrangian approach. Motility in particular cannot be modelled using the Eulerian method as the cell would be unable to

adjust its swimming behaviour in response to physiological requirements or external cues. Also the photo-adaptation processes cannot be accounted for without resolving each light history individually.

1.7.2 Fluid versus Particle Diffusivity

One issue that is generally ignored in biological applications of a Lagrangian particle tracking model is the fact that the eddy diffusivity of the fluid, K_f, may not necessarily be the same as the diffusivity of the particle, K_p. This discrepancy has been recognised in the specialist literature (Yudine, 1959; Csanady, 1963; Wells and Stock, 1983; Wang and Stock, 1993) but has gone almost unnoticed in the oceanographic literature until very recently (O'Brien et al., 2003). This section will determine if this discrepancy can be ignored in marine applications studying plankton dynamics, or whether corrections are necessary as O'Brien et al. (2003) suggest.

Two effects have been identified to influence the particle diffusivity K_p:

1. **The particle inertia** causes the particle to be less responsive to the rapid velocity changes that are characteristic of turbulent flow. The result can be either a decrease or increase in particle diffusivity depending on the particle size and density (Fung, 1993; Wang and Maxey, 1993; Wells and Stock, 1983; Wang and Stock, 1993).

2. **The crossing-trajectories effect** (Yudine, 1959; Csanady, 1963) is due to the free-fall velocity, w_p, of the particle (e.g. a sinking diatom). If this velocity is high compared to the turbulent velocity fluctuations, w', the particle trajectory will be significantly different from that of adjacent fluid points and the sinking particle will simply fall through the turbulent structures, thereby lose the velocity correlation with the ambient fluid environment and effectively diffuse less (Wells and Stock, 1983).

Particle Inertia

The inertia of a particle is usually quantified in terms of the so-called particle response time, τ_p, (sometimes also referred to as relaxation time) which is a function of the particle diameter d_p [m] and the particle density ϱ_p [$\mathrm{kg\,m^{-3}}$] in relation to the fluid density ϱ_f (e.g. Snyder and Lumley, 1971; Graham and James, 1996; Gouesbet and Berlemont, 1999):

$$\tau_p = \frac{d_p^2}{18\nu}\left(\frac{\varrho_p}{\varrho_f} + \frac{1}{2}\right) \tag{1.38}$$

with ν the kinematic viscosity of the fluid (typically $10^{-6}\,\mathrm{m^2\,s^{-1}}$ for sea water). Usually this parameter is divided by the fluid integral timescale, τ_f, to yield the Stokes number which determines whether or not the particle will be able to follow the turbulent flow. τ_f is constant only in homogeneous turbulence, however, and as we want to deal with inhomogeneous turbulence we will focus on τ_p. McAndrew et al. (1998) measured fluid and particle velocities

in inhomogeneous turbulence. Their results (Fig. 1.8) illustrate the effect of τ_p on a particle's ability to follow the turbulent motion of the fluid. Particles with $\tau_p = 10\,\mathrm{s}$ are virtually unable to follow the turbulent motions, while particles with $\tau_p = 0.1\,\mathrm{s}$ follow all but the most rapid fluctuations. If Eq. (1.38) is evaluated for a range of valid particle sizes and densities (the Stokes law applies to plankton particle sizes roughly up to 200 μm), we obtain response times that are about two orders of magnitude smaller than those in Fig. 1.8(b). It can thus be concluded that inertial effects on the particle diffusivity can be neglected for most live, marine phytoplankton and even fine sediments.

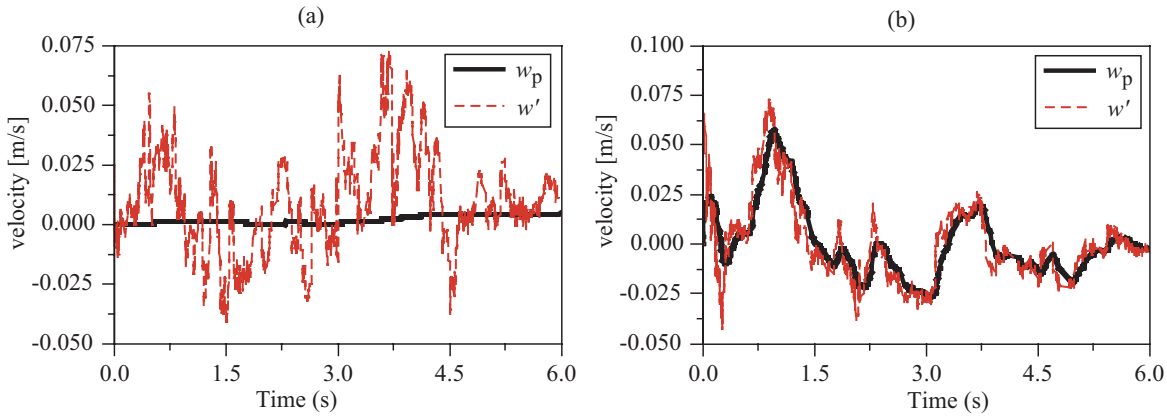

Figure 1.8: Particle velocity, w_p, compared to fluid velocity, w', for time constants (a) $\tau_p = 10\mathrm{s}$ and (b) $\tau_p = 0.1\mathrm{s}$ (from McAndrew et al., 1998).

The Crossing-Trajectories Effect

The crossing-trajectories effect depends on the magnitude of the particle's sinking or swimming velocity compared to the turbulent fluid velocities. The following correction has been derived by Csanady (1963):

$$\frac{K_p}{K_f} = \left(1 + \frac{\beta^2 w_p^2}{w'^2}\right)^{-1/2} \tag{1.39}$$

where β is a constant in the range $0.3 \leq \beta \leq 1$ depending on the turbulent flow characteristics (Wang and Stock, 1993). O'Brien et al. (2003) used the value of $\beta = 0.356$ suggested by Wang and Stock (1993) for flows in which the eddy decay time equals the turnover time, and take Eq. (1.39) one step further to produce

$$\frac{K_p}{K_f} = (1 + \beta^2\, \mathscr{P}^2)^{-1/2} \tag{1.40}$$

$\mathscr{P}$ is the Peclet number from Eq. (1.37). The use of Eq. (1.40) may not be appropriate when attempting to make quantitative predictions of particle distributions and primary production, as it contains a significant margin of error associated with the approximations that went into its derivation. There are three arguments to consider:

1. O'Brien et al. (2003) base this last equality in Eq. (1.40) on the relationships

$$K_f \sim w'\ell \sim w'h \tag{1.41}$$

from Tennekes and Lumley (1972) to equate w_p/w' from Eq. (1.39) with $\mathscr{P}$. As Tennekes and Lumley (1972) explain, their use of the '$\sim$' symbol implies a crude approximation which generally means that the non-dimensional coefficient that would make the relation an equation can be as large as 5 or as small as 1/5.

2. K in Eq. (1.37) corresponds to K_p as it is the mixing time scale of the particles that is relevant here and it should therefore not be replaced with K_f from the relationships in Eq. (1.41).

3. Spigel and Imberger (1987) define a parameter ϕ based on the ratio w_p/w', which they use in a similar fashion to how O'Brien et al. (2003) use the Peclet number (i.e. to determine whether sinking or mixing wins in a particular scenario). Their relationship is based on observational data which showed that sinking dominated for $\phi > 1$ and mixing won for $\phi < 1$. The proportionality factor in their relationship was 15, i.e. ($\mathscr{P} \equiv$) $\phi = w_p/(15w')$, which would introduce a considerable error into the approximations implied in Eq. (1.40).

The above arguments suggest that the error in obtaining K_p/K_f from Eq. (1.40) could be greater than one order of magnitude which would render any quantitative deductions for primary production problematic. Fig. 1.9 shows two specific examples that illustrate the effect of a factor 10 over-estimation of the crossing-trajectories effect which would result in a factor 10 under-estimation of the particle diffusivity, K_p, and thus a factor 10 increase in the Peclet number experienced by the particles [Eq. (1.37)]. Let us now assume, for argument's sake,

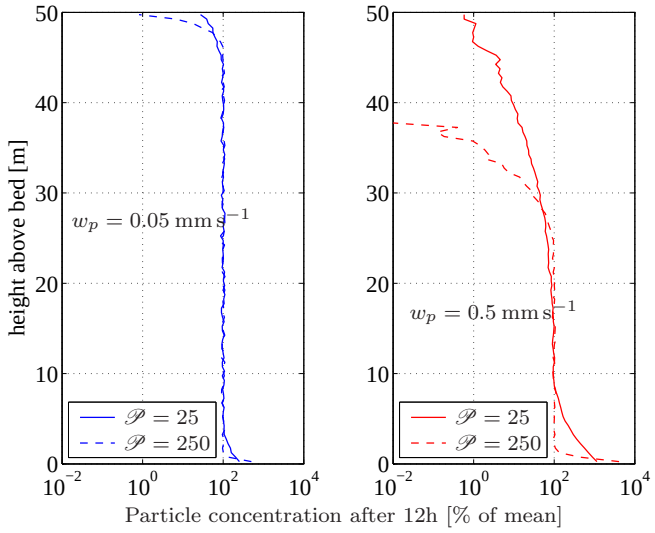

Figure 1.9: Example distributions of 20,000 particles that were initially uniformly distributed in a constant diffusivity field and tracked, using Eq. (2.18) with reflecting boundary conditions. The profiles represent the 20-minute time average after a simulation period of 12 h during which the cells were sinking at a constant rate w_p. The particles are binned into 0.5 m vertical intervals and the abscissa shows the concentration as a percentage of the mean. In both examples, the particles start to accumulate at the bottom and create a depleted area near the surface while the concentration in the central water column is mostly unaffected and remains close to 100%. The dashed curve in the right panel indicates that there are no particles present above 38 m. For both particle species, a factor 10 over-estimation of $\mathscr{P}$ has a significant effect on the particle distribution (see text).

that the solid line in both panels represents the 'correct' result, where K_p has been obtained in some quantitatively correct (but at present unknown) way from K_f. The dashed lines could then represent the result of a factor 10 over-estimation of the crossing trajectories effect which, as was argued above, is within the margin of error of Eq. (1.40). In both cases, the factor 10 increase in the Peclet number has a great effect on the number of particles present near the surface, as well as on the potential primary production if we added a light gradient and cell growth to the picture.

As an alternative approach, Hinze (1975) suggests a different criterion that can be used to determine whether $K_p \equiv K_f$. If a particle is caught in a coherent structure, such as an eddy, the crossing trajectories effect can be neglected if the particle stays inside this eddy over the entire eddy-lifespan. In other words, the displacement of the particle, relative to the fluid points, has to be smaller than the Kolmogoroff micro-scale $\eta = (\nu^3/\varepsilon)^{1/4}$ over the time it takes for the eddy to decay, i.e. the deformation time $\tau_d = \sqrt{\nu/\epsilon}$ (where ε is the dissipation of turbulent kinetic energy (TKE) per unit mass $[\,\mathrm{m^2\,s^{-3}}]$ and ν the kinematic viscosity $[\,\mathrm{m^2\,s^{-1}}]$). The relative velocity of the particle, w_p, must therefore be smaller than the characteristic velocity w_c:

$$w_p \overset{!}{<} w_c = \frac{\eta}{\tau_d} = (\varepsilon\,\nu)^{\frac{1}{4}} \tag{1.42}$$

For the wind mixed surface layers of the ocean, most shelf seas, and estuaries $\varepsilon > 10^{-6}\,\mathrm{m^2\,s^{-3}}$ and hence $w_c > 10^{-3}\mathrm{m\,s^{-1}}$ $(= 86.4\,\mathrm{m\,d^{-1}})$. As most live phytoplankton have sinking/swimming velocities well below $1\,\mathrm{mm\,s^{-1}}$, no correction should be necessary for these environments. In the deep ocean permanent thermocline or in stratified lakes, the dissipation range becomes $10^{-10}\,\mathrm{m^2\,s^{-3}} \leq \varepsilon \leq 10^{-8}\,\mathrm{m^2\,s^{-3}}$ and the critical velocities are $10^{-4}\,\mathrm{m\,s^{-1}} \leq w_c \leq 3\times10^{-4}\,\mathrm{m\,s^{-1}}$ which is within the range of some dinoflagellates and diatoms. For these particles the crossing-trajectories effect will therefore become relevant in low mixing environments and $K_f \neq K_p$. However, with our present knowledge of turbulence it is rather difficult to quantify this effect, due to the still unknown constants that would turn the relations in Eq. (1.41) into equations. This is one of the pressing issues for experimentalists studying turbulence because the difficulty lies in the measurement of w' and the determination of its relationship to K in a way that is generally valid.

From a biological point of view it can be argued, however, that immotile organisms that inhabit such stable environments are likely to have sinking velocities less than $0.1\,\mathrm{mm\,s^{-1}}$ as they would otherwise quickly sink out of the euphotic zone and die. Therefore, we should be able to use K_f instead of K_p as there are simply no biologically sustainable scenarios in which $\mathscr{P} \gg 1$ and the particles are sinking. For motile particles with $w_p > 0.1\,\mathrm{mm\,s^{-1}}$ in stable environments the argument runs slightly different. In those scenarios the vertical mixing time scale, $\tau_m = h^2/K$, will be of the order of weeks if not months and a further reduction due to the crossing-trajectories effect will only have a minor significance for the processes operating on biological time scales which are hours to days. So even for motile particles we should always be able to employ the fluid diffusivity. The last remaining particle species to consider are dead individual cells sinking out of the mixed layer. For this scenario we simply cannot say, with our present knowledge of turbulence, how different K_p and K_f are going to be, due to the

unknown constants that would transform the relations in Eq. (1.41) into equations.

1.8 Project Objectives

As the above summary has attempted to show, motility in realistic (i.e. inhomogeneous) representations of turbulence has not been investigated to date. This study will attempt to lead one step closer to a better understanding of this problem by using a representation of turbulence that accounts for its spatial inhomogeneity and temporal variability. The central question to this study is: Given the typical speeds and the observed turbulent velocity fluctuations, how is motility or sinking impacted upon by turbulent mixing, and how does this affect phytoplankton survival? This question will be examined for various turbulent environments ranging from estuarine (Chapter 3) over a shelf sea (Chapter 4) to a freshwater lake (Chapter 5). Some of the other issues that will be addressed in the course of this thesis are:

- what effect does the tidal periodicity of turbulence have on the swimming success of phytoplankton?
- how is the physiological state of the cells affected by the degree of turbulent mixing (photo-acclimation)?
- what role can motility play in a nutrient limited environment such as a stratified shelf sea where observations often show motile species as the dominant population?
- which swimming strategies are most successful in the various scenarios and which ones reproduce a picture that is most similar to observations (Lauria, 1998; Sharples et al., 2001)?
- how effective is turbulence at disrupting migration rhythms of the cells and how does this affect the growth of the organism (for the specific example of an artificially mixed freshwater lake)?

Chapter 2

Method

This chapter will introduce the main concepts behind the physical and biological models that have been developed to address the research objectives set out in Section 1.8. Section 1.7.1 discussed the issues of an Eulerian versus Lagrangian approach and the conclusion was reached that, for the issues under investigation in this study, a Lagrangian model is needed to be able to account for individual cell behaviour and physiological adaptation to the environment. In order to represent the environment as realistically as possible, the model also has to provide a direct link between ambient water column stability and the amount of vertical turbulent mixing. The model has to be dynamic in the sense that external physical forces like tidal currents, wind and temperature stratification should be reflected in the vertical turbulent mixing. In the present study, this link between the environmental forcing and the local amount of mixing is provided by a k-ε turbulence closure scheme (see Section 2.1.2). The external forces are implemented following the approach by Sharples (1999). The questions of motility and growth are addressed through a Lagrangian random walk approach (Section 2.2) in combination with a simple biological growth and photo-acclimation model (Section 2.3). The next sections provide a more detailed description of each of the above model components while the model behaviour is described in Section 2.4.

2.1 The Physical Model

The Phyto-1D model in its original version (see Sharples, 1999) is a one-dimensional vertical physical-biological coupled model for shelf seas. It provided the foundation from which the present model (see Fig. 2.1) has been developed. The main ingredient of the physical part of the model is the turbulence closure scheme (TCS) which provides the link between the ambient water column stability (driven by seasonal solar heating) and the amount of vertical turbulent mixing (mainly driven by tidal currents and surface wind stress). The Phyto-1D model is an Eulerian model to examine processes that occur over timescales of weeks to months or years. In the present study, the relevant time scales are usually of the order of days to a few weeks (limited also by the computationally more expensive Lagrangian approach). The physical

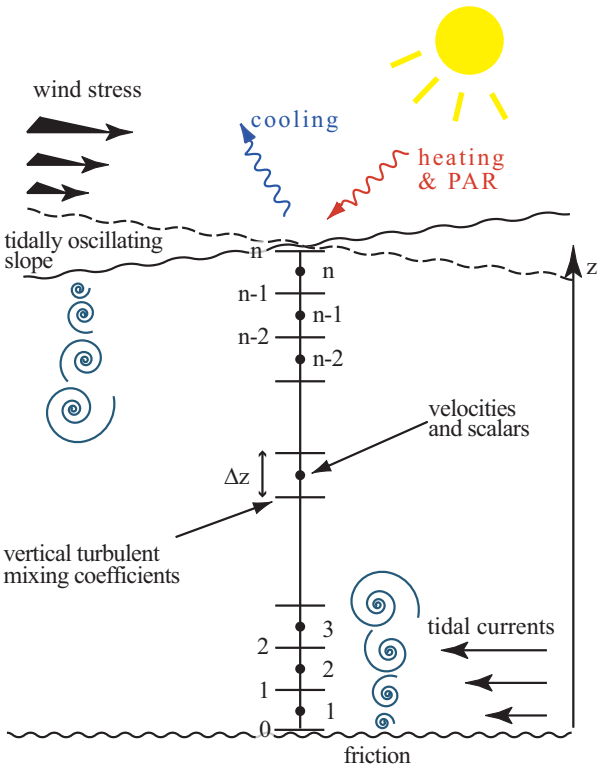

Figure 2.1: Schematic showing the components of the physical part of the Phyto-1D model. The velocities and scalars are calculated at the centre of the grid cell, the turbulent mixing at the boundaries. This diagram is adapted from Figure 1 in Sharples (1999).

component of Phyto-1D has therefore been simplified to meet the needs of the present study. The model will be used mainly to examine particular scenarios of only 1-2 days in duration (e.g. a spring tide scenario), and it is thus not necessary to account for heat exchange with the atmosphere. The incident solar radiation is only used to calculate the amount of primary production but not to heat the water column which is usually given a predefined temperature profile for each experiment. Wind forcing is also turned off in the experiments in order to be able to isolate the tidal signal in the results. During the development of the model it also became necessary to change the TCS from Sharples (1999). The new scheme is discussed in more detail in Section 2.1.2.

2.1.1 External Forcing

The tides are implemented by periodically oscillating the sea surface slopes (using the frequencies of the tidal constituents as frequencies of oscillation). These slopes produce pressure gradients which drive the tidal velocities. For all experiments the model uses only a one-dimensional equation of motion without Coriolis forcing

$$\frac{\partial u}{\partial t} = -\sum_{i=1}^{m} A_i \omega_i \cos\left(\omega_i t + \varphi_i\right) + \frac{\partial}{\partial z}\left(N_z \frac{\partial u}{\partial z}\right) \tag{2.1}$$

where t is time and N_z the vertical eddy viscosity. The A_i are the maximum tidal current amplitudes (in $[\,\mathrm{m\,s^{-1}}]$) for the m tidal constituents having the angular frequencies ω_i and

phases φ_i. At the seabed, a quadratic friction boundary condition is applied giving the stress produced by the tidal currents as (Sharples, 1999)

$$\tau_{seabed} = -k \varrho_1 u_1^2 \tag{2.2}$$

where k is the bottom drag coefficient (set to 0.003), ϱ_1 is the density of the bottom depth element and u_1 is the near bed velocity.

Since all the experiments use a predefined (static) temperature profile, the incident solar radiation is only used to calculate the primary production but not to heat the water column. Of the incident irradiance, 45% is assumed to be in the PAR spectrum and is distributed exponentially with depth according to the Beer-Lambert law (see Section 2.3.1). Since the temperature profile is static, the density ϱ [$\mathrm{kg\,m^{-3}}$] is calculated once only at the beginning of an experiment using a simplified quadratic equation of state based on the predefined temperatures T and a constant salinity of 34 (Sharples, 1999)

$$\varrho = 1027.39 - 0.076\,T - 0.0047\,T^2 \tag{2.3}$$

2.1.2 The Turbulence Closure Scheme

As was discussed in Section 1.2.5, there are several methods available for modelling turbulence in marine environments. A good compromise between computing costs and performance is achieved in the so-called two equation models of turbulence which apply the eddy diffusivity approximation to parameterise turbulence. Originally, the present model had been tested with the turbulence closure scheme (TCS) from Sharples (1999) which uses a differential transport equation for the turbulent kinetic energy (TKE) corresponding to a Mellor-Yamada level 2.5 closure (Mellor and Yamada, 1982). However, several authors reported instabilities in the Mellor-Yamada 2.5 TCS (Kantha and Clayson, 1994; Pufahl et al., 1997; Burchard and Deleersnijder, 2001). A comparison between the Mellor-Yamada level 2.5 TCS and a more recent scheme by Canuto et al. (2001) (Fig. 2.2) clearly shows how the Canuto scheme appears to perform far better than the original Mellor-Yamada (MY) scheme. The instabilities in the MY scheme could be remedied by the method of Galperin et al. (1988), but one major disadvantage of the MY scheme remains: it only allows for critical gradient Richardson numbers of up to 0.25. The Canuto scheme allows for $Ri_c \approx 0.85$ which is in better agreement with recent observations of mixing in the ocean (see discussion in Section 1.2.3). Therefore the original TCS from Sharples (1999) was abandoned and the new k-ε scheme from Canuto used instead. Most of the source code for this new scheme comes from the General Ocean Turbulence Model (GOTM) for which the source code and documentation are available online at http://www.gotm.net. This new TCS was introduced into the original Phyto-1D model by J. Sharples and has then been incorporated into the present model, only requiring minor adjustments. The main concepts of the Canuto scheme will now be presented.

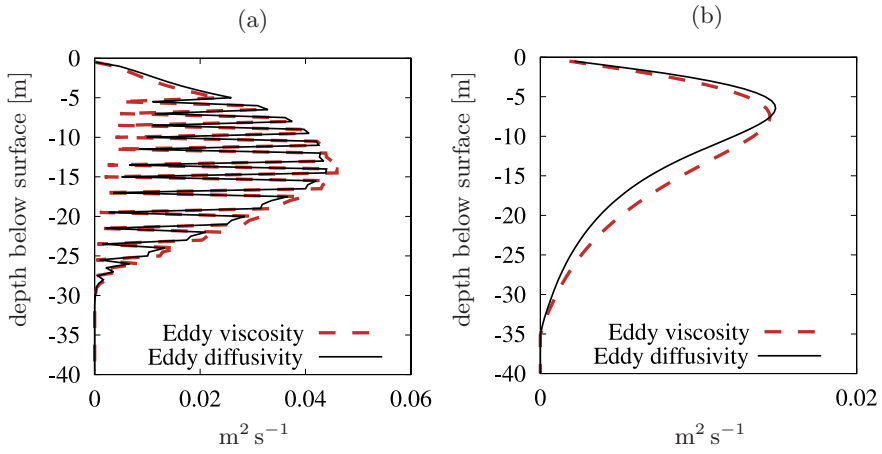

Figure 2.2: Comparison between the Mellor-Yamada level 2.5 turbulence closure scheme in (a), and the k-ε-scheme (b) by Canuto et al. (2001). Both graphs are from Burchard and Deleersnijder (2001) and were obtained from a Kato and Phillips (1969)-style wind entrainment experiment, where a surface mixed layer slowly penetrates into a stratified lower layer.

The Canuto et al. (2001) Model

Most two-equation turbulence models use the relations by Kolmogoroff and Prandtl to relate the turbulent exchange coefficients (eddy diffusivity K_z and viscosity N_z) to the product of a velocity scale with a length scale (cf. Eq. (1.29)):

$$N_z = c_\mu \sqrt{E} L \qquad \text{and} \qquad K_z = c'_\mu \sqrt{E} L \tag{2.4}$$

where E is the TKE in [J kg^{-1}] [cf. Eq. (1.6)], L the turbulent macro length scale in [m] [cf. Eq. (1.4)], and c_μ and c'_μ are the dimensionless so-called stability functions for momentum and mass respectively (see below). The stability functions control the interaction between mixing and stability in the water column. In the k-ε schemes, the length scale L which appears in Eq. (2.4) is substituted by the normalised dissipation rate ε (units [W kg^{-1}]):

$$\varepsilon = \left(c^0_\mu\right)^3 \frac{E^{3/2}}{L} \tag{2.5}$$

with the constant $c^0_\mu = 0.5562$ (Rodi, 2000). This equation follows directly from the energy cascade [Eq. (1.4)]. In order to obtain K_z and N_z we thus need to find E and ε which leads to the two governing equations in the k-ε models which can be derived from the Navier-Stokes equations (Rodi, 2000):[1]

k-equation:

$$\frac{\partial E}{\partial t} - \frac{\partial}{\partial z}\left(N_z \frac{\partial E}{\partial z}\right) = \underbrace{N_z\left[\left(\frac{\partial U}{\partial z}\right)^2 + \left(\frac{\partial V}{\partial z}\right)^2\right]}_{\text{shear production}} - \underbrace{K_z \overbrace{\frac{g}{\varrho}\frac{\partial \varrho}{\partial z}}^{N^2}}_{\text{bouyant prod./destr.}} - \underbrace{\varepsilon}_{\text{dissipation}} \tag{2.6}$$

[1] For consistency [cf. Eq. (1.6)] and to avoid confusion with other symbols defined later, the symbol for TKE 'k' from the k-ε schemes will be denoted as E.

with N the Brunt-Väisälä frequency. The following boundary conditions can be derived from the law of the wall (Burchard et al., 1999):

$$E = \left(\frac{u_b}{c_0}\right)^2 \text{ at } z = 0, \qquad \text{and} \qquad E = \left(\frac{u_s}{c_0}\right)^2 \text{ at } z = H. \tag{2.7}$$

where $u_{b/s}$ is the bottom/surface friction velocity. The second equation is the ε-equation:

$$\frac{\partial \varepsilon}{\partial t} - \frac{\partial}{\partial z}\left(N_\varepsilon \frac{\partial \varepsilon}{\partial z}\right) = \frac{\varepsilon}{E}\left(c_1 N_z \left[\left(\frac{\partial U}{\partial z}\right)^2 + \left(\frac{\partial V}{\partial z}\right)^2\right] - c_3 K_z N^2 - c_2 \varepsilon\right). \tag{2.8}$$

where N_ε is the vertical eddy diffusivity of ε, i.e. $N_\varepsilon = N_z/1.08$ (see Burchard et al., 1998, for a derivation). The c_i are empirical constants that result from the closure of the equations (see e.g. Rodi, 2000; Burchard et al., 1998):

$$c_1 = 1.44,\ c_2 = 1.92,\ \text{and } c_3 = \begin{cases} -0.629 & \text{, if } K_z N^2 \geq 0 \text{ (stable)} \\ 1 & \text{, if } K_z N^2 < 0 \text{ (unstable)} \end{cases} \tag{2.9}$$

A common approach to resolve the turbulent length scale is based on the assumption that it linearly decreases towards the boundary according to:

$$L = \kappa(\tilde{z} + z_0) \tag{2.10}$$

with the von Kármán constant $\kappa = 0.4$, the distance from the boundary $\tilde{z}$, and the roughness length of the boundary z_0. This leads to the boundary conditions for ε:

$$\varepsilon = \left(c_\mu^0\right)^3 \frac{E^{3/2}}{\kappa z_0}\bigg|_{\tilde{z}=0} \tag{2.11}$$

As a last step, to find K_z and N_z through Eq. (2.4), we need to specify the stability functions. The present model follows the approach by Canuto et al. (2001). Introducing the turbulent time scale $\tau_e = 2E/\varepsilon$ and using the substitution $\Sigma^2 = (\partial U/\partial z)^2 + (\partial V/\partial z)^2$ the stability functions from Eq. (2.4) are

$$c_\mu = \frac{2}{\left(c_\mu^0\right)^3} \frac{\left[s_0 + s_1(\tau_e N)^2 + s_2(\tau_e \Sigma)^2\right]}{D} \tag{2.12a}$$

$$c'_\mu = \frac{2}{\left(c_\mu^0\right)^3} \frac{\left[s_4 + s_5(\tau_e N)^2 + s_6(\tau_e \Sigma)^2\right]}{D} \tag{2.12b}$$

where $D = d_0 + d_1(\tau_e N)^2 + d_2(\tau_e \Sigma)^2 + d_3(\tau_e N)^4 + d_4(\tau_e N \Sigma)^2 + d_5(\tau_e \Sigma)^4$. The s_i and d_i are empirical constants (see Canuto et al., 2001, for more details).

Internal Mixing

One of the main shortcomings of local turbulence models is their failure to account for shear instability and internal wave activity. A common approach is to simply introduce a so-called background diffusivity K_{bg}. Other, more sophisticated approaches are those by Kantha and Clayson (1994) and Canuto et al. (2001). Each of the three mentioned approaches is available in the present model and their approach is briefly outlined below. A comparison of their performance is provided in Section 2.4.

The Kantha and Clayson (1994) model considers two different contributions to internal mixing: shear-induced instabilities (SI) and internal wave induced (IW) mixing. The shear instabilities are modelled as strongly decreasing with the gradient Richardson number Ri [see Eq. (1.22)]:

$$(N_z)^{\mathrm{SI}} = (K_z)^{\mathrm{SI}} = \begin{cases} 0 & , \text{for } \mathrm{Ri} > 0.7 \\ 5 \cdot 10^{-3}\,\mathrm{m^2\,s^{-1}} \cdot \left[1 - \left(\frac{\mathrm{Ri}}{0.7}\right)^2\right]^3 & , \text{for } 0 < \mathrm{Ri} < 0.7 \\ 5 \cdot 10^{-3}\,\mathrm{m^2\,s^{-1}} & , \text{for } \mathrm{Ri} < 0\,. \end{cases} \tag{2.13}$$

Internal wave induced viscosities and diffusivities are assumed constant

$$(N_z)^{\mathrm{IW}} = 10^{-4}\,\mathrm{m^2\,s^{-1}} \qquad \text{and} \qquad (K_z)^{\mathrm{IW}} = 5 \cdot 10^{-5}\,\mathrm{m^2\,s^{-1}}\,. \tag{2.14}$$

The Canuto et al. (2001) model is somewhat simpler in that it does not distinguish between the two above effects. The approach is based on measured data of vertical shear generated by breaking internal waves. By integrating over all wavenumbers it is possible to calculate the shear due to internal waves which they denote as Σ_{IW}. By analogy with Eq. (1.22) it is possible to define a Gradient Richardson number, $\mathrm{Ri}_{\mathrm{IW}}$, based solely on the shear contributions from internal waves: $\mathrm{Ri}_{\mathrm{IW}} = N^2/\Sigma_{\mathrm{IW}}$. Comparison of their model results with observational data produced $\mathrm{Ri}_{\mathrm{IW}} = 0.88\,\mathrm{Ri}$ which yields Σ_{IW}. By re-evaluating the stability functions from Eq. (2.12) (using Σ_{IW} instead of Σ) one then obtains the diffusivity and viscosity contributions due to internal waves only which, as in the Kantha and Clayson (1994) model, are then added to the previously calculated model diffusivity and viscosity.

The 'Background Diffusivity' approach is the simplest of the three models because it parameterises all internal mixing processes through constants, the background diffusivity and viscosity (K_{bg} and N_{bg}), which are simply added onto the model diffusivity and viscosity. They thus represent the minimum values below which K_z and N_z are not allowed to fall.

2.2 The Lagrangian Model

Having described the use of the k-ε-scheme to generate the stability-dependent turbulent diffusivities through the water column, the method will now be detailed that allows the use of these diffusivities in a Lagrangian description of particle movement.

2.2.1 The Random Walk

A crucial decision to take in the model is to resolve how the individual cells will move in response to turbulent diffusion. Commonly the turbulent particle movement is modelled through a random walk. As Visser (1997) demonstrates, not every random walk model is suitable for environments where the diffusivity is spatially non-uniform and the choice of the wrong model can lead to misinterpretations. This has been pointed out several times (e.g. Hunter et al.,

1993; Dimou and Adams, 1993; Spagnol et al., 2002) but erroneous models continue to appear in the literature (e.g. MacIntyre et al., 1995; Lizon et al., 1998; Kim et al., 2000). The following equation can be derived (Hunter et al., 1993; Visser, 1997) to calculate the particle displacement:

$$z_{n+1} = z_n + \underbrace{K'(z_n)\Delta t}_{\text{deterministic term}} + \underbrace{R\left[\frac{2\,K\big(z_n + \frac{1}{2}\,K'(z_n)\Delta t\big)\;\Delta t}{r}\right]^{1/2}}_{\text{random term}} + \underbrace{w_p \Delta t}_{\text{movement}} \tag{2.15}$$

where the subscripts of z refer to the time steps. K' in Eq. (2.15) is $\partial K/\partial z$ and w is the sinking/swimming velocity of the cell.[2] R is a random process of zero mean and variance r (e.g. $r = 1/3$ for $R \in [-1, 1]$).

The random walk is thus an iterative Markov process where the new particle position, z_{n+1}, is calculated only from the knowledge of the present position, z_n, but without knowledge of the previous particle history. It consists of a deterministic component and a diffusive, or random, component. The deterministic component causes a net displacement of the centre of mass of the suspended particles towards increasing diffusivity at a rate K'. This is necessary as neutrally buoyant particles would otherwise accumulate in low-diffusivity areas as shown by Visser (1997). The physical justification for the deterministic component is related to the possible eddy size in the water column. Let us consider the base of the thermocline, for instance, where the diffusivity drops sharply to very low values due to the increased water column stability. In this scenario, the deterministic term would displace away from the thermocline into the bottom mixed layer (BML). This is due to the fact that in the BML the eddies are much larger than within the thermocline and there is thus a gradient in eddy size in the water column. Since the larger eddies are more efficient at bringing about vertical mixing, the large eddies from the BML will drag down the particles more easily compared to the smaller eddies within the thermocline. This is expressed by the diffusivity gradient in the deterministic term. The last term on the RHS of Eq. (2.15) has been added to include particle sinking/swimming at velocity w_p, where w_p can be either a function of time (e.g. to simulate diurnal migration) or of the cell's vertical position z (e.g. to let it hunt for a particular isolume or nutrient concentration).

As Visser (1997) points out, the increased residence time of negatively buoyant plankton in the surface mixed layer (SML), often attributed to a reduction in sinking velocity at the base of the SML (e.g. Lande and Wood, 1987), now follows directly from the random walk model. A large gradient in K at the transition from the SML to the thermocline can produce large enough positive values of K', to partially compensate or even fully alleviate any sinking term. It should be noted, however, that this reduction in sinking velocity is not an active process due to physiological changes in the phytoplankton, but merely due to the deterministic component in Eq. (2.15) which is a mathematical requirement to achieve a uniform distribution if the particles are neutrally buoyant (e.g. if we would consider salt instead of plankton).

In order to be able to use Eq. (2.15) for a particular scenario, it is necessary that both K

[2] Note that for reasons of brevity, the vertical eddy diffusivity will simply be written as K and not K_z.

and K' be continuous and differentiable. This is important as any discontinuity can lead to artificial particle accumulations. Furthermore, the diffusivity profile should be locally (i.e. over the range of the expected turbulent displacement of a particle) well approximated by the first order Taylor expansion:

$$K(z) = K_0 + (z - z_0)K' \tag{2.16}$$

This criterion can always be met by ensuring that we choose a sufficiently small time step for the simulation

$$\Delta t \ll \mathrm{MIN}\frac{1}{|K''|} \tag{2.17}$$

where K'' is the second derivative of K with respect to z and MIN stands for the minimum over the region of interest. This equation constraining the time step is further refined below. For situations in which the diffusivity is vertically homogeneous, Eq. (2.15) simplifies to

$$z_{n+1} = z_n + R\left[\frac{2\,K(z_n)\;\Delta t}{r}\right]^{1/2} + w_p\Delta t \tag{2.18}$$

2.2.2 The Polynomial Fit

As mentioned above, both K and K' need to be continuous and differentiable over the entire region of interest where the random walk model from Eq. (2.15) is applied. A violation of either of these criteria will lead to artificial accumulations or depletions of particles at the discontinuities. As the model only outputs diffusivity values at discrete intervals, some interpolation is required in order to be able to evaluate Eq. (2.15) at continuous z-values and, depending on the profile, some smoothing may be necessary to be able to obtain a useable time step from Eq. (2.17).

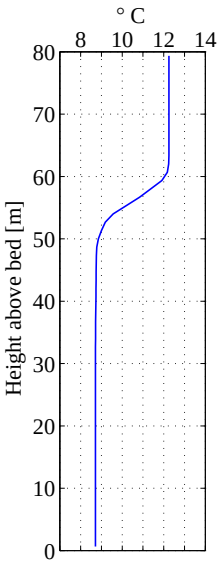

Figure 2.3: Temperature profile used to obtain the turbulence profile in Fig. 2.4.

Clearly, a mere linear interpolation between the discrete diffusivities that are obtained from the turbulence closure scheme will not suffice, as the first derivatives would be discontinuous at the grid points. A cubic smoothing spline has therefore been chosen to deliver both the interpolation and the smoothing. This ensures that both the first and second derivative are continuous and easily obtainable from the original K. For the solution of this least squares problem a routine based on the algorithm in de Boor (1978) is used. Obviously it is computationally more expensive to use a cubic spline rather than a simple polynomial. However, if the profile is complex, the use of piecewise polynomials delivers far superior results. This is illustrated in Fig. 2.4(a) which shows a snapshot of a typical diffusivity profile obtained from a k-ε turbulence-closure scheme for a stratified shelf-sea scenario. In this example, the salinity was constant with depth and any density stratification is due solely to temperature gradients. The temperature profile is shown in Fig. 2.3. The model has been forced with tidal currents only, producing the high diffusivities in the bottom layer. No wind mixing is present in this example.

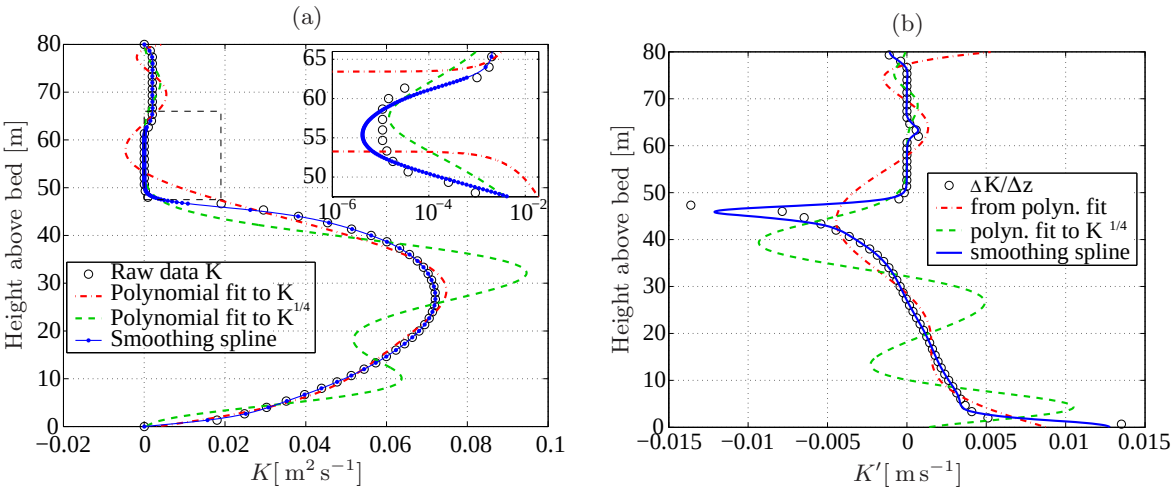

Figure 2.4: (a) Comparing the performance of three different types of polynomial fit to a model diffusivity profile. The single polynomials are of order 6 while the spline is cubic. (b) Comparing the derivatives of the various fits to the discrete model derivative $\Delta K/\Delta z$. Only the spline is able to reproduce the amplitudes of the model values sufficiently well.

The profile exhibits strong diffusivity gradients near the bottom boundary and at the base of the thermocline.

The dash-dotted line shows the fit using a single polynomial of order 6. It gives a good representation of the model K's up to about 45 m, but the fit becomes rather poor in the top 35 m, including a negative overshoot in the thermocline. This overshoot could be remedied by fitting the polynomial to $K^{1/4}$ instead, shown as a dashed line. The fit is now better in the thermocline as the enlargement in Fig. 2.4(a) shows (note the logarithmic scale of the abscissa) but worse in the lower half of the profile. The best overall fit is achieved with the cubic smoothing spline represented by the continuous line. In order to be able to cope with the strong gradients at the base of the thermocline, a finer grid had to be applied throughout the thermocline region to prevent negative overshoots. This is illustrated by the smaller vertical spacing of the dots in the fitted spline which show the break points of the piecewise polynomials. The superiority of the cubic splines becomes particularly clear once the performance of the first derivatives of each fit are compared [Fig. 2.4(b)]. For this example profile, Eq. (2.17) would require $\Delta t \ll 142$ s.

2.2.3 Effects of Boundaries on the Mean Particle Concentration

Boundaries in random walk simulations have two effects. The first is due to the reduced turbulent length scale near the boundaries, which causes the mixing and thus the diffusivity K to decrease towards the surface and the bed. The second is due to how the boundaries are implemented in the model, i.e. either as absorbing or reflecting. Many models use reflecting boundaries to allow for particle resuspension from the sea bed. However, it can be shown that a reflecting boundary, in combination with an inhomogeneous diffusivity, will produce artificial particle accumulations at the boundary.

To illustrate this point, consider the example profile from Fig. 2.5(a) which shows a typical profile for a water column that is influenced both by wind and tidal mixing. The maximum possible displacement of a particle in this profile after one time step of $\Delta t = 6$s using Eq. (2.15) is shown in Fig. 2.5(c). The pattern is asymmetric about $\Delta z = 0$ due to the deterministic term in Eq. (2.15). Clearly, particles close to the boundaries can be displaced 'into' the boundaries. By implementing a reflecting boundary condition the particles are reflected back into the model domain of $0 \leq z \leq H$ according to

$$z_{n+1} \rightarrow \begin{cases} -z_{n+1} & \text{, if } z_{n+1} < 0 \\ 2H - z_{n+1} & \text{, if } z_{n+1} > H \end{cases} \tag{2.19}$$

where H is the depth of the water column. If the turbulence is inhomogeneous at the boundary, and many models do produce a large drop in K at the boundaries due to the rapid decline of the turbulent length scale (cf. also Fig. 2.4), some non-uniformities in the probability density function (PDF) of Eq. (2.15) appear. Starting with a uniform distribution of neutrally buoyant particles, and assuming R in Eq. (2.15) to be perfectly uniform, then the PDF (i.e. the probability of finding a particle at a particular depth some time later) should be uniform as well. This is indeed the case for homogeneous turbulence and Eq. (2.18) but not for inhomogeneous turbulence and Eq. (2.15). While the PDF [Fig. 2.6(a)] is equal to 1 in the central part of the water column, non-uniformities appear at the bottom and the surface. The PDF predicts an accumulation at each boundary, followed by a depletion a small distance away from the boundary. This pattern is also observed in the model results [Fig. 2.6(b)]. While the average concentration in the inner bins remains close to 100%, it deviates from a uniform distribution as the boundaries become noticeable.

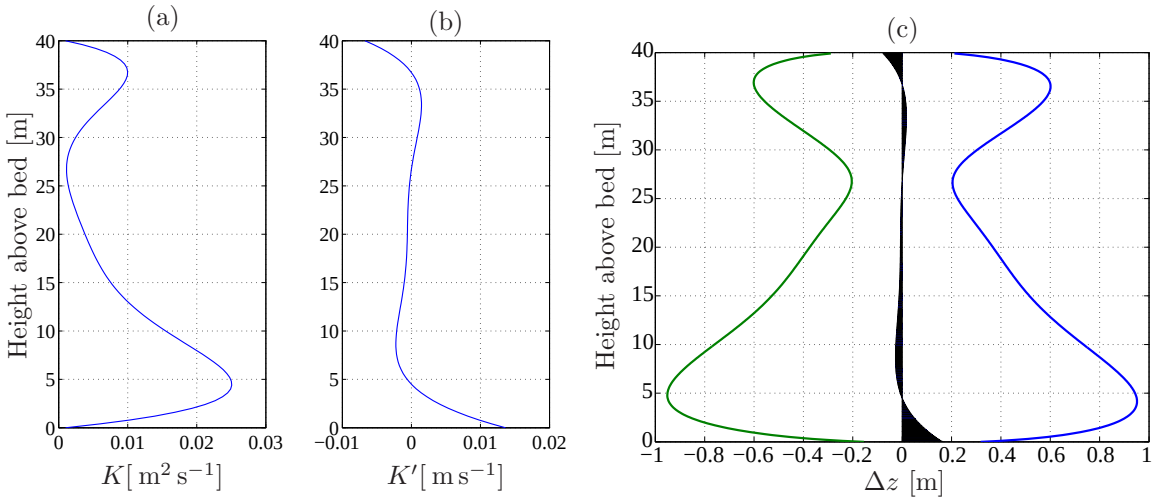

Figure 2.5: (a) An example diffusivity profile simulating wind and tide induced mixing as obtained from a k-ε turbulence closure scheme described in Burchard and Baumert (1995). The figure is a reproduction of Figure 1 in Visser (1997) and can be recreated using $K(z) = 0.001 + 0.0136245\,z - 0.00263245\,z^2 + 2.11875 \cdot 10^{-4}\,z^3 - 8.65898 \cdot 10^{-6}\,z^4 + 1.7623 \cdot 10^{-7}\,z^5 - 1.40918 \cdot 10^{-9}\,z^6$. (b) The derivative of the curve in (a). (c) Maximum possible displacement Δz of a particle as a function of depth during one time step of $\Delta t = 6$ s using Eq. (2.15). The shading in the centre of (c) illustrates the difference between the upward and downward displacements, showing the asymmetry caused by the deterministic term of the random walk.

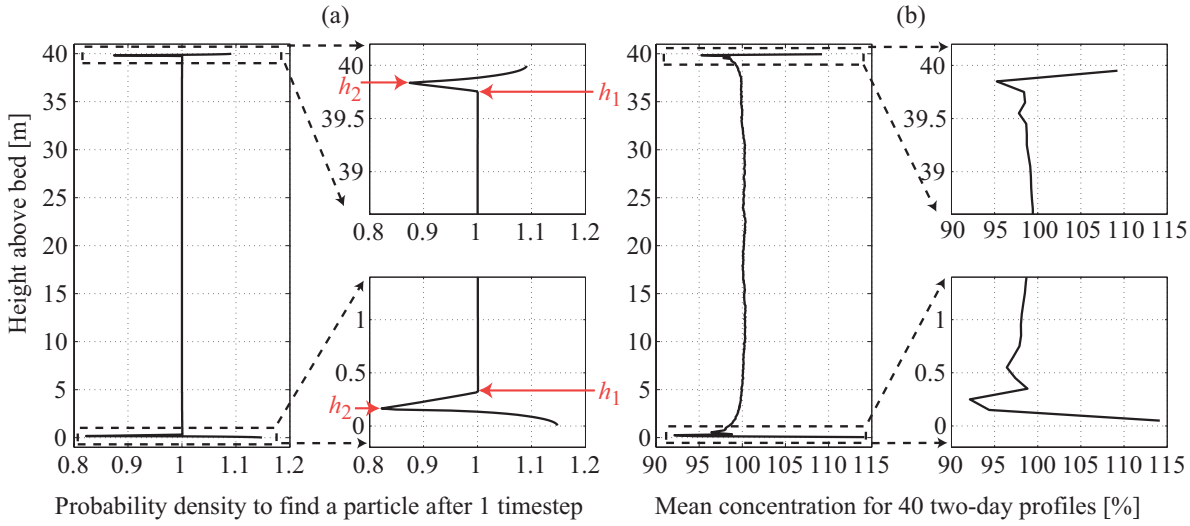

Figure 2.6: (a) The probability density function to find a particle for the diffusivity profile in Fig. 2.5(a), the random walk in Eq. (2.15) and one time step of $\Delta t = 6$ s. The vertical resolution is 1.0 cm. (b) The normalised mean distribution of 4000 particles from 40 experiments, where the particles were initially uniformly distributed in the diffusivity profile of Fig. 2.5(a) and traced for 48 h using Eq. (2.15) with time step $\Delta t = 6$ s. Each experiment used a different initialisation of the random number generator. The vertical resolution for this simulation is 10 cm. A concentration of 100% represents the concentration that would be expected if the particles were uniformly distributed. See main text for a description of h_1 and h_2.

The question that arises from these observations is why is it that the reflecting boundary condition fails in this manner? It is suggested that this error is systematic to the reflecting boundary condition and is caused by the fact that $K' \neq 0$ at the boundary. h_1 in Fig. 2.6(a) marks the point where the maximum possible displacement starts to overlap with the boundary, i.e. where it becomes possible for the particles to be displaced into the boundary. However, as we get closer to the boundary, K continuously decreases which means that none of the reflected particles will ever reach as far as h_1. h_2 in Fig. 2.6(a) marks the maximum distance from the boundary to which a particle can become reflected. The region between h_1 and h_2 is thus not replenished with reflected particles from below and has therefore a probability density that is less than unity. The area between h_2 and the boundary, on the other hand, receives an excess of particles, i.e. it receives *all* reflected particles from both regions combined which explains the recovery of the PDF and the eventual overshoot past unity. The distance of h_1 from the boundary and also the amplitude of the zig-zag behaviour depend on the time step. A smaller time step, for example, produces a smaller maximum displacement, and thus only particles in a smaller area near the boundary are now able to 'feel' its presence.

Ideally, we do not want the boundary to be noticeable, neither in the random walk nor in the particle distribution. So - as a thought experiment - we could erase the boundaries for a moment and imagine the presence of 'virtual' particles beyond the original boundaries which also obey Eq. (2.15). In an ideal case, these virtual particles should diffuse into the model domain with the same probability as the 'real' particles diffuse out of it and thus exactly compensate for the losses and keep the PDF at unity. For this to happen, both K and K' would have to fulfill the same criteria at the (now gone) boundaries as anywhere else in the model domain, viz. to be

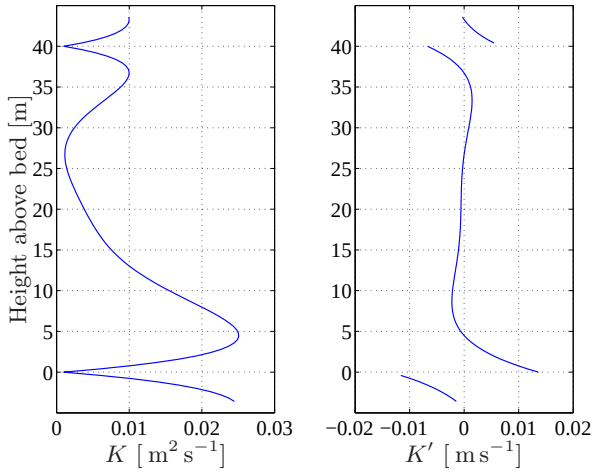

Figure 2.7: The reflecting boundary condition from Eq. (2.19) effectively mirrors the original profile from Fig. 2.5 at the boundaries (left panel). This produces a spike in K which results in a discontinuity in K' (right panel).

continuous and differentiable. By implementing a reflecting boundary condition, however, the K profile is effectively mirrored at the boundaries (the virtual particles reside in these mirrored extensions of K). If K decreases towards the boundary, the mirrored profile will have a spike at the boundary and K' is discontinuous (Fig. 2.7). This is why accumulations would occur in this thought experiment, despite the presumed absence of any boundary, and this is why the simple reflecting boundary condition fails in the actual experiment with the boundaries in place.

For the particular example profile used, the affected area in the PDF is limited to within approximately 40 cm of each boundary [cf. Fig. 2.6(a)]. In Fig. 2.6(b) the affected area is larger, extending several metres from the boundaries. The reason for this discrepancy lies in the fact that Fig. 2.6(a) represents the probability of finding a particle after just one time step, while Fig. 2.6(b) shows the mean concentration of 40 two-day simulations where these non-uniformities have been allowed to build up and spread. The particles start to accumulate rather quickly at the boundaries and a steady state is reached within a few hours. The following sections describe two possible methods for overcoming this boundary problem.

Creating a Random Mixed Layer[3]

In order to solve the reflecting boundary problem, we could take a different approach to Eq. (2.19) by insisting that all particles within some distance $D_{t/b}$ from the top/bottom boundary be well mixed according to

$$z_{n+1} \rightarrow \begin{cases} D_b P & \text{, if } \; z_{n+1} \leq D_b \\ H - D_t P & \text{, if } \; z_{n+1} \geq H - D_t \end{cases} \tag{2.20}$$

where P represents a random process between 0 and 1. $D_{t/b}$ should be equal to or larger than the distance of h_1 from the respective boundary in Fig. 2.6(a). For a given profile, $K(z)$, we need to find the two depths, z_t and z_b, at which the maximum possible displacement equals

[3]Some of the material in this section is based on suggestions from an anonymous reviewer of Ross and Sharples (2004).

the distance from the top and bottom boundaries, i.e. where

$$H - z_t = K'(z_t)\Delta t + R_{\max}\left[\frac{2\,K\big(z_t + \frac{1}{2}\,K'(z_t)\Delta t\big)\;\Delta t}{r}\right]^{1/2} \tag{2.21a}$$

$$z_b = -\left\{K'(z_b)\Delta t + R_{\min}\left[\frac{2\,K\big(z_b + \frac{1}{2}\,K'(z_b)\Delta t\big)\;\Delta t}{r}\right]^{1/2}\right\} \tag{2.21b}$$

and choose $D_{t/b}$ such that $D_t \geq H - z_t$ and $D_b \geq z_b$. The first term on the RHS of each equation is the deterministic term from Eq. (2.15) which usually displaces away from the boundary. The second term corresponds to the maximum possible positive ($R_{\max}$) and negative ($R_{\min}$) displacement by the random term of Eq. (2.15). For the profile in Fig. 2.5(a) and $\Delta t = 6$ s, these conditions yield $D_t \geq 0.29$ m and $D_b \geq 0.42$ m. For studies in which the diffusivity profile changes with time (due to variable wind or tidal forcing), it may become computationally too expensive to determine $D_{t/b}$ at every time step due to the implicit nature of Eq. (2.21). In this case a constant value for $D_{t/b}$ can be used as long as the conditions in Eq. (2.21) are met for all K profiles in the time series. To illustrate the effect of this method on the PDF, a constant value of $D_b = D_t = 1$ m has been used to produce the results in Fig. 2.8(a). Compared to Fig. 2.6(a), the improvement is considerable (note the difference in scale), although some small non-uniformities remain near the boundaries. The cause for these remaining non-uniformities is no longer related to the presence of the boundaries, however, as will be discussed in Section 2.2.4. The improvement in the PDF is mirrored by the more even particle concentrations shown in the right panel of Fig. 2.8(a).

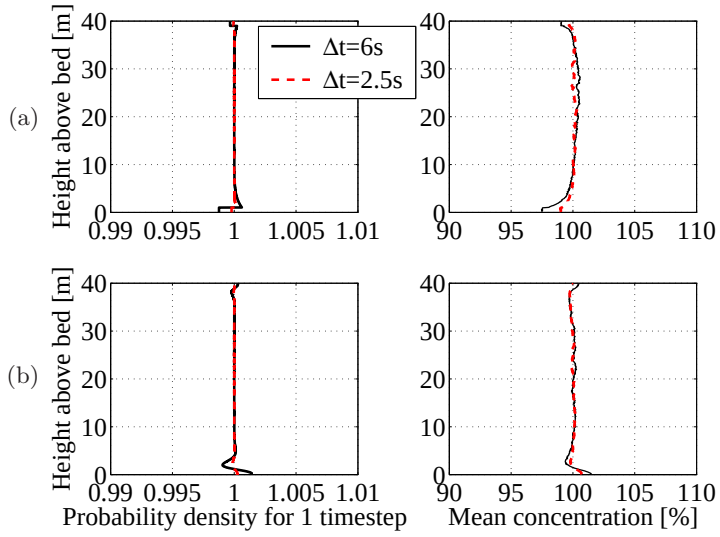

Figure 2.8: (a) PDF for the method using the random mixed layer of Eq. (2.20) with $D_t = D_b = 1$ m. A smaller time step is able to reduce the magnitude of the non-uniformities. The right panel shows the corresponding figure to Fig. 2.6(b). (b) PDF for the method using the cubic smoothing spline to force $K' = 0$ at the boundaries (Fig. 2.9). As in (a), the PDF is more uniform which results in a more even particle distribution.

Forcing $K' = 0$ at the boundaries

Although the above method was able to resolve the problem of the reflecting boundary condition, the proposed solution may not be suitable for certain applications since the particles loose their 'memory' due to their random placement ¡within the mixed boundary layer D. If the particles represent phytoplankton cells in a turbid water column, for example, their random placement in the top boundary layer D_t could expose the cells to large jumps in their received light intensity at every time step, as the PAR variation with depth is greatest near the surface boundary. Their new position (z_{n+1}) within D_t would in no way be correlated to their previous position (z_n). This may become particularly relevant in scenarios where $D_t \sim 1/k$ (where k is the light absorption coefficient). An alternative solution to the boundary problem is therefore provided which would enable the particles to maintain a consistent light history.

As discussed in the previous sections, the reason for the failure of the reflecting boundary condition was that $K' \neq 0$ at the boundaries. The profile from Fig. 2.5(a) was therefore modified in such a manner which would deliver the necessary condition of $K' = 0$. The circles in Fig. 2.9 show how such a modification might look. This new profile has been obtained by applying a cubic smoothing spline to the original profile (including its mirrored extensions) in Fig. 2.7. The circles indicate the locations of the breakpoints for the spline. Since the extended profile is symmetric about the boundaries, one automatically obtains $K' = 0$ at each boundary (see right panel in Fig. 2.9). This procedure attempts to balance three factors: minimise the manipulated area in the original profile, achieve $K' = 0$ at the boundary, and keep K'' small (i.e. maintain a reasonable time step). Larger K'' values would require higher CPU time as the model time step is constrained by the maximum of K'' [Eq. (2.17)]. The amount of smoothing in the cubic spline was chosen such that Eq. (2.17) for the modified profile would yield the same value as for the original, viz. $\Delta t \ll 190\,\mathrm{s}$. This could only be achieved by giving less weight to the original data points near the boundaries which allowed the spline to become sufficiently smooth.

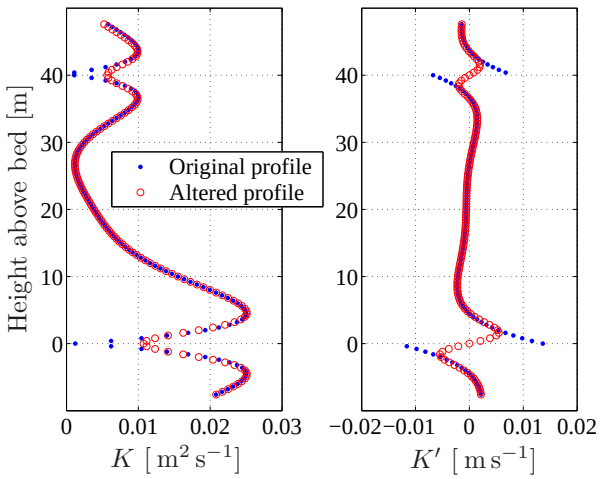

Figure 2.9: Smoothed profile from Fig. 2.7. The red circles represent the altered profile where the condition that $K' = 0$ has been imposed at the boundary. The profile has also been smoothed in order to obtain the same condition from Eq. (2.17) as for the original profile. This could be achieved by reducing the weight of the near-boundary data points (see text).

Fig. 2.8(b) shows the effect this has on the PDF. Although some wiggles remain near the boundaries, the improvement compared to Fig. 2.6 is again considerable and comparable to the previous method. This improvement can also be observed in the result from the model simulation. Compared to the original distribution [Fig. 2.6(b)], the effect of the boundaries is

much less severe, although still noticeable. The maximum deviation from 100% is about 0.5% at the surface and 1.5% at the bottom. Tests with various profiles showed that this error can be further reduced by making the model time step smaller as will be discussed in the following section.

2.2.4 Choosing the Time Step for the Simulation

In Section 2.2.1 it was shown that the time step for Eq. (2.15) is limited by the magnitude of the second derivative K'' through the inequality of Eq. (2.17). For the diffusivity profile shown in Fig. 2.5, this yields $\Delta t \ll 190\,\mathrm{s}$. Although the choice of $\Delta t = 6\,\mathrm{s}$ seems to meet this condition comfortably, inequalities are always difficult to implement in a quantitative manner and it would be desirable to have a more explicit condition of the form

$$\Delta t \lessapprox f\ \mathrm{MIN}\frac{1}{|K''|} \tag{2.22}$$

A closer look at the original PDF from Fig. 2.6(a) reveals a slight departure from unity already several metres away from each boundary [Fig. 2.10(a)]. This slight increase in the PDF is not visible in the particle distribution in Fig. 2.6(b) as it is masked by the much stronger boundary effect. By choosing a smaller time step of 2.5 s, the magnitude of the non-uniformity is reduced [dashed line in Fig. 2.10(a)]. A plot of $1/|K''|$ [Fig. 2.10(b)] shows that it is near the boundaries where the condition of Eq. (2.17) is likely to become critical for the profile from Fig. 2.5(a). It appears that once $1/|K''|$ reaches some critical threshold, the PDF begins to measurably deviate from unity. This is the cause of the remaining non-uniformities in the PDF in Fig. 2.8. If the time step is decreased, the departure from unity occurs closer to the boundary (i.e. at a higher value of $1/|K''|$). The two arrows in Fig. 2.10(b) roughly indicate the points of departure of the PDF from unity and although the magnitude of this deviation is small, it seems to have

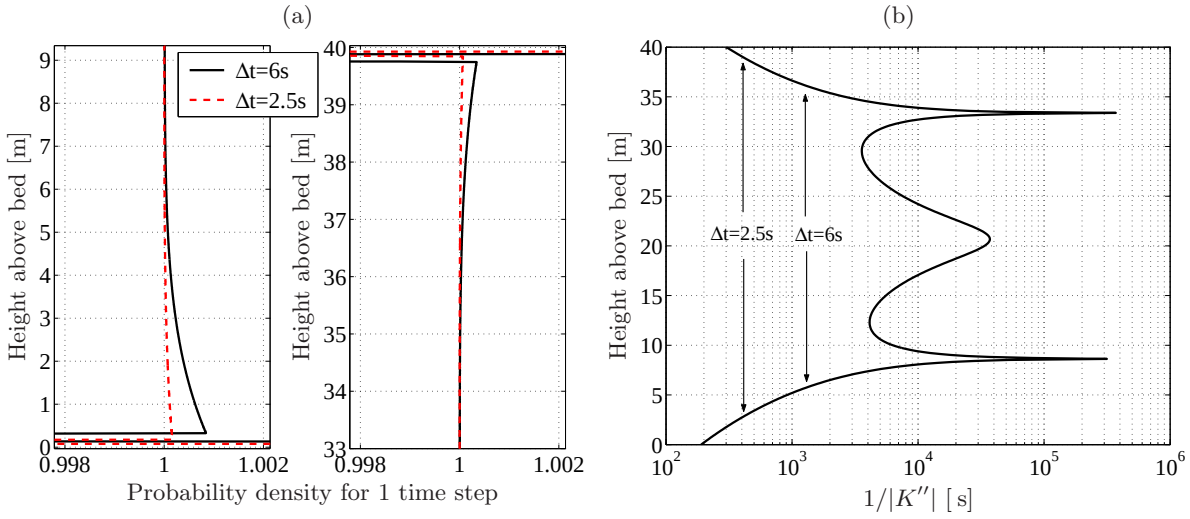

Figure 2.10: (a) Close-up view of the PDF from Fig. 2.6(a) at the bottom and top boundaries. The graph reveals an early departure of the PDF from unity that is not related to the presence of the boundaries but rather to the increase of $1/|K''|$ towards the boundaries which affects the time step allowed for the simulation. (b) Plot of $1/|K''|$ for the profile from Fig. 2.5(a). The arrows indicate where the PDF in (a) starts to depart noticeably from unity.

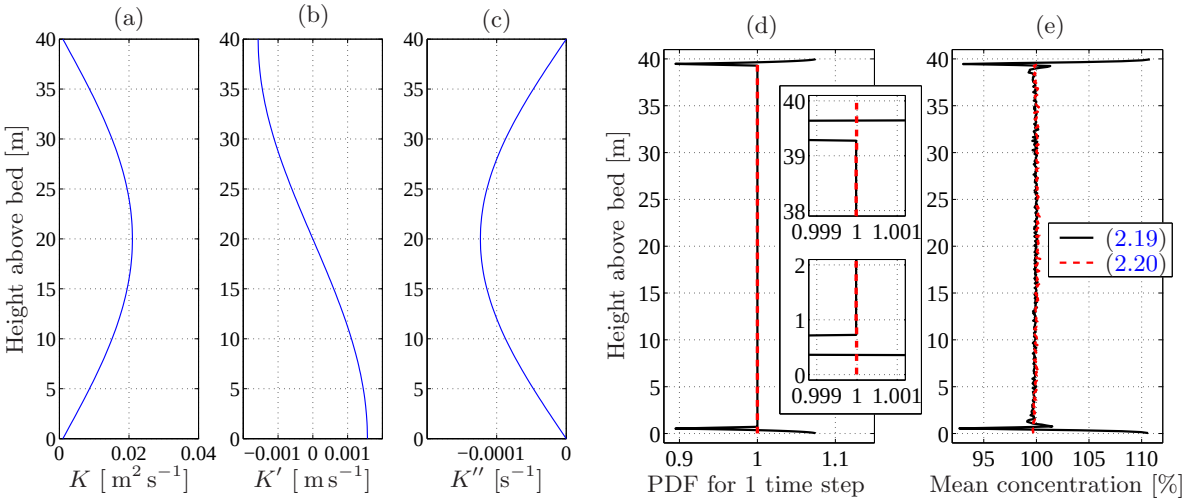

Figure 2.11: (a) Picture of the sine function from Eq. (2.23). (b) Derivative and (c) second derivative of the curve in (a). (d) PDF for Eq. (2.23) and one time step of $\Delta t = 60\,\mathrm{s}$ ($f = 1/130$). The continuous line shows the result for the reflecting boundary condition from Eq. (2.19) while the mixed layer approach from Eq. (2.20) has been used to produce the dashed line. As the close-up views show, the PDF of the mixed layer method never noticeably departs from unity. (e) Corresponding particle distributions. With an f-factor of 1/130, the departure of the dashed curve from the mean never exceeds 0.3% which is well within the statistical variability.

a significant effect still on the particle distributions [see the right panel in Fig. 2.8(a)]. For $\Delta t = 6\,\mathrm{s}$ this threshold is at $1/|K''| \approx 1300\,\mathrm{s}$ and for $\Delta t = 2.5\,\mathrm{s}$ the PDF starts to depart from unity at $1/|K''| \approx 420\,\mathrm{s}$. Hence we can determine f from Eq. (2.22) to be $f \approx 1/200$ which would require $\Delta t \lessapprox 1\,\mathrm{s}$ for the profile from Fig. 2.5(a). Several tests showed that this f-value produces particle distributions where the size of the accumulations becomes indistinguishable from statistical variations. f-values of $f \approx 1/100$ produce errors no larger than 1% which may still be acceptable for most applications.

Fig. 2.11 shows the PDF for the function

$$K(z) = 0.001 + 0.02 \sin\left(\frac{\pi z}{H}\right) \tag{2.23}$$

This function has the favourable quality that $1/|K''| \to \infty$ at the boundaries which also makes it a good candidate to test Eq. (2.20) without interference from the time constraint. The time step for the simulation was $\Delta t = 60\,\mathrm{s}$ ($f = 1/130$) which renders the mean particle distribution in a similar shape to the K profile from Eq. (2.23), i.e. slightly curved. In the central water column, the values are slightly above 100% and they become $< 100\%$ at the boundaries [not visible on the scale of Fig. 2.11(b)]. However, the departure from 100% is never greater than 0.3%.

2.3 The Biological Model

The diversity of phytoplankton species and the complexity of the individual physiologies make it impossible to design a biological model that is representative of every scenario. The intention was therefore to find a simple model that was able to reproduce certain observed properties of

phytoplankton growth and physiology (e.g. photo-acclimation), rather than trying to formulate a quantitatively accurate model to calculate 'exact' amounts of primary production. This section will describe the general part of the production model used for Chapters 3 and 4 which focuses on light requirements and response. The implementation of nutrients and further refinements or extensions to the present model are outlined in the respective chapters.

2.3.1 The Light Profile

Let us first consider the amount of light received by each cell per model time step Δt. The irradiance at a particular particle depth z_n obeys the Beer-Lambert equation

$$I(z) = I_0 c \, \mathrm{e}^{-k_t(H-z_n)} \tag{2.24}$$

where c is the fraction of the incident irradiance I_0 that is PAR (usually set to 45%) and k_t is the total absorption coefficient which is the sum of the background light absorption coefficient, k_{bg}, due to the natural turbidity of the water and other non-modelled cells, plus a contribution, k_s, from self-shading by the cells:

$$k_t(z_n) = k_{bg} + \underbrace{k_m \frac{\xi \, N(z_n)}{(H - z_n)\,1\,\mathrm{m}^2}}_{k_s} \tag{2.25}$$

where $N(z_n)$ is the number of particles above z_n. ξ is a scaling factor that accounts for the fact that there are only few particles in the model (usually 20 000) but much higher numbers in the actual water column. k_m is a cell-specific absorption coefficient (usually in $[\mathrm{m}^2\ (10^6\ \text{cells})^{-1}]$) that can be chosen to represent a single species or an entire group (see the individual chapters for details).

2.3.2 The Production Model

As discussed in Section 1.3.2, usually there cannot be just one P-I curve to describe primary production as a function of irradiance. The cells follow different curves, depending on their previous light history and physiological state. If the light intensity becomes too high, there may be a significant decrease in photosynthesis (photoinhibition) that is caused by a number of physiological reactions such as shrinkage of chloroplasts (see Section 1.3.2). The desired model should therefore be able to produce the observed variability in the P/I curves and allow for photoinhibition of the cell with a minimum number of parameters. The choice fell on the model by Denman and Marra (1986) which is based on the assumption that at any one time, the instantaneous production of a cell for a given light intensity will lie between a predefined maximum and minimum value. The maximum value is obtained if the cells had been left in the dark for several hours and are then exposed to light again. The minimum value is obtained for a fully inhibited cell that was previously exposed to several hours of high light intensities. The light response for these two extreme states is described by two different curves, which will be referred to as the fully dark-/light-acclimatised production, denoted as $P^{d/l}$:

$$P^{d/l} = P_m^{d/l} \left[1 - \exp\left(-I/I_{d/l}\right)\right] \tag{2.26}$$

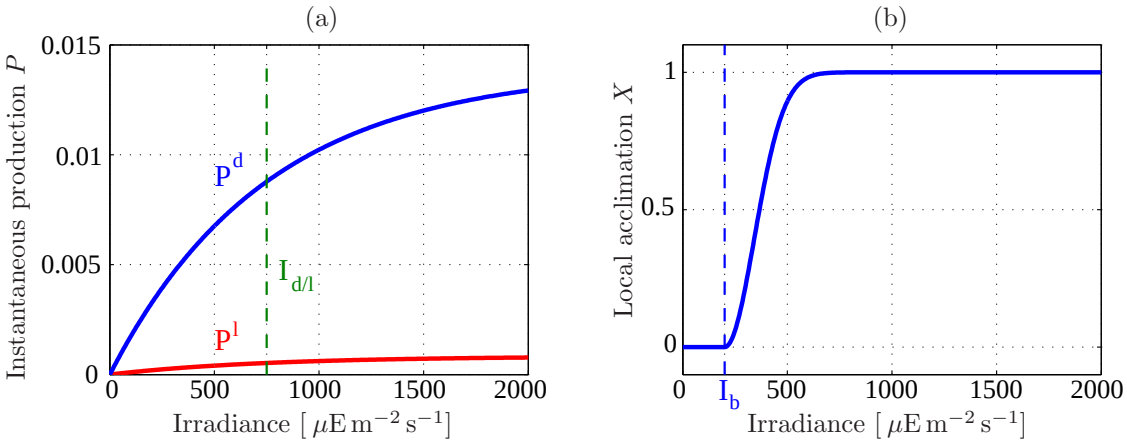

Figure 2.12: (a) Example of light/dark acclimatised production curves [arbitrary units]. (b) Local inhibition level.

where $I_{d/l}$ is the saturation onset for the dark-/light-acclimatised curves (equivalent to I_s in Fig. 1.4). A local inhibition parameter $X(I)$ can be defined which describes the inhibition a cell would achieve if it was held at a constant irradiance for a long time (i.e. a time longer than the acclimation time)

$$X(I) = 1 - \exp\left[-\left(\frac{I - I_b}{I_b}\right)^2\right] \tag{2.27}$$

where I_b is a user controlled parameter that determines at which irradiance the inhibition starts, i.e. where the instantaneous production curve starts to deviate from P^d. A graphic representation of both equations is shown in Fig. 2.12.

As the cells move through the light gradient, their cellular inhibition status Y changes according to

$$Y_{n+1} = Y_n + \frac{1}{\tau_a}\left(X(I) - Y_n\right)\Delta t \tag{2.28}$$

Thus the present inhibition status, Y_{n+1}, is based on the previous status, Y_n, and the cell is moving towards the inhibition level appropriate for the ambient irradiance level, $X(I)$, with the acclimation timescale τ_a. As τ_a is usually of the order of one hour while the time step Δt is of the order of seconds, the changes will be small but the cellular inhibition status Y always reflects the entire light history of the cell. Once Y is known, the instantaneous production can be calculated from

$$P = P^d + Y(P^l - P^d) - r \tag{2.29}$$

where r is a constant loss term to allow for cell respiration and mortality. Now it can be seen how the cellular inhibition status changes the instantaneous production. If the cell is fully inhibited ($Y = 1$), the production rate is simply $P^l - r$, i.e. equal to the high-light acclimatised or fully inhibited rate less the cost of respiration. If the cell has been kept in darkness for a long period, the photo-receptors will be fully open and the cellular inhibition status will be $Y = 0$ and thus $P = P^d - r$. Fig. 2.13 shows an example of this behaviour. In Fig. 2.13(a) a cell is being exposed to the sinusoidal light curve shown as a dash-dotted line. The resulting instantaneous production is shown as a continuous line. At sunrise (06:00h), the

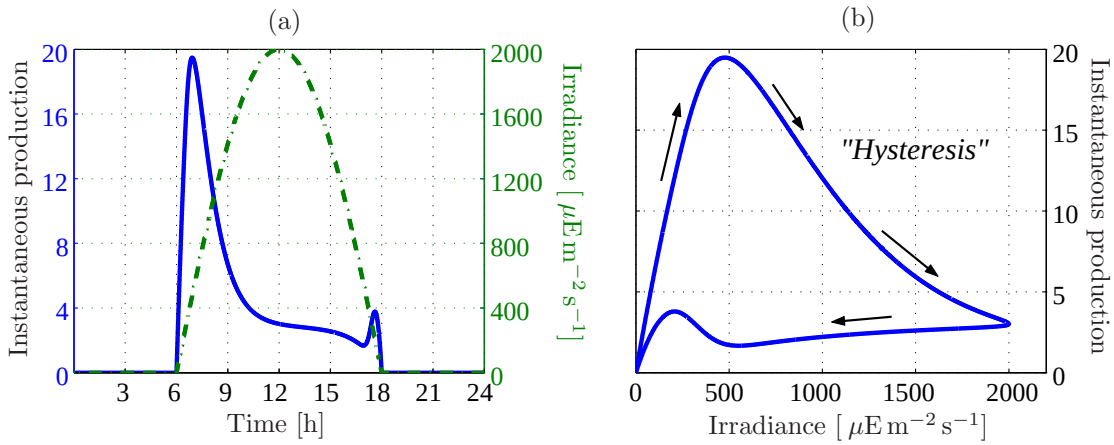

Figure 2.13: (a) Response of the instantaneous production (solid line) to a sinusoidal irradiance curve (dash-dotted line). After a sharp initial increase in production, the cells acclimatise to the increased irradiance leading to photo-inhibition. The production is thus not directly proportional to the irradiance and we observe a hysteresis effect which can be seen in the phase diagram in (b).

cells are dark-acclimatised and the production increases rapidly with increasing irradiance. At some point, the increasing inhibition leads to a sharp decrease in the production despite the increase in available irradiance. Although the irradiance curve is symmetric about noon, this symmetry is not observed in the production curve. This behaviour is known as 'hysteresis' in phytoplankton and can be seen more clearly in the phase diagram in Fig. 2.13(b).

Thus by defining only three main parameters, P_m^d, P_m^l and τ_a, together with the three minor shape parameters I_d, I_l and I_b, it is possible to obtain a photo-response model that produces photo-acclimation and -inhibition as well as hysteresis in the production response.

2.4 Testing the Model Behaviour

In order to ensure that the end result of a model output is reliable, it is important to test the individual components of the model. This will add credibility to the final product as a result of the various links and feedbacks between the model components. Much of the theoretical basis of the most important algorithms in the model has already been discussed in the previous sections. In this section it remains to verify experimentally their correct implementation and functioning.

2.4.1 Testing the Lahey Random Number Generator

Firstly, as Hunter et al. (1993) pointed out, not every random number generator is suitable to be used in random walk models. They differ significantly in their efficiency and, more importantly, in their 'randomness'. As a simple test, they suggest to compare the rate of increase of variance of a patch of modelled particles with the theoretical predictions. As Hunter *et al.* (1993) demonstrated, some of the commonly used random number genera-

tors can perform very poorly in this test, often yielding too low an increase in the variance which effectively simulates too low diffusivity values. Fig. 2.14 shows the results obtained for the Lahey Fortran random number generator for a patch of 4000 particles initially uniformly distributed about $z = 0$ in a constant diffusivity field of $K = 1/24\,\mathrm{m^2\,s^{-1}}$ with a time step of $\Delta t = 1\,\mathrm{s}$ and 10 000 iterations (solid blue line). Theory predicts that the variance should increase as $2K\Delta t$, i.e. by $1/12\,\mathrm{m^2}$ with every time step. The dashed lines in Fig. 2.14 indicate plus and minus one standard deviation from this prediction. The result lies well within these bounds and compares well to the curves obtained by Hunter et al. (1993) for the better random number generators in their test.

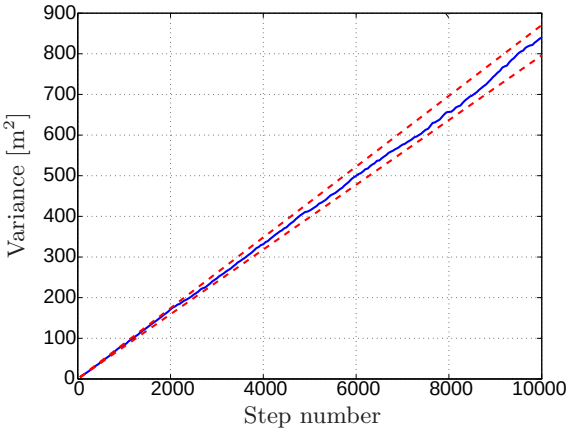

Figure 2.14: Results from the test of the Lahey Fortran random number generator (see text for explanation).

2.4.2 Testing the Random Walk Algorithm

The theoretical functioning of the random walk algorithm has already been demonstrated and its limitations outlined in Section 2.2. However, a true test for any random walk algorithm is the 'well mixed hypothesis' by Thomson (1984). Here, a uniform density of neutrally buoyant particles must remain at the same density even if the turbulence is inhomogeneous. The model was therefore used to reproduce Figure 3 in Visser (1997) where a total of 4000 neutrally buoyant particles are released into the diffusivity field shown in Fig. 2.15(a)[4] which is a re-

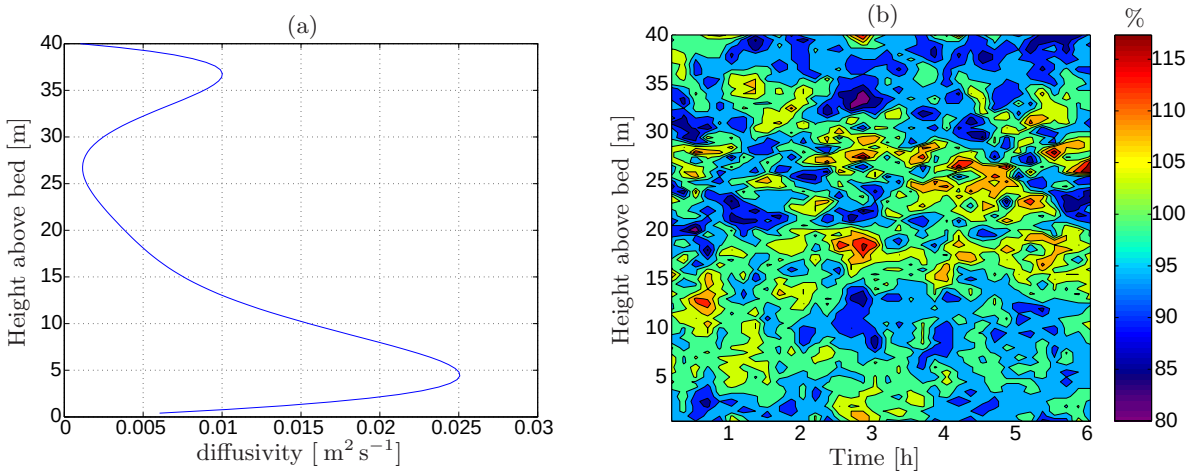

Figure 2.15: (a) A representative diffusivity profile simulating wind and tide induced mixing as obtained from a k-ε turbulence closure scheme described in Burchard and Baumert (1995). The figure is a reproduction of Figure 1 in Visser (1997). (b) Random walk of 4000 neutrally buoyant particles, initially distributed uniformly with depth, subject to the diffusivity profile in (a). The surface and bottom boundaries are reflecting. Units are percent of the average concentration of 100 $\mathrm{m^{-1}}$ and concentrations are averaged over 10 min periods.

creation of Figure 1 in Visser (1997). The particles are tracked for six hours using a time step of $\Delta t = 6$ s and the iteration from Eq. (2.15). The result is shown in Fig. 2.15(b). As in the published result, the pattern is virtually uniform, apart from some random fluctuations no greater than $\pm 20\%$ which appear to be grouped near the middle of the water column. The next section will examine the shape and size of these 'random' patches in more detail.

Effects of Averaging

Due to the nature of the Lagrangian approach, the volume of data produced often makes it necessary to output time- or space-averages of the data. Consider the previous examples where 4000 particles were tracked using a time step of 6 s. If the positions of every particle were output after every time step at, say, 1 cm vertical resolution, i.e. using 2 digits before and after the decimal point, one obtains 4000 particles $\cdot$ 6 bytes = 24 Kb every 6 seconds which would amount to about 345 Mb for 24 h. The position of the particles is therefore often output as one– to ten–minute averages only (e.g. Visser, 1997). If one wishes to use this data at a later point to address other questions, without having to re-run the entire model, care must be taken with how this averaged data are used, as the averaging process affects some of the statistical properties of the particle distribution.

In order to illustrate this point, 4000 particles were traced for 48 h in the (modified) diffusivity profile from Fig. 2.7 using the random walk from Eq. (2.15) with reflecting boundaries and a time step of $\Delta t = 6$ s. Fig. 2.16(a) shows the standard deviation (STD) of the particle distribution over the entire 48 hours before and after taking 10 minute means of the data.

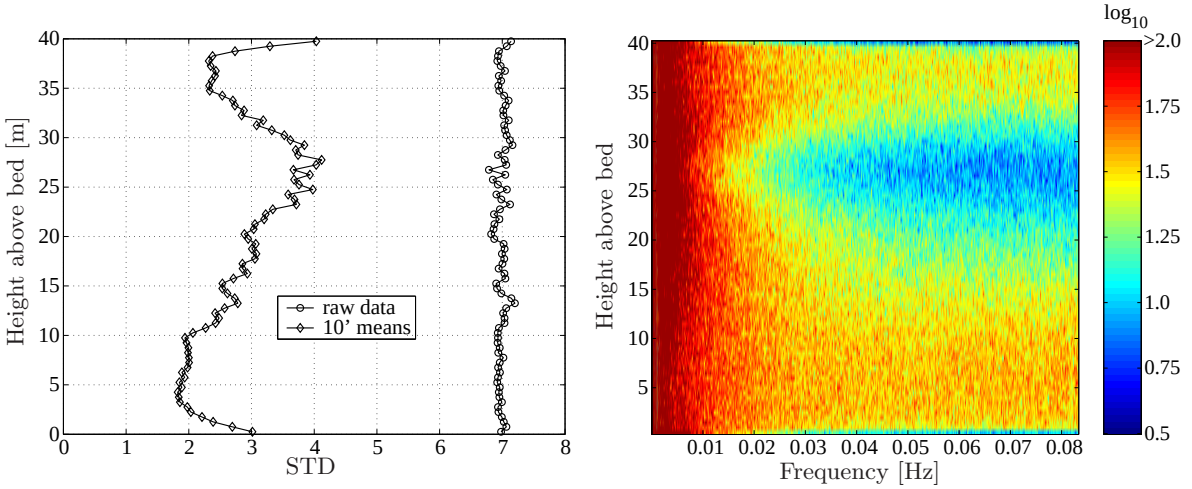

Figure 2.16: (a) Standard deviation of the particle concentration with and without averaging. (b) Fourier analysis of the frequency components in the particle concentration showing the logarithmic power spectrum for frequencies up to the Nyquist frequency $\nu_N = 1/(2\Delta t)$. The graph has been obtained in two steps: First the 48 h time series output of the (un-averaged) particle concentrations (binned into 0.1 m sized intervals) was Fourier transformed for each bin. This power spectrum was then Fourier transformed again, smoothed in its frequency domain using a modified Hanning filter to remove high frequency noise, and back-transformed using an inverse Fourier transform. The colour scale has been adjusted to give as much contrast as possible.

[4]The coefficients for this polynomial fit were obtained through private communication with Dr. Visser.

While the non-averaged data have a fairly uniform STD throughout the water column, the same curve for the 10-minute means does not look uniform at all but appears to have taken a shape similar to that of the diffusivity profile itself but reflected vertically, i.e. the STD is higher where the diffusivity is lower and vice versa. This could lead one to the wrong conclusion that a faulty random walk model has been used as there is no physical reason why the STD should be non-uniform provided that the sample period (in this case 48 h) is much greater than the local mixing time scales. The overall STD is lower which is to be expected after taking the means which effectively smoothes the data.

The cause for this non-uniformity clearly lies with the diffusivity profile. In the region of low diffusivities and small gradients (i.e. for $23\text{ m} \lesssim z \lesssim 32\text{ m}$), changes in the particle concentration occur rather slowly: if a bin contains a low/high number of particles, this bin is likely to contain a low/high concentration again for the next one or few time steps. At a depth where the diffusivity or the gradient is high, large changes in concentration can occur rapidly [Fig. 2.16(b)]. In these two areas, time averaging therefore has different effects. In the high diffusivity regions, time averaging will average *across* the statistical extremes, whereas in low diffusivity areas the averages might only span a single period of either low or high particle concentrations. This leaves more extreme values in the averaged data which results in a comparatively higher STD. The degree to which a STD profile is affected by the averaging process depends on the heterogeneity of the diffusivity itself and also on the time scale over which these fluctuations in the particle concentration occur in relation to the time over which the average is taken. The fluctuation time scale is proportional to the diffusivity so if the averaging time is very large, i.e. larger than the fluctuation time scale in the area with the lowest diffusivity, then the profile will remain more homogeneous. The only ways to avoid this problem are to output the position data at every time step or to perform any sensitive statistical calculations on the actual particle positions, i.e. while the model is running.

2.4.3 Testing the Different Internal Mixing Parameterisations

As a final test, we will examine the different internal mixing models that were outlined in Section 2.1.2. The parameterisations differ mainly in the amount of mixing that is added to the turbulent diffusivity calculated from the turbulence closure scheme. Fig. 2.17 shows the results for a model run using again the temperature profile from Fig. 2.3.

From all three implementations, the Canuto Model (CM) delivers the highest diffusivities throughout the water column. The Cantha-Clayson (CC) model delivers almost identical results to the simple background diffusivity (BG) model. This becomes particularly clear if we compare the individual profiles from Fig. 2.18. The only significant difference between the CC and BG model is at the very surface where the CC model drops to $10^{-6}\,\mathrm{m^2\,s^{-1}}$ while the BG model remains at $10^{-5}\,\mathrm{m^2\,s^{-1}}$. Within the thermocline the CM model delivers over five times higher mixing intensities than the other two. Based on comparisons with some observational data (e.g. Gargett, 1984) the Canuto model was therefore discarded for the experiments as the mixing within the thermocline is permanently elevated and rendered too high. Due to the

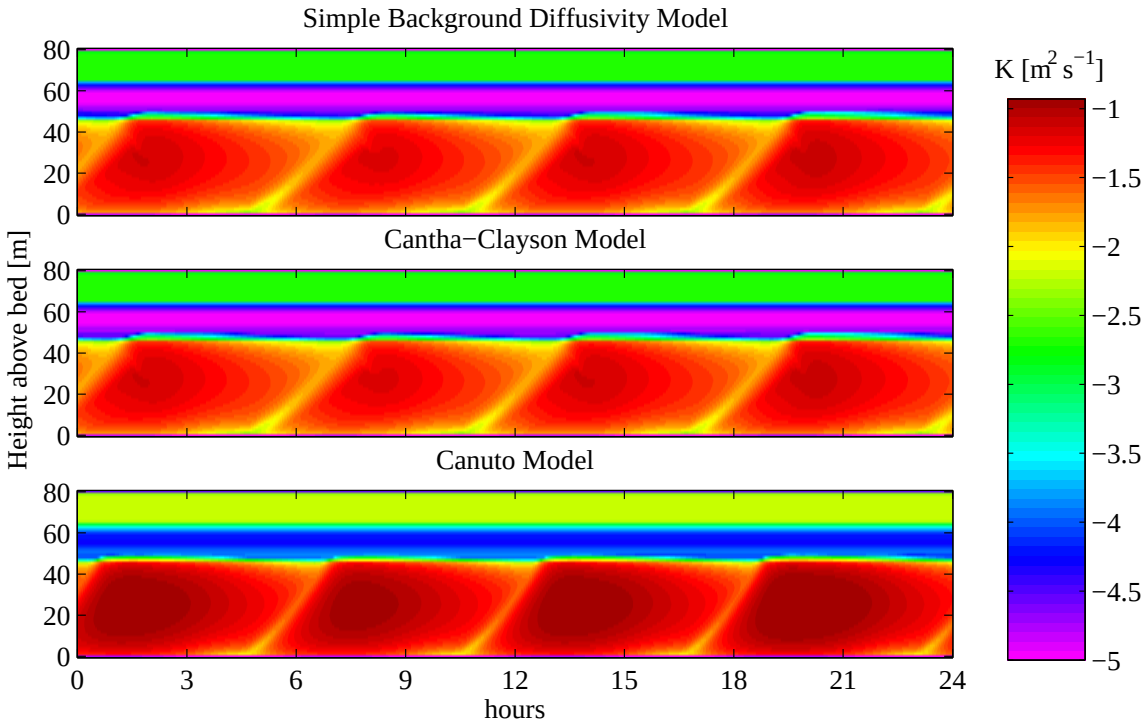

Figure 2.17: Comparing the three different internal mixing parameterisations. The experiment was forced with a strong M2 tide, corresponding to spring velocities in the North Sea. No wind mixing or irradiance input was applied. Instead the temperature profile was kept constant by preventing vertical temperature diffusion.

negligible differences between the CC and BG models, the BG model was chosen as it is the computationally cheaper approach.

This concludes the description of the more general aspects of the model. The following chapters will present the results of the simulations. In each chapter, the model has been set-up slightly different in order to account for the special requirements of the particular experiment. Each chapter will therefore describe the particular setup used in more detail.

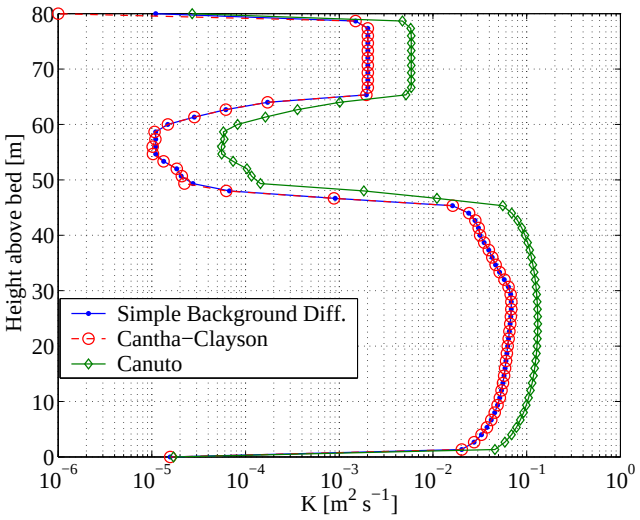

Figure 2.18: Comparing individual diffusivity profiles taken at 13.5 h from Fig. 2.17.

Chapter 3

Application to Tidally Energetic Estuarine Systems

In this chapter the model that was introduced in the previous section will be used to examine the effectiveness of motility in the tidally dominated estuarine system of Southampton Water, located on the south coast of England (see map in Fig. 3.1). Many authors have established the presence of motile plankton species in Southampton Water (Williams, 1980; Kifle, 1992; Lauria et al., 1999) and some have observed indications of a vertical migratory behaviour (Crawford and Purdie, 1992; Lauria et al., 1999). Southampton Water is a tidally energetic environment, however, where strong currents produce significant vertical turbulent mixing. The benefits of being motile in such an environment are therefore not as obvious as in an open ocean setting. This chapter will examine this issue.

The following sections will introduce the physical and biological characteristics of Southampton Water and explain the model setup for the later experiments. Two types of particles are released for the experiments: motile particles with various swimming speeds representing dinoflagellates and ciliates, and non-motile species with various sinking rates representing diatoms. Southampton Water is not nutrient limited (Ali, 2003, see below) and the growth model is thus based solely on the light availability. The results will examine whether motility leads to an increase in light availability and growth. The issue of photoinhibition is examined in the context of turbulent mixing and cell motility to evaluate whether an optimum swimming strategy exists which provides the cell with an optimum balance between light availability and inhibition avoidance.

3.1 Introducing Southampton Water

The partially mixed estuary of Southampton Water is located on England's south coast, forming the north-westerly extension to the Solent system (see Fig. 3.1). Southampton is an active port servicing mainly the car and oil industries which results in heavy ship traffic throughout the year. There are also frequent ferry services connecting Dock Head with the Isle of Wight

and Hythe on the western shore of the estuary. The main shipping channel is maintained at a depth of 10.2 m (below chart datum) in the upper estuary and at 12.6 m near the mouth (Hydrographic Office, 1997). The lower estuary is approximately 10 km long, and has a maximum width at high water of about 2.0 km with some intertidal mudflats along the western shore. The majority of the bed sediments consist of mud and sandy mud (Dyer, 1980).

Southampton Water has three tributary inlets: the rivers Test, Itchen and Hamble. Approximately 80-90% of the total freshwater output into the Solent is accounted for by the bigger Test and Itchen. The total freshwater input to Southampton Water constitutes about 1.3% of the neap tidal prism (Webber, 1980). The combined discharge of the Test and Itchen rivers can reach a maximum of over 35 $m^3 s^{-1}$ in late winter, declining to a minimum of less than 15 $m^3 s^{-1}$ in summer (Ribeiro et al., 2004). The flow of the Hamble river is negligible. For comparison, the tidal flow into the estuary reaches 7500 $m^3 s^{-1}$ on spring tides (Carr et al., 1980). Westwood and Webber (1977) examined the water exchange between the estuary and the Solent. Using salinity as a tracer they determined that the proportion of 'new water' entering Southampton Water on a neap tide was 32% of the flood tidal prism, indicating a high degree of flushing.

The general salinity structure along Southampton Water depends on the state of the tide and to a lesser degree on the seasonally changing freshwater input. In summer and autumn, surface salinities during high tide at Dock Head typically exceed 30, while in winter and spring, surface salinities during low tide can drop below 30 at the mouth of the estuary which has a yearly range in the vertical salinity difference between 0.5 - 3 (Phillips, 1980). The temperatures vary spatially and seasonally between 5.0 - 21.0°C with an annual mean temperature of 10.9°C (Carr et al., 1980).

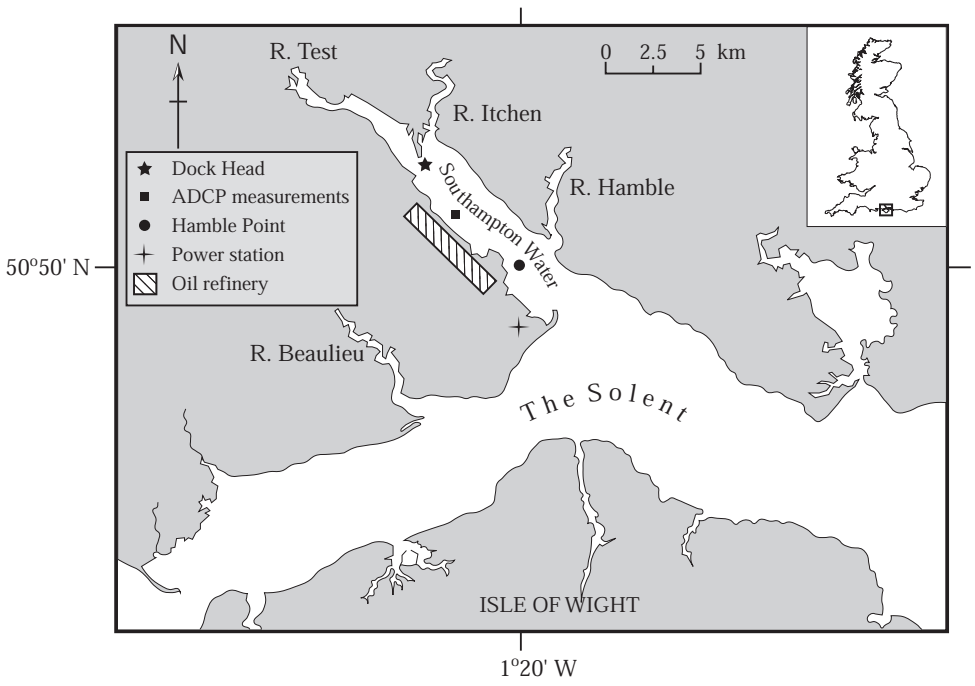

Figure 3.1: Map of Southampton Water and the Solent system.

3.1.1 The Tides in Southampton Water

The particular geometry of the English Channel and Solent system and resonance effects within Southampton Water result in a characteristic and rather complicated tidal signature which is dominated by the interaction of the M_4 and M_6 tidal constituents. A careful harmonic analysis of a long term data set yields over 20 significant constituents which, according to Webber (1980), makes the Solent tidal regime one of the worldwide most complex and difficult to explain.

Fig. 3.2(a) below shows the tidal current velocities measured by a 1200 kHz acoustic Doppler current profiler (ADCP) which was moored for 71 days in the location shown in Fig. 3.1[1]. The velocities show the v-component in a co-ordinate system that has been rotated so its ordinate coincides with the orientation of Southampton Water. The currents presented in this section are thus always true along-estuary velocities.

An almost monthly cycle can be observed in the data producing a comparatively *strong* neap tide on 6 March, followed by a *strong* spring tide, followed by a *weak* neap tide, followed by a *weak* spring tide, etc. This cycle is due to the N_2 tidal constituent ($T_{N_2} = 12.66$ h). Just like

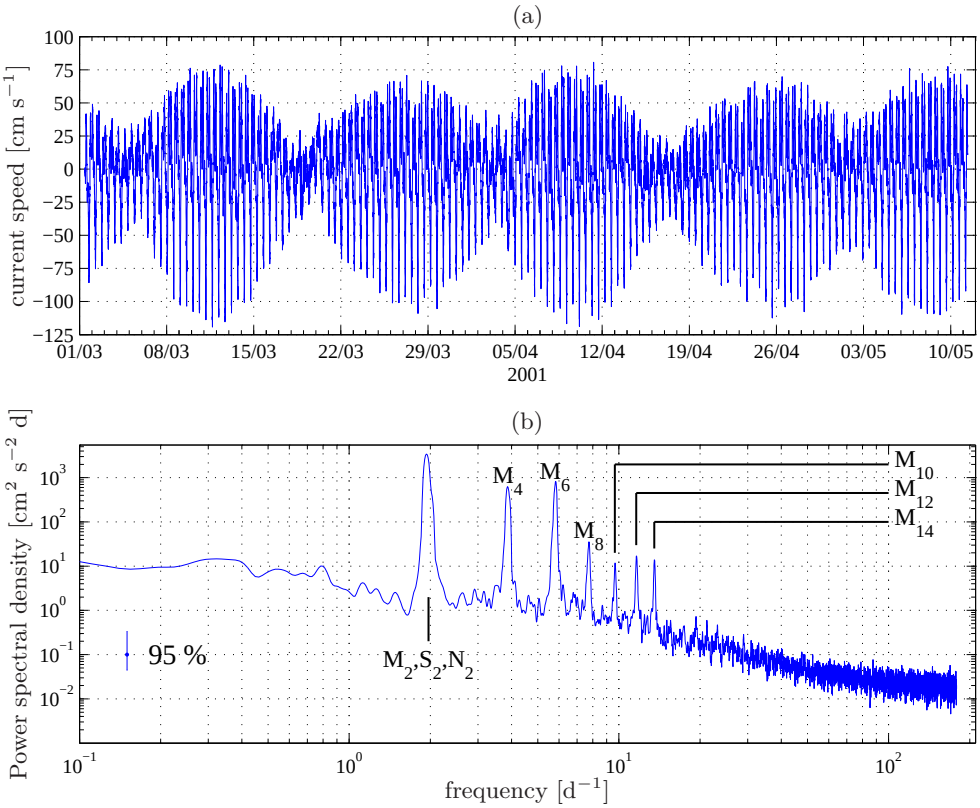

Figure 3.2: (a) Tidal velocities in Southampton Water from ADCP measurements. The currents shown have been depth averaged. Positive velocities are into the estuary. (b) Power spectrum of the tidal velocities, smoothed with 16 degrees of freedom. The main constituents are annotated and the error bar gives the 95% confidence interval from a χ^2 test.

[1]The raw data are courtesy of Cesar Ribeiro and Joanna Waniek from the Southampton Oceanography Centre.

the S_2 and M_2 constituents superimpose to produce the well known springs-neaps variation, M_2 and N_2 superimpose to produce a beat signal with the period:

$$T_b = \frac{2\pi}{\omega_{M_2} - \omega_{N_2}} = \frac{T_{M_2} T_{N_2}}{T_{N_2} - T_{M_2}} = 27.3 \text{ d}\,. \tag{3.1}$$

The power spectrum in Fig. 3.2(b) demonstrates that the tidal signal is characterised by the presence of shallow water constituents which combine to produce a highly asymmetric semi-diurnal tide [Fig. 3.3(a)]. Particularly at spring tides, these shallow water constituents lead to a prolonged flood phase, a water level stand at high water, and a rapid, short ebb tide [Fig. 3.3(b)]. The flood phase is split by a brief period of very low currents (the Young Flood Stand), while the high water stand (HWS), with negligible currents, can last up to 2 or 3 hours. The maximum ebb current is typically twice that of the maximum flood current. Spring ebb velocities range from just below $1\,\text{m}\,\text{s}^{-1}$ to over $1.4\,\text{m}\,\text{s}^{-1}$. Neap tides can have maximum ebb flows between $0.2\,\text{m}\,\text{s}^{-1}$ and $0.45\,\text{m}\,\text{s}^{-1}$.

From Fig. 3.3 three periods of differing lengths during which the mixing is reduced can be identified: The first occurs at the changeover from the ebb to the 1st flood and lasts only a few minutes; the second is the Young Flood Stand lasting for about 30 minutes; and the third is the extended HW stand of 2-3 hours. These periods will be of interest later, once the associated turbulent mixing is examined.

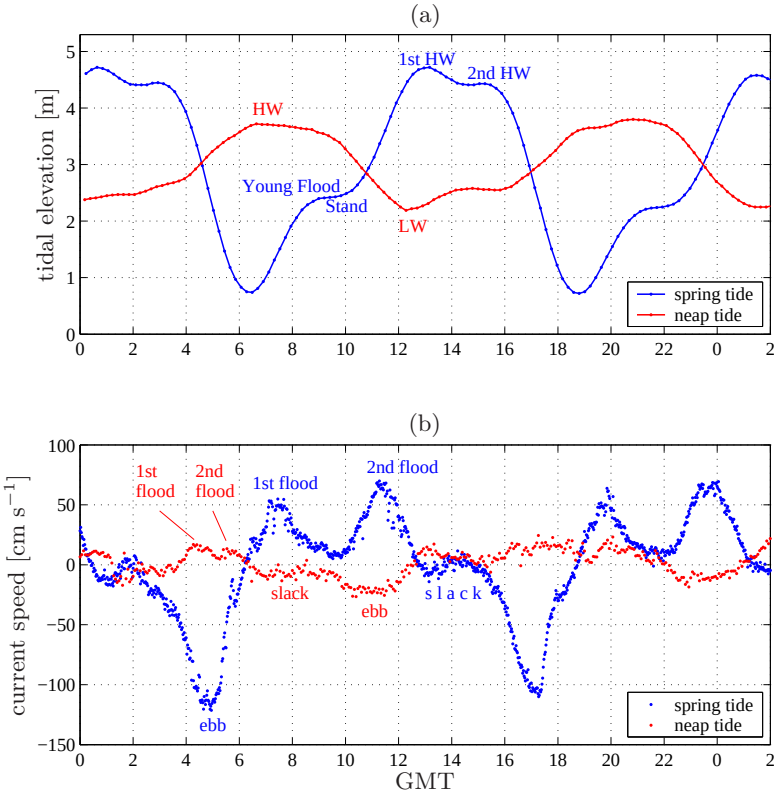

Figure 3.3: Typical tidal curves for Southampton Water: (a) Observed water level above chart datum at Dock Head during the spring tide on 15 November 2000 and the neap tide on 19 March 2001 [data courtesy of Associated British Ports (ABP)]. (b) Corresponding current velocities from ADCP measurements about 2.5 km down the estuary from Dock Head (see map in Fig. 3.1). The measurements are taken from approximately 1 m below the surface.

Estuarine Circulation

In order to estimate net transport of particles in an estuary, it is important to know the magnitude of the so-called estuarine or gravitational circulation. This sub-tidal transport gives an estimate for the net mass flux out of and into the estuary. The gravitational circulation is driven by the horizontal density gradient which exists in brackish waters like estuaries and fiords or generally in regions of freshwater influence (ROFI). Its main characteristic is the net seaward flow at the surface and a net landward transport by intruding saltier bottom water. This type of circulation is highly variable and its onset, persistence, and breakdown depends on the strength of the density gradient and also the vertical stability of the water column (Hansen and Rattray, 1965).

Ribeiro et al. (2004) examined the response of the estuarine circulation to changes in tidal and wind mixing in Southampton Water using the 71-day ADCP data from Fig. 3.2(a). During periods of low mixing, i.e. weak neap tides in combination with low wind mixing, the sub-tidal current strength reached values of over $0.1\,\mathrm{m\,s^{-1}}$ in the bottom and surface layer. They found that strong neap tides with ebb velocities of $0.4\,\mathrm{m\,s^{-1}}$ were sufficient to inhibit the onset of the gravitational circulation. Strong wind mixing has been observed to temporarily reduce the sub-tidal current strength or lead to the complete breakdown of the gravitational circulation. Since no significant changes in the freshwater input occurred during the deployment period, the onset of the estuarine circulation could be attributed to reduced tidal mixing (in the absence of wind mixing). During the entire 71-day deployment they observed only three short periods during which the gravitational circulation was well established. These periods coincided with the second, third, and fourth neap tide in Fig. 3.2(a) and persisted for a maximum of 4.5 days.

This information will become relevant later, when different particle swimming strategies will be examined, also in relation to minimising flushing losses from the estuary.

3.1.2 Tidal and Seasonal Changes in Turbidity

The light availability to the cells is very sensitive to the turbidity of the water. This section will therefore investigate the variability in turbidity, both on a diurnal and a seasonal time scale. The aim is to find a representative range of values for Southampton Water of the PAR absorption coefficient k_{bg} from Eq. (2.24).

Several factors can influence the water column turbidity. The most obvious ones are:

1. Resuspension of bed sediments due to an increase in tidal mixing as a result of increased shear stress.

2. Weekly and seasonal variations in the sediment load of the tributary rivers.

3. Ship generated turbulence and the resulting resuspension of bed sediments. After the passage of a larger container ship, oil tanker, or cruise liner the water in the wake usually shows a brown colour giving evidence of the amount of resuspension taking place.

4. Pollution by the oil refinery, the power plant (see Fig. 3.1) and general trade and sewage effluents that flow either directly into Southampton Water or its tributaries.

5. Self-shading effects from phytoplankton during periods of increased productivity (blooms).

While self-shading effects do not contribute to k_{bg} but will be included as a separate contribution k_s [see Eq. (2.24)], items 2.–4. from the above list largely depend on external and partially random factors (freshwater input, precipitation and soil erosion, ship traffic, sewage discharge) which cannot be parameterised in the model. The only factor that occurs with the required predictability is the tidal forcing of the currents. The following paragraphs will therefore examine to what degree diurnal and springs-neaps changes in the tidal current speeds are able to explain the observed variations in turbidity.

Observational data of current speed and turbidity, both courtesy of Cesar Ribeiro and Joanna Waniek, will be used for the analysis. The measured turbidity is a combination of k_{bg} and k_s and will therefore be denoted with k_t. The turbidity data were collected during six 13 h surveys on transects taking place between Dock Head and Hamble Point (see map in Fig. 3.1) using a towed, undulating minibat CTD with a mounted PAR light sensor. Table 3.1 provides a summary of the surveys. The PAR data were averaged to yield a representative profile for every 100-200 m of the transects. Only the PAR values that were at least three times larger than the sensor's 'dark' value were accepted and useable profiles were selected on the grounds that they had to contain at least four data points. A best line fit then yielded k_t from the linearised equation:

$$\ln I(z) = \ln I_0 - k_t z \qquad (3.2)$$

where z is the depth below the surface. As Fig. 3.4 illustrates, the above criteria for the selection of the data points produced very good fits to the data, but the observed variation is rather large as the values in Table 3.1 and the examples in Fig. 3.5 show. Part of the large variation can be explained solely on the grounds that the values stem from different parts of the estuary. Apart from this spatial variability, a comparison of the corresponding segments in each transect (which stem from roughly the same part of the estuary) also reveal a considerable temporal variability.

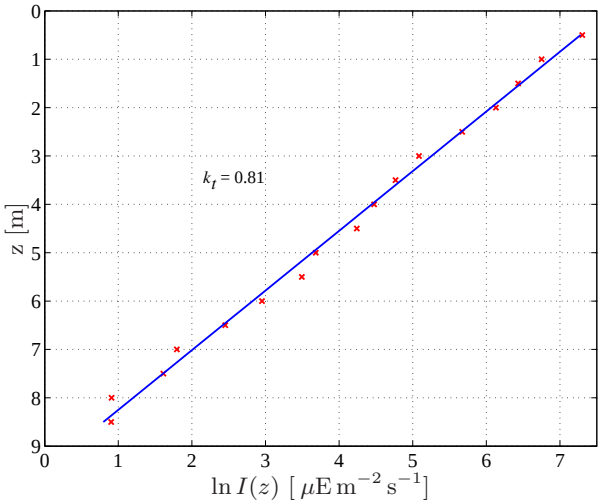

Figure 3.4: Example of the linear fit of the irradiance data. The plot shows the fit to a profile taken on August 22 around 12.40h, containing the surface PAR maximum for this survey of over 1400 μE m^{-2} s^{-1}.

On both days, a considerable but very localised increase in k_t appears during the first flood, approximately 3 h after the maximum ebb flow, about 4 km down-estuary from Dock Head. This could imply that sediments which were resuspended during the maximum ebb flow and carried down-estuary are brought back into the estuary with the incoming flood. However,

TABLE 3.1: Summary of the observational data for the PAR absorption coefficient k_t (in $[\,\mathrm{m}^{-1}]$). The tidal state at the time of observation is given in the abbreviated form S/N $\pm$ n, where S refers to spring tide, N is neap tide, and n is the number of days before (-) or after (+) the spring or neap tide.

date	15/11/00	22/11/00	08/03/01	15/03/01	08/08/01	14/08/01
tidal state	S+2	N+2	S−3	N−3	S+1	N
tidal range [m]	4.0	2.94	4.0	3.28	3.2	2.12
$[k_{t_{min}}\ k_{t_{max}}]$	0.84 1.79	0.56 1.52	0.39 1.41	0.71 1.33	0.65 1.32	0.50 0.87
$\overline{k_t} \pm$ 1STD	1.17 ± 0.19	0.89 ± 0.15	0.85 ± 0.13	0.87 ± 0.11	0.91 ± 0.13	0.69 ± 0.07

the fact that this phenomenon is rather localised and not present on the other survey days in November 2000 and August 2001, suggests other causes for this increase in k_t. Also the fact that on 15/03/01, an ebb flow of about $0.80\,\mathrm{m\,s}^{-1}$ should produce a 50% increase in k_t, while the subsequent flood flow of $0.55\,\mathrm{m\,s}^{-1}$ produces no increase in turbidity in the upper estuary at all, is rather peculiar. More probable causes for these phenomena are thus either passing ships or effluent from the oil refinery which is carried up the estuary with the incoming tide. Another mechanism could simply be finite patches of suspendeable material on the seabed, leading to patchy clouds of material in the water that the consecutive transects may or may not pass through.

Although Table 3.1 shows that k_t is generally higher at spring and lower at neap tide, no obvious temporal relationship between the immediate current strength and the absorption coefficient on shorter time scales could be found (at least not in the top 5-10 metres where the PAR sensor has enough light to operate). A more stringent correlation analysis yielded the same results as the visual inspection of the graphs. Apart from the springs-neaps variation there also seems to be a generally higher turbidity in winter with k_t decreasing towards summer.

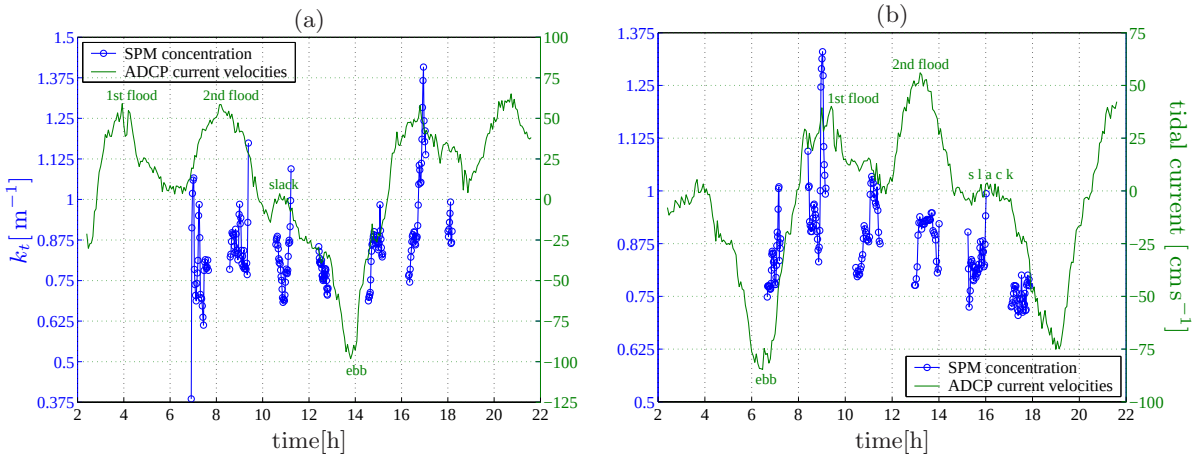

Figure 3.5: Example of the calculated k_t-values from the surveys on (a) 08/03/01 and (b) 15/03/01. Only the southbound transects are shown, i.e. the ones starting in the upper estuary at Dock Head and going towards the mouth of the estuary at Hamble Point. The length of each transect is about 5 km. The blue circles indicate the calculated values for k_t. The circles belonging to the same transect are connected with a solid blue line. The green lines show the along-estuary tidal velocities from the ADCP measurements.

This rather large spatial, temporal, and seasonal variability of k_t makes it difficult to choose a representative value for the model, especially since there seems to be no correlation in the top 5-10 m with the tidal current strength. The choice of k_t was therefore taken on the basis of the following observations:

- k_t is generally lower at neap than at spring tide. Both in the November 2000 and August 2001 surveys, $\overline{k_{t_\mathrm{s}}} \approx 1.3\,\overline{k_{t_\mathrm{n}}}$.
- The important months for phytoplankton production in Southampton Water are March to August (see Section 3.1.3).
- Although the range in k_t can be large, great increases appear to be very localised, short lived, and not related to the immediate current velocity. The effect on the mean value is thus rather small which is also reflected in the small standard deviation (Table 3.1).

Two mean values for k_t were therefore selected: one representative for a neap tide and the other for spring. The overall average value during the two March and August surveys (these months mark the beginning and end of the growth season) is $\overline{k_t} = 0.82 \pm 0.14\,\mathrm{m}^{-1}$. The neap and spring values were chosen to lie symmetrically about this value such that $\overline{k_{t_\mathrm{s}}} \approx 1.3\,\overline{k_{t_\mathrm{n}}}$. This yields: $\overline{k_{t_\mathrm{s}}} = 0.93\,\mathrm{m}^{-1}$ and $\overline{k_{t_\mathrm{n}}} = 0.71\,\mathrm{m}^{-1}$. In Section 3.2, it will be explained how these values are then split into a background and phytoplankton-specific absorption coefficient such that $k_t = k_{bg} + k_s$.

3.1.3 Phytoplankton in Southampton Water

According to Williams (1980), most photosynthesising organisms in Southampton Water are planktonic rather than benthic algae. Chlorophyll *a* values vary from about 1–2 mg Chl m^{-3} in winter to 10–20 mg Chl m^{-3} in summer. Bloom values are of the order of 40 mg Chl m^{-3}, but values of over 100 mg Chl m^{-3} have been observed (Crawford and Lindholm, 1997). Blooms have been observed as early as April and are usually composed of diatoms which start to be succeeded by autotrophic ciliates in late May and dinoflagellates in June (Kifle, 1992). Several authors have found a general horizontal decrease in Chl *a* concentration from mid-estuary seawards (Williams, 1980; Antai, 1989; Kifle, 1992; Lauria et al., 1999) which they attributed to increased tidal exchange of estuarine water with Solent water.

A recurring feature in Southampton Water are the red tide events caused by the non-toxic phototrophic ciliate *Mesodinium rubrum*. These events occur at irregular intervals and bloom events have been observed between May to late August (Kifle, 1992; Crawford and Purdie, 1992; Leakey, 1989). A survey of the bloom-forming species found in Southampton Water and their swimming and sinking velocities has been carried out. Table 3.2 gives a summary of the available data.

The motile species have moderate swimming velocities between 0.07-0.26 mm s^{-1} with the exception of the ciliate *Mesodinium rubrum* which has an outstanding burst speed of 8 mm s^{-1}.

TABLE 3.2: Phytoplankton species in Southampton Water compiled with data from Kifle (1992), Williams (1980), Eppley et al. (1967), Taylor (1987), Hasle and Syvertsen (1996), Crawford and Purdie (1992), Kamykowski et al. (1992), Jonsson and Tiselius (1990), Kuylenstierna and Karlson (2000) and Lauria (1998).

SPECIES	PHYTOPLANKTON GROUP	SEASON	SIZE RANGE [μm]	SINKING/SWIMMING SPEED
Non-Motile Species				
Asterionella japonica	diatom	April - late August	30–150 (apical axis)	
Biddulphia alternans	diatom	July - August	$\approx$ 10–20	
Biddulphia mobiliensis	diatom	April - July	80–300 (apical axis)	
Chaetoceros spp.	diatom (chain forming)	late August	10–40	5–20 μm s^{-1}
Coscinodiscus radiatus	diatom	April -July	30–180	0.08-0.1 mm s^{-1} (for *C. wailesii*)
Lithodesmium undulatum	diatom (chain forming)	April - July	37–93	
Rhizosolenia delicatula	diatom (chain forming)	April/May - June	9–22 (diameter)	
Rhizosolenia setigera	diatom	April - July	4–25	
Skeletonema costatum	diatom (chain forming)	mid April - May	5–25	4–17 μm s^{-1}
Thalassiosira sp.	diatom (chain forming)	April - July	12–78	7–27 μm s^{-1}
Motile Species				
Eutreptiella marina	euglenoid	mid - late May	10–80	
Mesodinium rubrum	ciliate (autotroph)	late May - late August	15–70	8 mm s^{-1} (burst speed)
Gonyaulax spp.	dinoflagellate	mid June	30–75	0.26 mm s^{-1} (*G. polyedra*)
Peridinium (=*Scrippsiella*) *trochoideum*	dinoflagellate	mid June - late August	20–100	0.07 mm s^{-1}
Phaeocystis sp.	prymnesiophyte	late May-June	3–8 (colony: 1–5 mm)	
Prorocentrum micans	dinoflagellate	mid June - late August	35–70	0.25 mm s^{-1}

Although the swimming behaviour of this species changes from rapid jumps to periods of no motion (Jonsson and Tiselius, 1990), vertical migrations of some 40 m d^{-1} have been observed in the Peru upwelling system (Smith and Barber, 1979) which corresponds to an average vertical displacement of almost 0.5 mm s^{-1}. Due to the turbulent mixing which forces the cell to readjust it's orientation, the average swimming velocity is likely to be > 0.5 mm s^{-1}.

Several authors have also addressed questions trying to relate the motile phytoplankton behaviour with the physical conditions in Southampton Water. Crawford and Purdie (1992)

for example, studied the vertical migratory behaviour of *Mesodinium rubrum* during a red tide event. Relating the cell distributions to stability and mixing over a full tidal cycle, they suggested that the cells used motility to avoid turbulence, with a superimposed positive phototactic diurnal migratory behaviour to avoid heavy losses due to surface flushing. Lauria (1998) examined both motile and non-motile phytoplankton, claiming that the periodicity in the turbulent mixing in Southampton Water would provide the niches for both diatoms and dinoflagellates to co-exist. Diatoms rely on the increased vertical mixing during the ebb and flood currents to become entrained into the photic zone while dinoflagellates utilise the slack water periods to aggregate near the surface and increase their light availability (see also Lauria et al., 1999). Following the findings of Crawford and Purdie (1992) for *Mesodinium rubrum*, she proposed a similar migratory behaviour for the dinoflagellates *Prorocentrum micans* and *Peridinium trochoideum*, and the motile euglenoid *Eutreptiella marina*.

The next sections will examine whether the required swimming speeds necessary to form the observed accumulations during slack water are in agreement with those pertaining to the local species. Two different behavioural swimming strategies will be examined: 1) given the high values for the PAR absorption coefficient k_t (see Section 3.1.2), Southampton Water is likely to be light rather than nutrient limited. The cells will therefore always hunt for light, i.e. swim constantly upward; 2) the hypothesis of diurnal vertical migration proposed by Crawford and Purdie (1992) for *Mesodinium rubrum*, and by Lauria (1998) for the dinoflagellate species from Table 3.2, will be tested in order to determine whether the swimming speeds of these species are sufficient to gain advantage from such a strategy.

3.2 Model Setup for Southampton Water Study

3.2.1 General

Stratification in Southampton Water is dominated by freshwater input and surface heating is therefore not important. For all experiments in this chapter, any heat exchanges between the surface water and the atmosphere have therefore been neglected. The surface irradiance is only used to determine the light availability (PAR) to each cell, which depends on the cell's vertical position in the water column and the light attenuation k_t (Section 3.1.2). The irradiance profile is given a semi-sinusoidal variation with the maximum occurring at 12 noon.

The model also neglects any vertical salinity variations. This may appear an unreasonable assumption, particularly considering that the surface-to-bottom salinity difference can cause density contrasts between $0.5 \lessapprox \Delta\varrho \lessapprox 3\,\mathrm{kg\,m^{-3}}$. However, the use of turbulence closure schemes to relate stability and mixing is notoriously unreliable in estuarine environments (e.g. Sharples et al., 1994). Even small vertical density gradients can severely dampen any vertical exchange, primarily because the models are unable to resolve adequately the internally-generated mixing (e.g. internal waves, internal lee waves). The approach taken here is to use the turbulence closure scheme to provide a link between tidal current speed and turbulent mixing, in the absence of vertical stratification. The typical values of the vertical diffusion coefficient

produced by the model are checked against observations made in Southampton Water using a microstructure turbulence probe (J. Waniek, pers. comm.). Wind driven mixing has also been excluded in the following experiments in order to keep the model as simple as possible and to be able to isolate the tidal signal in the results.

A strong source of turbulent mixing in Southampton Water is the velocity shear due to bottom friction as the tidal currents move across the sea bed. The observed springs-neaps variability in the turbulent mixing intensity can be linked to the springs-neaps variation in tidal current strength (J. Waniek, pers. comm.). Two different scenarios have therefore been chosen to represent the tidal extremes in Southampton Water:

- The **Neap Tide Scenario (NTS)**: for this experiment, the model will be set up to simulate neap tide conditions in Southampton Water.
- The **Spring Tide Scenario (STS)**: in this scenario the current strength and tidal phase will correspond to a spring tide in Southampton Water.

Due to the interaction between the N_2 and M_2 tidal constituents (see Section 3.1.1), the maximum (depth-averaged) ebb velocities at neap tide can range from $0.25\,\mathrm{m\,s^{-1}}$ during a weak neap to $0.50\,\mathrm{m\,s^{-1}}$ during a strong neap which produces great differences in the turbulent mixing. For spring tides, the corresponding values are $0.75\,\mathrm{m\,s^{-1}}$ and $1.1\,\mathrm{m\,s^{-1}}$. Two sub-variants of each scenario are therefore examined: a weak NTS/STS (wNTS/wSTS) and a strong NTS/STS (sNTS/sSTS, see next section).

In Section 3.1.1 we saw that three periods of reduced mixing occur during a semi-diurnal tidal cycle in Southampton Water. For the swimming efforts of the plankton cells, these periods will prove important as they provide them with a turbulence-break during which they will be able to adjust their vertical position more effectively. The timing of these breaks in relation to the daily irradiance maximum will also prove important for the light availability to the cells. Due to the complicated tidal signature of Southampton Water, the maximum/minimum tidal velocities can occur for up to two days either side of the actual spring/neap tide. In order to cover this entire range, and in order to examine the effect the slight phase change of the turbulence-breaks in relation to the irradiance maximum has on the light availability, the model is run for four consecutive days in each of the spring and neap scenarios. On each successive day the time at which these turbulence-breaks occur, will be shifted forward by about 50 minutes.

The following model parameters are calculated and set up using observational data:

- the tidal current amplitudes for both spring and neap tide and their temporal relation to the solar cycle,
- turbidity variations as a function of tidal mixing, and
- tidal depth variations.

3.2.2 Driving the Tides in the Model

For each of the above scenarios a representative day was chosen from the available ADCP data and the depth-averaged velocities harmonically analysed using the method described in Emery and Thomson (1998) to obtain the amplitudes and phases of the tidal constituents. Table 3.3 summarises the tidal characteristics of the chosen periods. Table 3.4 and Fig. 3.6 show the results from the harmonic analysis.

TABLE 3.3: Summary of the ADCP and ABP data used for the different scenarios in the Southampton Water simulation. The velocities are depth averages.

Scenario:	STS		NTS	
	weak	strong	weak	strong
date	16/01/02	19/09/01	17/04/01	02/05/01
length of time series [d]	1.15	1.15	1.15	1.15
tidal range [m]	3.61	4.87	1.56	2.39
max. flood [$\mathrm{m\,s^{-1}}$]	0.51	0.75	0.23	0.37
max. ebb [$\mathrm{m\,s^{-1}}$]	-0.82	-1.07	-0.28	-0.53

Since only about 27 h have been analysed to represent the spring and neap scenarios, it would have been sufficient to use the dominant M_2, M_4 and M_6 constituents only to achieve the essence of the observed tidal behaviour. In order to reach the full amplitudes, however, it was necessary to include also the weaker M_8, M_{10}, M_{12} and M_{14} constituents in the analysis. As can be seen (Table 3.4), the amplitudes of these higher harmonics are negligible in the wNTS and have only been included for reasons of consistency.

The phases shown in Table 3.4 generally do not agree with the model input phases. As was explained in Section 2.1, the tides in the model are driven by oscillating the sea surface slope,

TABLE 3.4: Velocity amplitudes (in [$\mathrm{m\,s^{-1}}$]) and phases (in radians between $-\pi$ and π) of the tidal constituents used in the model. The values shown have been obtained through a harmonic analysis of the ADCP data. Note that the phases in particular will be different from those used in the model (see main text). The last row gives the root-mean-square (standard deviation) of the error in the fit in [$\mathrm{m\,s^{-1}}$].

Tidal const.	period [h]	Weak Spring		Strong Spring		Weak Neap		Strong Neap	
		amp	ph	amp	ph	amp	ph	amp	ph
M_2	12.4206	0.353	2.756	0.473	2.613	0.157	-0.241	0.252	-0.267
M_4	6.2103	0.172	0.506	0.212	0.452	0.046	1.451	0.079	1.218
M_6	4.1402	0.272	-2.614	0.300	-2.775	0.073	1.727	0.127	1.701
M_8	3.1052	0.031	2.316	0.044	2.412	0.006	0.885	0.021	-1.995
M_{10}	2.4841	0.052	-1.879	0.052	-1.451	0.001	1.801	0.012	0.521
M_{12}	2.0701	0.034	-1.889	0.049	-2.766	0.007	3.075	0.034	0.012
M_{14}	1.7744	0.035	1.591	0.052	0.602	0.005	0.590	0.018	1.129
rms of error:		0.042		0.038		0.027		0.048	

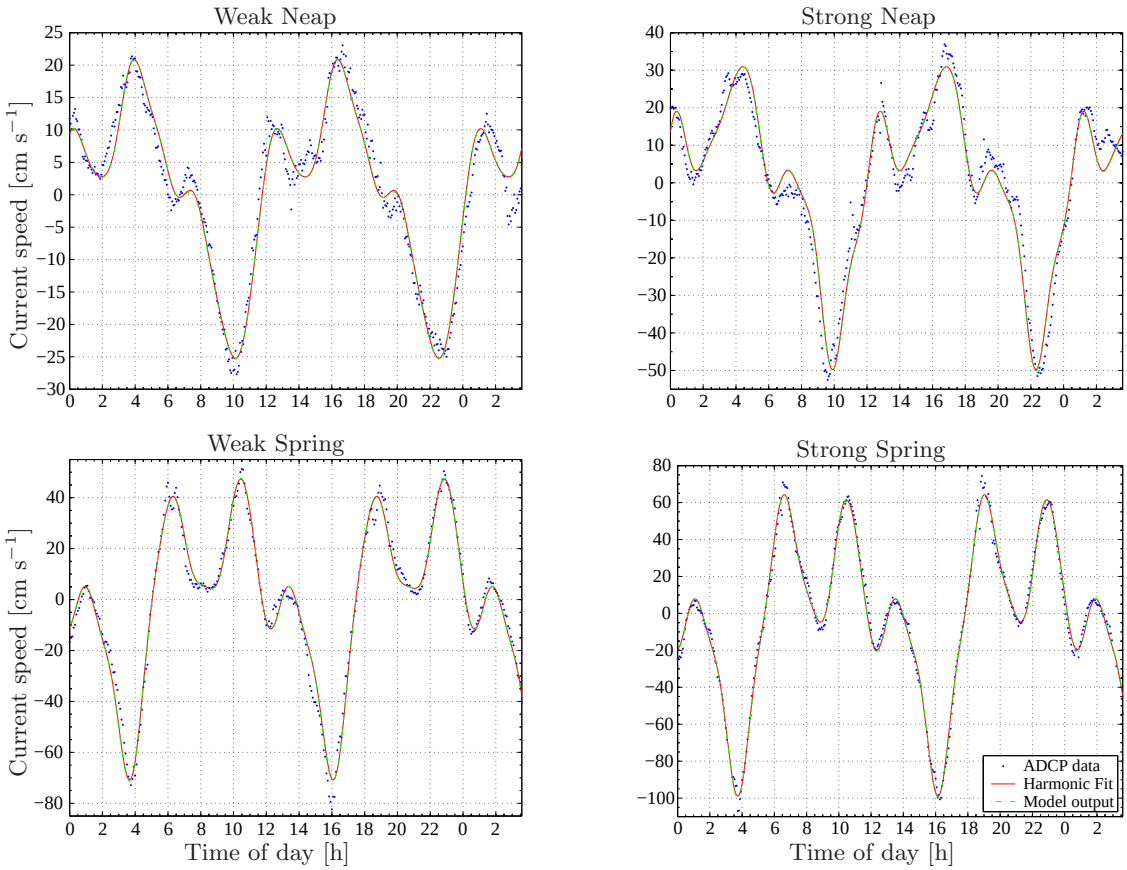

Figure 3.6: Depth averaged velocities for the neap and spring tide scenarios. The graphs contain the original ADCP data, the fitted curve using the M_2 through to M_{14} constituents and the depth average of the velocity output from the model.

thereby creating pressure gradients from which the current speeds are calculated. Ideally one might expect the slope phases to be the same as the speed phases. The reason for the discrepancy is that friction with the seabed alters the response of the currents to the slope which becomes particularly important in this case as the water is very shallow. The model phases that drive these sea surface slope oscillations were therefore determined by harmonically analysing the model velocity output and varying the input phases until the phase relation of the output velocities matched those from the harmonic analysis of the ADCP data. A small negative bias has been added to the slopes to generate the net seaward flow which was present in the ADCP data. The discrepancy between the model output and the fit to the ADCP data is negligible (Fig. 3.6).

3.2.3 Determining the Changes in Water Level

In particular during a spring tide the tidal range in Southampton Water can represent over 35% of the mean water depth. It is therefore important to take changes of water depth into account as they will influence the light availability to the cell as the proportion of the water column above the compensation depth varies. The observations of the tidal depth variations are taken

from a tidal prediction data-set provided by Associated British Ports (ABP) for Southampton Water Dock Head. Those data are only used to scale the model calculations of water height which are derived directly from the model velocities (see Appendix A). Section 3.4.5 describes how they are integrated into the Lagrangian model.

3.2.4 Physics Model Output for Southampton Water

Fig. 3.7 shows an example of the simulated current and mixing structure for the simulation of a strong spring tide scenario. Compared to observations, the timing of the tidal currents can be regarded as an 'early' scenario. The currents shown for the sSTS in Fig. 3.6 depict a 'late' scenario where the ebb flow does not start until approximately 15:00 h. In the model this is represented by day 4 of the consecutive 96 h output.

Each semi-diurnal cycle is characterised by three main pulses of TKE which correspond to the three tidal flows. The turbulence is generated at the bottom boundary through frictional

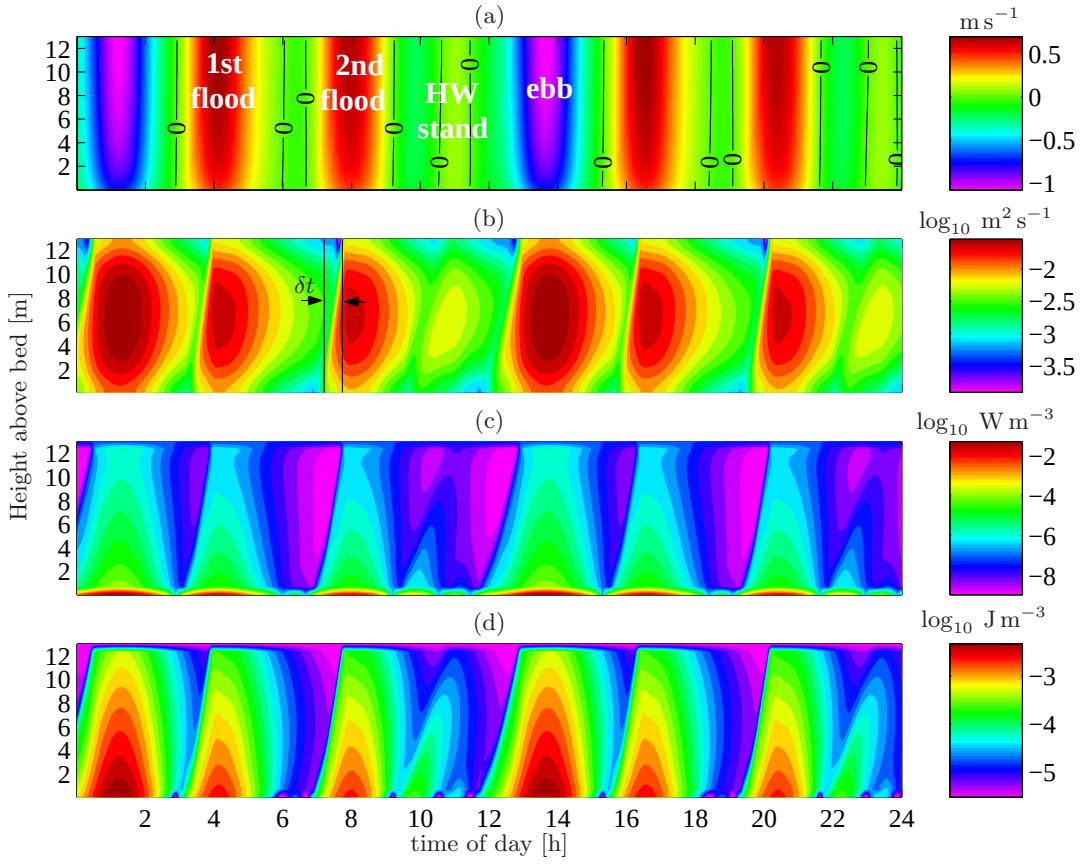

Figure 3.7: Model output of the first 24 h of the 4 day output for Southampton Water simulating sSTC. The water depth was kept constant at the mean of 13 m. (a) Tidal along-estuarine velocities, (b) eddy diffusivities, (c) TKE dissipation, and (d) TKE. The diffusivities shown are those used for the particle tracking, i.e. they have been smoothed using cubic smoothing splines in order to force $K' = 0$ at the boundaries (see Section 2.2.3). In order to keep the profile sufficiently smooth, and thereby reduce the constraint on the time step for the random walk (see Section 2.2.4), the diffusivities at the boundaries are not allowed to drop to the background value of 10^{-5} m^2 s^{-1} (as is the case in the raw model output).

forces with the sea bed and slowly propagates upwards through the water column (hence the slightly slanted shape in the diffusivities – see below). It is also near the sea bed where most of the TKE is dissipated. In accordance with the turbulent length scale, the diffusivity maximum occurs near the centre of the water column and decreases towards the boundaries. The varying maxima of K during these events correspond to the varying tidal current strengths. A characteristic window of about 2.5 hours appears during the high water stand during which the tidal mixing is significantly reduced.

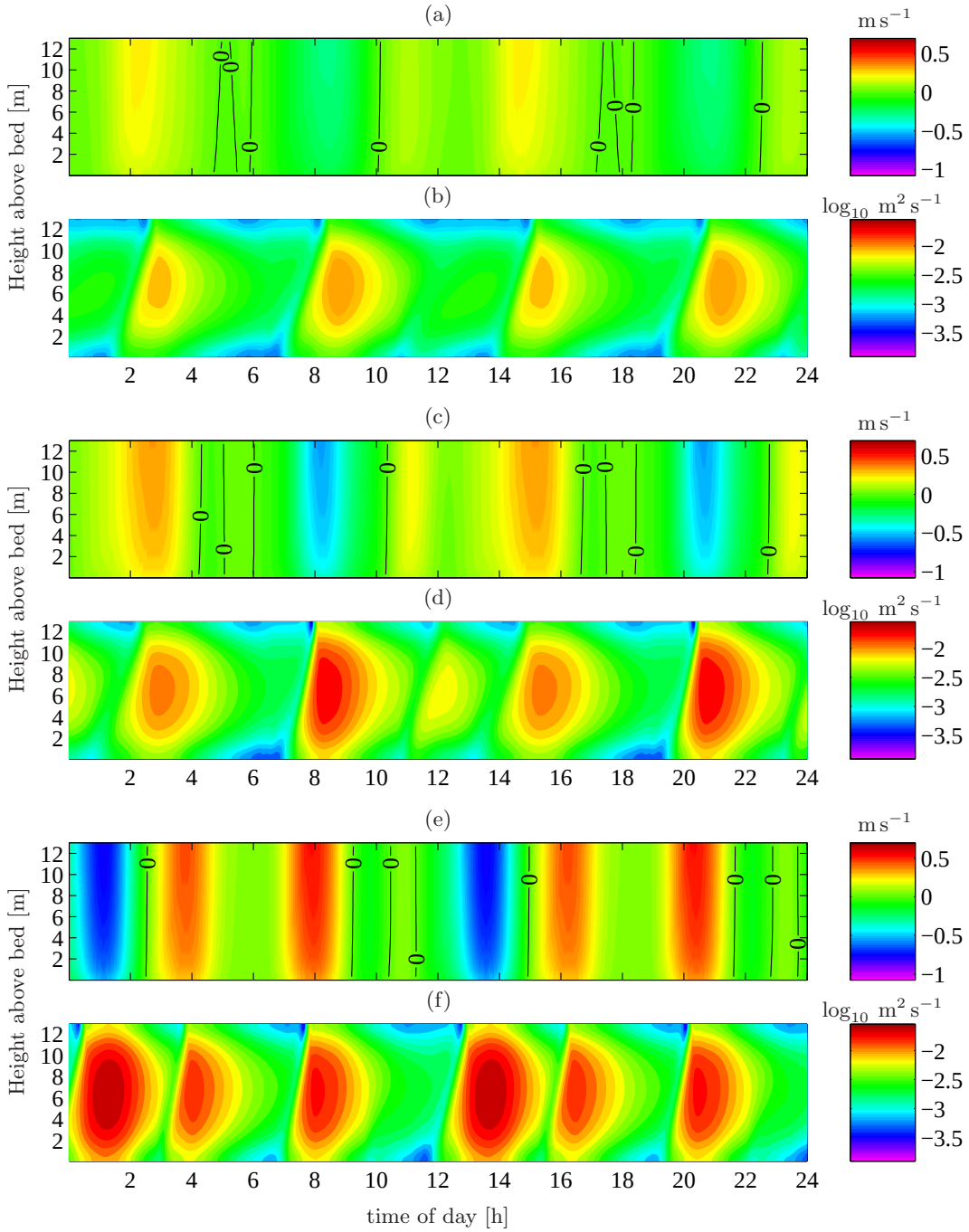

Figure 3.8: Comparing the tidal velocities and mixing for (a)&(b) the weak neap, (c)&(d) the strong neap, and (e)&(f) the weak spring scenario. The colour range is the same as in Fig. 3.7 to allow for direct comparisons.

Because the turbulence is generated at the bottom but needs to propagate upwards to reach the surface, the same diffusivity values are not reached at the surface until $\delta t \approx$ 20-40 minutes after they get generated (depending on the tidal segment) [Fig. 3.7(b)]. Since dissipation works equally well over the entire water column, the decay of the diffusivity is more symmetric than the build-up. This results in periods of high mixing that are overall shorter near the surface compared to the bottom.

Although the panels in Fig. 3.7 are idealised representations of Southampton Water, failing to represent the degree of anisotropy and short-term intermittency encountered in field observations, the absolute values obtained for K are of the same order of magnitude as values calculated from observational data (J. Waniek, pers. comm.). The results obtained from the particle tracking should therefore give a good indication of how well the phytoplankton cells can use their motility in these diffusivity fields.

The current and mixing behaviour of the other 3 scenarios (Fig. 3.8) illustrate the differences associated with different phases of the spring-neap cycle. The tidal current amplitudes and the resulting eddy diffusivities are reduced considerably. Due to the smaller gradients, the bottom generated turbulence propagates more slowly towards the surface and the time lag has increased to $\delta t \approx$ 45-70 minutes depending on the scenario and tidal segment.

How effectively the plankton cells can use their motility in these various mixing regimes will be explored in Section 3.3 while the differences in light availability and growth are outlined in Section 3.4.

3.2.5 Biology Setup

The performance of the phytoplankton cells in terms of primary production will be calculated from the equations introduced in Section 2.3.2. Self-shading is incorporated through a cell-specific absorption coefficient k_m from Eq. (2.25). Both diatoms and dinoflagellates are given the same value for k_m, based on the assumption that about 30-40% of the water column turbidity consists of cell shading effects from these two groups. This estimate is based on observational data of cell counts in Southampton Water from Lauria (1998) and Ali (2003). Given the values of k_t from Section 3.1.2 this yielded

$$k_m = 0.2\,\mathrm{m}^2(1000 \text{ model particles})^{-1} \tag{3.3}$$

At any one time, there are 20 000 model particles in the water, 10 000 diatoms (i.e. negatively buoyant particles) and an equal number of dinoflagellates (motile particles). The depth averaged absorption coefficient produced if these cells are evenly distributed is thus

$$\overline{k_s} = k_m \frac{20\,000\,\text{particles}}{13\,\mathrm{m} \cdot 1\,\mathrm{m}^2} = 0.3\,\mathrm{m}^{-1} \tag{3.4}$$

Using the results from Section 3.1.2, this yields a background absorption coefficient of $k_{bg} = 0.41\,\mathrm{m}^{-1}$ for neap and $0.63\,\mathrm{m}^{-1}$ for spring tide conditions.

The values for the dark and light-acclimatised maximum production from Section 2.3, P_m^d and P_m^l, are chosen to represent the observed differences in the specific growth rates for diatoms

TABLE 3.5: Summary of the model parameters used in the Southampton Water study.

Symbol	Meaning	Units	Values	
Physical				
Δt	Model time step for random walk	s	6.0	
Δz	Vertical resolution position data output	m	0.5	
H	Mean water depth	m	13.0	
I_0	Maximum surface irradiance at noon	μE m^{-2} s^{-1}	1450.0	
k_{bg}	background attenuation coefficient (neap & spring)	m^{-1}	0.41 & 0.63	
N	Number of particles (per species and sinking/swimming velocity)		10 000	
Biological			dinofl.	diatoms
I_d	Dark production saturation onset light intensity	μE m^{-2} s^{-1}	750.0	750.0
I_l	Light production saturation onset light intensity	μE m^{-2} s^{-1}	750.0	750.0
I_b	Lower inhibition threshold	μE m^{-2} s^{-1}	250.0	250.0
k_m	Cell-specific attenuation coefficient	m^2 (10^3 cells)$^{-1}$	0.2	
P_m^d	Max. dark accl. production	arbitrary	0.0135	0.032
P_m^l	Max. light accl. production	arbitrary	0.00027	0.00064
r	cell respiration		0	
τ_a	Acclimation time scale	min	60.0	
w	Swimming/Sinking velocities	mm s^{-1}	0 to 0.5	0 to -0.1

and dinoflagellates (Broekhuizen, 1999). More specifically, Ali (2003) measured the specific growth rates for the diatom *Thalassiosira rotula* and the dinoflagellate *Prorocentrum micans* for different nutrient-to-carbon ratios. Using the same light and nutrient regimes for both species, the diatom showed a specific growth rate that was on average 2.4 times higher than for the dinoflagellate. The values of P_m^d and P_m^l in the model are chosen to reflect this difference. The intention is only to compare the performance between the motile and non-motile cells and not to calculate actual quantities of primary production. The respiration rate r has therefore been set to zero as any differences in growth are already contained in P_m^d and P_m^l. The actual magnitudes of P_m^d and P_m^l are arbitrary choices using $P_m^d = 50 \cdot P_m^l$ as in Nagai et al. (2003). No information was available on the photo-acclimation behaviour of the two species. Both species are therefore given the same values for the light response parameters I_b and $I_{d/l}$ using again the values from Nagai et al. (2003). It may appear odd that the inhibition onset I_b occurs at a significantly lower irradiance than the saturation onset $I_{d/l}$ which raises the question of why a cell should start to become inhibited if the irradiance is still far below the saturation level. One should also bear in mind that I_b is just the inhibition *onset*, i.e. it describes the irradiance at which the cells *begin* to deviate from the fully dark acclimatised production. The cells do not become fully inhibited until much higher irradiances are reached (usually exceeding $2I_b$). This can also be observed in the original Denman and Marra (1986) configuration of the model where the authors fitted a curve with $I_b = 0$ to lab culture data of primary production. For the purposes of the present study, the actual magnitudes of I_b and $I_{d/l}$ are not particularly important as they do not affect the results of the production study which is mainly comparative in nature (e.g. Fig. 3.17). They would only become relevant if actual magnitudes of production were to be calculated. The Table 3.5 gives a summary of the parameter values used.

3.3 Results from the Particle Tracking

A total of 20 000 particles were released into the physical structures shown in Fig. 3.7 and Fig. 3.8, of which 10 000 belong to the motile species and 10 000 are negatively buoyant. Their location was tracked for a total of 96 hours while they perform a random walk according to Eq. (2.15). For all the results shown in this chapter, the particles were randomly distributed at the beginning of the simulation. For the data output, the particles have been collected in 0.5 m size bins to achieve manageable file sizes (see Section 2.4). All particle concentrations are plotted in percent of the average concentration $\widehat{C}$ ($\widehat{C} = 10\,000/13 \approx 769.2\,\mathrm{m}^{-1}$) unless specified otherwise. A value of 150% thus indicates that the concentration in this particular bin is $1.5\,\widehat{C}$.

3.3.1 Motile Particles

In order to test the effectiveness of motility, the cells are given a fixed and constant upward swimming direction. Given the light limitation in Southampton Water, this may already seem a plausible swimming strategy. It is only used here, however, to test the effectiveness of the different swimming velocities at overcoming the turbulent mixing. By having a constant upward velocity, the particles will accumulate at the surface and the magnitude of these accumulations is used as an indication to gauge the effectiveness of motility over mixing. If motility is very successful, the cells will accumulate in high numbers at the top. If the turbulent mixing prevails, the cells will be kept well mixed and homogeneous throughout the water column.

The first series of plots in Fig. 3.9 correspond to the timing and intensity of the tidal mixing shown in Fig. 3.7(b) and Fig. 3.8(b). In both scenarios the neutrally buoyant particles show a random distribution over the entire tidal cycle with concentrations between $95\% < C < 105\%$. The colour scale has been designed to visualise this interval in good detail as this case of $w = 0$ represents a crucial test for the model to ensure that any structures seen for $w \neq 0$, are solely due to the particle's motility and do not represent artifacts introduced by the random walk.

As the swimming velocity is increased, the water column becomes increasingly divided into a depleted lower half and a more enriched top half, indicated by the approximately horizontal 100% contour line separating them. In both scenarios, the cells are able to utilise their motility during the breaks in the turbulent mixing. In the spring tide scenario, the accumulations are periodically eroded by the strong mixing pulses whereas in the weak neap tide scenario, the surface concentrations are higher and persist for longer. It becomes clear that at neap tide even the slower swimmers have a chance to overcome the turbulent mixing. Only the ebb flow is strong enough in this scenario to partially disperse the cells. The weak spring and strong neap scenarios (not shown) look similar to their counterparts from Fig. 3.9. They differ in the amplitude and duration of the accumulations as the mixing lies between the two extreme cases shown here.

With this initialisation, where the particles are uniformly distributed at $t = 0$, the model takes between 5-10 hours to reach a steady state, depending on the swimming velocity and

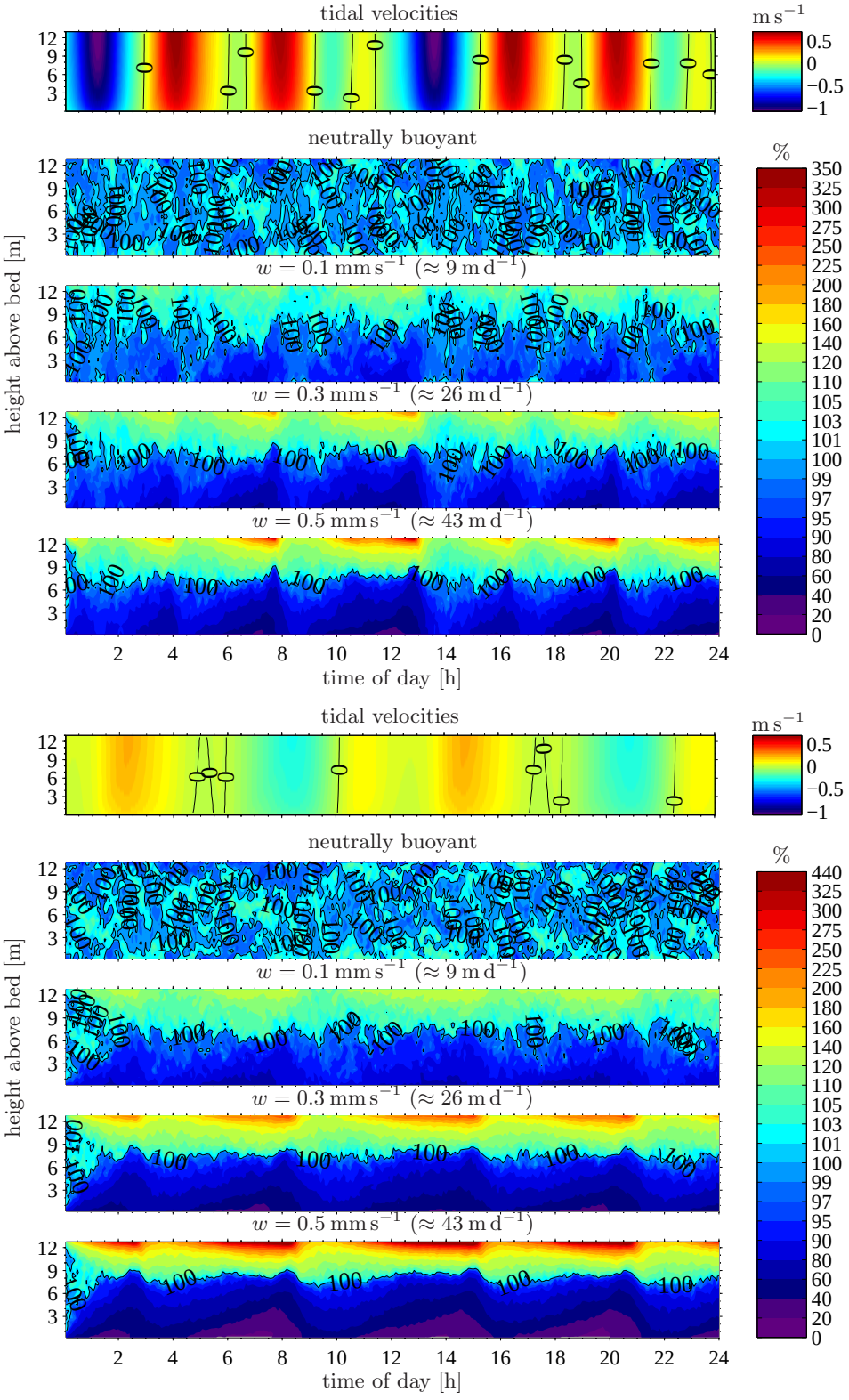

Figure 3.9: Relative particle concentrations with different swimming velocities for the strong spring tide scenario (top series) and a weak neap tide (lower series). Plotted are 5 minute averages with a 0.5 m vertical resolution. The tidal velocities are shown for reference. Apart from the top element, the colour scales for the particle concentrations are identical in both series. The colour scale is nonlinear to visualise the important regions. The top value at the colour scale always gives the highest observed concentration in each figure.

tidal scenario. The term 'steady' refers here to a state in which subsequent periodic surface accumulations do not differ in shape and intensity apart from small statistical variations which are due to the random component in Eq. (2.15).

Fig. 3.10 shows the corresponding Peclet numbers to Fig. 3.9 for three different swimming velocities. In Fig. 3.10(a), almost the entire water column appears in a shade of blue for the weakest swimmers, which indicates that the Peclet number is less than one for the entire tidal cycle and the mixing time scale is always less than the swimming time scale. As the velocity is increased, gaps start to appear between the tidal segments. A comparison between the times of the particle accumulations in Fig. 3.9 and the times of the gaps, clearly shows that the times when $\mathscr{P} > 1$ coincide with the times when accumulations appear at the surface. For the weak neap tide in Fig. 3.10(b), $\mathscr{P} > 1$ for the two faster swimmers during most of the tidal cycle which is mirrored by the higher and longer lasting accumulations in Fig. 3.9.

Yet another way to look at the particle concentrations which might yield different insights, is shown in Fig. 3.11. This graph shows the relative cumulative concentrations for particles with $w = 0.5\,\mathrm{mm\,s^{-1}}$ measured from the surface down. The curves are plotted for the two extreme states during the semi-diurnal cycle: the most heterogeneous distribution occurs at the end of the high water stand and the most homogeneous distribution during the ebb flow. In the most heterogeneous case in the weak neap tide scenario, about 80% of the particles are in the top half of the water column and over 50% are concentrated in the top 2.5 m. During the strong spring tide, the distribution is less heterogeneous but still shows 70% of the particles in the top half of the water column. The 50% mark is now 3.5 m below the surface. The graph also shows that the mixing during a strong spring tide is strong enough to render the distribution almost perfectly homogeneous only with a slight bias towards the surface remaining. During a weak neap tide, on the other hand, the mixing is not strong enough and the distribution maintains a strong bias towards the surface. The arrows indicate the range of concentration

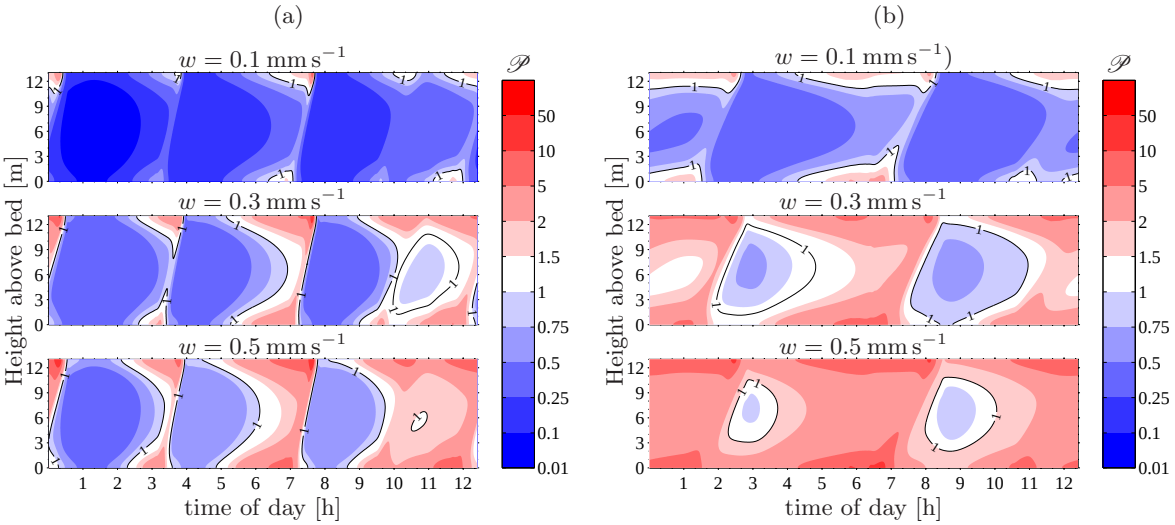

Figure 3.10: Peclet numbers for one tidal cycle of (a) the strong spring tide and (b) the weak neap tide scenario. Plotted are the results for three different swimming velocities. These figures were obtained by assuming a mixing depth of $h = 13$ m and using the diffusivities from Fig. 3.7(b) and Fig. 3.8(b) in Eq. (1.37).

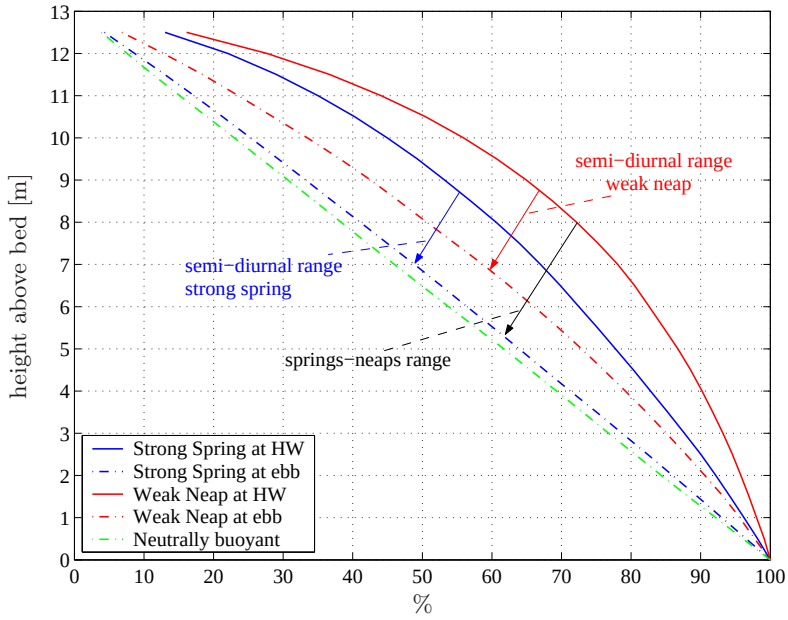

Figure 3.11: Cumulative particle concentrations for particles with $w = 0.5\,\mathrm{mm\,s^{-1}}$ at the two tidal extremes. The solid lines show the cumulative relative concentrations at the end of the high water stand (HW) when the near-surface concentrations are the highest. The dash-dotted lines show the concentrations after the onset of the ebb flow when the strong turbulent mixing has brought the concentrations to the most homogeneous state during the semi-diurnal cycle. The dash-dotted green line is the reference showing the cumulative concentration for neutrally buoyant particles.

distributions between these two extremes. The black arrow indicates the expected range over an entire springs-neaps cycle. For particles with $w < 0.5\,\mathrm{mm\,s^{-1}}$ both lines shift closer to the reference line and the range between the extremes decreases. Note that the curves shown here represent again the five minute averages. For a given euphotic depth, these graphs are very useful as they allow determination of the percentage of the cells above the euphotic depth which are able to photosynthesise.

3.3.2 Non-Motile/Sinking Particles

For non-motile particles such as diatoms that generally possess negative buoyancy, we expect to see the opposite picture. During periods of reduced mixing they will accumulate at the sea bed and when the tidal currents pick up again, they will be resuspended and distributed more evenly throughout the water column. If the magnitudes of the sinking velocities are the same as in Fig. 3.9, then the corresponding figure of particle distributions would simply be an inverted version of Fig. 3.9. However, the diatoms present in Southampton Water generally have sinking velocities less than $0.1\,\mathrm{mm\,s^{-1}}$ (Table 3.2). By examining the result for motile particles with $w = 0.1\,\mathrm{mm\,s^{-1}}$ in Fig. 3.9, it is clear that diatoms will remain well mixed almost throughout the entire springs-neaps cycle. The equivalent plot to Fig. 3.11 but for particles sinking at $w = -0.1\,\mathrm{mm\,s^{-1}}$ is shown in Fig. 3.12. During a strong spring tide, the bias towards the sea bed is almost negligible with over 45% of the cells in the top half of the water column at the end of the high water stand. The ebb flow essentially produces a fully

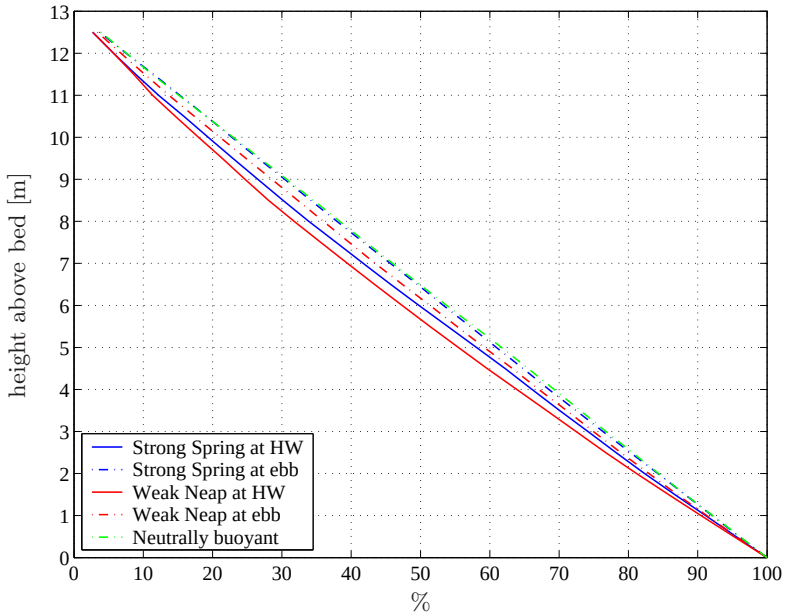

Figure 3.12: Cumulative particle concentrations for particles with $w = -0.1\,\mathrm{mm\,s^{-1}}$ at the two tidal extremes. (see Fig. 3.11 for further explanations).

homogeneous distribution. Even during a weak neap tide just under 45% of the cells remain in the top half of the water column.

In comparison, motile cells are able to accumulate closer to the light but given that dinoflagellates grow slower and have higher light requirements than diatoms, this might not be a decisive advantage. Their higher position in the water column might only become relevant once their numbers increase to such levels that they start to significantly shade the diatoms below [e.g. during a *Mesodinium* bloom event (Crawford and Purdie, 1992)].

3.3.3 Comparing the Results with Observations

Having presented the results from the particle tracking, this section will attempt a comparison with observations to elucidate whether the observed patterns in the model are indeed realistic representations of Southampton Water.

As mentioned earlier, two studies have been conducted in Southampton Water that examined vertical migrations and the use of motility in relation to turbulent mixing. The dinoflagellate species studied by Lauria et al. (1999) had swimming velocities of $w = 0.25\,\mathrm{mm\,s^{-1}}$ (*Prorocentrum micans*) and $w = 0.07\,\mathrm{mm\,s^{-1}}$ (*Peridinium trochoideum*). The authors observed surface accumulations of these species during slack water periods which became dispersed into a homogeneous distribution once turbulence intensified during ebb and flood currents. The same pattern has been observed by Crawford and Purdie (1992) for the ciliate *Mesodinium rubrum*. Although the results from the discrete sampling methods used in both studies cannot be compared quantitatively to the model simulations, the results presented in the previous sections indicate that the swimming velocity of $w = 0.25\,\mathrm{mm\,s^{-1}}$ for *Prorocentrum* and in particular the

(average) velocity of $0.5\,\mathrm{mm\,s^{-1}}$ for *Mesodinium* (Smith and Barber, 1979) should be sufficient for them to overcome the turbulent mixing during the slack water periods. The surface accumulations formed in Fig. 3.9 are in good agreement with observations. The model results could also confirm the observation that the cells are unable to resist the turbulent mixing during the ebb and flood as they become homogenised throughout the water column (Lauria et al., 1999). The published swimming velocity for *Peridinium trochoideum* of $0.07\,\mathrm{mm\,s^{-1}}$ (Table 3.2) on the other hand seems insufficient for the turbulent mixing in Southampton Water. Given that even during a weak neap tide, the Peclet number will always be less than unity for this species [see top panel in Fig. 3.10(b)], this swimming velocity should have only negligible effects on their vertical position. In addition, $0.07\,\mathrm{mm\,s^{-1}}$ translates into just $25\,\mathrm{cm\,h^{-1}}$ which is not enough to cover any significant vertical distance during the slack water periods which only last up to 3 h.

Both studies (Crawford and Purdie, 1992; Lauria et al., 1999) suggested that the motile species in Southampton Water might pursue a migratory strategy which would cause them to swim to the bottom layers before low water in order to minimise the down estuary excursion with the ebb flow. With the changeover to the flood phase, they would start to swim upward into the surface layers to maximise the distance travelled up the estuary with the flood. Considering the net outflow of the estuary due to the freshwater input at the head and the occasionally well developed estuarine circulation in Southampton Water this strategy could help to minimise the overall flushing losses of the cells. However, during the ebb flow itself the mixing is strong and this low position in the water column cannot be maintained. On days when the slack water preceding the ebb flow occurs near midday it also seems improbable that the cells would actively swim downwards, thus leaving the euphotic zone when the light availability would be approaching the maximum. A cell would also struggle to cover the required vertical distances to reach the near surface water just before the flood flows as the slack preceding the first and second flood are limited to about 30-45 minutes which seems short even for the fastest cells. The benefit of such a strategy appears thus limited and a light based strategy would seem more feasible.

3.4 Primary Production

We have seen that the swimming velocities of motile species in Southampton Water may be sufficient to allow positioning within the water column at certain stages of the tidal cycle and at certain times within the spring-neap cycle. This section will attempt to quantify this advantage in terms of light availability and primary production. A total of 12 different particle species from the two different phytoplankton groups were examined: 6 sinking species with $0 \geq w \geq -0.1\,\mathrm{mm\,s^{-1}}$, and 6 swimming species with $0 \leq w \leq 0.5\,\mathrm{mm\,s^{-1}}$. Due to the limitation in computing power, it was not possible to include all the 12 species in the same same experiment as there would not have been a statistically sufficient number of particles for each species. To achieve a 'steady' state in the particle distributions, i.e. a state in which recurring particle distributions at a certain stage of the tide are 'identical', it was necessary to

have at least 10 000 particles per species. Each experiment is therefore seeded with an initial population of 20 000 particles, 10 000 motile ones and 10 000 that are non-motile. The species pairs were chosen such that the fastest, second fastest, etc. swimmers and sinkers were together in one experiment, e.g. the species with $w = 0.5\,\mathrm{mm\,s^{-1}}$ and $w = -0.1\,\mathrm{mm\,s^{-1}}$ were together, and the species with $w = 0.4\,\mathrm{mm\,s^{-1}}$ and $w = -0.08\,\mathrm{mm\,s^{-1}}$, etc. until the two neutrally buoyant species of each group were competing with each other. The latter combination will be used to test the effect of the different parameters used in the growth functions (Table 3.5) for each group.

3.4.1 Comparing the Light Availability

Before comparing the production of the two different phytoplankton groups, this section will provide some results on the light availability to the cells. By light availability we mean the maximum received PAR of a cell over a given time interval, irrespective of whether the cell is able to utilise this light for photosynthesis or not. This is meant as a proxy for potential growth, i.e. a measure that is independent of the chosen growth and light-response functions.

On a spring tide, the motile particles accumulate at the surface during the high water stand which occurs between 09:30 h and 12:30 h on day 1 (see Fig. 3.7). This timing results in a much increased light availability [Fig. 3.13(a) and (c)]. The ebb starts at about 12:45 h with the maximum turbulence at about 13:30 h (Fig. 3.7). As a result, the light received by the motile cells drops significantly and is only slightly above the amounts received by the sinking particles. In the wSTS [Fig. 3.13(c)] this is more pronounced, as the overall lower mixing allows for higher surface concentrations during the high water stand.

During a neap tide, the overall light availability is higher for all cells due to the lower background turbidity (Table 3.5). The effect of the different background turbidities becomes clear by comparing the light availabilities for the neutrally buoyant particles. In the neap scenarios, the light availability for cells with $w = 0$ is about 30% higher throughout the light period. It is no coincidence that this value corresponds to the 30% higher total turbidity $k_t = k_{bg} + k_s$ for an even particle distribution [see Section 3.1.2 and Eq. (3.4)]. Let us consider the light profiles for two different absorption coefficients k_1 and k_2

$$I_1(z) = I_0 \exp\left(-k_1\, z\right) \qquad \text{and} \qquad I_2(z) = I_0 \exp\left(-k_2\, z\right) \tag{3.5}$$

The total light available throughout the water column from these profiles is

$$\hat{I}_{1,2} = \int_0^H I_0 \exp\left(-k_{1,2}\, z\right) \mathrm{d}z = -\frac{I_0}{k_{1,2}} \left[1 - \exp\left(-k_{1,2} H\right)\right] \tag{3.6}$$

and the ratio of both yields

$$\frac{\hat{I}_1}{\hat{I}_2} = \frac{k_2}{k_1} \frac{1 - \exp\left(-k_1\, H\right)}{1 - \exp\left(-k_2\, H\right)} \approx \frac{k_2}{k_1} \quad \text{if } k_1 \sim k_2\,. \tag{3.7}$$

Thus if the two attenuation coefficients are not too different from each other, the difference in the light availabilities of uniformly distributed particles follows directly from the ratio of k_2

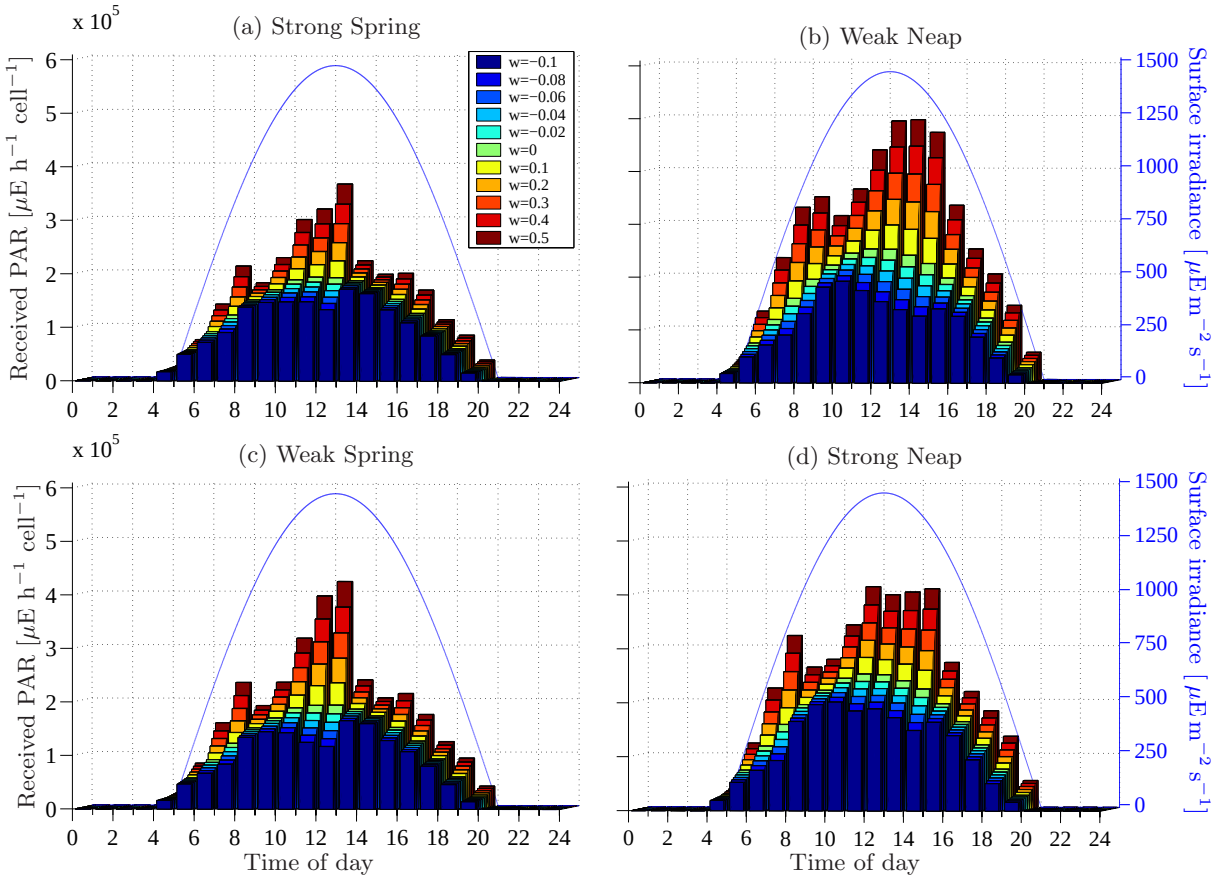

Figure 3.13: Total received PAR (light availability) per cell for the 5 different swimming velocities (shades of red and yellow), the 5 different sinking velocities (shades of blue) and neutrally buoyant particles (green). Each bar represents the average amount of light received per cell during one hour. The graphs correspond to the mixing scenarios and particle concentrations that were shown in Fig. 3.7, Fig. 3.8 and Fig. 3.9. They represent the first (early) day of the 96 h consecutive output for each scenario and can thus be directly compared to the particle distributions in Fig. 3.9. The blue line in the background shows the course of the *total* surface irradiance. 45% of this total is assumed to be PAR. The light period is 16 h which corresponds to May or mid July in Southampton.

to k_1. In the present case of $k_{t_s} = 1.3\,k_{t_n}$ (Section 3.1.2) the ratio of the exponential terms in Eq. (3.7) differs only negligibly from unity.

Clearly these considerations only apply to neutrally buoyant particles, that are uniformly distributed throughout the water column but not to uneven distributions that are biased towards the surface or the seabed. This becomes clear if we compare the light availabilities for the top 1 m only, say, i.e. if we insert $H = 1$ m into Eq. (3.7). Then the ratio of the exponential terms is significantly different from unity (if $k_2 = 1.3\,k_1$) which produces a light availability that is only 10% higher at neaps than at springs. If the particles thus accumulate at the surface the different turbidities will not have the full effect and the overall difference in light availability will be less than k_2/k_1. The opposite effect occurs if the particles accumulate at the bed and the surface layers become depleted.

For the comparison between the spring and neap tide scenarios in Fig. 3.13 this means that the faster the cells swim, i.e. the greater the bias in their population distribution towards

the surface, the smaller the effect of the different background turbidities and the more the differences in the light availability are due to differences in the turbulent mixing. For negatively buoyant cells, the opposite is true as they will always have a population distribution that is biased towards the bed. As this bias is much less due to the lower sinking velocities, their light availability should always be reduced by a factor that is ~ 1.3.

During neap tide, the high water stands occur roughly around 06:00h and 18:00h which is a less favourable timing for motile particles in terms of light availability (neglecting photoinhibition) as their ability to reach the surface is not rewarded by the high light doses they would receive at noon. Nevertheless, compared to the spring tide scenarios, the motile cells have a much higher light availability than the negatively buoyant particles throughout the tidal cycle which is due to the combined effect of the lower background turbidity and the generally much lower mixing. If the experiment is repeated with identical background turbidities (results not shown), the motile cells still receive more light during the neap scenarios, but in the wSTS the daily average light availability of the motile cells comes within reach (between 95-98%) of that achieved in the sNTS. The more favourable timing of the high water stand at springs is thus able to almost completely alleviate the differences in the mixing between these two sub-variants.

Fig. 3.14 shows the average daily totals per cell for each species and scenario, i.e. the average received light per day from days one to four. The inter-daily variability among the 4 days in the 96 h output for each experiment has been found to be negligible. The slight phase shifts of the tide on each consecutive day in relation to the sun had thus no effect on the received daily total. On average, the light received by the fastest swimmers is 1.69 to 2.62 times higher than for the fastest sinkers. In terms of production it is difficult to estimate how these differences in light availability will translate into differences in growth. Considering that the growth rate of the non-motile cells in the experiment is 2.4 times higher than for motile species (Table 3.5), it seems that during the two spring and the strong neap scenarios, the fastest swimmers will not be able to alleviate this difference through the increase in light

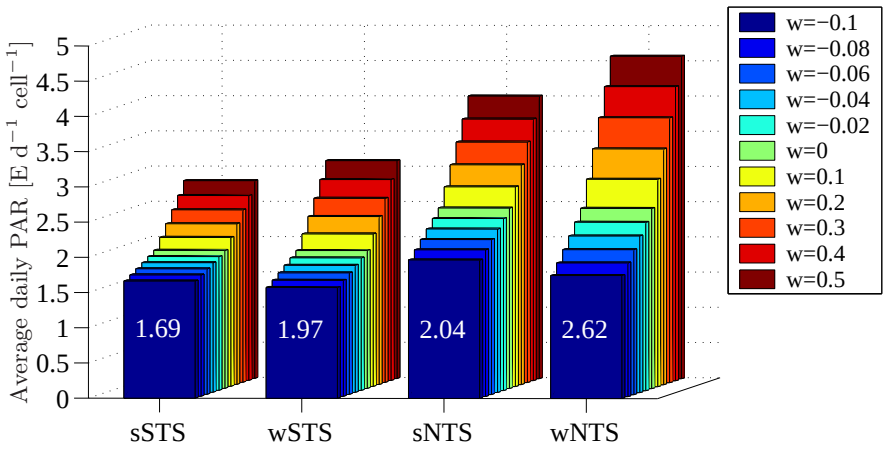

Figure 3.14: Comparing the available PAR over 24 h for all particle species and tidal scenarios. The bars represent the received PAR during one day, averaged over the 4 days of consecutive output for each tidal scenario. The numbers indicate how much more light the fastest swimmers receive compared to the fastest sinkers.

availability, independent of the growth function used. It is only in the weak neap scenario that the advantage in light availability appears sufficient to compensate for the difference in growth rates. The question that remains, however, is how much of this available light can actually be used in photosynthesis and how much will be 'lost' due to photoinhibition. The following section will be able to answer this question.

3.4.2 Comparing Production

As it is impossible to display the results for each of the 12 particle species, only some examples will be shown before comparing the ensemble averages for all species. The first example in Fig. 3.15 shows the total local production P of all cells and the average cellular acclimation status Y for neutrally buoyant diatoms in a strong spring tide scenario, using the growth parameters from Table 3.5. As the particles are neutrally buoyant, the production is fairly homogeneous and mirrors the course of the intensity of the available light. The production is limited to the top 3-4 metres of the water column. Towards noon there is a slight decrease noticeable as the cells become more inhibited due to the increased residence time near the surface during the high water stand between 09:30 h and 12:30 h on day one of a spring tide scenario. As the ebb flow starts, the inhibition near the surface drops as the cells become more mixed and the production increases slightly (see also Section 3.4.4). For neutrally buoyant dinoflagellates, the results are identical except that the maximum production is only 25, i.e. by a factor of about 2.4 less which corresponds to the difference in maximum growth rate set

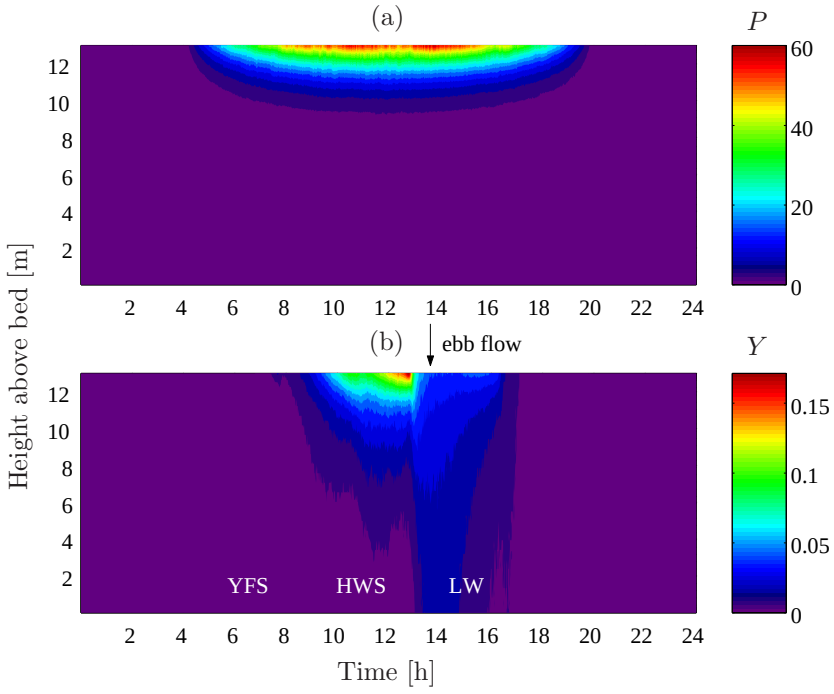

Figure 3.15: Growth and acclimation for neutrally buoyant diatoms for day one of the strong spring tide scenario. (a) The total production per minute summed over all particles in each depth bin (arbitrary units). (b) The average inhibition status Y of the cells. YFS, HWS and LW indicate the times of the Young Flood Stand, the High Water Stand, and Low Water respectively.

out in Table 3.5. Hence, without any motility, the diatoms would win the growth race, simply due to their higher maximum growth rate. This is true also if the overall daily production is compared (not shown). The question is thus, to what extent will the motility be able to alleviate this disadvantage of slower growth.

A comparison between the fastest sinkers and fastest swimmers for the sSTS (Fig. 3.16) shows that production is less uniform due to concentrations of particles accumulating during the high water stand (see Fig. 3.9). For the motile particles, the maximum production occurs during the highest surface accumulations just before the onset of the ebb flow, i.e. at about 12:30 h. For the sinking particles, the production is suppressed during this time, due to the shading by the motile cells. During the slack water period, the negatively buoyant particles also sink out of the near surface water. However, given that their sinking velocity is only -0.1 mm s^{-1}, this is not enough to account for the observed decrease in production as they would only cover a maximum distance of 0.36 m per hour. During the ebb flow, the surface accumulations disappear (Fig. 3.9) and the production for the sinkers increases again. The maximum growth for the dinoflagellates is higher during the high water stand but overall the diatoms have a higher production in the subsurface layers as they need less light to achieve the same growth. The production per particle (not shown) is fairly homogeneous due to the periodic tidal mixing which homogenises the water column, i.e. at the end of a day most particles will have received similar amounts of light.

Fig. 3.17 shows the normalised production, averaged over the 4 day output for each scenario and species combination. Several pieces of information can be extracted from this graph and several interlinked factors need to be considered to explain this picture. As a first observation, the total production on a spring tide day is about 75-80% of that achieved during a neap tide. The main cause is the difference in turbidity since we have $k_{t_n} \approx 0.77\, k_{t_s}$.

The total production appears to be the same for both the strong and weak variants and remains fairly constant throughout a scenario for different species combinations. While the

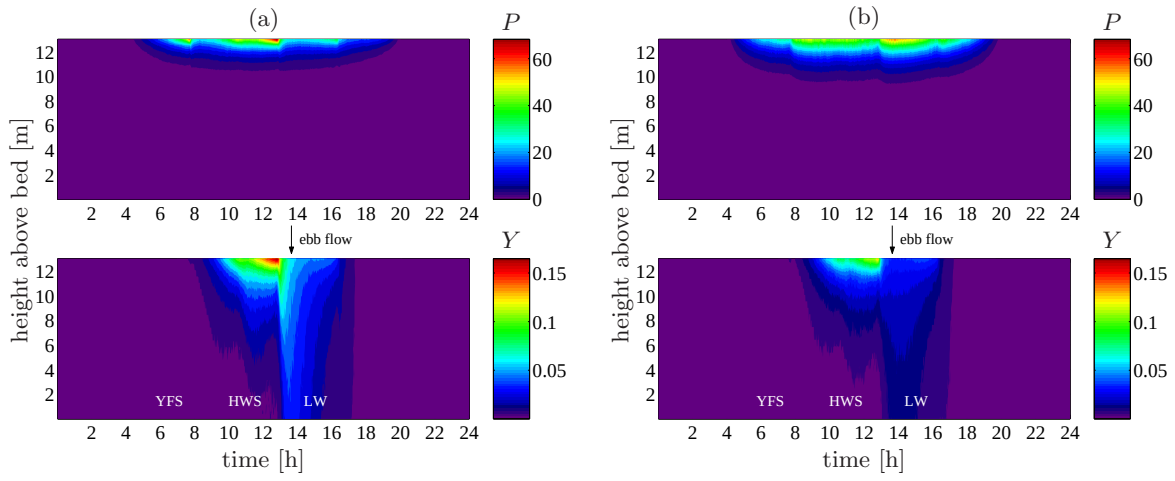

Figure 3.16: (a) Production (top) and acclimation status (bottom) for motile cells with $w = 0.5\,\mathrm{mm\,s^{-1}}$ during day one of a sSTS. (b) The equivalent plots for negatively buoyant particles sinking at $w = -0.1\,\mathrm{mm\,s^{-1}}$. YFS, HWS and LW indicate the times of the Young Flood Stand, the High Water Stand, and Low Water respectively.

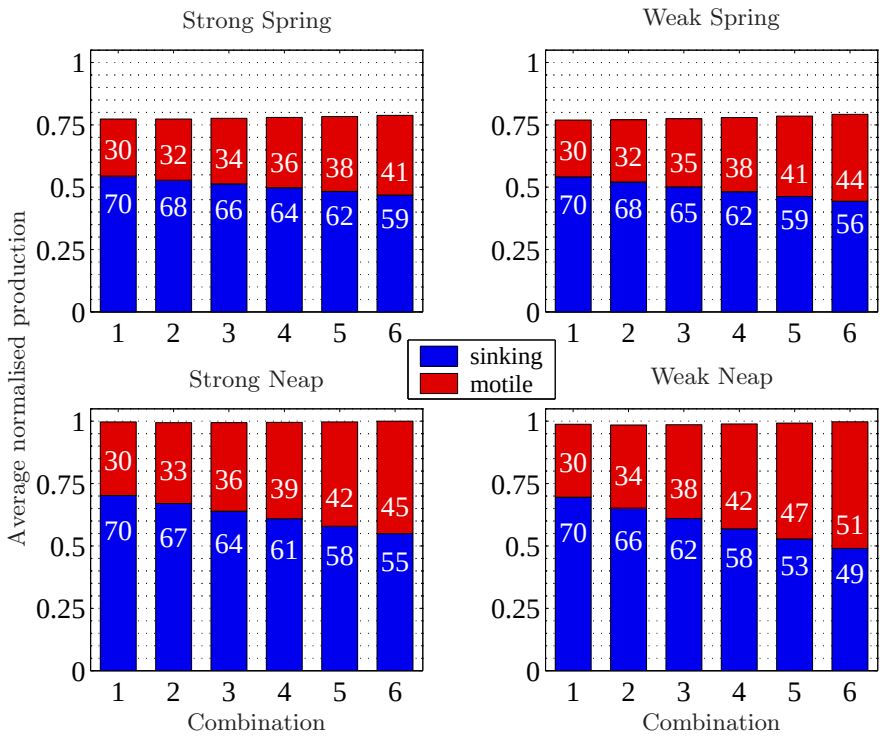

Figure 3.17: Comparing the average production for all species and scenarios. The results have been normalised to the maximum production encountered for a species combination. Each bar represents one experiment in which a combination of motile and sinking particles were present. Combination 1 represents the two neutrally buoyant species from each group, and as the combination number increases, the swimming and sinking speeds increase. Combination 6 is thus an experiment that contained the fastest from each group: motile cells with $w = 0.5\,\mathrm{mm\,s^{-1}}$ and cells sinking with $w = 0.1\,\mathrm{mm\,s^{-1}}$. The numbers give the percentage that each species contributed to the total daily production.

lower mixing during the weak variants is to the advantage of the motile species, it is to the disadvantage of the other. The total production is thus similar but the shares in the total production for the motile and non-motile species differ between the weak and strong variants. At neap tide, the increase in light availability to the motile species is about 2.4 times higher than the decrease experienced by the non-motile cells in the same experiment [Fig. 3.18(b)]. At spring, this ratio is about 2.8. It is by mere coincidence that these differences roughly correspond to the difference in the growth rate between the motile and non-motile cells and that the overall production thus remains fairly constant throughout a scenario. The choice of the species combinations for a particular experiment also means that as the swimming velocity is increased the sinking velocity increases as well. If the species were put together at random, the height of the bars in Fig. 3.17 would be much more variable.

A closer inspection of the bars in Fig. 3.17 reveals that in the neap scenarios, the total production slightly decreases with increasing combination number. Only for the faster swimmer/sinkers does the total production surpass the initial value for the neutrally buoyant combination. At spring tide, there is a small but continuous increase of production with combination number. Both these effects are due to different increases/decreases in light availability [Fig. 3.18(a)]. In the neap scenarios, the ratio of the increase to the decrease in light avail-

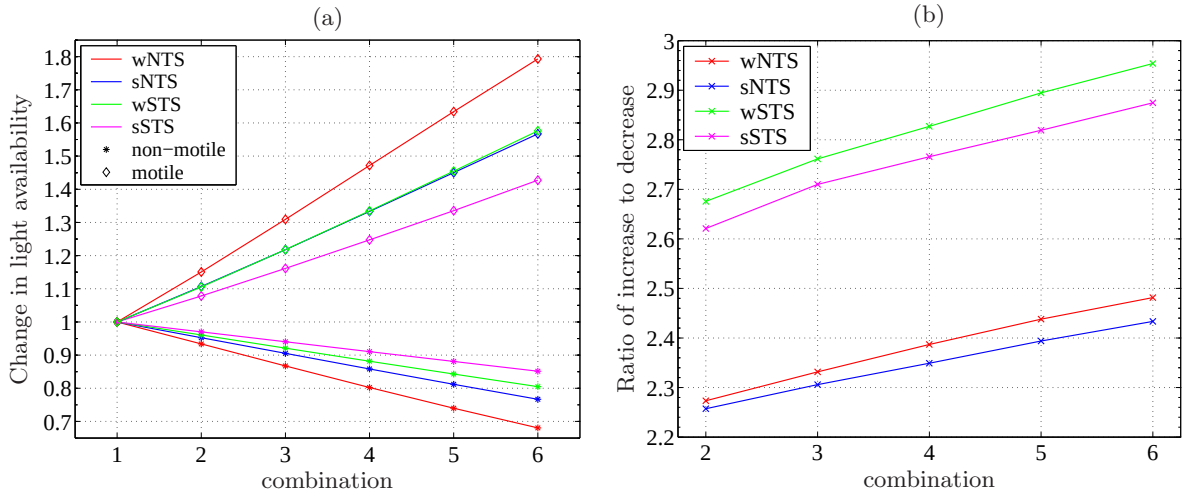

Figure 3.18: (a) Relative increase/decrease in light availability for increasing swimming/sinking velocity (i.e. combination number) with respect to neutrally buoyant particles (combination 1). (b) Ratio of the increase to the decrease. E.g. for the fastest swimmer/sinker combination in the wNTS, the motile cells increase their light availability compared to neutrally buoyant particles by about 80%. The sinking particles in the same experiment experienced a reduction of about 32% down to 68%. The ratio of increase to decrease is thus $80/32 = 2.5$.

ability is initially less than the ratio of the growth rates of 2.4. Only for higher combination numbers does the ratio exceed 2.4. In the spring scenarios, the ratio is always above the 2.4 threshold which explains the continual increase in production with combination number.

As the combination number increases, also the share of the motile cells in the total production increases from initially 30:70 to almost 50:50. The initial ratio of 30:70 ($\approx$ 1:2.4) corresponds to the different growth rates. As the swimming/sinking velocities increase, the populations become more biased towards the surface/bed and the contributions to the total production thus shift in favour of the motile cells. The diatoms are able to maintain a higher production throughout all the experiments with the only exception of Combination 6 during the wNTS.

One interesting aspect in Fig. 3.18(a) is that the increase in light availability for the motile cells in the wSTS is approximately the same as in the sNTC, although the current amplitudes and thus the mixing are higher in the wSTC than in the sNTC (see Fig. 3.8). The reason for this equal increase is the more favourable timing of the high water stand during a spring tide where it occurs near noon compared to early morning/late afternoon during a neap tide.

3.4.3 Optimum Swimming Strategy

Given the high light intensities at the surface, the question arises whether it would not be more beneficial for the motile cells to employ a different strategy than swimming constantly upwards. By aiming at a couple of metres below the surface they could avoid becoming too inhibited which would result in significantly reduced growth. If we assumed for a moment, that the cells would acclimatise to the ambient light instantaneously, we could replace Y in Eq. (2.29) with X and calculate the production directly as a function of light intensity. With the parameter values from Table 3.5, the result (Fig. 3.19) points towards the existence of an

optimum light intensity $I_{opt} > I_b$ at which the production has a maximum.

In the phase plot of Fig. 3.19(b) it can be seen that this maximum growth occurs at an inhibition value of approximately $X \approx 0.1$ (this value changes very slightly with different choices of I_b, I_d and I_l). In the real world, Y lags behind X due to the finite acclimation time τ_a. If a cell is exposed to the irradiance profile from Fig. 3.20(a), for example, X will become fully inhibited rather quickly while Y lags behind [Fig. 3.20(b) and (c)]. In terms of production, this particular cell would achieve the maximum production with an inhibition of $Y \approx 0.2$ during the early morning and a second, lower maximum with $Y \approx 0.65$ in the early evening [Fig. 3.20(d)]. If we added the variability caused by the turbulent mixing, the picture becomes rather complex and it is no longer obvious whether there exists an optimum inhibition level Y_{opt} that would be valid for all light histories.

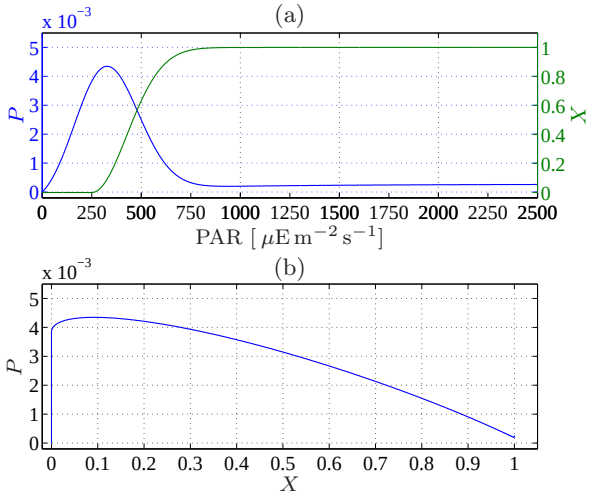

Figure 3.19: (a) Plot of the instantaneous production P from Eq. (2.29) (blue curve) for the parameter values from Table 3.5. The cellular acclimation status Y in the equation has been replaced with the local inhibition parameter X, plotted as a green curve. (b) Phase diagram of P versus X.

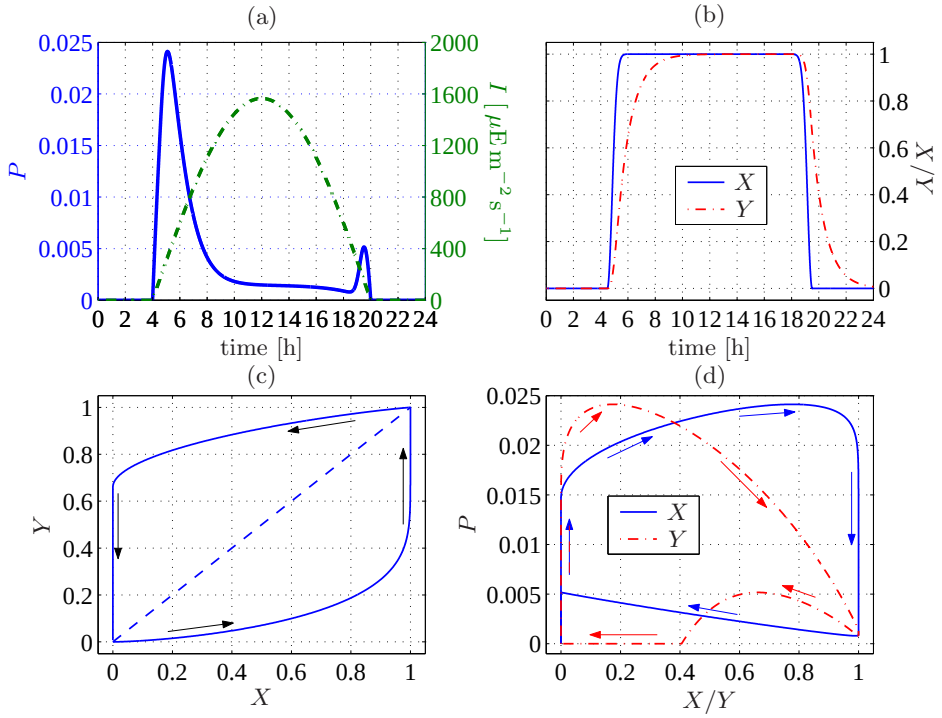

Figure 3.20: (a) Instantaneous production P of a cell that experiences the light profile shown. (b) Local (X) and cellular (Y) inhibition parameters for the light profile from (a). (c) Phase diagram of Y versus X showing the time lag of Y versus X. The dashed line would represent the phase diagram without time lag. (d) Production P versus inhibition parameters X and Y.

Several experiments were therefore conducted in search of the optimum inhibition threshold. The cells are given the following swimming strategy:

$$w_n = \begin{cases} -w & \text{, if } Y_n > Y_c \wedge X(z_n) > Y_c \\ w & \text{, otherwise} \end{cases} \tag{3.8}$$

In other words, if both the cellular inhibition status Y_n of the n-th particle as well as the local inhibition parameter $X(z_n)$ at the particle depth z_n are greater than a critical value Y_c, the particle reverses its direction and swims down. Note that both, X and Y have to exceed Y_c for this to happen. So as the cell ascends, it will keep ascending even if the light environment will potentially lead to $Y_n > Y_c$ if the particle stays there long enough (in comparison to the acclimation time scale τ_a). Due to the acclimation time scale being 1 h this may not happen for some time and the cell will be able to exploit the high irradiances near the surface without being inhibited.

Fig. 3.21 shows the results for the extreme case of a wNTS in combination with the fastest swimming velocity of $w = 0.5\,\mathrm{mm\,s^{-1}}$ which should give the most drastic change as the motility is at its maximum, while the mixing at its minimum, i.e. it will be the easiest scenario for the cells to follow this swimming strategy without much interference from turbulence. In addition, the irradiance maximum has been increased from 1450 $\mu\mathrm{E\,m^{-2}\,s^{-1}}$ of the previous experiments (Table 3.5) to the maximum, observed in Southampton on a clear day in early summer of $I_0 = 3120\,\mu\mathrm{E\,m^{-2}\,s^{-1}}$ (45% of which are PAR) and also the inhibition threshold I_b has been lowered from 250 to 150 $\mu\mathrm{E\,m^{-2}\,s^{-1}}$. The parameters thus create optimal conditions for the above swimming strategy to be successful since the high irradiance levels in combination with the low inhibition threshold should lead to strong photoinhibition in the cells that swim constantly up and accumulate at the surface.

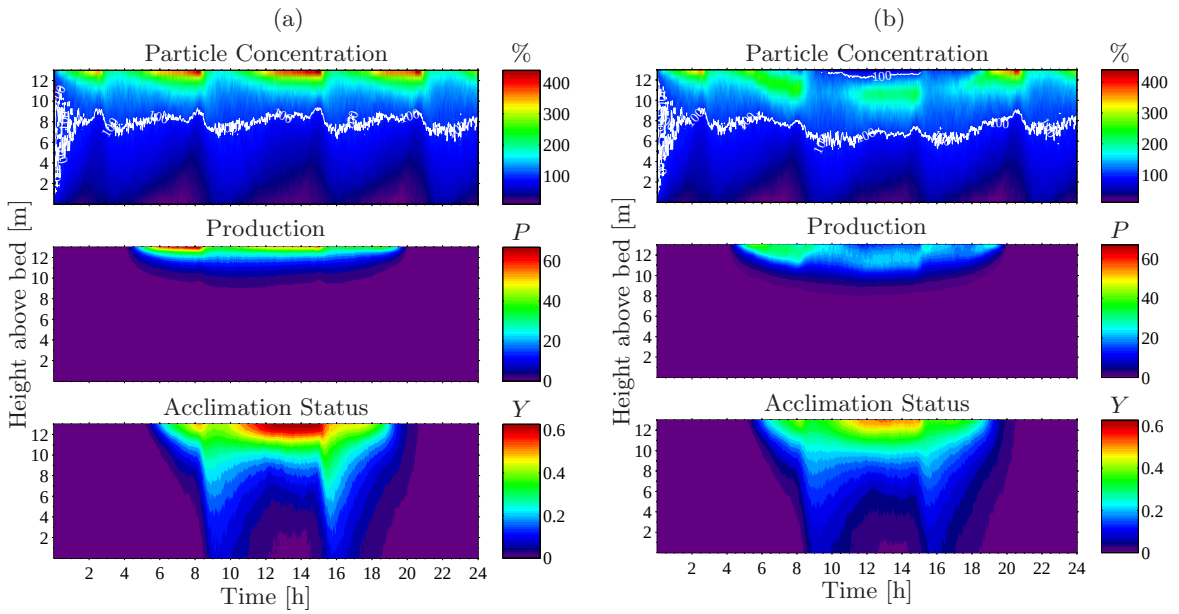

Figure 3.21: Comparing the local production and acclimation status for different swimming strategies. In (a), the cells were swimming constantly upward. In (b) the cells followed the optimal swimming strategy from Eq. (3.8). The model was run with a maximum midday irradiance of $I_0 = 3120\,\mu\mathrm{E\,m^{-2}\,s^{-1}}$ (45% of which are PAR) and a lower inhibition threshold of $I_b = 150\,\mu\mathrm{E\,m^{-2}\,s^{-1}}$.

This intuitive assumption is not confirmed by the results, however. For this particular experiment Y_c from Eq. (3.8) has been set to 0.1 from Fig. 3.19. The top panel in Fig. 3.21(a) shows how the particles that swim constantly upward accumulate in high numbers at the surface. The particles that follow the swimming strategy from Eq. (3.8) [Fig. 3.21(b)] accumulate about 2-3 metres below the surface. As a result the average inhibition level is lower for those particles but also the production seems less than for the cells in (a). Integrated over all particles and the entire 24 h, the production is about 6% higher for the particles in (a) compared to (b). If the experiments are repeated with different values for Y_c, the best result that could be obtained for the strategic swimmers is that they are able to match the production of the cells that simply swim upward. This match was achieved for $Y_c = 0.4$. This result is somewhat puzzling.

The resolution of this paradox is linked to the graph in Fig. 3.22. It shows the depth and time distribution of $X(I)$ for the above particle distributions and irradiance. Already shortly after 06:00 h the irradiance at the surface starts to drastically exceed I_b and the local inhibition status becomes equal to unity. As the sun rises higher into the sky, the maximum inhibition progresses deeper into the water column. However, the average inhibition of the cells in Fig. 3.21(a) never exceeds $\overline{Y} = 0.6$ and only reaches this level for about 3-4 h from midday to early afternoon. The turbulent mixing provides a constant exchange of cells between the surface and the subsurface layers. On average the cells are not as inhibited as they 'should be' for the ambient irradiance and therefore can exploit the high irradiance near the surface. For the cells it is thus more (or at leat equally) beneficial to be at $Y = 0.6$ and close to the surface, rather than at the lower Y_c and lower down in the water column. In addition, it is more difficult for the cells to maintain a certain depth in the interior of the water column as the mixing is generally higher there due to the larger turbulent length scale. This explains why the subsurface accumulation in Fig. 3.21(b) is more diffuse compared to the surface accumulations in Fig. 3.21(a).

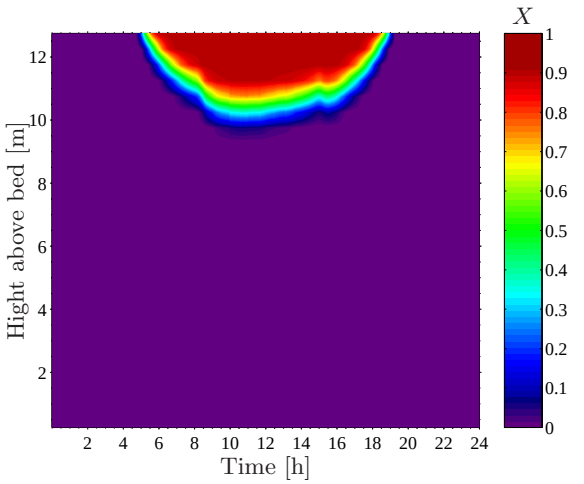

Figure 3.22: Local inhibition status X for the particle distribution and light levels from Fig. 3.21(a).

In order to eliminate the effect of the time lag between X and Y and to ensure that it is indeed the mixing which causes this result, the experiments were re-run with the unrealistic acclimation time scale of $\tau_a = \Delta t = 6$ s. The cells would thus instantly acclimatise to their ambient light environment. As a result, the cells became considerably more inhibited and the production decreased by about 50% for both swimming strategies. The overall production remained equal for both strategies, however.

3.4.4 Mixing versus Photo-acclimation

Let us now revisit the results in Fig. 3.16. They showed how the cells become increasingly inhibited during the high water stand and then the ebb flow homogenises the water column. A hypothesis was outlined in Section 1.3.2 in which Marra (1978*a*) and Falkowski (1983) suggested the vertical heterogeneity of suitably chosen physiological parameters could be used to infer the level of turbulent mixing in the euphotic zone. A hypothesis for which Lewis et al. (1984*b*) found some observational evidence (see Section 1.3.2). Let us now define an acclimation number $\mathscr{A}$ similar to the Peclet number from Eq. (1.37) by relating the acclimation time scale to the mixing time scale

$$\mathscr{A} = \frac{\tau_a}{\tau_m} = \frac{\tau_a K}{h^2} \tag{3.9}$$

We could hypothesise that, in analogy to the Peclet number, if $\mathscr{A} \gg 1$, then the mixing occurs faster than the acclimation and the physiological parameter should be homogeneous throughout the water column. If $\mathscr{A} \ll 1$, the cells acclimatise to the light environment faster than they are mixed and a vertical structure in the physiological parameter should appear.

This is exactly what is happening in Fig. 3.16. Fig. 3.23(a) shows the above defined acclimation number $\mathscr{A}$ for the sSTS and Fig. 3.23(b) contains again the acclimation status of the cells from Fig. 3.16(a). During the high water stand between 09:30 h and 12:30 h, $\mathscr{A} \ll 1$ and as a consequence a vertical gradient in the inhibition parameter Y develops. With the ebb flow the mixing and thus $\mathscr{A}$ increases resulting in a more homogeneous distribution of Y as can be seen in the three profiles in Fig. 3.23(c). As $\mathscr{A}$ never reaches unity, a slight gradient remains as can be seen in the last profile taken. If the acclimation time scale is doubled from 1 h to 2 h (resulting in a doubling in $\mathscr{A}$) the profile becomes virtually homogeneous.

These results thus seem to back the hypothesis by Marra (1978*a*) and Falkowski (1983) and the observations by Lewis et al. (1984*b*). To obtain an estimate for the turbulent intensity

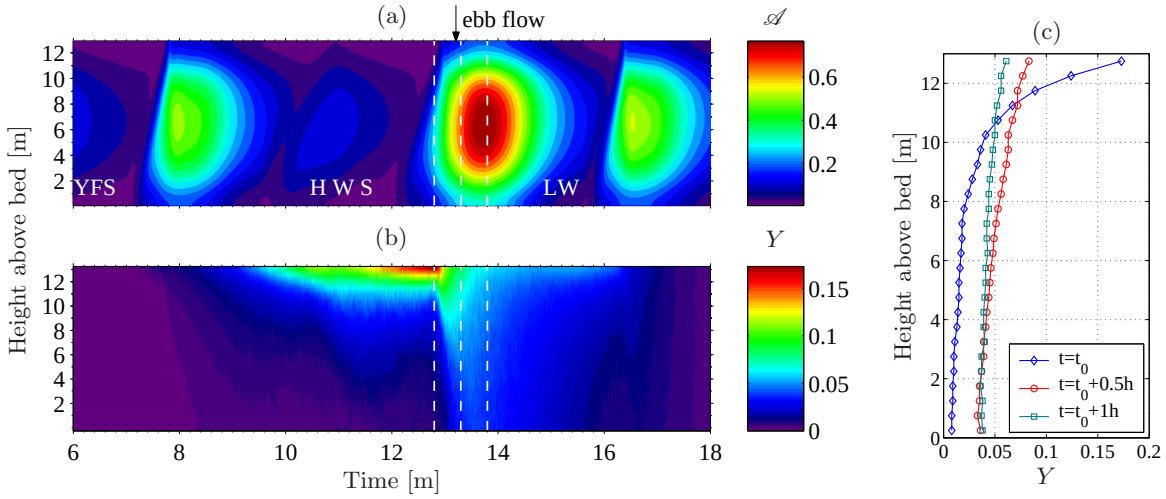

Figure 3.23: (a) Acclimation number from Eq. (3.9) for the sSTS and an acclimation time scale of $\tau_a = 1$ h. (b) Acclimation status of the cells from Fig. 3.16(a). The dashed white lines indicate the locations of the vertical profiles from (c) which are taken 30 minutes apart. YFS, HWS and LW indicate the times of the Young Flood Stand, the High Water Stand, and Low Water respectively.

one would simply need to know the acclimation time scale τ_a of a particular physiological parameter and monitor the change in the vertical gradient in this parameter. If the duration of the mixing event is of the same order of magnitude or longer than τ_a, the change in the gradient can be used to establish a mixing time scale which, after choosing an appropriate value for the mixed layer depth, should provide a rough estimate of the eddy diffusivity K.

3.4.5 Taking into Account the Tidal Variations in Water Depth

In a real estuary, the total water depth varies with the incoming and outgoing tides. Especially in turbid estuaries such as Southampton Water, this could affect the light availability to plankton cells. This section will therefore explain the effect of a varying water level on the previous results. As most model calculations are insensitive to small variations in the total water depth, the physical part of the model (i.e. the part that produces the turbulent mixing) was kept running with a fixed depth. Variations in depth were only included in the calculation of light distribution and in the particle tracking. The particles are tracked using the mean water depth but the velocities in the random walk are scaled to account for the shorter/longer vertical distances as the water level is lower/higher than the mean. In order to ensure that there was a fixed correlation between the water level and the tidal velocities, the height variations were derived directly from the model velocities using observational data only to scale the tidal range produced. The method of how this is achieved is described in Appendix A. While in the fixed depth case, the light availability is calculated from

$$I(z_n) = I_0 \exp\left[-k_t(H - z_n)\right] \tag{3.10}$$

where H is the fixed depth and z_n the height of the n-th particle above the sea bed, in the variable depth case, the following equation is used:

$$I(z) = I_0 \exp\left\{-k_t \left[h(t)\left(1 - \frac{z}{H}\right)\right]\right\} \tag{3.11}$$

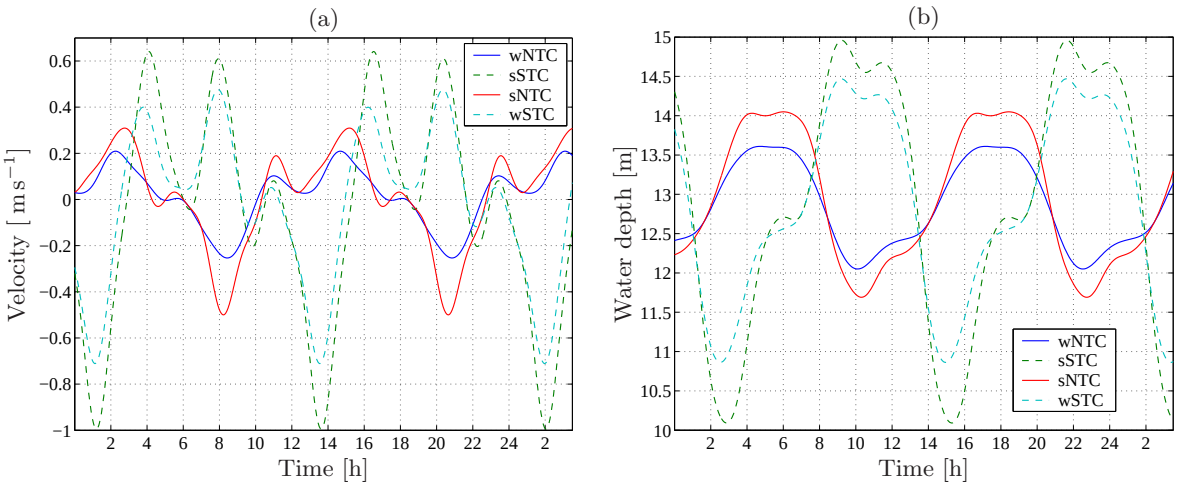

Figure 3.24: (a) Depth averaged tidal velocities from the model output of the first 27 hours of each scenario (cf. Fig. 3.6). (b) Total water depth calculated from the velocities in (a) using the method described in Appendix A.

where $h(t)$ is the variable water depth that is calculated from the model velocities. In the model, $h(t)$ is updated every five minutes. Fig. 3.24(b) shows a plot of $h(t)$ for each scenario.

As a result, the light availability for motile cells is reduced as the slack water periods usually coincide with the highest water levels, and thus they need to swim further to reach the surface. The sinking cells reach their highest production during and just after the ebb flow when their distribution has been homogenised by the tidal mixing. It is also right after the ebb when the water level is the lowest and the euphotic depth extends through a greater percentage of the water column than at high tide.

Fig. 3.25 shows a comparison of the light availability for all particle species and scenarios. Overall, the motile cells are doing less well and their average light availability is reduced by 3-5% depending on the scenario. For the negatively buoyant cells, the overall light availability was only slightly reduced by about 0.5-1.5% depending on the scenario. The motile cells thus lost some of their advantage in the light availability compared to Fig. 3.14. If the actual overall production is compared (not shown), the results are essentially identical to those shown in Fig. 3.17 except that the share of the motile cells in each experiment is occasionally reduced by 1%.

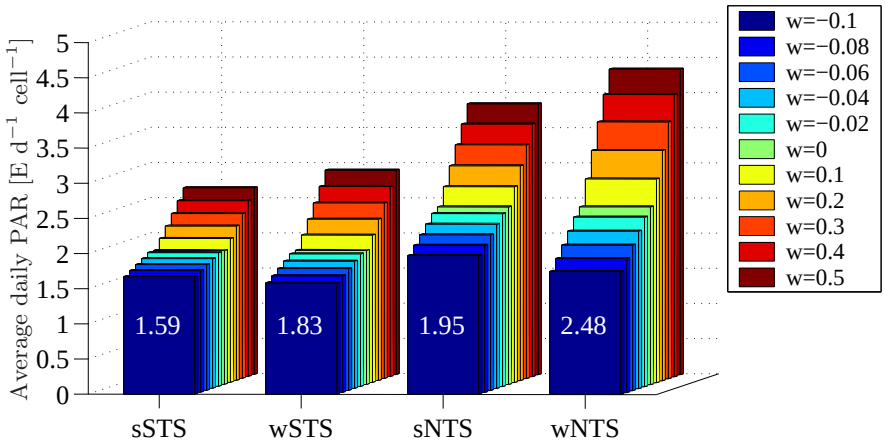

Figure 3.25: Equivalent plot to Fig. 3.14 for the variable height experiment.

3.5 Summarising the Results for Southampton Water

Most of the findings from this chapter are easily transferable to any other estuary as long as the mixing in that estuary is known. The results of the Southampton Water study show that even if the tidal currents themselves may be strong and produce enough turbulence to hinder any directional swimming efforts, it is the breaks inbetween the tidal pulses that the motile cells can utilise to adjust their vertical position. If these breaks are long enough for the cells to cover a significant distance (e.g. move higher into the euphotic zone), this can lead to significant increases in their light availability which can compensate for the generally slower overall growth rates of motile species (e.g. Broekhuizen, 1999). Southampton Water

is somewhat special in that it has a slack water period that extends up to three hours and provides the motile cells thus with an excellent break from the turbulent mixing. In estuaries with similar mixing intensities but where the slack water periods are shorter, one would expect to see the motile cells less successful and thus less abundant.

3.5.1 Cell Motility

In Section 3.3.1 the effectiveness of motility for the tidal mixing in Southampton was discussed. The results showed that on a spring tide, the mixing dominates during the main tidal segments, while the cells are able to use their motility during the various periods when the tidal mixing is reduced, i.e. during the young flood stand and the extended high water stand to form accumulations at the surface (Fig. 3.9). The Peclet number was found to be a good indicator to predict the times during which the swimming could be utilised effectively against the turbulent mixing (Fig. 3.10). At neap tides, the Peclet numbers were generally lower which was mirrored by the increased number of particles accumulating at the surface. Towards the end of the high water stand, and generally during neap tides, the motile cells were able to achieve a significant bias in their population distribution towards the surface (Fig. 3.11). The ebb and flood flows are usually strong enough to quickly re-homogenise the particle distribution. Both the accumulations and the re-homogenisation during ebb and flood are in good agreement with observational studies by Crawford and Purdie (1992) andLauria et al. (1999). However, the periodic re-homogenisation of the particle distribution would make it difficult for them to pursue any diurnal or turbulence avoidance strategy as suggested by these authors (see also the discussion in Section 3.3.3). Due to the much lower sinking velocities of diatoms, their distribution in the water column remains fairly uniform throughout the tidal cycle (Fig. 3.12).

3.5.2 Light Availability, Production and Photo-acclimation

The bias of the motile population towards the surface resulted in a significantly higher light availability compared to the non-motile cells (Fig. 3.13 and Fig. 3.14). The results for each scenario depend on the relative timing of the tidal mixing in relation to the solar irradiance cycle. If the slack water in the STS occurred with a neap timing, for example, i.e. near 06:00 h and 18:00 h, the motile cells would not be able to increase their light availability to the extent shown. If we assume a 2.4 times higher growth rate for diatoms, only the fastest swimmers are able to match the production achieved by diatoms through their increased light availability (Fig. 3.17). This result is strongly dependent on the ratio of the maximum production rates ($P^m_{d/l}$) chosen for the different phytoplankton groups in the production model. For more similar production rates, the motile cells will match the production of the diatoms already for lower swimming velocities and vice versa. This result did not seem to depend on the maximum irradiance I_0, the saturation onset parameters $I_{d/l}$ or the acclimation time scale τ_a, as long these parameters are chosen to be the same for both groups. If we start to choose different parameters for the two groups then the balance shifts. A shorter acclimation time scale for diatoms, for example, would cause higher inhibition levels in this group and shift the results

in favour of motile cells while a lower diatom saturation onset parameter would shift the results more in favour of diatoms. If those parameters are kept the same for both groups, their absolute value simply influences the absolute production but the relative picture from Fig. 3.17 is fairly robust. It also seems unaffected by the inclusion of the tidal variations in water depth (Section 3.4.5) or by trying different swimming strategies. A comparison yielded almost identical production levels for cells that were swimming constantly upwards compared to those following an optimal swimming strategy [Eq. (3.8)] although this swimming strategy was able to decrease the general inhibition level in the cells (Fig. 3.21). It was argued that this can be attributed to the fact that the cells are always 'under-inhibited', i.e. the turbulent mixing causes a constant exchange of cells which leads to a cellular inhibition status Y that is on average always lower than expected (X) for the given irradiance level (Fig. 3.22). These 'under-inhibited' cells in the surface layer are able achieve production levels that are equal or slightly above those achieved by the less inhibited cells that follow the optimum swimming strategy and are therefore at lower irradiance levels deeper down in the water column. By defining an acclimation number [Eq. (3.9)], it was possible to explain the changes in the vertical heterogeneity of the acclimation status in a similar fashion as the Peclet number could be used to explain the heterogeneity in the particle distributions. This confirms the suggestions by Marra (1978*a*) and Falkowski (1983) and gives an experimental backing to the observations by Lewis et al. (1984*b*).

Chapter 4

Application to Tidally Energetic Shelf Seas

Shelf seas provide a challenging environment for phytoplankton. The interplay of mixing and stratification create an ever–changing environment and the spatial separation of their primary resources, light and nutrients, further complicates their situation by producing the so-called phytoplankton-dilemma (e.g. Klausmeier and Lichtmann, 2001, see below). Nevertheless, shelf seas form one of the most productive ecosystems for primary producers in the world's oceans. The importance of the spring bloom as a food source for secondary producers and the pelagic ecosystem as a whole has long been recognised (Sverdrup, 1953). New evidence is emerging, however, which suggests that the periodic subsurface blooms in stratified shelf seas may outweigh the importance of the short lived spring bloom by fuelling the water column throughout summer (Richardson et al., 2000). Observations show that most phytoplankton species in such stratified environments are motile (Richardson et al., 2000; Sharples et al., 2001). Given that a large proportion of the world's oceans has either a permanent or seasonal thermocline, an understanding of the role of motility and the underlying physical processes governing primary production in these areas is therefore essential, especially if these processes are about to change as predicted by many climate models.

The present chapter will examine these issues for a tidally energetic stratified shelf sea environment. Section 4.1 will introduce some of the relevant issues that are important to understand the challenges faced by plankton in shelf seas. The model setup for the later experiments is explained in Section 4.2. The experiments focus on two main issues: the first series of experiments (Section 4.3) examines the effectiveness of motility in general in a stratified and tidally energetic shelf sea environment; in the second part (Section 4.4) the biology is added to the model and the performance of one motile and one non-motile species is compared over a springs neaps cycle to examine which species emerges as more successful. A summary of the main results is provided at the end of the chapter in Section 4.5.

4.1 Phytoplankton Survival in Shelf Seas

Phytoplankton in shelf seas are faced with what is usually termed the 'phytoplankton dilemma'. This term refers to the fact that light is abundant near the surface while nutrients are supplied from below. Especially in stratified shelf seas, this can produce real challenges for phytoplankton as there is often only a rather narrow depth band that has sufficient quantities of both resources and is also physically stable enough to prevent them from being drawn into the bottom mixed layer.

The thermocline acts as a strong barrier against vertical transfers of nutrients which often leads to the scenario shown in Fig. 4.1. These observations were taken in August 1999 in the Western English Channel aboard RV Challenger. The ship remained stationary for two complete tidal cycles with almost hourly CTD casts and turbulence measurements using a FLY profiler (Sharples et al., 2001). The top panel shows how the phytoplankton were mainly concentrated in a narrow band at the base of the thermocline where the concentrations reach values > 50 mg chl m^{-3}. The biomass maximum was dominated by the motile coccol-

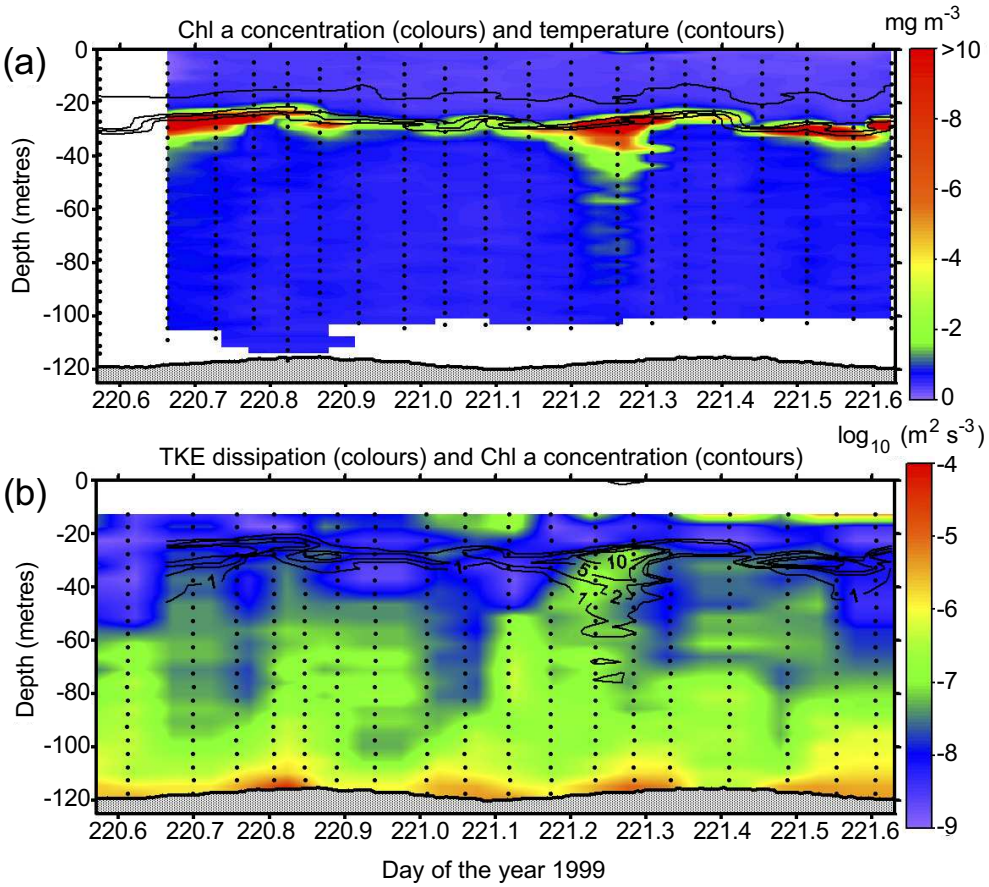

Figure 4.1: Observations in the Western English Channel from aboard RRS *Challenger* in August 1999 from Sharples et al. (2001). (a) The chlorophyll maximum is located in a narrow band at the base of the thermocline. The temperatures are contoured every 2°C. (b) As the turbulent mixing reaches higher into the thermocline (day 221.25) some of the phytoplankton are drawn into the bottom mixed layer. The vertical dotted lines represent the times of the CTD (a) and FLY (b) casts.

ithophore *Calyptrosphaera oblonga* with cell diameters between 10-15 μm. Fig. 4.2 shows a picture of a sample population taken during this cruise. In general, coccolithophores are known to be able to grow well under low light conditions (Lalli and Parsons, 2002) with some species reaching their maximum abundance at depths of about 100 m in clear, tropical oceanic water. Some species of coccolithophores have been reported to achieve growth rates of 1 doubling per day at irradiance levels of 7 W m^{-2} (Brand and Guillard, 1981). On the day of the observations from Fig. 4.1, the population maximum was at the 5% light level (Sharples et al., 2001), receiving an average of 6 W m^{-2} over the light period (4 W m^{-2} if averaged over 24 h). Considering that at a latitude of 50°, the irradiance in August can reach surface averages of over 250 W m^{-2} [averaged over 24 h from data of the NCEP/NCAR 40-year Reanalysis Project, see Kalnay et al. (1996)], this would leave 12.5 W m^{-2} at the 5% light depth which appears sufficient for *C. oblonga* to achieve the required growth rates to produce the high observed biomass.

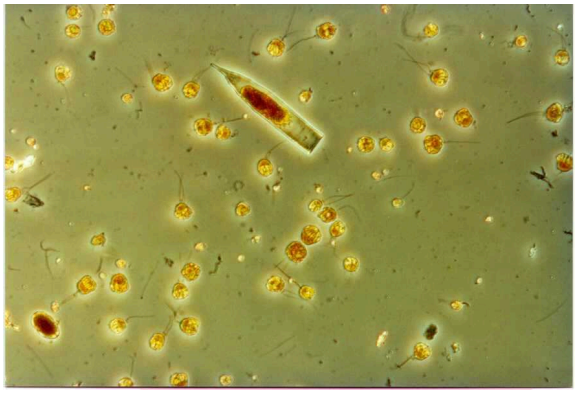

Figure 4.2: The coccolithophore *Calyptrosphaera oblonga* with a larger zooplankton. Image courtesy J. Sharples.

The tidal pulses of TKE dissipation can be seen at the seabed [Fig. 4.1(b)]. One of these pulses manages to reach up higher into the thermocline (around day 221.25) thereby eroding part of the biomass into the bottom mixed layer. The fate of these eroded cells, i.e. the question of whether they were able to regain access to the thermocline area, is unclear, as the ship remained stationary while this patch was moved away from the ship's position in the tidal current.

A closer look at one of the profiles reveals why the cells are concentrated in such a narrow band. The profile from Fig. 4.3 was taken just after day 221.5 in Fig. 4.1. Fig. 4.1(a) showed a strongly stratified water column with a top-to-bottom temperature difference of over 8°C. Due to a continuous nutrient uptake by phytoplankton trapped in the surface mixed layer (SML) and the thermocline preventing significant re-supply from the bottom mixed layer, the nutrients in the SML have become depleted. This can be seen from the discrete water sample analysis in Fig. 4.3. The bottom layer temperature profile was mixed to within the noise of the sensor (+/- 0.001°C), which suggests that the nitrate would exhibit a similarly sharp step at the base of the thermocline as the temperature. The dashed blue line has been added as a tentative connection, based on the output from the SUV-6 spectrophotometer. The red dashed line shows the squared Brunt-Väisälä frequency and serves as an indication for the water column stability. The chlorophyll maximum is about 1 m below the stability maximum and at the upper edge of the nitracline.

The depth of the chlorophyll maximum is thus a result of the phytoplanktons' effort to maximise their light availability by being as close as possible to the surface, while at the same time

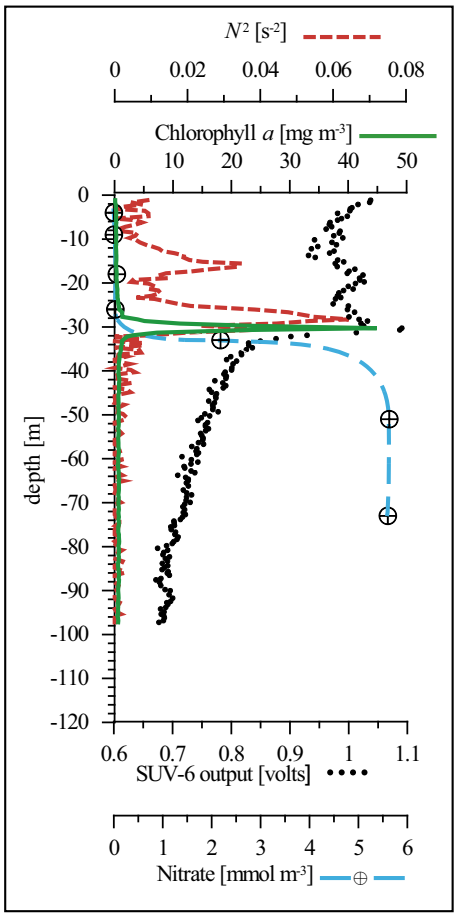

Figure 4.3: Chl a concentration (mg m^{-3}), squared Brunt-Väisälä frequency (s^{-2}), nitrate concentrations from water sample analysis (mmol m^{-3}), and the raw output from the SUV-6 in situ spectrophotometer.

having sufficient nutrients to be able to photosynthesise. The only location where this seems possible is at the base of the thermocline which, as the observations in Fig. 4.1(a) showed, is also a potentially hazardous location as the cells are in constant danger of being eroded into the bottom mixed layer.

The main processes which drive the transfer of nitrogen down the gradient are internal waves or shear driven by internal oscillations. The supply due to turbulent diffusion, i.e. $K\ \mathrm{d}N/\ \mathrm{d}z$ is very weak, and the layer of phytoplankton in the subsurface chlorophyll maximum (SCM) are able to intercept all of it (as demonstrated by the negligible nitrogen concentrations in the surface layer). Thus, it seems that in order to be successful in these conditions, it becomes necessary for the cells to possess some form of motility which would allow them to reach the very source of this nitrogen before any competitor does. Almost all the cells found in the chlorophyll maximum were motile, which suggests that motility could indeed be an advantage for survival in this type of environment. Given the very narrow depth-band in which the chlorophyll was concentrated, the swimming velocities of the cells must be much greater than the turbulent velocities at the base of the thermocline. The main questions which the following sections will attempt to address are thus:

- Given the high turbulence in the bottom layer of a tidally energetic shelf sea and the evidence of erosion of cells into this layer, does the ability to swim provide a mechanism for regaining access to the SCM?

- If a motile and a neutrally buoyant species co-habit the thermocline, does motility lead to the dominance of that species by giving it an advantage in intercepting the weak upward flux of nitrate?

- Is it possible to quantify the extent of any advantage in terms of growth of biomass?

Before providing the answers to these questions, the next section will describe the physical and biological setup used in the experiments.

4.2 Model Setup

4.2.1 The Physics

The setup of the physical part of the model is essentially identical to Chapter 3 with the exception that density variations are taken into account in this case and are able to alter the turbulent mixing. The turbulence is forced through tidal currents and the particle displacement is calculated using Eq. (2.15). The diffusivities obtained from the turbulence closure scheme

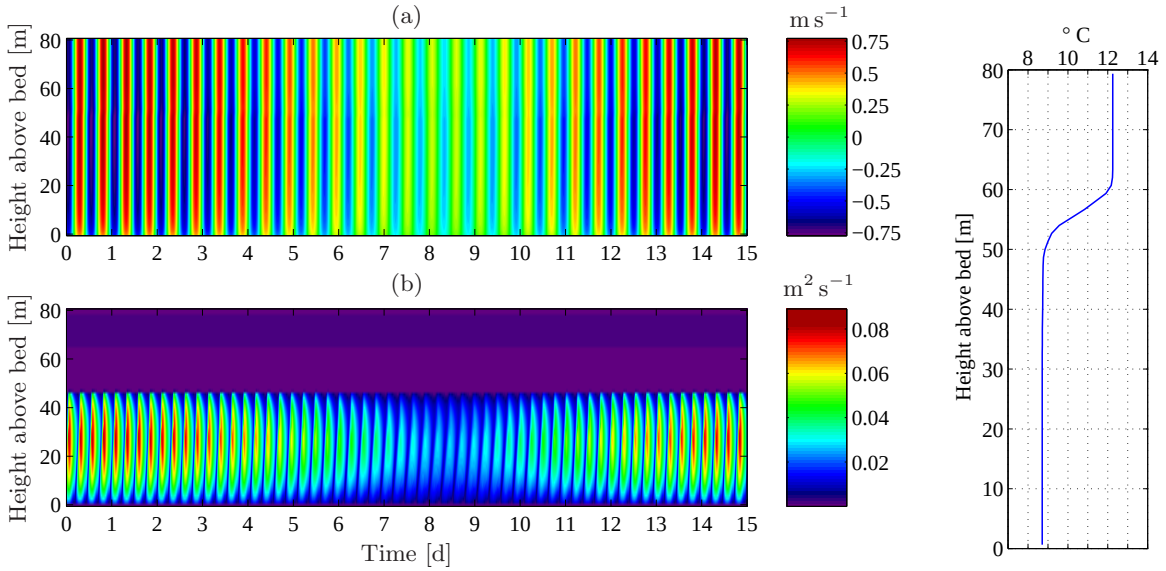

Figure 4.4: (a) Springs-neaps variation of tidal current strength. (b) Associated model eddy diffusivities for the constant temperature stratification shown on the right. In the surface mixed layer the values for K are about $3 \cdot 10^{-3}$ m^2 s^{-1}, in the centre of the thermocline $K \approx 10^{-5}$ m^2 s^{-1}.

are smoothed using the method from Section 2.2.2 and $K' = 0$ is forced at the boundaries as described in Section 2.2.3.

The tides are driven with a simple M_2/S_2 combination, such that the current strength at spring tide is slightly above the values observed by Sharples et al. (2001) which were obtained partway between neap and spring. The ratio of S_2:$M_2$was set to the equilibrium tide ratio of 0.465 (Emery and Thomson, 1998). The modelled spring neap cycle of currents [Fig. 4.4(a)] drives a cycle in the mixing [Fig. 4.4(b)], limited to the bottom layer by the imposed form of the temperature profile (Fig. 4.4 inset). No wind mixing was applied, so that the results could be interpreted in terms of the tidal forcing variability only. The stratified experiments use the constant temperature gradient shown here, i.e. there is no heat exchange with the atmosphere and no diffusion of the temperature gradient by the turbulent mixing. The turbulent mixing will therefore be able to intrude into the base of the thermocline and the depth of the intrusion will vary with the tidal current strength (see below), but it cannot erode the stability of the temperature stratification. Tests where the temperature diffusion was enabled showed negligible differences in the results over a springs-neaps cycle and diffusion was therefore discarded as a means to speed up the simulations.

4.2.2 Light and Nutrient Dynamics

In Chapter 3 we could assume that the estuary was only light but not nutrient limited. The growth model could therefore be formulated based solely on the light availability to the cells. In shelf seas, and in particular in stratified shelf seas, this is no longer a valid assumption and we need to include the possibility of nutrient limitation. The simple light-based growth model from Section 2.3 is therefore extended by a nutrient model in which the cells are able to take up a nutrient from the water, store it up to a maximum nutrient-to-carbon ratio, and consume it when they produce carbon during photosynthesis. The model is very simple in that it neglects temperature effects on the growth and respiration rates and that it uses nitrogen as the only nutrient, thereby neglecting other important nutrients such as phosphate or silicate. The latter can become limiting in particular for diatoms. While the main model remains in a Lagrangian formulation, the nutrient is modelled on a Eulerian grid (Broekhuizen, 1999) (see below).

Fig. 4.5 gives a summary of the programme flow. Each model particle represents initially 100 000 'real' cells, each of which is given a carbon content of $2 \cdot 10^{-6}$ mg C. The model contains a lower carbon threshold, W_{starve}, at which some of the cells die (i.e. the number of real cells per model particle is reduced) and an upper level, $W_{fission}$, at which the cells divide (and the number of real cells per model particle doubles). Table 4.1 gives a summary of the main parameters used. For the nutrient uptake a Michaelis-Menten type function of the ambient nutrient concentration N is used

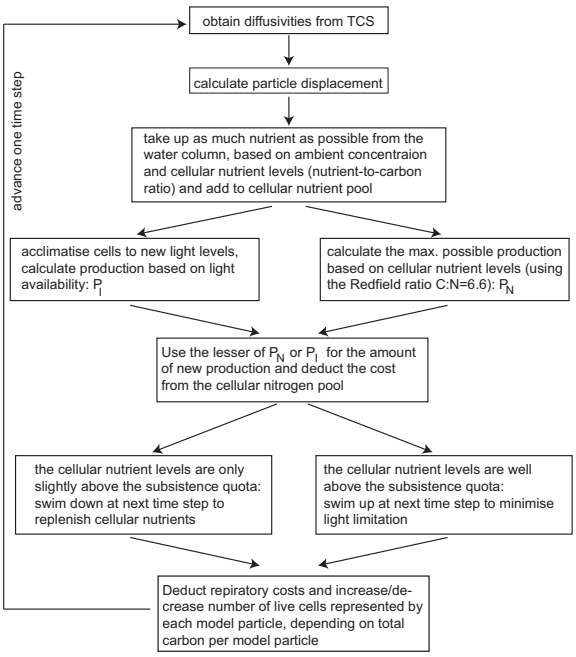

Figure 4.5: Flow diagram for the shelf sea experiments showing one of the swimming strategies used.

$$U = U_m \left(1 - \frac{Q}{Q_{max}}\right) \frac{N}{\kappa_N + N} \qquad (4.1)$$

Q is the cellular nitrogen-to-carbon ratio which needs to remain above a subsistence quota Q_{min} and below a maximum storage quota Q_{max}. U_m is the maximum uptake rate and κ_N the half-saturation constant. Once the uptake is added to the cellular nutrient pool, the maximum possible carbon production based on the light availability using the Denman and Marra (1986) formulation from Section 2.3 is calculated. If the cell has sufficient nitrogen to produce the calculated amount of carbon (light limitation), the cellular carbon content increases and the cost is deducted from the nutrient pool using the Redfield ratio of C:N = 6.6 (Sharples, 1999). If the cell does not have sufficient nitrogen (nutrient limitation), the entire amount of cellular nitrogen that is above the subsistence level is used for carbon production leaving the cell at the subsistence quota. After each time step the cell also respires at the rates given in Table 4.1.

The ambient nutrient concentration in each model bin thus changes according to

$$\frac{\partial N}{\partial t} = \frac{\partial}{\partial z}\left(K\frac{\partial N}{\partial z}\right) - \sum_{i=1}^{n} U_i \tag{4.2}$$

where U_i is the uptake of nitrogen in [mg N] by the i-th particle in the bin containing a total of n particles. Nutrient is added to the bottom mixed layer at a constant rate R_N through resuspension at the seabed with a boundary condition applied to the bottom depth cell of the model (Sharples, 1999)

$$\Delta N_1 = R_N(N_b - N_1)\Delta t \tag{4.3}$$

where N_1 is the nutrient concentration in the bottom depth cell and N_b the maximum value for near bed dissolved organic nitrogen (DIN) (Table 4.1). This simulates the resupply of nitrate to the overlying water through bacterial regeneration of organic to inorganic nitrogen in the bottom sediments. This is often the dominant source of inorganic nitrogen to water in stratified shelf seas away from sources of freshwater or the shelf edge. Another important source to the bottom layer can be regenerated nitrogen by grazers. Although the effect of grazing on the biomass is included in the loss terms of the growth equation, recycled nitrogen as such is neglected as a possible nutrient source in the model.

For the fully dynamic experiment (Section 4.4) two different swimming strategies will be tested. The diagram in Fig. 4.5 shows the program flow for one of the swimming strategies which is based on the physiological state of the cell. If the cell is approaching the subsistence nutrient quota, it will swim down towards higher nutrient concentrations. If it has sufficient nitrogen

TABLE 4.1: Physiological parameters for the motile and non-motile cells in the experiments. The sources are: 1 = Sharples (1999), 2 = Broekhuizen (1999), 3 = Sharples et al. (2001) and 4 = assumed.

SYMBOL	MEANING	UNITS	VALUES		REF.
Physical					
H	total water depth	m	80		4
I_0	irradiance at midday	μE m^{-2} s^{-1}	2300		4
k_{bg}	background absorption coefficient	m^{-1}	0.09		3
N_b	max. value for near bed DIN	mg N m^{-3}	70.0		3
R_N	input rate of DIN by resuspension	s^{-1}	$1.8 \cdot 10^{-5}$		1
Biological			motile	non-motile	
I_b	lower inhibition threshold	μE m^{-2} s^{-1}	150	150	4
$I_{d/l}$	saturation onset light intensity	μE m^{-2} s^{-1}	50	50	3
κ_N	DIN half saturation concentration	mg N m^{-3}	3.0	3.0	1
k_m	cell spec. absorption coef.	m^2 (mg cell. C)$^{-1}$	0.004	0.004	2
P_m^d	max. dark acclimatised production	mg C (mg cell. C d)$^{-1}$	1.5	2.5	3,2
P_m^l	max. light acclimatised production	mg C (mg cell. C d)$^{-1}$	0.08	0.12	4
Q_{min}	subsistence nutrient quota	mg N (mg cell. C)$^{-1}$	0.056	0.056	1
Q_{max}	max. cellular nutrient quota	mg N (mg cell. C)$^{-1}$	0.28	0.28	1
r	cellular metabolic rate	mg C (mg cell. C d)$^{-1}$	0.1	0.1	4
U_m	max. nitrogen uptake rate	mg N (mg cell. C d)$^{-1}$	0.5	0.5	2
w	vertical sinking/swimming velocity	mm s^{-1}	0.1	0.0	4
W_{starve}	min. cellular carbon	mg C (cell)$^{-1}$	$1 \cdot 10^{-6}$	$1 \cdot 10^{-6}$	2
$W_{fission}$	max. cellular carbon	mg C (cell)$^{-1}$	$3 \cdot 10^{-6}$	$3 \cdot 10^{-6}$	2

then it could potentially produce more if it was at higher light intensities and hence it swims up towards the light. During night time, if the cellular nitrogen levels are sufficiently above the subsistence quota, the cell will swim upwards to be as high as possible in the water column once the sun rises again. In the second tested swimming strategy, the cells follow a certain nutrient isoline which coincides with the half saturation concentration (HSC), κ_N, for nutrient uptake.

Before examining the results of this fully dynamic biological-physical model, the next section will focus on the issue of motility and examine its use in a stratified and tidally energetic shelf sea.

4.3 Swimming versus Mixing at the Thermocline

Given the frequent observation of motile cells in the temperate shelf sea summer thermocline, the ability to swim is implicated as a potentially important survival mechanism for phytoplankton. This is particularly the case when the surface layer has been depleted of nutrients, so that the optimal region for primary production is at the source of nutrients being mixed into the thermocline from the bottom layer. This section will attempt to quantify the basic advantage of motility in terms of the Peclet number [Eq. (1.37)].

The graphs in Fig. 4.6 show the model output for one tidal cycle during a spring and neap tide from Fig. 4.4. During the spring tide, the bottom mixed layer is dominated by the turbulent mixing except for the medium to fast swimmers ($w \gtrsim 0.3\,\mathrm{mm\,s^{-1}}$) for which short periods of $\mathscr{P} > 1$ appear in the bottom layer associated with low current speeds. During neap tide, these periods become longer and also the slower swimmers with $0.15 \lesssim w \lesssim 0.3\,\mathrm{mm\,s^{-1}}$ might be capable to overcome the turbulent mixing. The thermocline itself appears in both scenarios in deep red colours for any of the shown swimming velocities which implies that even the slowest swimmers will be able to use their motility in this environment. The mixing in the surface layer is the same for both scenarios as the tide generated bottom turbulence dissipates in the thermocline and has thus no effect on the turbulent intensity in the SML. In the absence of wind, the turbulent mixing is weak and the phytoplankton cells should be able to utilise their motility also in the SML.

As the choice of the length scale used to calculate the Peclet number is somewhat arbitrary (the approximate depth of the bottom mixed layer of $h = 49\,\mathrm{m}$ was chosen to produce the graphs in Fig. 4.6), a series of experiments has been conducted in which the cells were given the swimming strategy of trying to maintain a certain depth in the water column. In the first experiments, this depth was chosen to lie within the thermocline. This produced high accumulations of particles, as the mixing does not penetrate into the thermocline and the cells are protected, using their motility effectively to maintain the prescribed depth. In the subsequent experiments – in accordance with the above observations that showed how the nitracline is often located at the base of the thermocline – the cells were aiming deeper and deeper in the water column, in order to find a maximum depth at which they were able to

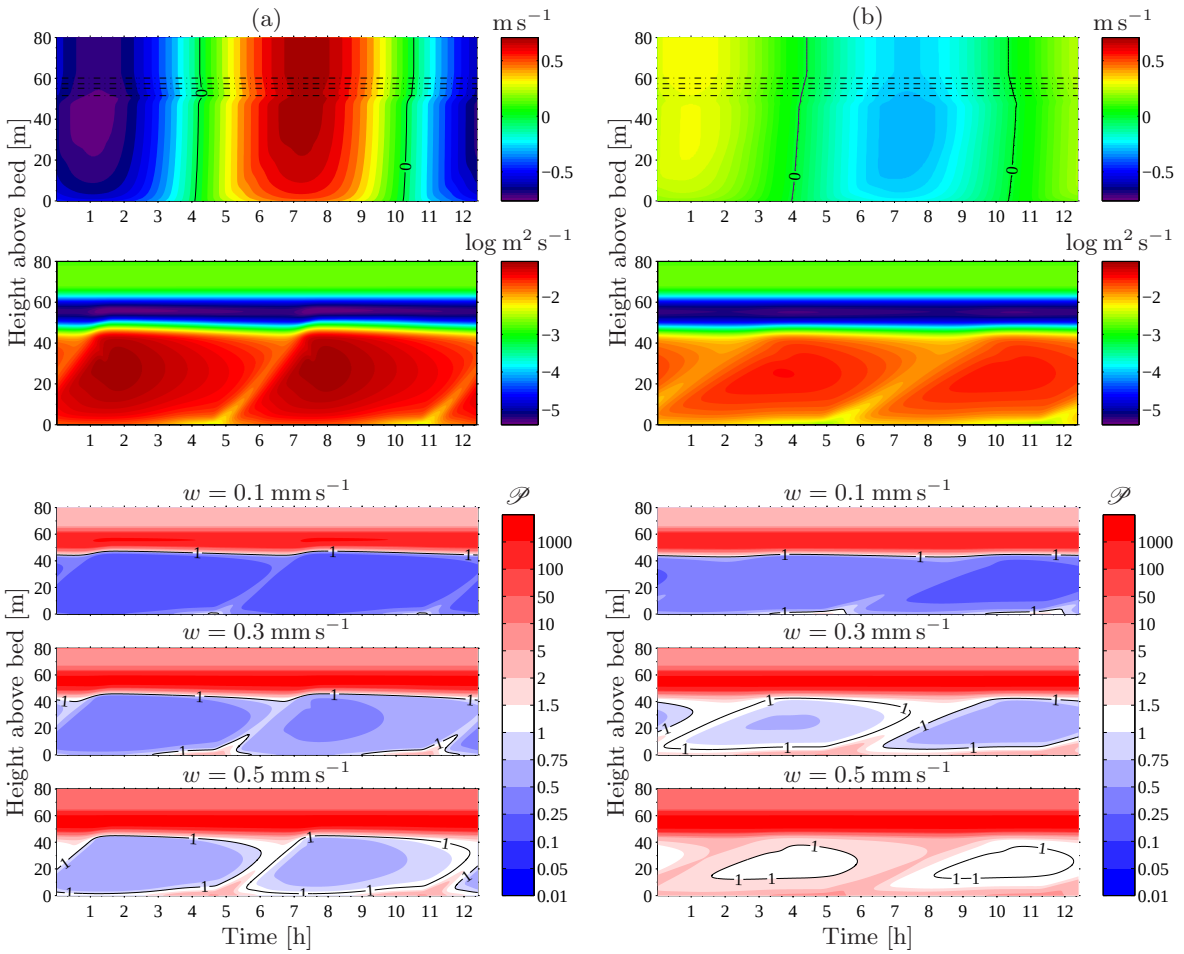

Figure 4.6: Model output for (a) a spring and (b) a neap tidal cycle. The top panels show the tidal velocities with the temperatures from Fig. 4.4 contoured as dash-dotted lines. Below are the calculated eddy diffusivities (after applying the cubic smoothing splines – note the logarithmic scale). The bottom figures show the associated Peclet numbers, $\mathscr{P}$, for three different swimming velocities ranging from 0.1 to 0.5 mm s^{-1} (using the depth of the bottom mixed layer as the length scale: $h = 49$ m).

maintain a significant particle density. Fig. 4.7 shows the results for the most extreme case where cells with $w = 0.3\,\mathrm{mm\,s^{-1}}$ were aiming for a depth of $h = 49$ m (above the bed). At this depth, the tidal mixing pulses start to significantly carve into the base of the thermocline and the small accumulations of cells that form between the mixing pulses from the ebb and flood flows are periodically eroded into the bottom mixed layer. The swimming velocity of $0.3\mathrm{mm\,s^{-1}}$ appears to be sufficient for the accumulations to recover once the mixing is decreased again, i.e. these cells are able to regain access to the subsurface chlorophyll maximum once eroded into the bottom layer. If the experiment is repeated with a lower swimming velocity, the particles do not only fail to regain the thermocline but the concentrations are much lower than in Fig. 4.7(b). In order to obtain the same high concentrations, the particles would have to aim slightly higher than 49 m where they are more protected from the tidal mixing pulses. This demonstrates the real benefit of being motile in this environment. As can be seen in Fig. 4.8, the faster a cell can swim, the deeper it should be able to maintain its position in the water column. A species with $w = 0.5\,\mathrm{mm\,s^{-1}}$, for example, can out-compete a cell with $w = 0.1\,\mathrm{mm\,s^{-1}}$ by several metres. In a nutrient gradient as sharp as that in Fig. 4.3 this could

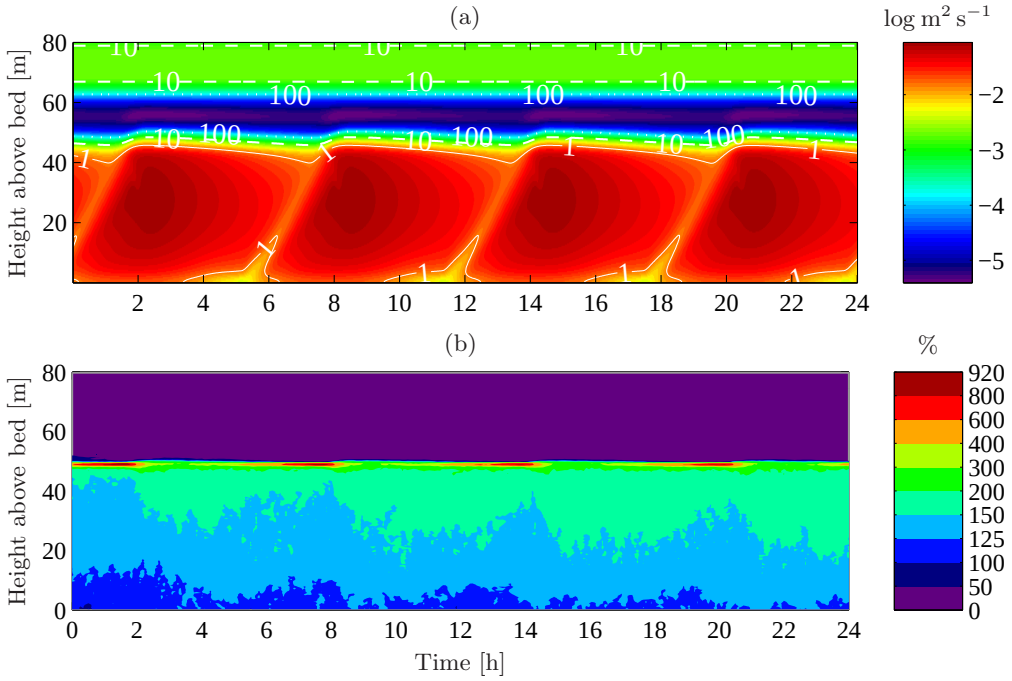

Figure 4.7: (a) Vertical eddy diffusivities during a spring tide. The contours show the Peclet numbers for the swimming velocity $w = 0.3\,\mathrm{mm\,s^{-1}}$ and bottom mixed layer depth $h = 49m$. (b) Particle distribution for cells that are constantly swimming at $w = 0.3\,\mathrm{mm\,s^{-1}}$ towards a depth of $h = 49\,\mathrm{m}$. Initially the cells were uniformly distributed. The picture shows the particle concentrations for the second day of the simulation.

represent a crucial advantage, determining which species is successful in the competition for nutrients.

Having demonstrated that motility provides the cells with a potential competitive advantage in this environment, we can now ask how neutrally buoyant cells would perform under these conditions. Fig. 4.9 shows a comparison between these two different particle species. The neutrally buoyant particles remain uniformly distributed throughout the bottom mixed layer

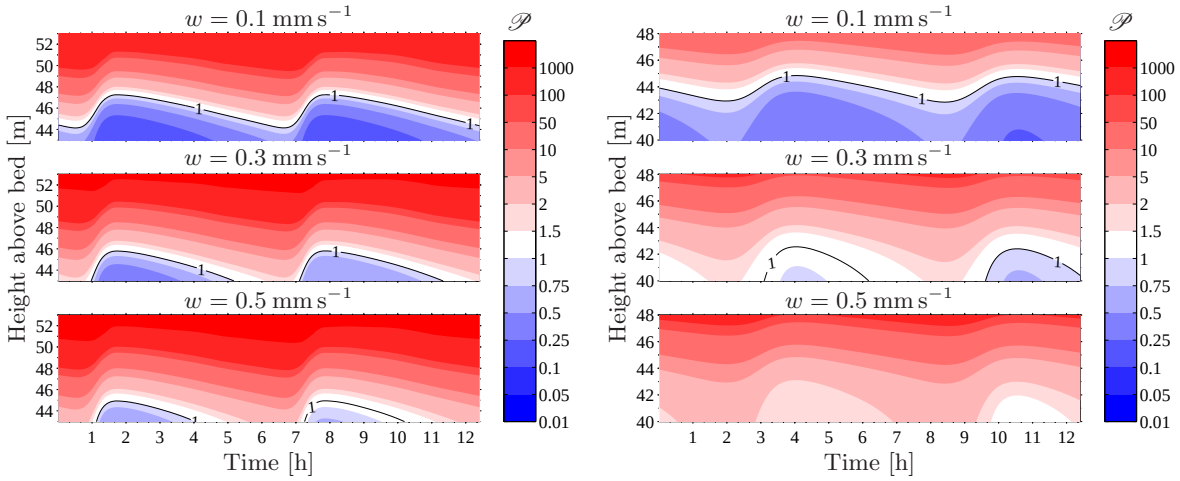

Figure 4.8: Zoomed image of the lower thermocline region from Fig. 4.6 for (a) spring tide and (b) neap tide. Motile phytoplankton can maintain their vertical position in regions where $\mathscr{P} > 1$.

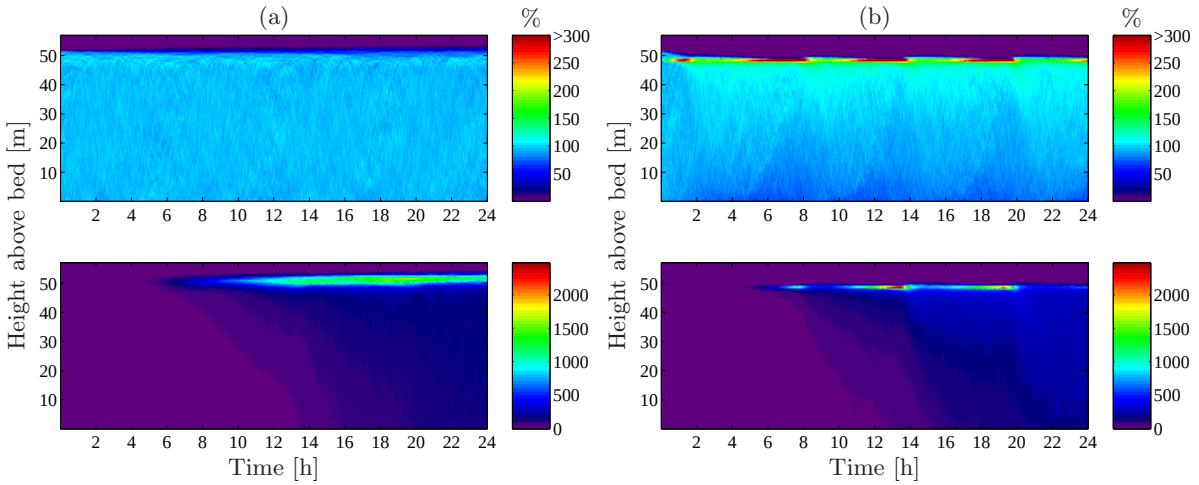

Figure 4.9: For this experiment, the cells were initially uniformly distributed in the bottom mixed layer ($0 \leq z \leq 52$ m). The top part of the water column is devoid of particles and is therefore not shown. The particles in (a) are neutrally buoyant while the particles in (b) swim with $w = 0.3\,\mathrm{mm\,s^{-1}}$ towards $h = 49$ m. The top panels show the actual particle distributions where each particle is given a weight of one. In the bottom panels, the particles are weighted according to their potential production if nutrients are not limiting (arbitrary units).

(top panel). If the particles are weighted according to their production (potential growth), however, then the population is only able to survive at the base of the thermocline above a certain level where the residence times are high enough and they are protected from the tidal mixing. The motile cells are able to achieve comparable production rates about 2-3 m deeper in the water column than their neutrally buoyant competitors. This advantage gained by motility could be crucial in the competition for nutrients, particularly when the thermocline itself might be only 1-5 metres thick. If nutrients were included, the neutrally buoyant cells would soon find themselves above the nutricline and therefore unable to photosynthesise. This will be examined in more detail in a fully dynamic competition experiment between neutrally buoyant and motile cells which will be presented in the next section.

4.4 A Fully Dynamical Springs-Neaps Cycle

The previous section could ascertain the effectiveness of motility in reaching a certain depth in the water column. If the nutrients are limiting, however, as in the surface layer of the environment illustrated in Fig. 4.3, the question remains whether or not the small swimming speeds of the cells are sufficient to facilitate higher growth rates compared to non-motile species. Sharples et al. (2001) observed the motile coccolithophore *Calyptrosphaera oblonga* with cell diameters between 10-15 μm as the dominant species. Since the swimming speed of this particular species is unknown, we can use the empirical relationship from Okubo (1987) which relates the Reynolds number, $\Re$, to the length scale, l, of an organism (cf. Section 1.1.1)

$$\Re = \frac{w\,l}{\nu} = 1.4 \cdot 10^6 \cdot l^{1.86} \tag{4.4}$$

By using a value of $\nu = 10^6\ \mathrm{m^2\,s^{-1}}$ for the kinematic viscosity, one obtains an empirical relationship for the swimming velocity (Mann and Lazier, 1996, p.14)

$$w = 1.4 \cdot l^{0.86} \tag{4.5}$$

Inserting a cell diameter of 15 μm yields an estimate for the swimming velocity for *C. oblonga* of $w = 0.1\ \mathrm{mm\,s^{-1}}$. This is at the lower end of the spectrum for motile phytoplankton and represents thus a good test of whether even small swimming velocities are able to provide the cells with a competitive advantage.

The experiments were initiated with 10 000 motile cells with $w = 0.1\ \mathrm{mm\,s^{-1}}$ and an equal number of neutrally buoyant cells. Both types of cells were initially uniformly distributed in the water column. The primary production is calculated based on the light-nutrient model from Section 4.2.2. As the computations at this level become rather expensive, the experiments are seeded with a high initial biomass, i.e. each model particle is given a high initial carbon weight to represent many real cells. This leads to high initial growth and thus quick nutrient depletion in the SML reducing the number of days needed to reach the limiting situation. In order to further reduce the time required for one experiment, the SML is also initialised with an already reduced nutrient concentration compared to the bottom mixed layer (Fig. 4.10). The nutrient concentration in the SML is still considerably above the half saturation concentration (HSC) of the cells but starting with a lower initial concentration simply means that fewer days are required before the limiting stage is reached. The change in nitrogen in each depth cell is modelled with Eq. (4.2). The neutrally buoyant cells are given almost twice the growth rate of the motile cells (see Table 4.1) to account for the higher doubling rates of diatoms compared to motile species such as dinoflagellates or coccolithophores (Broekhuizen, 1999).

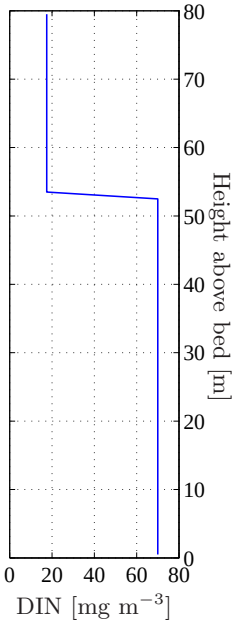

Figure 4.10: Initial nutrient distribution at the beginning of an experiment.

As was discussed in Section 1.5, it is impossible to determine the decision process (if one can speak of such a thing in a single celled organism) which causes a cell to change its swimming direction. Given that this section attempts to examine a nutrient limited scenario, two main swimming strategies have been chosen where the decision about the swimming direction is nutrient-based. The first strategy focuses on the external nutrient concentration alone, and the second strategy is based on the intracellular nutrient levels. In both cases it is assumed, however, that once nutrients are becoming limiting, a cell will instantly 'know' where to find higher concentrations, viz. deeper in the water column, and adjust its swimming direction accordingly. It is impossible to verify how realistic this assumption is because it is unknown whether the cells are able to orient themselves along nutrient gradients or whether they simply encounter higher concentrations 'by chance'. For the latter approach the cells could simply increase their swimming activity (in any direction) once nutrients become limiting and continue in this direction if the conditions become more favourable, otherwise change to a new random direction. It would

cease swimming once sufficient concentrations have been encountered[1]. Clearly, this random approach would be less effective for a cell than the deterministic approach, especially if the cell was far from any significant nutrient gradient. If the small swimming velocity of a cell is to have any effect at all in an environment such as a tidally energetic shelf sea, the assumption has to be made that the cell is indeed capable of orienting itself along some external cues, be they gravity, light or nutrient gradients. Based on these arguments the deterministic approach has been chosen for the following experiments. The next section will explain each strategy in slightly more detail and present the results from the experiments.

4.4.1 Results from a Nutrient Concentration Based Swimming Strategy

By analogy with the arguments from Section 1.5 where it was hypothesised that a cell might use its motility to find higher nutrient concentration rather than to consume them more quickly (by overcoming the diffusion limitation), it will be assumed here that a cell is able to detect that the ambient nutrient concentration is about to become limiting. As outlined above, it is also assumed that the cell is able to follow a deterministic swimming behaviour, i.e. it will be able to know where to find higher nutrient concentrations and swim towards them (which is usually down). If the external nutrient concentration is above a certain threshold, the cell will swim up in order to minimise the light limitation. The external concentration threshold which decides whether the cell swims up or down has been set to the half saturation concentration (HSC) of the cells, i.e. $3\,\mathrm{mg\,N\ m^{-3}}$ (see Table 4.1).

Fig. 4.11 shows the particle and nutrient distribution for this swimming strategy. On the first day, nutrients are not yet limiting and the motile cells begin to accumulate near the surface as

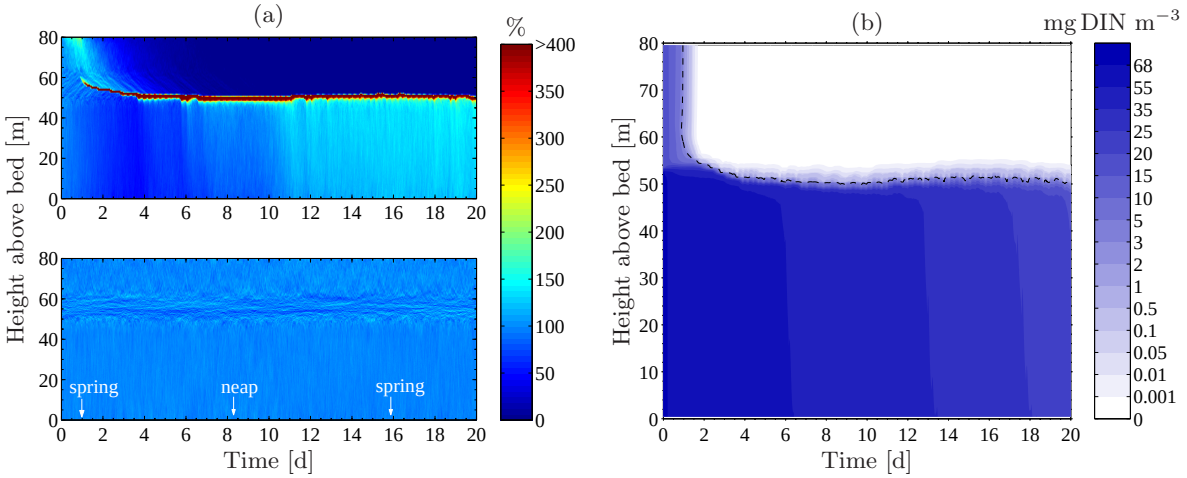

Figure 4.11: (a) Particle concentration for motile (top) and neutrally buoyant particles (bottom). The colour scale has been chosen to cover a range only up to 400% to keep some features visible. The maximum concentration in the top panel is over 5000% (reached on days 4, 5 and 6). Towards the end (day 18) the maximum concentrations has dropped to about 1000%. (b) The nutrient distribution during the experiment. The dashed line shows the location of the half saturation concentration.

[1]This swimming strategy was originally brought forward in connection with the turbulence avoidance hypothesis

they swim up. On the second day, nutrients start to become limiting near the surface and the motile cells in the SML begin their downward migration in pursuit of the HSC. On the fourth day, most of the cells from the bottom mixed layer have arrived at the base of the thermocline where the concentrations reach over 5000%, that is about 35% of all particles are concentrated in the accumulations at the concentration maximum. As time progresses, the nutricline is pushed deeper and the particles follow accordingly. As a consequence, they get closer to the tidal mixing and the number of particles in the concentration maximum decreases as more are drawn into the bottom mixed layer. The depth of the half saturation concentration reaches a maximum at neap tide and shallows slightly again as the tidal velocities increase towards springs. The amplitude of this variation is about 1.5–2 m (see below).

Fig. 4.12 shows the associated production for both particle species. On the first day, nutrients are not limiting and the carbon production is high throughout the SML. Due to photoinhibition of the near-surface cells, the maximum production occurs several metres below the surface. As more and more of the motile cells arrive from the bottom mixed layer at the base of the thermocline, self shading becomes noticeable in the shallowing of the zero-production contour line in Fig. 4.12. Overall, the compensation depth is lower for the non-motile cells due to their higher production rate (Table 4.1).

At the beginning of each day, the zero-production contour reaches all the way to the surface although the nutrients are depleted ($< 10^{-6}$mg N m^{-3}) above 60 m from about day 3 onwards. This is due to the fact that some particles diffuse up from the thermocline at night that have sufficient cellular nutrients for a short growth period as the sun rises. The cellular nutrients become rapidly depleted, however, and the carbon production is short lived. From about day 13 onwards this contour disappears in the top panel because no more motile cells are left in the

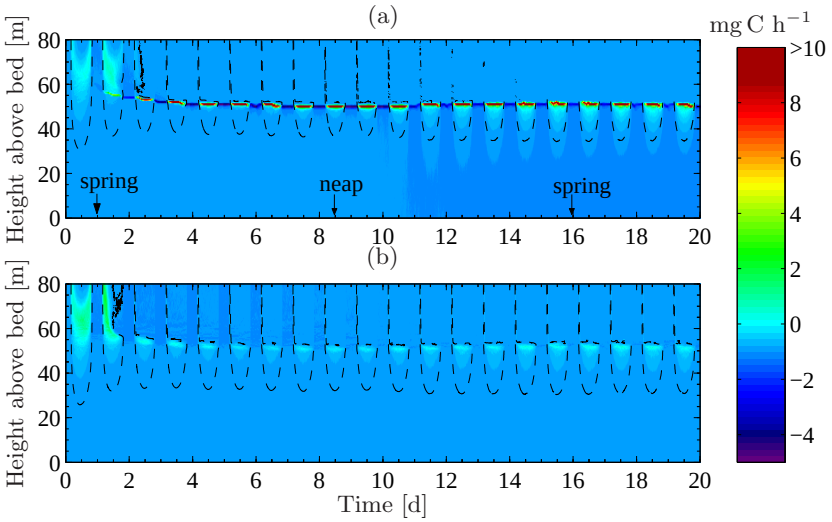

Figure 4.12: Carbon production in each depth bin for (a) motile and (b) neutrally buoyant particles. The instantaneous production values have been scaled from per time step to per hour. The maximum values reached are 24.6 mg C h^{-1} during day 6 and 7 and shortly after neap tide. The dashed line indicates the level of zero production, i.e. the areas within the dashed lines have sufficient nutrients and light to enable positive net growth. The lower part of the curve gives an indication for the compensation depth.

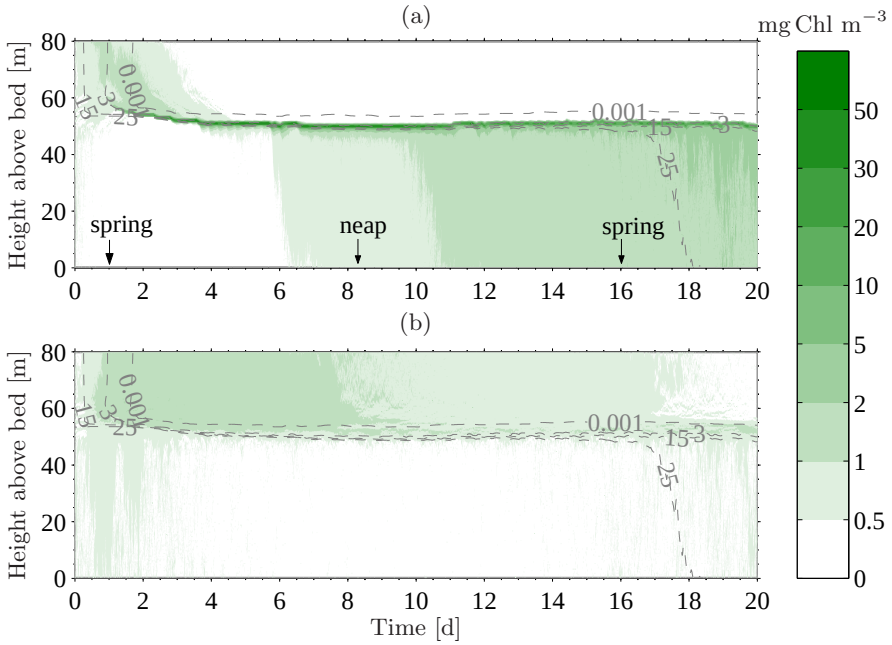

Figure 4.13: Approximate chlorophyll *a* concentration of (a) motile and (b) non-motile cells. This graph has been obtained by assuming a constant carbon to chlorophyll ratio of 50:1 (e.g. Sharples, 1999). Thus the amount of cellular carbon in each depth bin has been divided by 50 to obtain this picture. The dashed lines show the nitrogen contours in [mg DIN m^{-3}].

SML. Towards the second spring tide, the production at the concentration maximum decreases due to the reduced number of cells in each bin.

An estimate of the chlorophyll concentration (Fig. 4.13) shows that the neutrally buoyant cells increase chlorophyll biomass in the SML during the first two days, but as nitrogen becomes limiting the biomass gradually decreases. During neap tide, the amount of chlorophyll in the bottom mixed layer is below 0.5 mg Chl m^{-3}. Towards the second spring tide, the self shading of the motile cells is reduced as more of them are drawn into the bottom mixed layer and the chl concentrations of the non-motile cells begin to increase in the bottom mixed layer while continuing to decrease in the SML. For the motile cells, the biomass is concentrated in a very narrow band of 1m thickness centred around the HSC nutrient isoline. As the nitracline is pushed deeper, more and more cells are drawn into the bottom mixed layer, especially as the currents increase again towards spring tide.

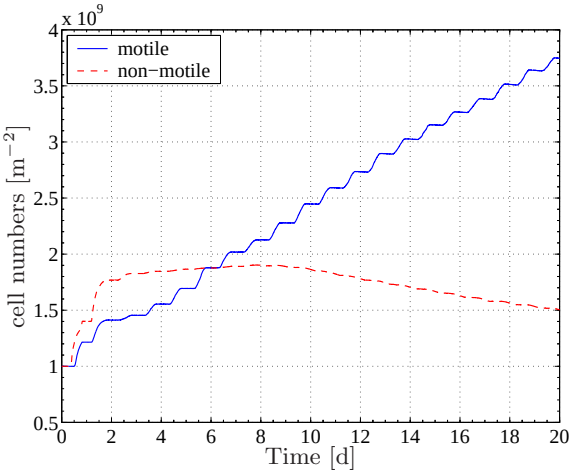

Figure 4.14: Change in total cell numbers for motile and non-motile species.

Overall, the motile cells are performing much better than their neutrally buoyant competitors

and are able to significantly increase their cell numbers (Fig. 4.14). The population growth is not sustainable, however, as the decreasing nitrogen in the bottom mixed layer indicates. This reduction in nitrogen would be less severe if re-cycling of respired and grazed phytoplankton nitrogen were re-introduced to the nutrient pool.

4.4.2 Results from a Nutrient Quota Based Swimming Strategy

This section examines a slightly different swimming strategy in which the choice of the swimming direction is based on the physiological state of the cell. Instead of using the external nutrient concentration as a cue, the decision is now based on the cellular nutrient quota. The cell will always be in an upward mode to minimise light limitation, unless the cellular nutrient pool is starting to become depleted, i.e. it approaches the subsistence quota. In this case the cell will swim down towards higher nutrient concentrations and only swim up again once the cellular nutrient quota is above a certain threshold.

The choice of this threshold is somewhat arbitrary and is based on the assumption that the cell will notice that it is running our of nutrients *before* the subsistence quota is reached. For the following experiments, the threshold has been set to 150% of the minimum subsistence quota for the cell (see Table 4.1). Whenever the cellular nutrient-to-carbon ratio drops below this level, the cell will switch to a downward swimming mode.

Fig. 4.15(a) shows the resulting particle distributions from this swimming strategy. Compared to Fig. 4.11(a), the distribution is more diffuse, only reaching about one fifth of the previous concentration maximum. The concentration in the bottom mixed layer reaches its minimum around neap tide and more particles are drawn down again as the tidal velocities increase. In the SML the minimum is reached around day 12 with an increase noticeable towards day 20.

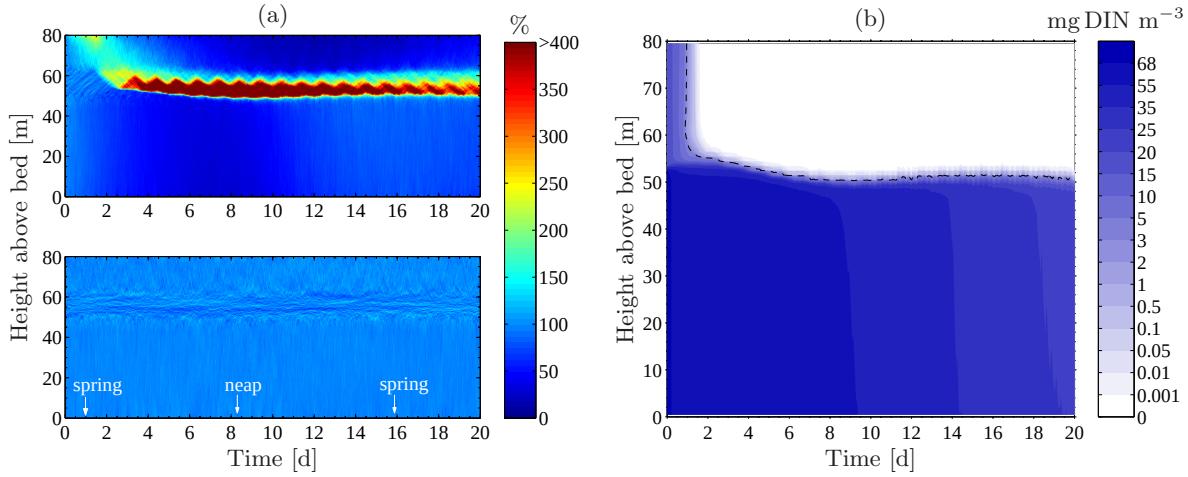

Figure 4.15: (a) Particle concentrations for motile (top) and neutrally buoyant particles (bottom). The colour scale has been chosen to cover a range only up to 400% to keep some features visible. The maximum concentration in the top panel is over 1100% (reached on around day 7). Towards the end (day 18) the maximum concentration has dropped to about 450%. (b) The nutrient distribution during the experiment. The dashed line shows the location of the half saturation concentration.

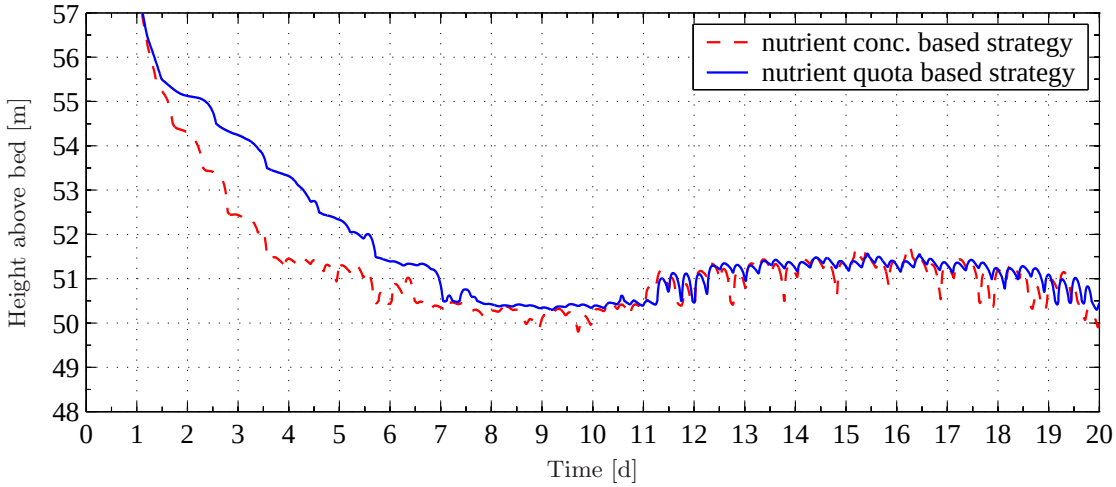

Figure 4.16: Comparing the course of the half saturation concentration contour for both swimming strategies.

Overall the particles stay higher in the water column, however, and therefore less particles become entrained into the bottom mixed layer.

There is also a clear diurnal signal in the particle distribution which points to small periodic vertical migrations of the cells. Due to the small swimming velocities, the amplitudes of these migrations are only about 3-4 m. The cells only take a 'dip' into the nutrient rich layers and then slowly start to ascend towards the light only to run out of nutrients at some point and swim down again. The migrations are linked to the solar cycle and are independent of the tides. The nutrient depletion in the SML occurs in the same amount of time as in the previous experiment [Fig. 4.11(b)]. Initially, the HSC contour line is pushed down more slowly, however, as more particles are higher in the water column. From day 8 until day 20, the HSC contour lines for both swimming strategies are at the same depth. Only occasionally do they diverge as can be seen more clearly in Fig. 4.16. There is also a clear tidal signal visible with the isolines being pushed up periodically by the tidal mixing.

Compared to Fig. 4.12 the production [Fig. 4.17(a)] is spread more across several depth bins which corresponds to the more diffuse particle distribution in general. The value in any one bin is therefore not as high as the maximum reached in Fig. 4.12 which is reflected also in the lower maximum chlorophyll concentration [Fig. 4.17(b)].

Overall, the increase in cell numbers for the motile cells occurs at a similar rate as in the previous experiment (Fig. 4.18). While the growth of the motile cells had somewhat slowed down in Fig. 4.14 from about day 8 onwards, in this scenario, the growth appears to slightly accelerate from this day onwards, resulting in higher biomass at the end of the simulation. The non-motile cells fared less well in this experiment which may be due to increased nutrient uptake by the motile cells and higher shading effects.

Fig. 4.19 shows why the second swimming strategy is slightly more successful. The concentration maximum for the second strategy is broader and also on average about 2-3 m higher in the water column. The cells thus remain more within the thermocline where they are better protected from the bottom turbulence and have a potentially higher light availability. In terms

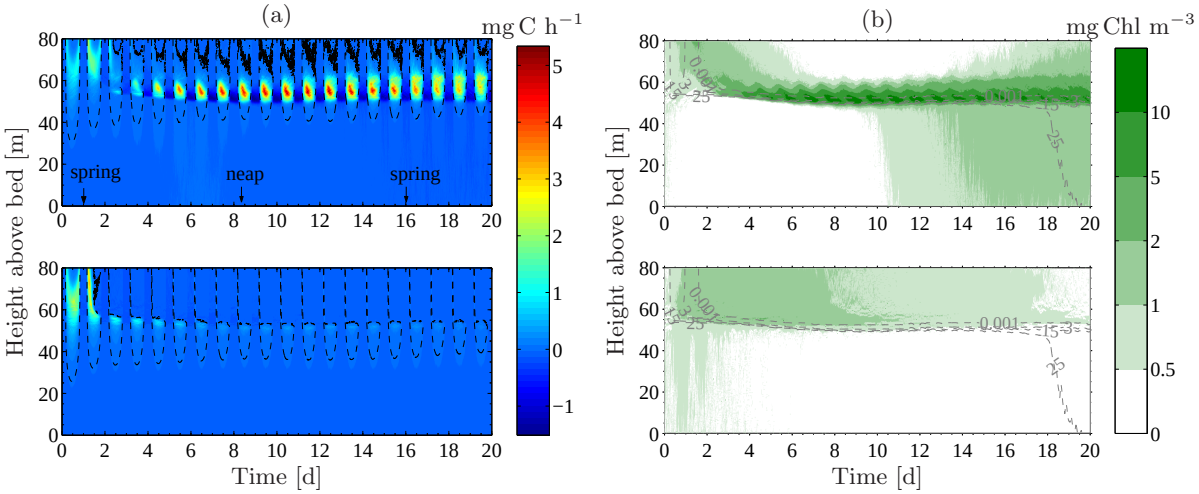

Figure 4.17: (a) Carbon production in each depth bin for motile (top) and neutrally buoyant particles (bottom). The instantaneous production values have been scaled from per time step to per hour. The areas within the dashed line again contain the depth bins which were able to achieve positive net growth. (b) Approximate chlorophyll *a* concentration for motile (top) and non-motile cells (bottom). Again a constant carbon to chlorophyll ratio of 50:1 has been assumed and the amount of cellular carbon in each depth bin has been divided by 50 to obtain this picture. The dashed lines show the nitrogen contours in [mg DIN m^{-3}].

of stability, the concentration maxima from Fig. 4.19(a) remain about 2-4 m below the stability maximum (indicated by the minimum in the diffusivity) for the particular temperature stratification used (Fig. 4.4). Fig. 4.19(b) shows the location of the centre of mass of the model particles and the biomass.

With the nutrient quota based swimming strategy, the centre of mass of the cells remains on average about 10m higher in the water column than for the nutrient concentration based strategy. Towards the end of the experiment, when the HSC isoline is deepening again (see Fig. 4.16) and more of the cells following this isoline are drawn into the bottom mixed layer [Fig. 4.11(a)], the discrepancy between both experiments reaches almost 15 m. If the cells in the previous experiment were following a lower nutrient isoline than the HSC, they would be able to remain slightly higher in the water column and might therefore be able to achieve similar growth rates in the second half of the experiment as the cells in Fig. 4.18.

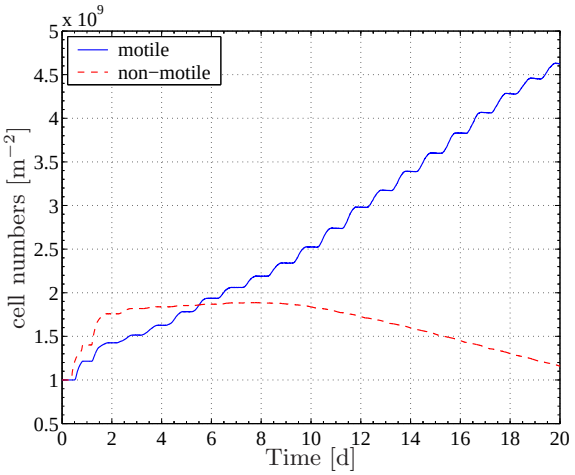

Figure 4.18: Change in total cell numbers for motile and non-motile species.

In summary, it could be shown that even a small swimming velocity of $w = 0.1$ mm s^{-1} is able to provide the cell with a sufficient competitive advantage over neutrally buoyant cells. Despite the much higher growth rate of the non-motile species, the motile cells were able to have a significantly higher production which

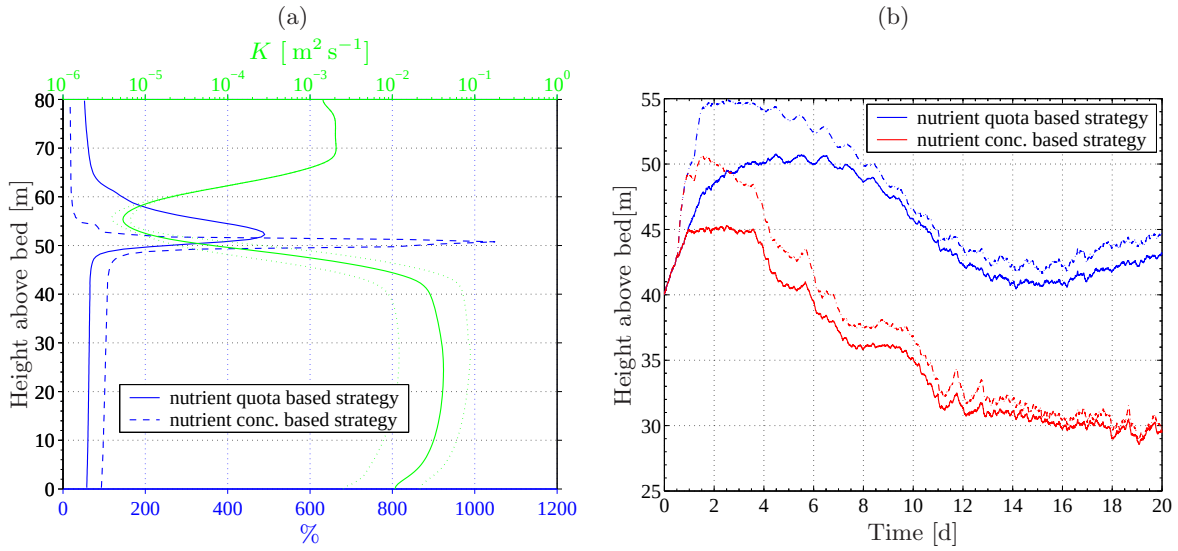

Figure 4.19: (a) Comparing the time averaged particle distribution for the entire 20-day output and both swimming strategies. The green line shows the mean eddy diffusivity over a springs-neaps cycle and the dotted lines give the maximum/minimum at each depth. (b) Depth of the centre of mass for the two swimming strategies. The solid lines represent the model particles and the dash-dotted lines are the centres of the biomass where each model particle is weighted according to the amount of carbon (i.e. the number of real cells) it represents.

resulted in a 4-5 fold increase in cell numbers over the length of the simulation. Non-motile cells only initially showed significant production while the nutrients were not yet limiting. In a nutrient limited situation, the cell numbers decreased in both experiments. If both particle species were given identical growth rates, these differences in production would be even more pronounced.

4.5 Summary and Discussion

In stratified environments, where nutrients are limiting in the SML, observations often show a predominance of motile species such as flagellates and coccolithophores (e.g. Margalef, 1978; Mann and Lazier, 1996; Richardson et al., 2000; Sharples et al., 2001). This chapter therefore examined the use of motility in a stratified but tidally energetic shelf sea environment.

The first question posed at the start of this chapter (Section 4.1) concerned the potential use of motility in regaining access to the SCM after the tidal mixing in the bottom layer has eroded some of the phytoplankton out of the SCM. The results in Section 4.3 could show that moderate to high swimming velocities of $2w \gtrapprox 0.3\,\mathrm{mm\,s^{-1}}$ were required to regain the thermocline sufficiently quickly if the cells are eroded from the SCM (Fig. 4.6 and 4.7). While even small velocities appear sufficient to manoeuver within the thermocline (Fig. 4.6), higher velocities will allow the cells to maintain their positions at greater depths (Fig. 4.8) placing them closer to the nutrient source and thus providing them with exclusive access to the weak nitrate flux across the thermocline ahead of the non-motile or less motile competition. This last point already leads to the second question raised in Section 4.1. Comparisons with neutrally

buoyant particles showed that by having a small to moderate swimming velocity, the motile cells are able to achieve sufficiently long residence times several metres deeper in the water column (Fig. 4.9). As longer residence times equate to higher light availabilities, the motile cells were capable of receiving the same light dose in slightly more turbulent environments which would enable them to outcompete the non-motile cells once nutrients become limiting.

This hypothesis has been tested in Section 4.4 which showed the results from a fully dynamical model that compared the performance of neutrally buoyant and motile cells over a springs-neaps cycle under nutrient limited conditions in the SML. Results for two different swimming strategies have been shown. The first strategy (Section 4.4.1) is based on the external nutrient concentration and the second (Section 4.4.2) on the internal nutrient quota of the cell. Despite the low assumed swimming velocity of $w = 0.1\,\mathrm{mm\,s^{-1}}$, the motile cells performed considerably better with both swimming strategies than their neutrally buoyant competitors. The latter had a 65% higher maximum production rate, but the biomass of the motile cells increased 4-5 fold during the experiments while the biomass of the neutrally buoyant cells started to decline as soon as nutrients became limiting in the SML (Fig. 4.14 and Fig. 4.18). The increase in the motile cell population seemed unaffected by the nutrient limitation and continued throughout the experiments.

A sensitivity analysis showed that these results are essentially unaffected by the initial population size or slightly different swimming strategies (where the cell follows half or one third of the HSC for example) as long as the light intensity at the lower thermocline is sufficient for the cells to have a positive net growth. In one experiment (not shown), the initial population size had been reduced by a factor of ten and thus nutrients became limiting about 2 days later in the SML. The final result remained the same, however, as the cell numbers of motile and non-motile cells had reached a ratio of about 1:4 after 20 days as in Fig. 4.14 and Fig. 4.18. The overall increase was much larger, however, giving a 2700% increase in motile cell numbers after 20 days (compared to only about 400% with the higher initial population size) and a 1000% increase in non-motile cell numbers (compared to only up to 50% before). This latter increase was only due to the prolonged period without nutrient limitation, however, and as soon as the limitation set in, the non-motile cell numbers started to decline.

The change from neap to spring tide proved to be a 'dangerous' time for the motile cells as the increased mixing caused part of the biomass in the SCM to be drawn down into the bottom mixed layer. With their small velocities of $w = 0.1\,\mathrm{mm\,s^{-1}}$ the cells did not manage to recover the previous concentration density (in terms of model particles) by the following neap tide which suggests that these velocities were insufficient to overcome the turbulent mixing in the bottom mixed layer. Nevertheless, the lost cells were replaced by new production and overall the cell numbers continually increased.

Over the course of a springs-neaps cycle, the nutricline also performed small oscillations which are linked to the differences in turbulent intensity between the two tidal extremes (Fig. 4.16). The nitracline was lowest during neaps and highest at springs. It should be noted, however, that the model had not yet reached a steady state during these 20 day simulations, with a

clear transient behaviour superimposed on the springs-neaps variability. If the simulation was kept running for a longer period, the cell numbers are bound to decrease again until a final balance is reached between nutrient consumption and nutrient input at the bottom depth element [Eq. (4.3)]. If the experiment was started with less initial carbon in the water (i.e. each model particle would represent fewer real cells) then the equilibrium state would still be reached but in a slower asymptotic fashion. The population growth shown is not sustainable as the decreasing nitrogen in the bottom mixed layer indicated. Longer model runs with grazing and the inclusion of re-cycled nitrogen would therefore be required to examine the steady state of this system.

The comparison between the two different swimming strategies showed only small differences in the overall production. They yielded almost the same increase in cell numbers but quite dissimilar particle and biomass distributions (Fig. 4.19). The diurnal behaviour in the nutrient quota based strategy (Fig. 4.15(a)) is very interesting, as it provides (in theory) a testable prediction. The similarities between the results from the nutrient concentration based strategy (Fig. 4.13) and the observations by Sharples et al. (2001) (Fig. 4.1) are striking, however, providing a strong argument in favour of this latter approach. It could be hypothesised, that more complex organisms (e.g. animals, humans) would also favour this latter strategy as they might be capable to *predict* that the present environmental conditions will lead to a shortage of food in the near future and therefore move to more favourable environments (e.g. seasonal migrations of birds, whales, etc.). It is difficult to judge, however, how much of this survival instinct is transferable to a single celled organism, especially since the second strategy did in fact lead to a slightly higher increase in cell numbers.

Chapter 5

Turbulent Mixing and Toxic Blooms in a Freshwater Lake

In this chapter the model is applied to the hypertrophic freshwater Lake Nieuwe Meer near Amsterdam in The Netherlands, where the cyanobacterium *Microcystis aeruginosa* forms toxic nuisance-blooms in summer. In an attempt to control these bloom events, the local water management authorities began to artificially mix the lake in 1993 which led to a significant drop in the number of *Microcystis* colonies per unit volume and a shift in the species composition from a cyanobacteria-dominated community in summer to a mixed community of flagellates, green algae and diatoms. *Microcystis* benefits from a positive cell buoyancy which moves them towards the light in stable environments with low mixing, thus providing them with a competitive advantage over negatively buoyant species. The reasoning behind the artificial mixing was thus to eliminate this buoyancy advantage by keeping the turbulence intensity sufficiently high.

Lake Nieuwe Meer represents an almost ideal open air laboratory to which the present model can be applied. The physics is tightly controlled through the artificial mixing system and the biology well known through long term monitoring studies (Visser et al., 1995*b*, 1996; Jungo et al., 2001). With the present model it should thus be possible to not only demonstrate the effect of the artificial mixing on the growth performance of *Microcystis aeruginosa* but also determine the duration and intensity of the artificial mixing required to eliminate the competitive advantage of cell buoyancy and prevent the blooms from occurring. This could lead to considerable energy savings in the operation of the artificial mixing installation.

The following sections will introduce the physical and biological characteristics of Lake Nieuwe Meer, briefly reviewing the available observations and experimental results. The model set-up is discussed in relation to these observations and the results are presented in Sections 5.5 and 5.6. Most of the observational physical data in this section is courtesy of a joint measurement campaign carried out by J. Sharples, C.M. Moore and the present author. The biological data and growth functions are courtesy of Jutta Passarge and Jef Huisman from the University of Amsterdam.

5.1 Introducing Lake Nieuwe Meer

The recreational Lake Nieuwe Meer is situated about 20 km south of Amsterdam in The Netherlands. It forms part of the nutrient-rich Rhine basin and is connected to the canals of Amsterdam. In the recent past, further nutrients have been added to the sediment by dumping dredged sludge from the canals into the lake. As a consequence, the lake is highly eutrophic (hypertrophic). The mean volume of the water body is $18 \cdot 10^6$ m^3 with a mean residence time of 16–32 years (Jungo et al., 2001) and total surface area of 1.3 km^2 (Van der Veer et al., 1995). The lake has a maximum depth of 30.5 m and a mean depth of 18 m (Visser et al., 1995*b*). The mean euphotic depth of the lake is usually less than 5 m with seasonally varying PAR absorption coefficients between 1-2 m^{-1}. In the years prior to the aeration, the water column would stratify in summer and the cyanobacterium *Microcystis aeruginosa* dominate the phytoplankton community, forming large scums with toxin release into the water causing damage to fish and humans.

It has been shown (Köhler, 1992) that *Microcystis* benefits from a stable, stratified water column. This species has gas vacuoles which provide the cells with a positive buoyancy leading to high biomass concentrations near the surface. As a result they are able to meet their own requirements for light while shading their competitors in the water column below. In a deep, artificially mixed lake, *Microcystis* loses this advantage as they are no longer able to influence their vertical position according to their physiological requirements. This has been shown in several previous studies where artificial mixing was able to prevent blooming of *Microcystis* (e.g. Reynolds et al., 1984; Toetz, 1981).

The local water management authorities installed a bubble pump system in 1993 as this was

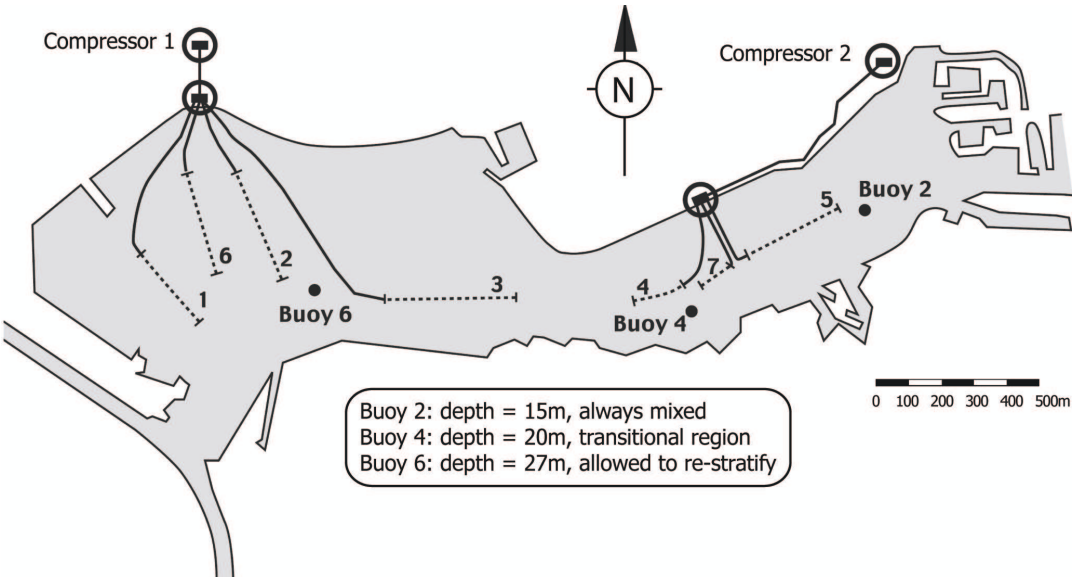

Figure 5.1: Lake Nieuwe Meer near Amsterdam in The Netherlands. The pressurised air is supplied by two compressors and enters the lake along several conduits at the bottom. The dashed parts correspond to the perforated parts along the conduits where the air is released for the mixing. This figure is adapted from Huisman et al. (2004).

considered a better option to control the bloom events on a short term rather than reducing the excess nutrient load. Two compressors provide the pressurised air which is conducted to the lake bottom where it is released through small holes along the conduits (Fig. 5.1). The rising air bubbles lead to enhanced vertical mixing which results in a breakdown of the temperature stratification and a reduced growth of the *Microcystis* population. The phytoplankton community shifts to become more diversified, comprising flagellates, green algae and diatoms (Visser et al., 1996). The pump system was designed to yield a vertical mixing velocity of $0.28\,\mathrm{mm\,s^{-1}}$ to exceed the mean positive buoyant velocity of *Microcystis* of $0.031\,\mathrm{mm\,s^{-1}}$ and approach the maximum flotation velocity of $0.72\,\mathrm{mm\,s^{-1}}$ (Visser et al., 1996). This resulted in a total volume of $13\,\mathrm{m^3\ min^{-1}}$ of air being pumped into the lake.

5.2 Introducing *Microcystis aeruginosa*

The cyanobacterium *Microcystis aeruginosa* is a common inhabitant of many eutrophic freshwater lakes in mid to late summer. The individual cells have average diameters of between 3-5 μm and possess gas vesicles that provide them with positive buoyancy. Like all autotrophs, *Microcystis* produces carbohydrates (mainly glucose) during photosynthesis and consumes them in the absence of light as part of cell respiration. A simple relationship exists for *Microcystis* between the stored amount of intracellular glucose and the cell density and thus its buoyancy (Kromkamp and Mur, 1984; Visser et al., 1997, see below). In a stable water column, *Microcystis* shows a pattern of vertical migration that can be explained by an increase in cell density due to carbohydrate accumulation in the light and a decrease in cell density due to utilisation of carbohydrates in the dark (Visser et al., 1997). This generally results in positive buoyancy during the first part of the day and negative buoyancy in the late afternoon and evening (Ibelings et al., 1991). If the irradiance is optimal for glucose production, the cells might be capable of reversing their buoyancy more than once per day.

Microcystis tends to form large colonies of 1000 cells or more per colony. According to Ibelings et al. (1991), the average colony diameter is of the order of 50 μm while the largest colonies can reach over 200 μm in diameter. As a result, they are able to achieve significant rising velocities of over $0.4\,\mathrm{mm\,s^{-1}}$ for the largest colonies (Jungo et al., 2001).

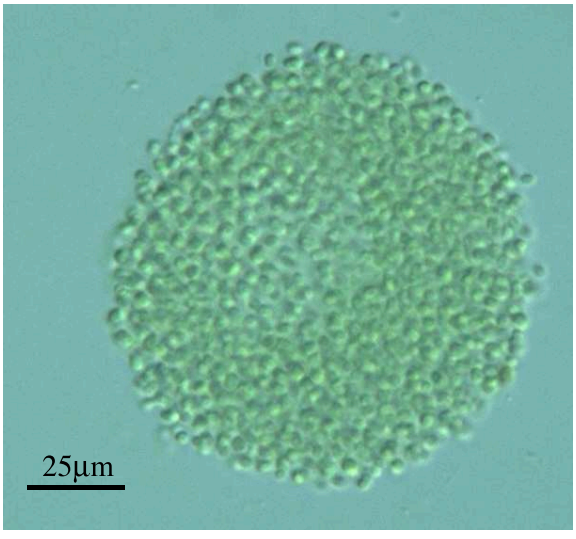

Figure 5.2: A colony of *Microcystis aeruginosa*. Image courtesy J. Passarge, Univ. Amsterdam.

The following model equations are based on unpublished results from batch culture studies of *Microcystis* colonies taken form Lake

TABLE 5.1: Summary of the variables and parameter values used in the cell-specific equations for *Microcystis*.

Symbol	Meaning	Value	Unit
Γ	cellular glucose content		μmol gluc $(10^6\,\text{cells})^{-1}$
Γ_{starve}	min. glucose content	1.5	μmol gluc $(10^6\,\text{cells})^{-1}$
I_{opt}	optimal light intensity	277.5	$\mu\text{E}\,\text{m}^{-2}\,\text{s}^{-1}$
I_c	compensation point	10.94	$\mu\text{E}\,\text{m}^{-2}\,\text{s}^{-1}$
N_0	fit constant Eq. (5.1)	0.0029456	μmol gluc $(10^6\,\text{cells}\ \ \mu\text{E}\,\text{m}^{-2}\,\text{s}^{-1})^{-1}$
c	fit constant Eq. (5.1)	-0.0309776	μmol gluc $(10^6\,\text{cells min})^{-1}$
a_1	fit constant Eq. (5.1)	$-9.52 \cdot 10^{-4}$	min^{-1}
a_2	fit constant Eq. (5.1)	$-4.7 \cdot 10^{-6}$	μmol gluc $(10^6\,\text{cells min})^{-1}$
μ_0	fit constant Eq. (5.2)	0.0206	d^{-1}
s	fit constant Eq. (5.2)	4.20625	10^6 cells $(\text{mmol gluc d})^{-1}$
b_1	fit constant Eq. (5.3)	972.2	$\text{kg}\,\text{m}^{-3}$
b_2	fit constant Eq. (5.3)	0.6848	$10^6\,\text{cells}\ (\mu\text{mol gluc})^{-1}\ \ \text{kg}\,\text{m}^{-3}$
b_3	fit constant Eq. (5.3)	0.0222	$(10^6\,\text{cells}\ (\mu\text{mol gluc})^{-1})^2\ \ \text{kg}\,\text{m}^{-3}$

Nieuwe Meer, and have been obtained through private communication with Jutta Passarge from the University of Amsterdam.

5.2.1 Estimation of Growth Rates

If the incident irradiance is above a certain threshold, the so-called compensation point, I_c, for net glucose production, *Microcystis* are able to increase their intracellular glucose levels. If the irradiance is below this compensation point, the cell will consume more glucose than is produced, leading to a net decrease. Due to the abundance of nutrients in Lake Nieuwe Meer, the primary production can be calculated based solely on the light availability to the cell. The following two equations can be used to calculate the rate of intracellular glucose increase/decrease [μmol gluc $(10^6$ cells min$)^{-1}$] ($R^2 = 0.88$):

$$\text{rate of increase:} \quad \frac{\partial \Gamma}{\partial t} = N_0\, I\, \text{e}^{-\frac{I}{I_{\text{opt}}}} + c \ \text{, if } I > I_c = 10.9\,\mu\text{E}\,\text{m}^{-2}\,\text{s}^{-1} \tag{5.1a}$$

$$\text{rate of decrease:} \quad \frac{\partial \Gamma}{\partial t} = a_1 \Gamma + a_2 \ \text{, if } I \leq I_c = 10.9\,\mu\text{E}\,\text{m}^{-2}\,\text{s}^{-1} \tag{5.1b}$$

They are identical to Eq.(6) and Eq.(7) in Visser et al. (1997) but the values of the fit parameters differ slightly (see Table 5.1). The rate of increase is proportional to the received irradiance I and can be expressed as a simple exponential with a fall-off beyond the optimum irradiance I_{opt}. *Microcystis* shows negligible signs of photo-acclimation (J. Passarge, pers. comm.) but considerable photoinhibition as can be seen in Fig. 5.3(a). If the ambient light intensity is below the compensation point, I_c, the rate of decrease is directly proportional to the intracellular glucose content Γ. This is true even down to very low glucose concentrations of about 1.5 μmol gluc $(10^6$ cells$)^{-1}$ which represents the minimum value obtained in the lab experiments (J. Passarge, pers. comm.).

The specific net growth rate, μ [d^{-1}], is proportional to the net glucose accumulation/depletion

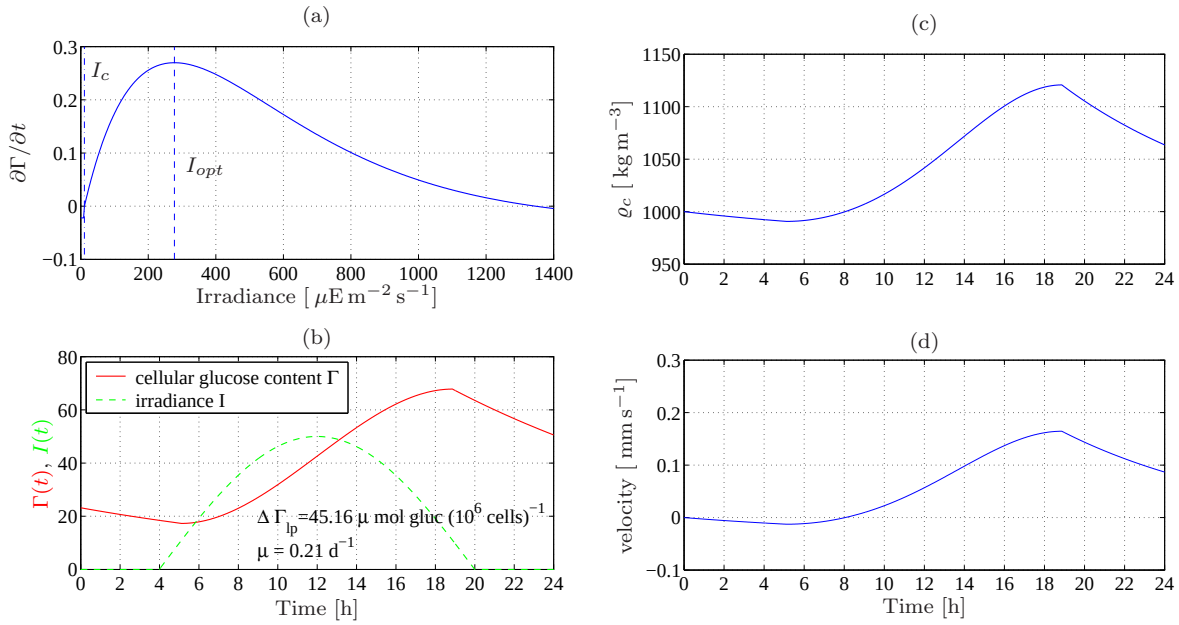

Figure 5.3: (a) Light-dependent rate of glucose change $\partial\Gamma/\partial t$ [μmol gluc $(10^6$ cells min$)^{-1}$] for a range of irradiances. (b) Cellular glucose content $\Gamma(t)$ [μmol glucose $(10^6\,\text{cells})^{-1}$] (solid line) for *Microcystis* cells exposed to the sinusoidal irradiance curve $I(t)$ [μE m^{-2} s^{-1}] (dashed line). The total accumulation of glucose over the light period ($\Delta\Gamma_{\text{lp}}$) and the resulting specific growth (μ) are given for this particular example using Eq. (5.2). (c) Cell density as a result of the change in intracellular glucose from (b), calculated using Eq. (5.3). Initially the cells start with a glucose level that gives them neutral buoyancy. (d) Resulting potential vertical Stokes velocities from Eq. (1.36) for the cell densities from (c) and a colony diameter of $d = 50\,\mu$m.

during the light period, $\Delta\Gamma_{\text{lp}}$ [mmol gluc $(10^6$ cells$)^{-1}$], ($R^2 = 0.94$):

$$\mu = s\Delta\Gamma_{\text{lp}} + \mu_0 \tag{5.2}$$

with the values of the fit parameters listed in Table 5.1. The interplay of Eq. (5.1) and Eq. (5.2) is demonstrated in Fig. 5.3(b) for an example sinusoidal light profile.

5.2.2 Change of Cell Buoyancy

Microcystis cell density, ϱ_c [kg m^{-3}], is a function of the intracellular glucose content Γ [μmol gluc $(10^6$ cells$)^{-1}$] and can be described with the following equation ($R^2 = 0.997$):

$$\varrho_c = b_1 + b_2\,\Gamma + b_3\,\Gamma^2 \tag{5.3}$$

using the empirical constants from Table 5.1. For neutral buoyancy, i.e. $\varrho_c = 1000\,\text{kg m}^{-3}$, the intracellular glucose content is thus $\Gamma_0 = 23.18\,\mu$mol gluc $(10^6$ cells$)^{-1}$. For any cell density, the sink/rise velocity can be determined through the Stokes law [Eq. (1.36)]. Using the above mentioned minimum of $\Gamma_{starve} = 1.5\,\mu$mol gluc $(10^6$ cells$)^{-1}$ and a large colony diameter of $d_c = 200\,\mu$m, we obtain a maximum rising velocity of $w_{max} = 0.58\,\text{mm s}^{-1}$. This value is close to the published maximum velocity of $0.72\,\text{mm s}^{-1}$ from Visser et al. (1995*b*) which is obtained for colony diameters of 220 μm. Fig. 5.3(c) and (d) show the effect of the light profile from Fig. 5.3(b) on the cell density and thus the potential vertical cell velocities.

5.3 Observational Results

The artificial mixing in Lake Nieuwe Meer began in 1993 when the compressors ran continuously from early spring till late summer. Due to the considerable energy costs, first attempts were made in 1994 to operate the compressors intermittently during the spring season. The aeration was turned off and if the weekly monitoring indicated an increase in water column stratification or a shift in species composition, the mixing was turned on again. As a result the energy costs for the artificial mixing could be reduced by 75% in spring or by 27% over the entire year (Visser et al., 1996).

Due to these past experiences, the local water management authorities agreed to conduct an experiment in 2002 and 2003 in Lake Nieuwe Meer. Over the course of the summer of 2002, the mixing was operated intermittently in order to study the transition in species composition from the mixed scenario to the stratified scenario and vice versa. In 2003 only the bubbling system of compressor 1 was periodically switched on and off on a strict fortnightly cycle. During the experiment, the physical, biological and chemical structure of the water column was closely monitored.

The following sections summarise the results from the biological and physical sampling that took place in Lake Nieuwe Meer. The model set-up for the later experiments is based on the key findings outlined in these sections.

5.3.1 Biological Sampling

In terms of biomass, the artificial mixing in Lake Nieuwe Meer significantly reduced the total number of *Microcystis* cells in the water column. Table 5.2 shows the average abundance of *Microcystis* in the pre-mixing year of 1991, the first year of artificial mixing in 1993, and for 1994 when the mixing was intermittent during spring and continuous during summer. The data in the first column show the actual colony counts and is courtesy of Petra Visser, Univ. Amsterdam.

TABLE 5.2: *Microcystis* abundance in Nieuwe Meer.

year	colonies ml^{-1}	cells m^{-3}	mixing
1991	84.5	$84.5 \cdot 10^9$	off
1993	2.6	$2.6 \cdot 10^9$	on
1994	13.5	$13.5 \cdot 10^9$	on/off

The data in the second column are calculated, based on an average cell diamter of *Microcystis* of 4.5 μm, average colony diameter of 50 μm, and assuming 75% efficiency in occupancy of the colony volume by the cells (J. Passarge, pers. comm.) which yields about 1000 cells in a 50 μm colony.

During the first two years of artificial mixing, a significant shift in species composition was observed from an almost mono-specific *Microcystis* community in the years prior to 1993 to a much more diverse community that was dominated by diatoms (mainly *Cyclotella* and *Stephanodiscus*), large green algae (mainly *Scenedesmus sp.* and *Chlorella vulgaris*) and some flagellates (Visser et al., 1996).

5.3.2 Physical Sampling

In 2002 and 2003 a key requirement of the experiments with different mixing regimes was, for the first time, to quantify the turbulent mixing rates in the lake and the development or destruction of vertical stability. In both years moored temperature loggers were used to monitor the vertical temperature profile. The time series in Fig. 5.4 shows the changeover from a mixed to a stratified and back to a mixed water column, in response to the artificial mixing being turned off and on. It also shows clear diurnal signals while the mixing is on which give evidence of surface stratification during the day and re-homogenisation at night due to surface cooling and convective overturning. Weekly deployments of a Self-Contained Autonomous Microstructure Profiler (SCAMP) were used to derive the vertical eddy diffusivities from measurements of temperature micro-structure following the method from Sharples et al. (2001). The SCAMP also delivers the depth dependent distribution of light and chlorophyll fluorescence. It was deployed at fixed stations indicated as buoy 2, buoy 4 and buoy 6 in Fig. 5.1. At each station, 10 consecutive sampling profiles were collected in order to capture the intermittent nature of turbulent mixing. A summary of the profiles for 2002 is provided in Appendix B.

In the summer of 2002, both compressors were used in the experiment, allowing for the entire lake to re-stratify. In 2003, only compressor 1 was turned off periodically while compressor 2 was kept running continuously. Thus only the western part of the lake re-stratified while the eastern part was kept well mixed throughout the summer. This partial stratification effectively created three micro-zones in the lake: a stratified zone at the western end, a mixed zone in the east and a transitional, or frontal zone inbetween. This is illustrated with the example profiles in Fig. 5.5. In Fig. 5.5(a), the western end (Buoy 6) shows strong temperature stratification which is less pronounced at Buoy 4 and absent at Buoy 2. The low turbulent diffusivity clearly reflects the high water column stability that can be inferred from the temperature profiles. The profile taken at Buoy 4, for instance, shows two thermoclines: one between 5-6 m and one around 15 m. At these depths, the diffusivity profile drops to low values of 10^{-5} m^2 s^{-1}. This

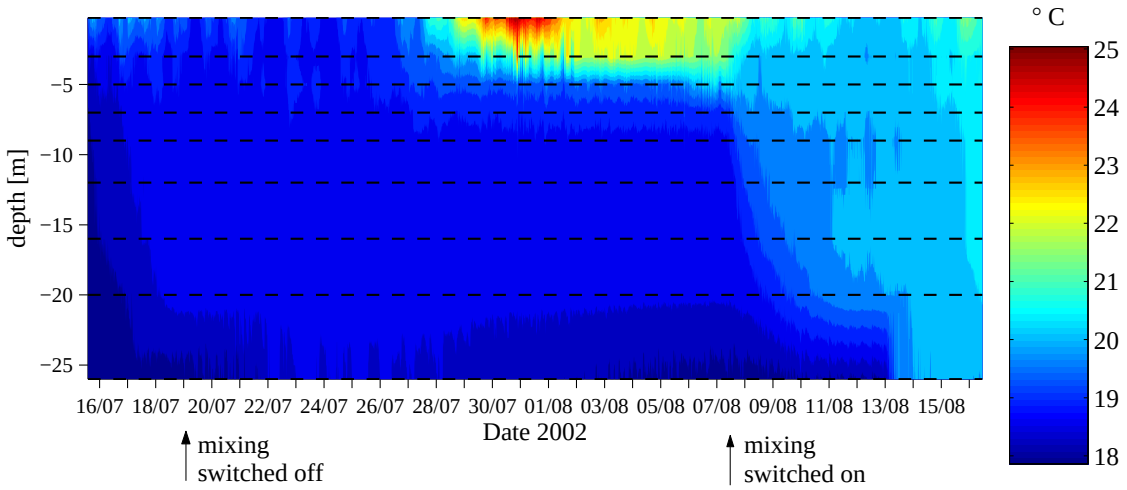

Figure 5.4: Temperature time series from the moored loggers in Nieuwe Meer, slightly North of Buoy 6. The horizontal dashed lines indicate the depths of the loggers.

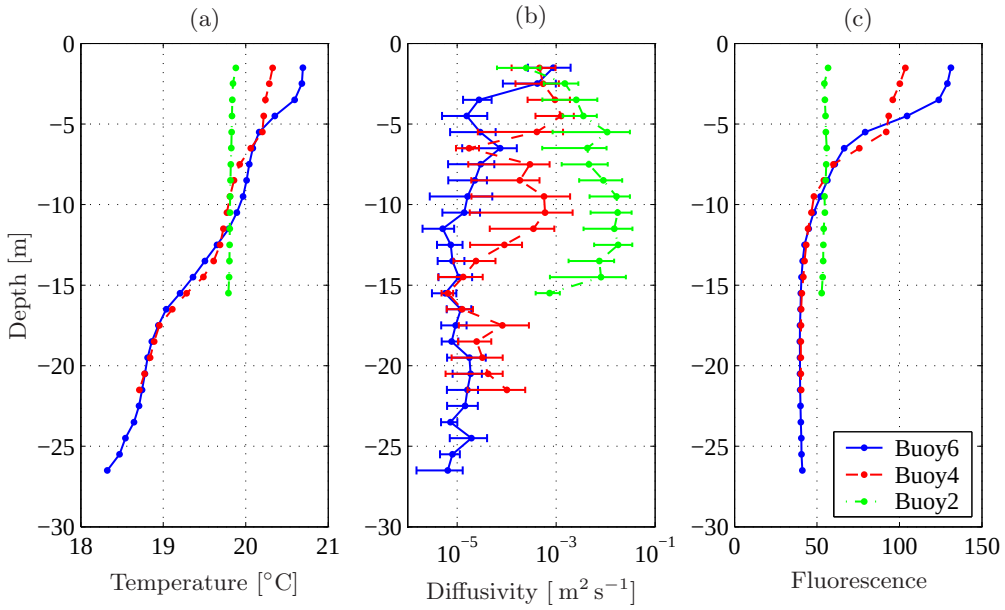

Figure 5.5: Representative profiles from Lake Nieuwe Meer taken on 30 June 2003 at the locations shown in Fig. 5.1. They show the characteristic water column structure at the end of a no-mixing cycle (the mixing had been turned off on 18 June, and back on 3 July). The horizontal bars in the diffusivity profiles represent the 95% confidence limits from the 10 consecutive casts. They serve as a measure for the natural intermittency of turbulence.

can also be seen for the profile of Buoy 2 where a small temperature stratification causes the mixing to decrease in the top 2-3 m. The increased water column stability at Buoys 4 and 6 produced an elevated concentration of phytoplankton in the top 5 m of the water column which can be seen in the fluorescence signal in Fig. 5.5(c). For comparison, in the two years preceding the installation of the artificial mixing, the top-to-bottom temperature difference in mid summer was of the order of 12°-15°C in the deepest part of the lake (Visser et al., 1996).

The 5 m depth roughly corresponds to the 1% light level in Lake Nieuwe Meer. On average, the PAR absorption coefficient during the 2002 campaign measured by SCAMP was about $k_t = 1.25\,\mathrm{m}^{-1}$ (see Appendix B). The aeration conducts are installed 1 m above the lake bed (Jungo et al., 2001) with the intention to prevent resuspension of lake bed sediments. Nevertheless, differences are apparent at Buoy 4 between the mixed and the non-mixed case. When the mixing is on (see Fig. B.5, Fig. B.7 and Fig. B.9), $\overline{k_{tmix}} \approx 1.43\,\mathrm{m}^{-1}$ and if the mixing is turned off (see Fig. B.2 and Fig. B.3) $\overline{k_{tstrat}} \approx 1.18\,\mathrm{m}^{-1}$. At Buoys 2 and 6, the artificial mixing did not seem to have an effect on the turbidity which remained close to the overall average for Buoys 2 and 6 of $\overline{k_t} \approx 1.2\,\mathrm{m}^{-1}$.

From the two year sampling on Lake Nieuwe Meer, the following generalisations can be derived:

- When the mixing is turned on, the temperature stratification disappears within a few days and the turbulent diffusivity is of the order of 10^{-2} - $10^{-1}\,\mathrm{m}^2\,\mathrm{s}^{-1}$ and vertically uniform at all three sampling stations. Only occasionally, on very calm sunny days, a thin temperature stratification at the very surface can be observed which leads to a locally and temporarily reduced mixing near the surface with values dropping to between

10^{-3} - 10^{-2} $m^2\,s^{-1}$. During the night, convective overturning would usually erode this small temperature gradient (Fig. 5.4).

- When both compressors are switched off (2002), the water column can take several days to re-stratify depending on the weather conditions (Fig. 5.4). The diffusivity drops to about 10^{-5} $m^2\,s^{-1}$ and is vertically homogeneous unless there is sufficient wind forcing which can increase the near surface diffusivity values to about 10^{-3} $m^2\,s^{-1}$.

- When only compressor 1 is switched off (2003), the western part of the lake stratifies within several days while the eastern part is kept mixed by compressor 2. The stratification is generally less strong ($\Delta T \approx 3°C$ compared to $\Delta T \approx 7°C$ when both compressors were switched off). The diffusivity still drops to similar values as in 2002 in the stratified area around Buoy 6, i.e. 10^{-5} $m^2\,s^{-1}$. In the intermediate area around Buoy 4, the diffusivity is between 10^{-5} - 10^{-3} $m^2\,s^{-1}$, and stays near 10^{-2} $m^2\,s^{-1}$ in the mixed part near Buoy 2 (unless the surface stratifies).

- Apart from Buoy 4, where the aeration seems to cause some entrainment of bed sediments, the turbidity k_t of the lake is unaffected by the mixing and remained fairly consistently between 1.15 and 1.25 m^{-1} throughout the sampling period.

From these generalisations, a set of diffusivity profiles has been constructed to represent the various mixing scenarios. Together with the results from the biological observations and the cell-specific growth and buoyancy functions from Section 5.2, they form the basis for the model setup.

5.4 Model Setup

The numerical experiments in this chapter are designed to examine the effect of turbulent mixing on the performance of *Microcystis* and answer questions regarding critical mixing thresholds for *Microcystis* which would be able to prevent bloom events (see e.g. Huisman et al., 2004). Instead of using measured diffusivity profiles in the numerical experiments it was therefore decided to use realistic representations of the different observed mixing scenarios discussed in the previous section. The biological setup is dictated by the results of lab culture studies and field observations which have been summarised in Section 5.3.1 and Section 5.2. Table 5.3 provides a summary of the main physical model parameters while the biological parameters

Table 5.3: Parameter values for the Lake Nieuwe Meer model set-up.

Symbol	Meaning	Value	Units
k_m	specific light atten. coef.	0.0340	m^2 $(10^{10}$ cells$)^{-1}$
k_{bg}	background light atten. coef.	1.1	m^{-1}
H	depth (=mean lake depth)	18	m
Δz	vertical resolution for output	0.2	m
Δt	time step for simulations	0.1-5	min

have been summarised in Table 5.1.

5.4.1 Turbulence Profiles

The observations throughout the two-year sampling period showed consistent values of turbulent mixing combined with the natural intermittency that is inherent to turbulence [expressed by the horizontal bars in Fig. 5.5(b)]. It was therefore decided to create several representative profiles to describe the observed conditions in Lake Nieuwe Meer rather than employ a single observational profile. Three main scenarios will be examined:

1. The mixed case, where both compressors are switched on and the mixing is high throughout the lake. The mixing is only reduced locally if the surface becomes stratified during the day due to solar heating.

2. The stratified case, where both or only one of the compressors are turned off. This results in generally very low mixing in the part of the lake that is unmixed. Higher mixing is observed near the surface if the wind speed is sufficiently high.

3. The intermediate case occurs around buoy 4 when only compressor 2 is switched off, as was the case in 2003. The mixing is intermediate and both a reduction or increase towards the surface are possible depending on the weather conditions.

Each of these three scenarios is accounted for with a set of profiles (Fig. 5.6). The sets consist of a generic profile where the mixing is homogeneous with depth and one or two subvariants to account for possible weather influences. The natural intermittency of turbulence is incorporated into the model through a randomly chosen profile from within the bounds given in each of the panels from Fig. 5.6. A varying constant is added to or subtracted from the particular profile, the sign and magnitude of which is chosen randomly from a centre weighted distribution. The shape of the profile and the derivative are thus preserved. This approach was chosen mainly due to practical reasons as it speeds up the simulation process since the cubic spline would otherwise have to be re-evaluated after each change of the profile.

The time step is chosen depending on the profile. For the generic stratified scenario, for example, where turbulent displacements are small, a time step of five minutes was sufficient. In the mixed case, or if the diffusivity varied with depth, a smaller time step of $\Delta t = 6\,\mathrm{s}$ was applied.

5.4.2 Turbidity and Self-Shading

During the two-year sampling campaign, the measured PAR absorption in Lake Nieuwe Meer during summer was between 1.1-1.4 m^{-1}. Studies of lab cultures of *Microcystis aeruginosa* (Huisman et al., 1999) yielded a cell-specific light absorption coefficient of

$$k_m = 0.0340\,\mathrm{m}^2(10^{10}\mathrm{cells})^{-1} \tag{5.4}$$

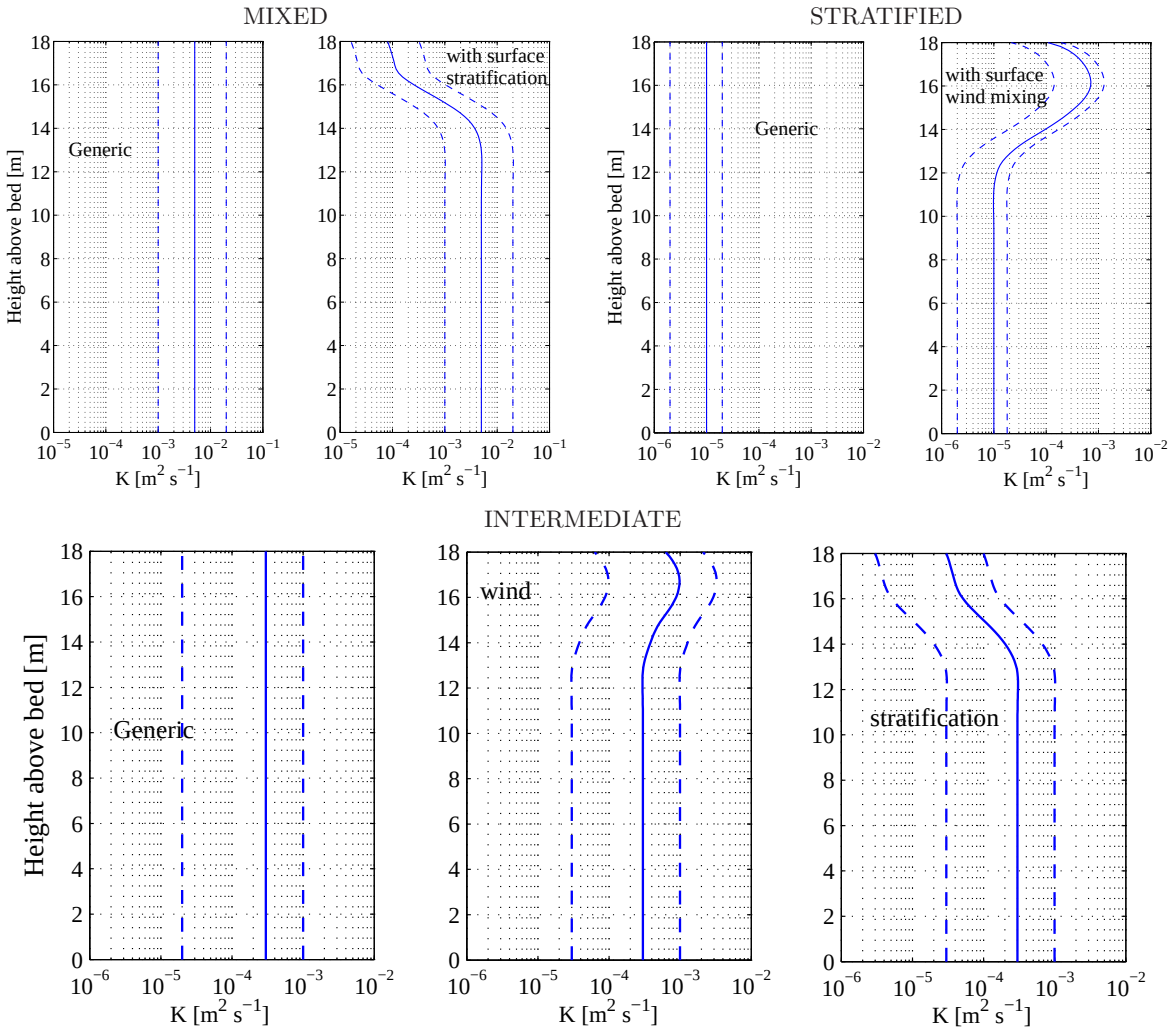

Figure 5.6: The turbulence profiles used for the numerical simulations of the three different scenarios: mixed, stratified and intermediate. Each scenario has one generic profile where the diffusivity is constant with depth. External forces due to wind or surface stratification are accounted for with different profiles. The dashed lines represent the bounds up to which the profile is allowed to deviate from the mean.

Based on the cell counts from Table 5.2, a value of $1.1\,\mathrm{m}^{-1}$ has therefore been chosen to represent the background turbidity, due to non-*Microcystis* organisms and other suspended particles. The contribution of *Microcystis* to the turbidity is then calculated from the cell-specific absorption rate from Eq. (5.4) and added to this background turbidity. At any particular depth, $\tilde{z}$, the total absorption coefficient of the above water column is thus

$$k(\tilde{z}) = k_{bg} + k_m \frac{\xi\, N(\tilde{z})}{(H - \tilde{z})\,1\,\mathrm{m}^2} \tag{5.5}$$

where $N(\tilde{z})$ is the number of particles above $\tilde{z}$ (note that $z = 0$ at the bed and $z = H$ at the surface). In some experiments, different particles will represent different colony sizes and thus cell numbers. In these cases the total biomass, i.e. the number of cells represented by each model particle is used in Eq. (5.5). ξ is a scaling factor that accounts for the fact that there are only 20 000 particles in the model compared to about $1.5 \cdot 10^{12}$ cells m^{-2} in the pre-mixing years and about $1.45 \cdot 10^{11}$ cells m^{-2} after 1993 (Table 5.2). The number of model particles has thus to be scaled up in order to obtain representative values for the self-shading. The light

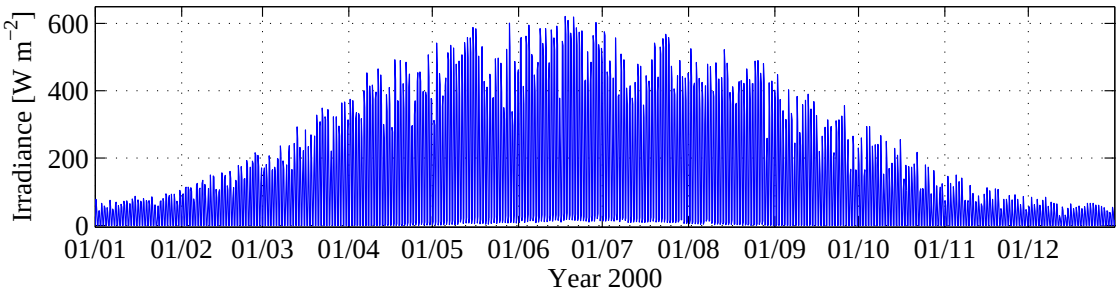

Figure 5.7: Representative year for the irradiance data from the NCEP/NCAR 40-year Reanalysis Project for the co-ordinates (5°E, 52.5°N) from http://www.cdc.noaa.gov/ (see Kalnay et al., 1996). The data consist of 6 h averages for the period from 1 January 1993 to 31 December 2003.

intensity at a particular depth $\tilde{z}$ is then calculated from the Beer-Lambert equation:

$$I(\tilde{z}) = I_0 \, \exp\left[-k(\tilde{z})(H - \tilde{z})\right] . \tag{5.6}$$

Fig. 5.7 shows that the maximum irradiance at the latitude of Lake Nieuwe Meer is of the order of 615 W m^{-2}. As the data are averaged over 6 h periods, this maximum represents the average irradiance between either 06:00 h to 12:00 h or 12:00 h ro 18:00 h. Assuming a semi-sinusoidal variation and a maximum day length of 16.5 h the noon maximum can be estimated as $I_{0\,max} \approx 750$ W m^{-2}. In the experiments, both I_0 and the length of the light period have been varied to examine the performance of *Microcystis* in different seasons.

5.4.3 The Biological Setup

The biological equations in the model follow those described in Section 5.2 and Section 5.3.1. At the beginning of each experiment, the particles are randomly distributed throughout the water column and are given enough glucose to make them neutrally buoyant. Each model particle represents initially one real colony. If the colony diameter would become too large, the colony is split into two equal halves. The colony size increases with the specific growth [Eq. (5.2)]:

$$d_{n+1} = d_n \, \sqrt[3]{(1+\mu)} \tag{5.7}$$

Due to cell division, the average cellular glucose content is reduced by

$$\Gamma_{n+1} = \frac{\Gamma_n}{1+\mu} \tag{5.8}$$

The cells are not allowed to fall below the starvation threshold of $\Gamma_{starve} = 1.5\,\mu$mol gluc $(10^6$ cells$)^{-1}$. No negative growth or losses due to grazing have been incorporated. In some experiments the colony diameter is initially uniform for all particles, in others, the diameters are chosen from a random Poisson-shaped distribution such that the mean of the distribution coincides with the observed mean colony diameter of $\overline{d_c} = 50\,\mu$m (Ibelings et al., 1991) (Fig. 5.8).

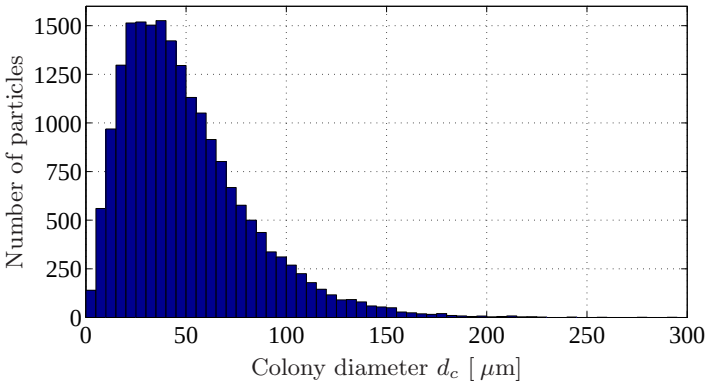

Figure 5.8: Random Poisson-shaped distribution of colony diameters assigned to the 20 000 model particles. For this figure the diameters have been binned into 5 μm intervals and the mean of the distribution is $\overline{d_c} = 50$ μm.

5.5 Model Results – Individuals

Due to the various feedbacks between the biological model equations, it appears advisable to examine the performance of individual cells before considering the ensemble averages. This will yield a better understanding of the underlying processes and elucidate the behaviour of the system.

5.5.1 Performance Without Mixing

In this section, the biological equations are applied to a number of particles without turbulence. That is, the particle trajectories are calculated solely based on their buoyancy, without any random component. This is intended to show the behaviour of the undisturbed system. A similar study has been carried out (Visser et al., 1997) to which the present results will be compared.

The Effect of Colony Size

The colony size affects the system through the Stokes equation [Eq. (1.36)]. The larger the colony, the larger its potential vertical velocity for the same glucose content. For certain colony diameters, stable migratory modes appear in which the cells perform periodic vertical migrations that are synchronised with the daily irradiance cycle. The values of the colony diameters for which these stable modes appear, depend on the day length, i.e. the number of hours of daylight, and also on the supplied irradiance itself (see below) which affects the compensation depth. For a

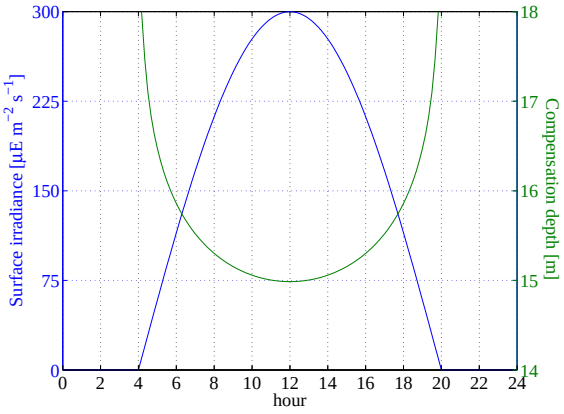

Figure 5.9: Light profile with corresponding compensation depth for the experiments in Fig. 5.10.

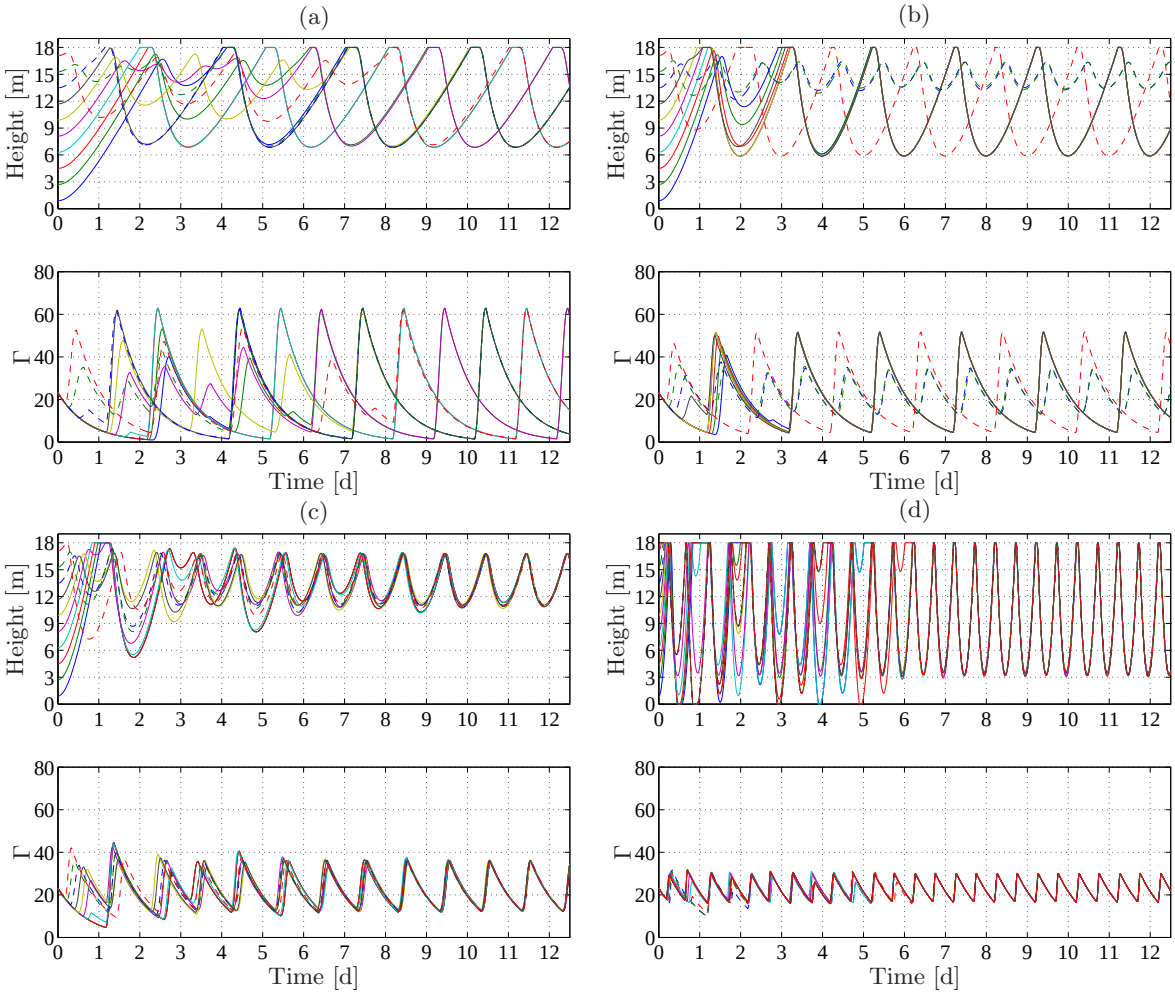

Figure 5.10: Example of 10 different particle trajectories (top panels) and corresponding glucose content Γ [μmol gluc $(10^6$ cells$)^{-1}$] (lower panels). (a) For a colony diameter of 79 μm one stable mode appears with a period of 3 days. The vertical velocities reached (not shown) are between -0.2 and 0.3 mm s^{-1}. (b) For a colony diameter of 112 μm, a different mode with period 2 days appears and at the same time, those particles that were initially only a few metres below the surface, occupy the diurnal mode. The vertical velocities for these sizes are between -0.2 and 0.5 mm s^{-1} for the cell in the 2-day mode and between -0.1 to 0.2 mm s^{-1} for the cells in the diurnal mode. (c) and (d) show the trajectories for particles with $d_c = 150\,\mu$m and $d_c = 470\,\mu$m respectively. The vertical velocities are (c) -0.2 to 0.4 mm s^{-1}and (d) -1.25 to 1.5 mm s^{-1}.

given day length, a certain colony diameter will provide the cells with the 'right' velocity so their vertical oscillations are in resonance with the daily irradiance curve leading to stable repeated trajectories of consistently large amplitudes. Fig. 5.10 shows four examples for the semi-sinusoidal light curve from Fig. 5.9. In Fig. 5.10(a), the colony diameter is $d_{c1} = 79\,\mu$m. Due to the absence of light (the compensation depth is always above 15 m) the deeper particles consume glucose, become positively buoyant and rise to the surface. The particles close to the surface start to produce glucose after sun rise, become more negatively buoyant and start to sink. After a transitional period of about 1 week, all cells follow a stable trajectory with a 3-day period. Fig. 5.10(b) shows the same picture but for a colony size of $d_{c2} = 112\,\mu$m (note that $2d_{c1}^2 = d_{c2}^2$). Here most of the particles occupy a trajectory with a 2-day period. Only the particles that were initially about 3-5 m below the surface occupy a diurnal migratory

mode. If the colony size is further increased, the particles in the 2-day mode will reach the surface earlier, i.e. more towards the beginning of the dark period, and linger there until the irradiance increases again. The 2-day mode trajectories thus exhibit flat tops. As the diameters reach about 150 μm all cells follow a stable diurnal mode [Fig. 5.10(c)]. Within the range $150 \lessapprox d_c \lessapprox 450\,\mu$m, the size of the colony only affects the depth of the migrations but not the period. The larger a colony within this range, the deeper the migrations. Only for extremely large colonies that have $d_c \gtrapprox 450\,\mu$m would it be possible to perform stable semi-diurnal migrations, where they surface twice per day [Fig. 5.10(d)].

For all intermediate colony diameters, the pattern is very chaotic as the vertical velocities in relation to the irradiance do not provide the cells with a rhythm that is in resonance with the diurnal cycle. This is illustrated in Fig. 5.11 which shows the results for the mean colony diameter of 50 μm. For colony diameters less than d_{c1} the results are less clear. A 4-day mode can be observed, but the transitional period becomes much longer as the initial conditions become more important for the slower vertical velocities. Hence those particles whose initial depth happens to be right, will fall into the 4-day mode rather quickly, but others take much longer. Clearly, the slow swimmers will also be disturbed more in their rhythm, once the turbulent mixing is included (Section 5.5.2).

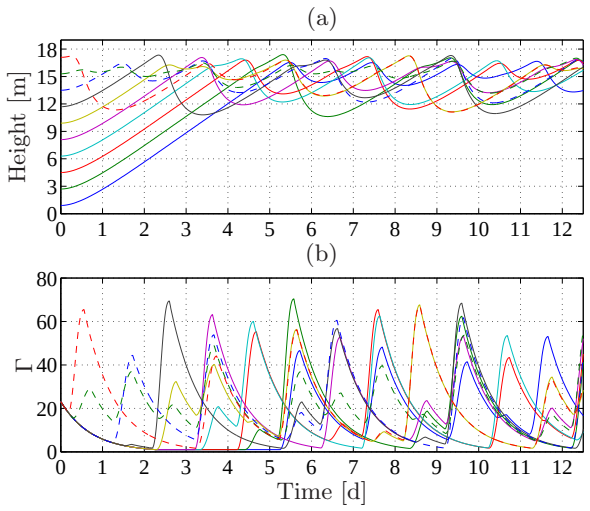

Figure 5.11: (a) Particle trajectories for 10 colonies with $d_c = 50\,\mu$m. (b) Cellular glucose content Γ [μmol gluc $(10^6$ cells$)^{-1}$].

These results already demonstrate one difficulty with the specific growth function for *Microcystis* from Eq. (5.2). This equation is only valid if the net glucose accumulation during the light period is positive since only positive values for $\Delta\Gamma_{\mathrm{lp}}$ have been measured and went into its derivation (J. Passarge, pers. comm.). Only the very large colonies with $d_c \gtrapprox 150\,\mu$m were able to perform diurnal migrations in the above examples. Medium to large sized colonies will perform migrations which can leave them below the compensation depth for more than 24 h, i.e. over an entire light period which results in a negative $\Delta\Gamma_{\mathrm{lp}}$. Eq. (5.2) is not valid for such conditions. This issue will be discussed again in Section 5.6 when the ensemble results will be presented.

Effect of the Irradiance Curve

The light period provides the colonies with a predefined frequency to which they can resonate if they possess the correct vertical velocities (i.e. diameter). In the absence of any periodicity, i.e. under a constant irradiance, the cell trajectories behave similar to dampened harmonic oscillators in that the amplitudes decrease with time (not shown). However, the analogy is not

complete as the frequency of the cell oscillations is not constant but increases with time. A change in the light period from 16 h, to 14 h or 12 h for example, did not affect the diameters for which stable trajectories are obtained as the cells leave the photic zone before midday and do not resurface until after sunset.

The maximum light intensity (i.e. the amplitude of the semi-sinusoid in Fig. 5.9), on the other hand, greatly influences the values for the above colony diameters as it affects the compensation depth of the cells. If I_0 is increased, the amplitudes of the migrations increase and the necessary velocities (and therefore colony diameters) required to perform these deeper migrations have to increase as well. If the light maximum is doubled, for example, the colony diameter which provides the cells with the required velocities to perform the stable 3-day oscillations from Fig. 5.10(a) is $\tilde{d}_{c1} = 88\,\mu$m. The trajectories reach down to 3 m height above the bed and the observed velocities are within the range of $-0.1 \lessapprox w \lessapprox 0.5\,\mathrm{mm\,s^{-1}}$. The stable diurnal mode appears already for diameters $d_c \approx 170\,\mu$m. The trajectories are much shallower than in Fig. 5.10(d), however, only reaching to about 9 m above the lake bed. They also do not reach the surface but start to reverse at about 16 m. The higher irradiance has thus considerably decreased the amplitude of the oscillations which means that smaller colonies are now able to achieve the required velocities.

If the experiments are repeated with an irradiance maximum of $I_0 = 1000\,\mu\mathrm{E\,m^{-2}\,s^{-1}}$ as in Visser et al. (1997), the required diameter to reproduce the modes in Fig. 5.10(a) becomes $100\,\mu$m while the minimum diameter for the first stable diurnal mode remains at about $170\,\mu$m. In Visser et al. (1997) these values are slightly different but due to the unknown attenuation coefficient used, a more detailed comparison of the results is not possible.

5.5.2 Performance With Mixing

The previous section could be considered as a rather artificial exercise as turbulence is never completely absent in the real world. Nevertheless, it provides some insight into the behaviour of the system without any disturbing influences. Clearly, turbulence is a disturbing influence to the cells as the artificial mixing in Lake Nieuwe Meer was able to prevent *Microcystis* blooms. This section therefore examines to what degree turbulence affects the migratory rhythm of *Microcystis* and whether there is a critical turbulent intensity for the cells.

Prior to any experimental analysis it already appears obvious that colonies with different sizes will be affected differently by the turbulent mixing. While small colonies have low vertical velocities and are thus easily disrupted by turbulence, larger colonies quickly (w increases $\propto d_c^3$) become capable of velocities that could allow them to maintain their migratory rhythm if the mixing is low as in a stratified lake environment. In the previous chapters, the Peclet number has proven itself to be a useful measure for gauging particle swimming success in the presence of turbulence. Fig. 5.12 shows the Peclet numbers for different colony diameters and eddy diffusivities. This graph is representative only of the extreme velocities reached under conditions of maximum depletion/accumulation of cellular glucose. For all intermediate stages, the velocities and therefore the Peclet numbers will be lower than in Fig. 5.12. This graph

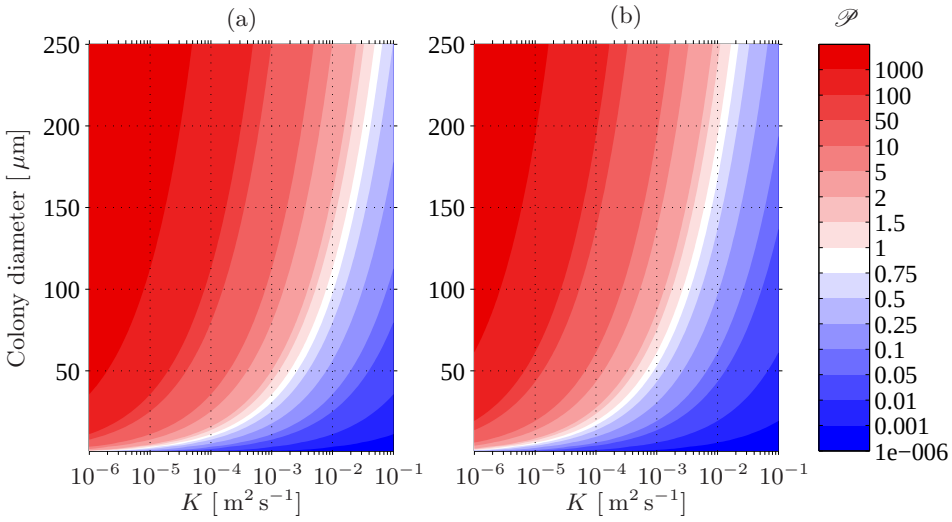

Figure 5.12: Peclet number using the colony diameter as a proxy for the maximum obtainable sinking velocity (a) and the maximum possible rising velocity (b). The extreme velocities are based on the maximum/minimum cell density from Visser et al. (1997) and J. Passarge (pers. comm.). The mixed layer depth for this graph is 18 m.

can thus be used to gauge whether a particular colony, that has been deprived of light and whose cellular glucose is at the starvation threshold, will be able float to the surface (and vice versa). For the average colony diameter of $\overline{d}_c = 50\,\mu$m, it can be seen that the Peclet number for the maximum rising velocity drops below unity for diffusivities $K \gtrapprox 7 \cdot 10^{-4}\,\mathrm{m^2\,s^{-1}}$. This suggests that colonies of this size will not only be unable to perform their vertical migrations but also struggle to reach the surface if they are in desperate need of light. The value for this critical turbulent intensity increases with colony diameter. For $K \approx 10^{-2}$, which corresponds to the turbulent intensity reached in Lake Nieuwe Meer when the artificial mixing is turned on (see Fig. 5.5), it appears that even the largest colonies will be struggling to overcome the turbulence.

Fig. 5.13 shows the effect of turbulence on the particle trajectories. In a weakly mixed environment where the turbulent intensity is similar to a stratified lake environment (see Fig. 5.5), the particles are able to perform vertical migrations on very distinct and deterministic trajectories that only show a small degree of jittering produced by the turbulent mixing [Fig. 5.13(a)]. Turbulence disrupts the resonance effect which was present in Fig. 5.10(a) and the trajectories are more individualistic. If the diffusivity is increased to intensities representative of the artificially mixed Lake Nieuwe Meer, the picture becomes very chaotic without any discernible coherent trajectories [Fig. 5.13(b)].

Investigation of the variabilities in the cellular glucose in the stratified and mixed cases highlights a problem with the equation used for cell growth [Eq. (5.2)]. In the mixed scenario, the peaks in the glucose content are generally lower, but most cells show a positive net glucose increase over the light period [Fig. 5.13(b), lower panel]. In the stratified case, the cells can have a strong increase on one day and a decrease for the following 1-2 days [Fig. 5.13(a), lower panel]. Although the increase in the mixed case is less, it occurs daily which is reflected in the mini-ensemble averages in Fig. 5.14. On average, the specific growth function from Eq. (5.2)

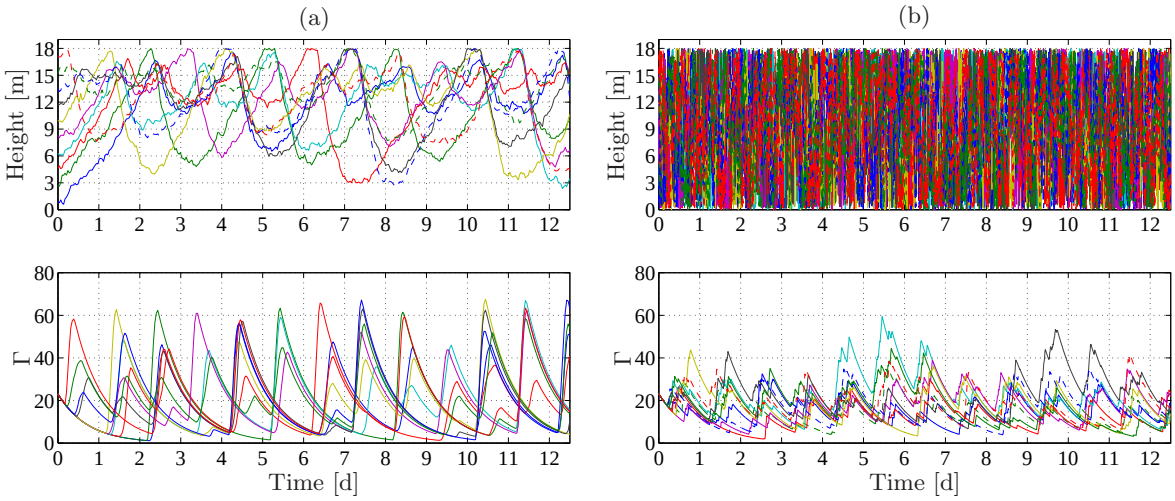

Figure 5.13: Corresponding figures of the particle trajectories (top panels) and glucose content Γ [μmol gluc $(10^6$ cells$)^{-1}$] (lower panels) to Fig. 5.10(a) ($d_c = 79\,\mu$m) showing the effect of turbulent mixing. In (a) the eddy diffusivity was held constant at $K = 10^{-5}\,\mathrm{m^2\,s^{-1}}$ representing the generic stratified scenario from Fig. 5.6. In (b) the diffusivity has been $K = 10^{-2}\,\mathrm{m^2\,s^{-1}}$ and is thus representative of the generic mixed scenario. While the time step was 6 s the data are plotted only every 5 minutes to reduce the file size.

would therefore yield similar rates for the specific growth for both the mixed and stratified scenario[1]. The observations in Lake Nieuwe Meer clearly show, however, that this cannot be correct. It also seems unlikely that a cell which increases its glucose by a certain amount from starvation level should have the same probability of cell division as a second cell that shows the same positive glucose increase but from a much higher initial base. In the first case, the cell will still be low in glucose despite the increase, whereas the second cell now has high glucose reserves. According to the growth function from Eq. (5.2), these two individuals would have the same capabilities of cell division, i.e. specific growth. This appears paradoxical as a cell that is struggling to stay above the starvation threshold should be much less likely to divide than a cell that is at a more comfortable glucose concentration. Although these results are based on one example with only 10 particles and one colony diameter, the next section will show that they are still valid if the ensemble average of 20 000 colonies of varying size is

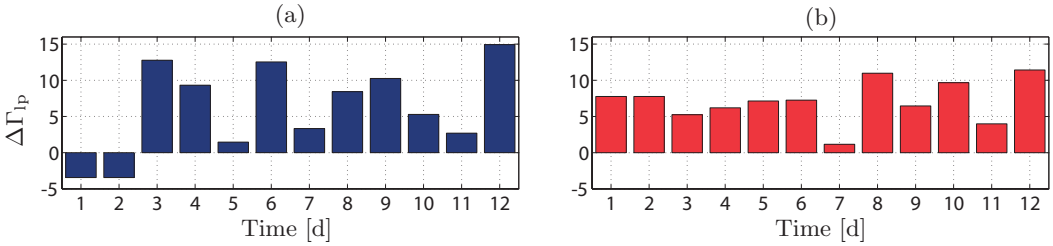

Figure 5.14: Average change of glucose, $\Delta\Gamma_{\mathrm{lp}}$ [μmol gluc $(10^6$ cells$)^{-1}$], during the light period for (a) the stratified and (b) the mixed scenario from Fig. 5.13. On average, and by neglecting the first two days which are transients, the overall growth rate using Eq. (5.2) becomes about equal in both scenarios.

[1] If the maximum irradiance is increased from $I_0 = 300\,\mu\mathrm{E\,m^{-2}\,s^{-1}}$ (which was used in Fig. 5.13) to $1000\,\mu\mathrm{E\,m^{-2}\,s^{-1}}$ which is more representative of summer conditions in Lake Nieuwe Meer, this becomes even more pronounced as the growth rates would then be significantly higher in the mixed than in the stratified scenario.

examined. A different condition for cell division will therefore be formulated which is based on the cellular glucose content rather than on the daily increase.

5.6 Model Results – The Lagrangian Ensemble

The previous section provided some insights into the performance of individual cells under varying environmental conditions. This will facilitate a better understanding of the results presented in this section which will focus on the performance of the Lagrangian ensemble. Due to the difficulties encountered with the specific growth equation [Eq. (5.2)], two sets of results will be presented. The first set uses the empirical Eq. (5.2) to calculate the increase in cell numbers and the second approach uses an alternative formulation that is based on the cellular glucose content (see below).

Both sets of experiments are initialised with the random Poisson-shaped distribution of colony diameters from Fig. 5.8. The irradiance maximum is set to 600 W m^{-2} ($\approx$ 1100 μE m^{-2} s^{-1} PAR) to represent summer conditions in Lake Nieuwe Meer (cf. Fig. 5.7). The maximum compensation depth at midday is therefore between 3.5-4.2 m below the surface, depending on the biomass.

5.6.1 Results Using Eq. (5.2)

It has been shown in the previous section that, while the ensemble of particles may always show a net increase in glucose during the light period (Fig. 5.14), individual cells clearly can experience a net decrease in Γ (Fig. 5.13). Since Eq. (5.2) is only defined for positive growth, however, the effect of negative growth, i.e. the cell mortality, is unknown. Due to this lack of empirical data, any cell mortality formulation would be necessarily arbitrary. Instead, and especially since any such formulation would be identical for both the mixed and stratified scenarios, the decision was taken to focus on the potential for growth rather than actual changes in biomass. The cell diameter and glucose content of the cell are therefore left unaffected by a negative $\Delta\Gamma_{\mathrm{lp}}$ and the model only measures positive growth.

Fig. 5.15 shows the first set of results for the generic stratified scenario from Fig. 5.6. After a transitional period of 3-4 days, most particles become concentrated in a band below the surface. The cells accumulate sufficient amounts of glucose already during the early hours of the morning to render the near surface layers almost devoid of particles for several hours either side of midday. Only the very small colonies whose vertical velocities are too small, will linger near the surface. The average glucose content is therefore very high as can be seen in Fig. 5.15(c). Γ had to be constrained in the model to remain $\Gamma \leq \Gamma_{max} = 56\,\mu$mol gluc ($10^6$ cells)$^{-1}$ as these small colonies would otherwise keep accumulating glucose up to unrealistically high concentrations. The choice of Γ_{max} was based on the published maximum density for *Microcystis* of $\varrho_{max} = 1080\,\mathrm{kg\,m^{-3}}$ (Visser et al., 1997). The biomass distribution [Fig. 5.15(d)] significantly differs from the actual particle distribution. The larger colonies represent a much

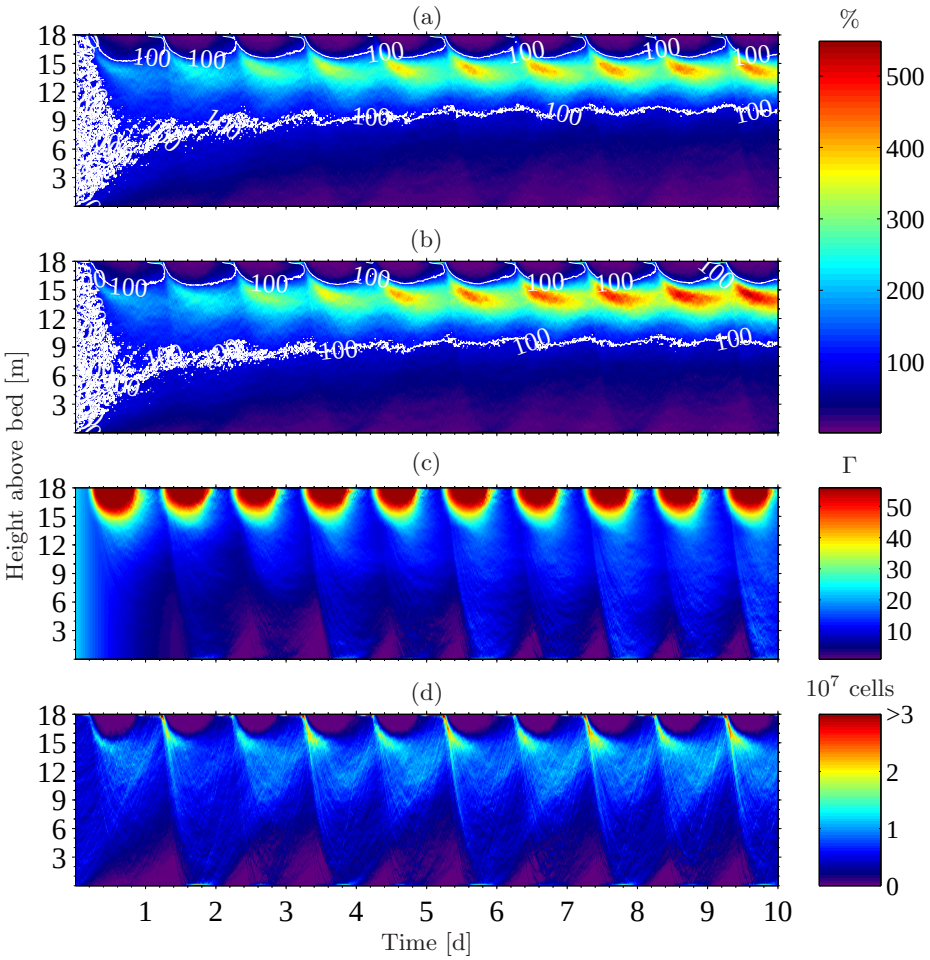

Figure 5.15: Model output for the generic stratified scenario and Eq. (5.2). (a) shows the model particle distribution where each particle is given a weight of one. In (b), the particles are weighted according to how much they have grown. The scale is in percent of the original mean concentration, i.e. for 20 000 particles. (c) shows the average glucose content in each depth bin. The amount of glucose is limited to 56 μmol gluc $(10^6$ cells$)^{-1}$ (see text). (d) shows the distribution of biomass, i.e. each model particle from (a) has been converted to the actual number of cells it represents depending on the colony diameter.

larger biomass than the smaller ones and the distribution in Fig. 5.15(d) therefore mainly shows the location and movements of these large colonies.

Fig. 5.16 shows the same results for the generic mixed scenario. Due to the high mixing, the particles remain homogeneously distributed throughout the experiment. In the weighted particle distributions [Fig. 5.16(b)] a slight increase is noticeable over the course of the simulation. The glucose concentration is more homogeneous compared to Fig. 5.15(c) and shows a clear diurnal signal which extends to the lake bed.

In terms of light availability, the particles in the stratified scenario receive less light than in the mixed case [Fig. 5.17(a) and (b)]. While the daily availability in the latter follows the semi-sinusoidal course of the daily irradiance curve, in the former the maximum availability occurs near 08:00 h and decreases during the rest of the light period as the surface becomes almost devoid of particles. In the mixed scenario, the high turbulence prevents the cells from

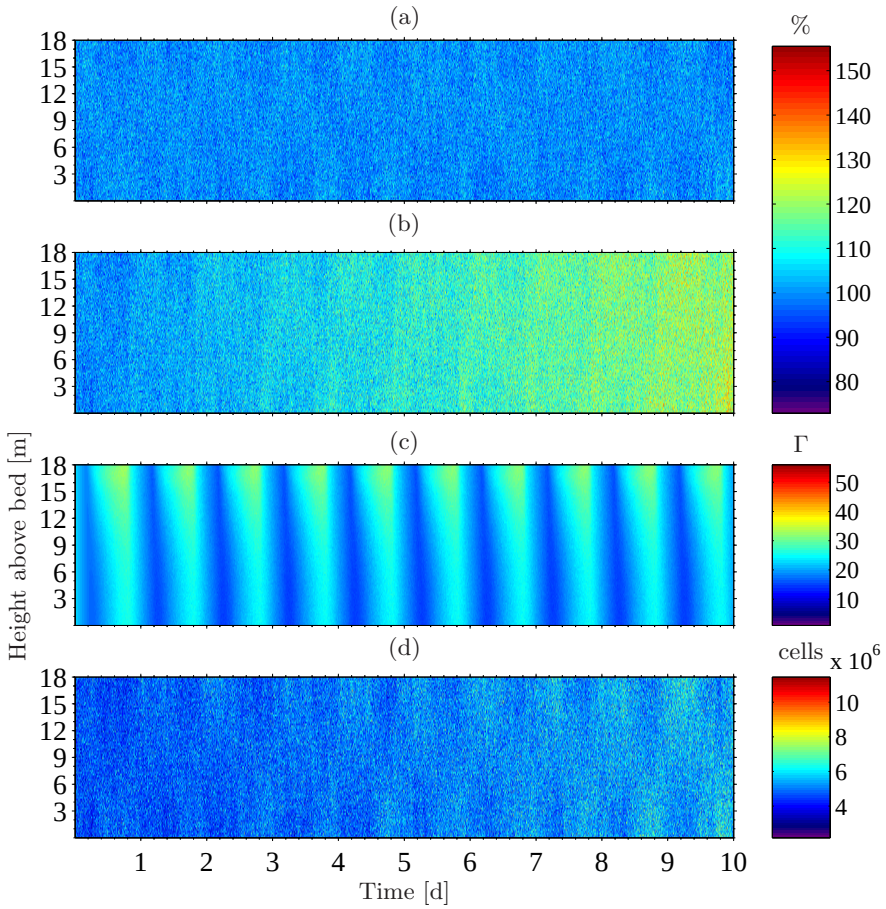

Figure 5.16: Corresponding model output for the generic mixed scenario. See caption of Fig. 5.15 for a description.

descending as their density increases and thus leads to this higher light availability. In terms of growth [Fig. 5.17(c)], the cell numbers in both scenarios increase at the same rate. The step-

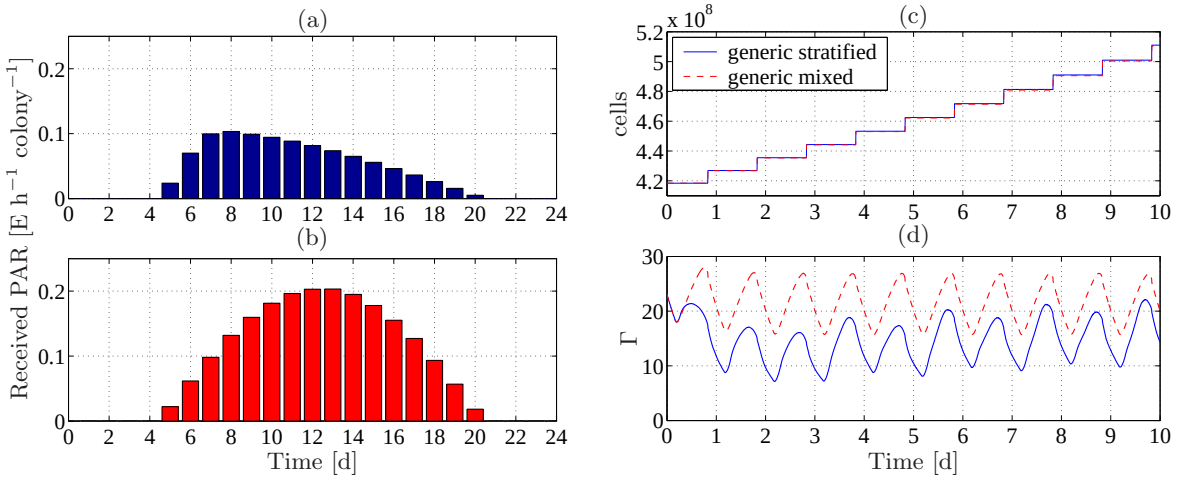

Figure 5.17: Integrated hourly light availability of the cells in (a) the stratified and (b) the mixed scenario. (c) Increase in cell numbers (biomass) for the two scenarios. (d) Course of the average cellular glucose content, Γ [μmol gluc $(10^6$ cells$)^{-1}$].

like function is a result of the implementation of the growth function. The model determines Γ at the beginning and the end of the light period. At sunset, the growth is calculated and applied at the same time to each colony. The mean glucose content [Fig. 5.17(d)] follows a diurnal cycle and is on average higher in the mixed than in the stratified scenario.

Both scenarios thus exhibit the same increase in biomass which is clearly unrealistic as observations show a decrease in *Microcystis* cell numbers if the artificial mixing is operating in Lake Nieuwe Meer. This is a result of the ensemble effect of the growth equation problem highlighted at the end of Section 5.5.2.

5.6.2 Results Using a Different Growth Formulation

A different growth parameterisation has therefore been formulated. It is based on the same approach that was applied in the previous chapters where the specific growth was based on the cellular carbon, or in this case the cellular glucose content, rather than the net glucose increase over the light period. In this modified model, all cells within a colony divide if the average glucose content in the colony exceeds Γ_{max} (again, corresponding to the maximum observed density for *Microcystis*). The new colony radius then becomes

$$d_c^{n+1} = d_c^n \cdot \sqrt[3]{2} \tag{5.9}$$

and the glucose content of the daughter cells is set to half the original value of the mother cell. As a result, the colony will change from being at its maximum negative buoyancy to be only slightly negatively buoyant. The number of divisions a cell can perform is limited to a maximum of one per day as the small colonies which are 'trapped' in the high irradiance layers near the surface would otherwise perform 2-3 divisions per day which is too high for *Microcystis* (J. Passarge, pers. comm.).

For this growth formulation, the particle distributions in the stratified scenario [Fig. 5.18(a)] look very similar to those in Fig. 5.15(a) (note the different colour scale). The plot of the weighted particle distributions in Fig. 5.18(b) already suggests that the increase in cell numbers for this growth formulation will be substantially higher than with the previous model which is also confirmed by the plot of the biomass in Fig. 5.18(d). The mean glucose concentration [Fig. 5.18(c)] in each depth bin also seems the same for this growth model as in the previous section. In the early hours of the morning, the pattern looks slightly more patchy near the surface compared to Fig. 5.15(c) as this is the time when most cell divisions take place and the glucose contents of these new cells is halved. Apart from a slightly higher increase in the particle numbers, the results for the mixed scenario [Fig. 5.18(e) to (h)] are very similar to those shown in Fig. 5.16.

Fig. 5.19(a) shows how the stratified scenario now exhibits a 2.5-fold increase in biomass which is considerably higher than with the previous growth model [Fig. 5.17(a)]. The increase in the mixed scenario is only slight in comparison. The average glucose content is still lower in the stratified scenario but the curve shows a distinct increase towards the end of the simulation period which indicates that it might at some point reach the levels of the mixed case. The real

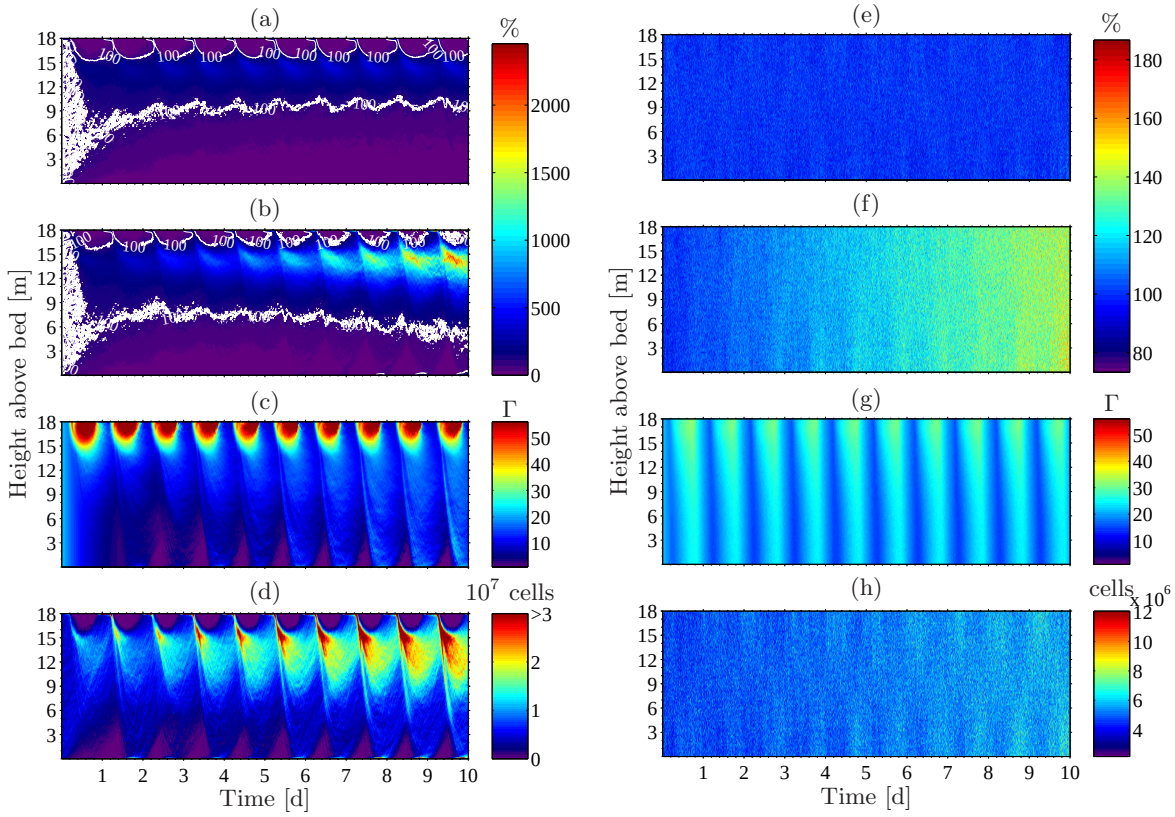

Figure 5.18: Model output with the different growth formulation for the stratified (a)-(d) and mixed (e)-(h) scenarios. The meaning of each panel is identical to Fig. 5.15.

growth rate can be seen in Fig. 5.19(c) which shows the hypothetical increase in model particles due to cell division[2]. The initial 20 000 particles have increased to over 87 000 in the stratified and about 28 000 in the mixed case. These represent average growth rates of $\overline{\mu}_s = 0.16$ d^{-1}

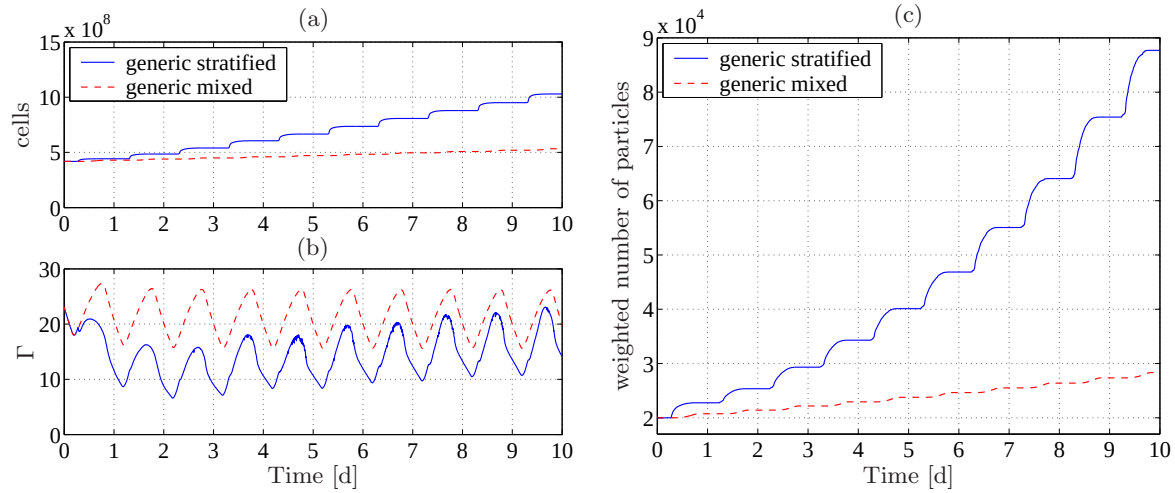

Figure 5.19: (a) Increase in total biomass (cell numbers) for both scenarios. (b) Cellular glucose content Γ [μmol gluc (10^6 cells)$^{-1}$]. (c) Increase in model particles due to cell division.

[2]Note that the number of model particles does not increase but only the weight of each particle, i.e. whenever the colony represented by the model particle reaches Γ_{max} and divides, the weight of this model particle is doubled. The increase in the weight thus shows the true net growth rate.

and $\overline{\mu}_m = 0.035\ \mathrm{d}^{-1}$ in the stratified and mixed case respectively. The relative increase in the particle weight (by a factor 4.4 and 1.4 for the stratified and mixed case) is thus higher than the increase in biomass [factors 2.45 and 1.27 resp., see Fig. 5.19(a)] which indicates that most of the cell divisions occur in the small colonies that are unable to regulate their vertical position as effectively as the larger assemblages. As a result, the distribution of colony diameters has shifted from the original Poisson-shaped distribution to a more even distribution with a higher mean diameter of over 70 μm (Fig. 5.20). The present model entirely neglects grazing which mainly affects the smaller colonies as the larger ones become increasingly difficult to ingest for zooplankton. In the real lake environment, the heavier losses of the smaller colonies might therefore be able to compensate for their higher growth rates and keep the mean diameter near the original value of 50 μm.

From these results the impression might arise that the lower the mixing, the better *Microcystis* might perform. As a comparison of all seven scenarios from Fig. 5.6 reveals, this is by no means the case [Fig. 5.21(a)]. The generic intermediate scenario with a vertical diffusivity of $K = 3 \cdot 10^{-4}\ \mathrm{m^2\,s^{-1}}$ shows a higher increase in biomass than the generic stratified scenario which has $K = 10^{-5}\,\mathrm{m^2\,s^{-1}}$. The best overall performance is achieved in the stratified scenario that shows higher turbulence near the surface due to wind mixing. Even in the mixed scenario a high increase in biomass can be achieved if the surface is more stable due to temperature stratification. Clearly, in the real world none of these scenarios will persist for any length of time, e.g. the mixed surface-stratified scenario will only occur during a few hours on calm and sunny days and the stratification will break down at night due to convective overturning. On average, the increase in biomass in the mixed scenario will therefore still be much less than in the stratified scenario which alternates between stable stratification on calm days to higher surface turbulence on windy days. In the experiments, the choice was made to keep the scenarios constant throughout the 10-day simulation period in order to be able to clearly identify the differences in performance between each scenario.

The dependence of the biomass increase on the turbulent mixing is shown in Fig. 5.21(b). It appears that the productivity increases up to a certain turbulence threshold above which production sharply declines. Clearly, the magnitude of this cut-off is strongly dependent on

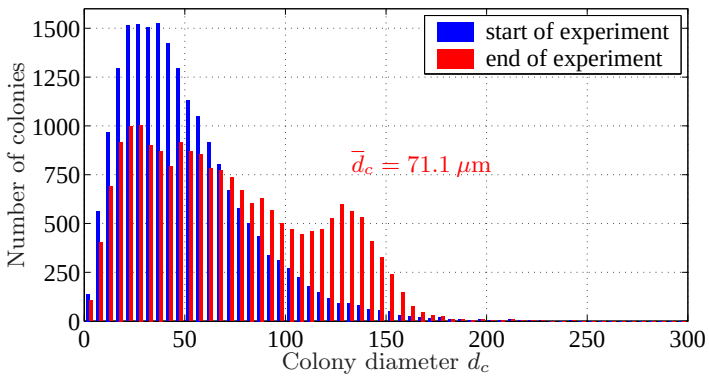

Figure 5.20: Comparison of the distribution of colony diameters at the beginning and the end of the experiment for the stratified scenario. The bin size is 5 μm.

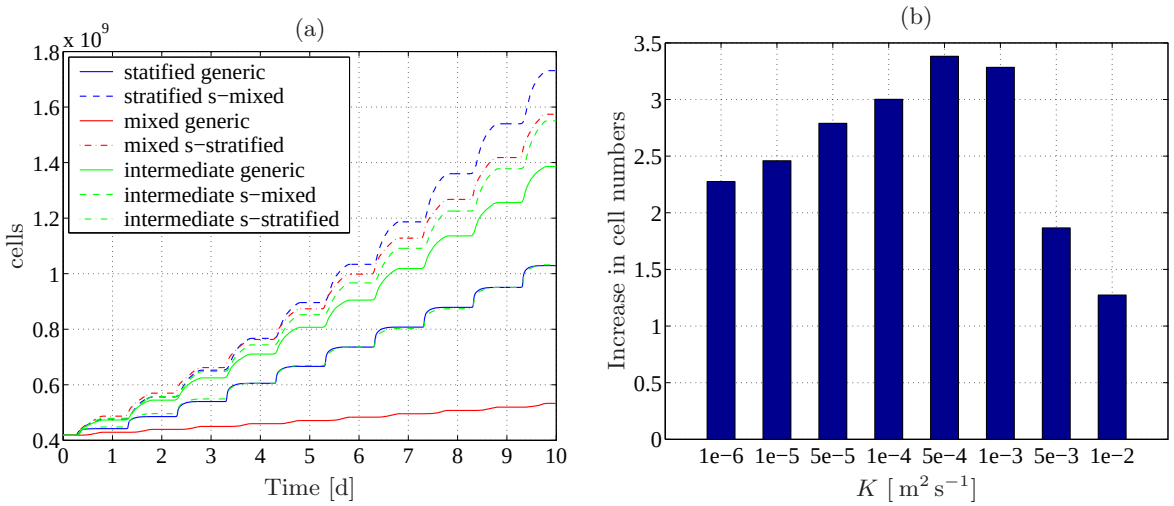

Figure 5.21: (a) Comparison of the increase in cell numbers for all scenarios from Fig. 5.6. The terms for surface stratification and surface mixed have been abbreviated as 's-stratified' and 's-mixed'. (b) Factor of increase in cell numbers as a function of mixing intensity. The abbreviated notation of the form 5e-3 has been used for $5 \cdot 10^3$. These results were obtained with homogeneous turbulence profiles, i.e. $K(z) = \text{const}$.

the particular choice of the growth formulation. In the present case, the cell is unable to divide unless it reaches the critical glucose value of $\Gamma_{max} = 56\,\mu$mol gluc $(10^6$ cells$)^{-1}$. In the stratified scenario, the medium to larger colonies sink out of the photic zone as they accumulate more glucose and thus fewer cells reach Γ_{max} than in the intermediate case where some of the medium sized colonies will be kept longer within the photic zone and are therefore more likely to reach the critical glucose level. As the mixing is increased further, the residence time in the photic zone becomes too short for all colony sizes and they do not receive enough light to reach Γ_{max}. The value for the turbulence cut-off thus increases (decreases) as Γ_{max} is decreased (increased). The choice of the present value was based on published data for the maximum cell density but this is not sufficient to conclude that a cell cannot also divide with lower cellular glucose concentrations.

5.7 Summary and Discussion

In this chapter, the Lagrangian model was used to examine the performance of the colony forming cyanobacterium *Microcystis aeruginosa* in the eutrophic freshwater Lake Nieuwe Meer. As a result of the alternating cell buoyancy which changes as a function of glucose content, *Microcystis* is able to perform vertical migrations in stable environments such as temperature stratified lakes. Mixing of the lake appears to disrupt this migratory behaviour, leading to a reduction in *Microcystis* cell numbers.

The results in Section 5.5 showed that the periodicity and depth of these vertical migrations are strongly dependent on the colony size and surface light intensity. The trajectories of smaller colonies only 're-surface' every 3-4 days, while larger colonies are able to perform bi-diurnal or diurnal migrations due to their higher Stokes velocities. In the presence of weak turbulence,

medium to large sized colonies are able to follow discernible trajectories while the turbulent intensities produced by the artificial mixing in Lake Nieuwe Meer make any deterministic migration impossible, even for the largest colonies.

The empirical growth function from Eq. (5.2) provided some difficulties in the model as it is only defined for net positive glucose increases but does not account for cells that show a decrease in glucose over the light period. Despite the possibility of a decrease in Γ for individual colonies, the ensemble always showed an increase (cf. Fig. 5.14) which might explain why only positive values of $\Delta\Gamma_{\mathrm{lp}}$ have been measured in the laboratory studies that led to the formulation of Eq. (5.2). This growth equation also leads to the paradoxical situation in which there is no relation between the ability to grow and the 'health' (or glucose content) of the cell. Therefore a barely-surviving cell can grow as well as a cell that has more comfortable glucose reserves as long as they both show the same incremental increase in glucose, which appears contrary to intuition. The most important argument, however, that eventually led to the formulation of an alternative growth function in the model is that Eq. (5.2) produced the same population increase in the mixed and stratified scenarios which is clearly in disagreement with observations.

The alternative growth model must be classified as more qualitative in nature since the only quantitative reference point is the maximum observed cell density for *Microcystis* which has been used to determine the glucose threshold at which the cell divides. Nevertheless, this formulation was able to reproduce the observed differences in productivity between the stratified and mixed scenarios. The results also suggested the existence of a critical turbulence threshold up to which the production gradually increases and above which the production sharply decreases. This last result is somewhat speculative, however, as the value of the critical turbulence is strongly dependent on the growth formulation, i.e. Γ_{max}. Nevertheless, this result could be tested in Lake Nieuwe Meer or adequate laboratory setups.

The question remains whether the failure of Eq. (5.2) and the success of the alternative growth model are due to the previously discussed problems inherent in Eq. (5.2) or simply due to the Lagrangian model itself. Given that the results of the previous chapters did not reveal any difficulties with the Lagrangian model, the assumption can be made that the particular formulation of Eq. (5.2) might have caused the model to fail. It would be necessary, however, to verify this assumption and the existence of a glucose threshold for cell division in further laboratory studies.

This part of the thesis should be considered as work in progress in collaboration with the Aquatic Microbiology group at the University of Amsterdam. Further work will be required to strengthen the results presented here. Nevertheless, these preliminary findings raised some important questions on how the growth of *Microcystis* can be quantified.

Chapter 6

Summary and Conclusions

The present study examined the bio-physical interactions between phytoplankton and their marine environment. The main focus was placed on the motility of the cells and the interplay with the turbulent mixing encountered in various situations. Several case studies have been conducted to elucidate the conditions in which motility may provide a decisive competitive advantage that may become causative of species changes through seasonal cycles (e.g. species succession in temperate seas) and in different regions of the world's oceans. The main objectives were twofold. The first part saw the design of a physically realistic and numerically robust Lagrangian particle tracking model (Chapter 2). In the second part, this model has been applied to differing environmental settings in which both motile and non-motile cells are able to co-exist (Chapter 3) or where motile cells (or cells capable of buoyancy regulation) dominate the species composition (Chapters 4 and 5). The numerical experiments tried to assess the degree to which motility was responsible for the observed species compositions in the studied environments. The following paragraphs will provide a summary of the key findings and give suggestions for further work.

The tool which has been developed to conduct the experiments for the present research has been described in Chapter 2. It consists of a realistic physical model which provides the turbulent mixing as a function of the observed stability, and a Lagrangian random walk model to track individual phytoplankton cells through the water column. Several issues arose during the model development (particle accumulations at boundaries, fluid versus particle diffusivity, etc.) for which solutions had to be found. Due to the rather recent advent of desktop computers that are powerful enough to perform the expensive Lagrangian calculations, these issues have not previously been addressed in the oceanographic literature. The model was thoroughly tested to ensure that the output for the later experiments was reliable and that any appearing patterns were caused by the particular system under investigation and thus no artifacts produced by the model itself.

The first case study to which the model was applied has been presented in Chapter 3. It examined the use of motility in the macro-tidal estuary of Southampton Water, located on the southern coast of the UK. The combination of strong tidal mixing, high nutrient con-

centrations, low visibility, and common wisdom would predict a predominantly non-motile phytoplankton population for this estuary since negatively buoyant groups such as diatoms generally have lower light requirements, higher growth rates and require higher turbulent intensities to minimise sinking losses. The advantage of motility in such a highly turbulent environment is therefore not obvious, especially considering that the swimming speeds of most motile species are on average lower than the turbulent velocities in Southampton Water. Observations clearly show, however, that dinoflagellates reach high concentrations in summer and motile ciliates are even capable of producing significant red tide events. By recreating the tidal current signature and associated mixing intensities, it was possible to find a possible explanation for this apparently paradoxical co-existence. While the non-motile cells benefited from the high turbulent mixing, the motile species benefited from the periodic absence or reduction in turbulent intensity due to slack water periods or low current velocities. The particularly long duration of these slack water periods in Southampton Water and their timing in relation to the diurnal irradiance maximum meant that motile cells could significantly increase their light availability throughout the springs-neaps cycle. Depending on the relative differences in growth rates between the two groups, this increased light availability may lead to similar overall production levels and thus explain their co-existence in this environment. The success of motility in relation to the turbulent intensity could successfully be predicted through the Peclet number which has therefore been used throughout this thesis to evaluate the effectiveness of motility in the different scenarios.

Chapter 4 examined the very different setting of a stratified shelf sea where variable tidal mixing in combination with temperature stratification create a highly dynamic and therefore challenging environment for phytoplankton. The presence of a thermocline divides the water column into three virtually separate micro-habitats: a surface layer where light is abundant and turbulent mixing of intermediate strength; a bottom layer where light is limiting and turbulence is high due to tidal mixing; and a stratified zone (the thermocline itself) that divides the previous two and acts as a stable barrier against vertical exchanges. This situation is representative of most temperate seas in mid to late summer or tropical waters that show a permanent stratification throughout the year. The vertical compartmentalisation of the water column usually results in the scenario where nutrients are depleted in the surface layer and abundant in the bottom layer but the thermocline facilitates only a slow vertical exchange. In this situation the key to success for a species is likely to be based on its ability to access the small nutrient flux across the thermocline before it can reach any competitor. The experiments with motile and neutrally buoyant particles showed that small swimming velocities were already sufficient for the cells to maintain a certain depth within the thermocline which allowed them to intercept the small upward flux of nitrate. Most of the cells were also able to remain within the safeguarding perimeter of the thermocline which protects them from being drawn into the light limited bottom mixed layer. Once eroded into this deeper layer, only moderate to high swimming velocities would facilitate a regaining of the thermocline. In comparison, the neutrally buoyant cells did not exhibit positive growth during the nutrient limited period as they were unable to simultaneously access sufficient amounts of both light and nutrients to photosynthesise.

In Chapter 5 the model was applied to the eutrophic fresh water Lake Nieuwe Meer in The Netherlands, where the colony-forming cyanobacterium *Microcystis aeruginosa* forms toxic nuisance booms in summer. This organism shows a pattern of vertical migration in a stable water column that can be explained by an increase in cell density due to carbohydrate accumulation in the light and a decrease in cell density due to utilisation of carbohydrates in the dark. These buoyancy changes thus provide the organism with a passive form of motility which adjusts the cell's vertical position according to its physiological state. In order to control these toxic bloom events the lake has been equipped with an aeration system to artificially mix the water column during spring and summer thereby disrupting the vertical migrations. The model was used to examine the effect of this disruption on the growth performance of *Microcystis*. The empirical growth equation for *Microcystis* created some difficulties as it originated from standard laboratory measurements of large ensemble averages which proved unsuitable to describe the performance of the individual cells in the Lagrangian model. An *ad hoc* growth model was therefore formulated combining available empirical data with plausible assumptions. The results from this alternative growth formulation clearly showed how the turbulent intensities produced by the aeration system are able to disrupt the migratory rhythm of the cells and significantly decrease their growth. The existence of a critical turbulence threshold was detected as the growth of *Microcystis* initially increased with rising turbulent intensities. Above a certain threshold, further increases in turbulence became detrimental to *Microcystis* resulting in a rapid decrease in productivity. Due to the only semi-quantitative growth model, this latter result should be treated with caution, however, as it crucially depends on the growth formulation used. Nevertheless, this prediction could easily be tested through stepwise increases in the mixing intensity produced by the aeration system in Lake Nieuwe Meer or in a suitable laboratory setup.

Overall, this study demonstrated how phytoplankton motility can be used to the cell's advantage in different turbulent environments furthering the understanding of the underlying processes which affect species competition and may cause species succession.

In terms of further work, the following points seem worthwhile to pursue as part of further investigations and refinements of the model:

- The present model represents an ideal tool to investigate individual based processes such as photo-acclimation or photoinhibition. This area was only briefly touched upon in this work but the results appear promising. A more detailed analysis of the relationship between the relevant parameters (mixing depth, turbulent intensity and acclimation time scale) might yield a real quantitative tool to derive turbulent mixing intensities purely from the vertical heterogeneity of suitably chosen physiological parameters which can be measured more easily than the turbulence itself.

- By including a more realistic nutrient formulation in Chapter 4 it would be possible to answer questions regarding nutrient fluxes across the thermocline which would enable estimates of the associated subsurface production. This production occurs at depths which are hidden from the view of satellites, whose global biomass estimates are often

used in climate models that rely on accurate representations of carbon sources and sinks. A more dynamic model including temperature diffusion and simulations, covering longer periods, may therefore provide the necessary insights into these mechanisms and enable a more precise estimate of this hidden production. The results could also lead to a better understanding of the geographical differences in primary and the associated secondary production.

- The investigation of different swimming strategies provided some interesting results in this study. A more detailed analysis could produce some testable hypotheses which might yield insights into the cell physiology and the processes which drive the individual behaviour.

- The inclusion of further species in the lake experiment of Chapter 5 would allow for direct comparisons between the performance of the different species. It could be examined how a varying turbulent mixing affects each species and thus leads to changes in the species composition. Suitable Lagrangian growth formulations for each species need to be found, however, to enable realistic and quantitatively accurate comparisons.

- The critical depth paradigm could be revisited with this Lagrangian formulation to investigate different ratios of euphotic zone depth to mixed layer depth as recent Eulerian investigations (e.g. Huisman and Sommeijer, 2002) have revived interest in this issue.

Appendices

Appendix A

Relating Tidal Current Speed with Water Height

The water level in an estuary is a function of the mean current speed that transports water out of or into the estuary. For the derivation of the relationship let us assume a rectangular basin like in the schematic of Fig. A.1.

Let $\overline{v^d}$ be the depth-averaged flow at time t and $\overline{v^{d,t}}$ the depth- and time-averaged (residual) flow (where the time average has been taken over an integer multiple of the tidal period). The instantaneous average flow through the cross-sectional area A at the time $t = 0$ into/out of the estuary is then $\overline{v}_0 = \overline{v^d}_0 - \overline{v^{d,t}}$. The increase in volume V per model time step Δt is either:

$$\frac{(\Delta V)_0}{\Delta t} = \overline{v}_0 \, A_0 = \overline{v}_0 \, x \, z_0 \tag{A.1}$$

or using $V = x\,y\,z$

$$\frac{(\Delta V)_0}{\Delta t} = x \, y \, \frac{(\Delta z)_0}{\Delta t} \tag{A.2}$$

and hence

$$\frac{(\Delta z)_0}{\Delta t} = \frac{z_0}{y} \, \overline{v}_0 \; . \tag{A.3}$$

In other words, if we know the depth averaged tidal flow, we can calculate the height increment

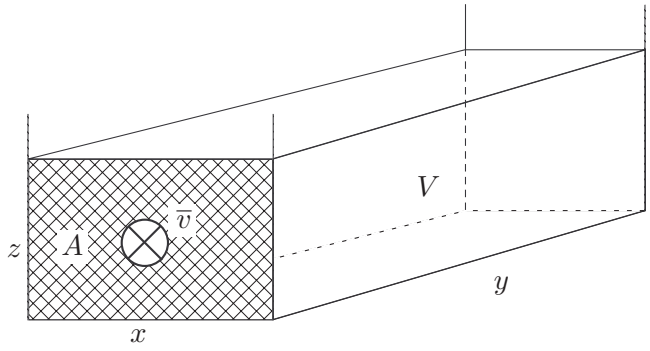

Figure A.1: Schematic estuary.

after every time step from the previous height and current speed (apart from a constant factor related to the geometry of the estuary). In general we get:

$$z_{n+1} = z_n + (\Delta z)_n = z_n + \frac{z_n\,\overline{v}_n\,\Delta t}{y} \tag{A.4}$$

$$= z_n \left(1 + \frac{\overline{v}_n\,\Delta t}{y}\right) . \tag{A.5}$$

This yields a time series of tidal water heights z_i. In the real world, where estuaries are not rectangular and constant in depth, there will be some additional factors which needed to be taken into account but if we know the actual tidal range of the estuary we do not need to know these factors but can simply scale our time series z_i to cover the observed tidal range.

The result of such an analysis is shown in Fig. A.2 below. The first graph applies Eq. (A.5) to the depth-averaged model velocities, output for a spring tide in Southampton Water. The results are scaled to the observed maximum and minimum and compare well with the predicted tidal heights. That this works both ways is shown in Fig. A.2(b) where the model velocity output is compared with the tidal velocities calculated from the predicted tidal elevations.

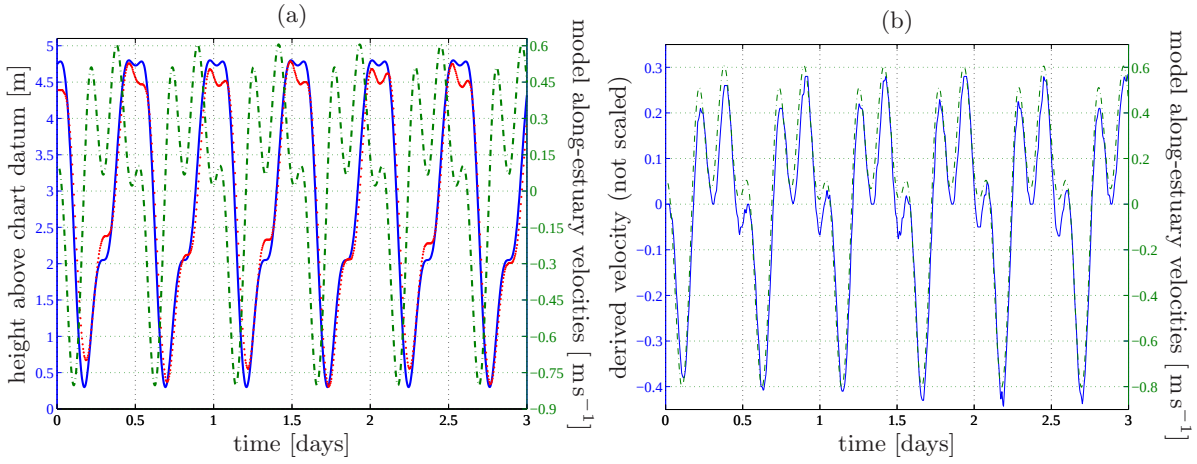

Figure A.2: (a) Calculated water level above chart datum (solid blue) from the integrated (depth-averaged) model velocities (green dash-dot) using Eq. (A.5) (after scaling) shown with the predicted tidal elevations at Southampton Dock Head (red dots). (b) Comparing the tidal along estuary velocities during spring tide from the model (green dash-dot) with the derivative of the (predicted) water heights during a spring tide at Southampton Dock Head (without scaling).

Appendix B

SCAMP Profiles for Lake Nieuwe Meer

This section lists the SCAMP profiles obtained during the physical measurement campaign on Lake Nieuwe Meer in 2002. All figures are courtesy of J. Sharples.

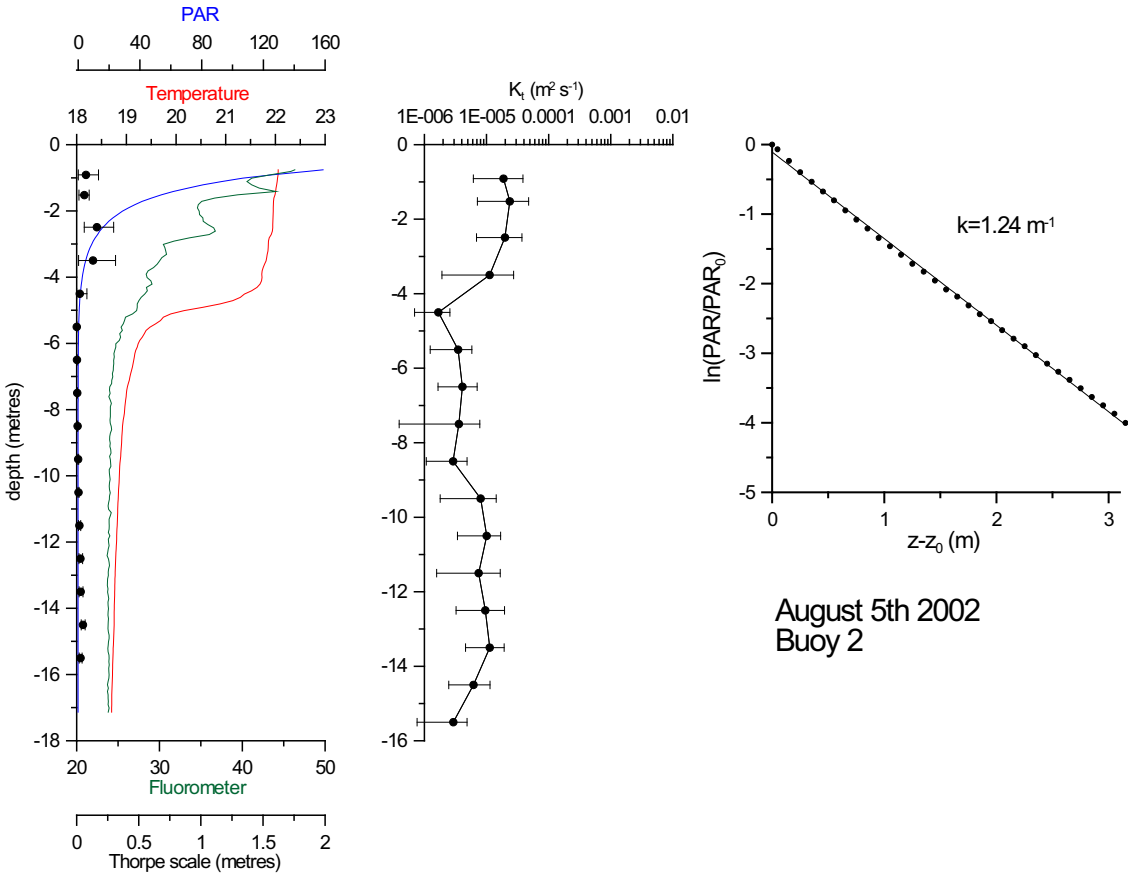

Figure B.1: SCAMP profiles for 5 August 2002 at Buoy 2.

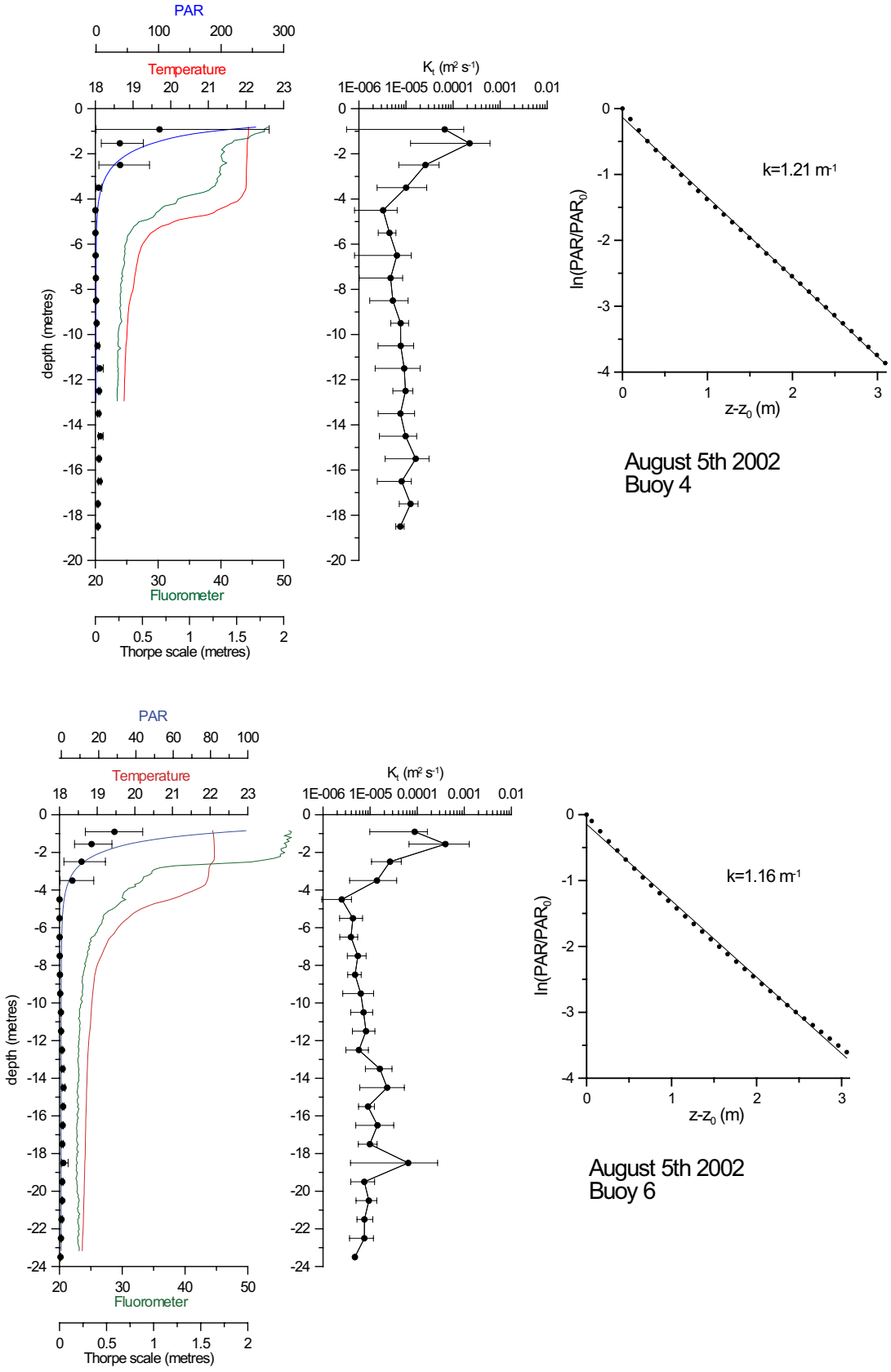

Figure B.2: SCAMP profiles for 5 August 2002 at Buoys 4 (top) and 6 (bottom).

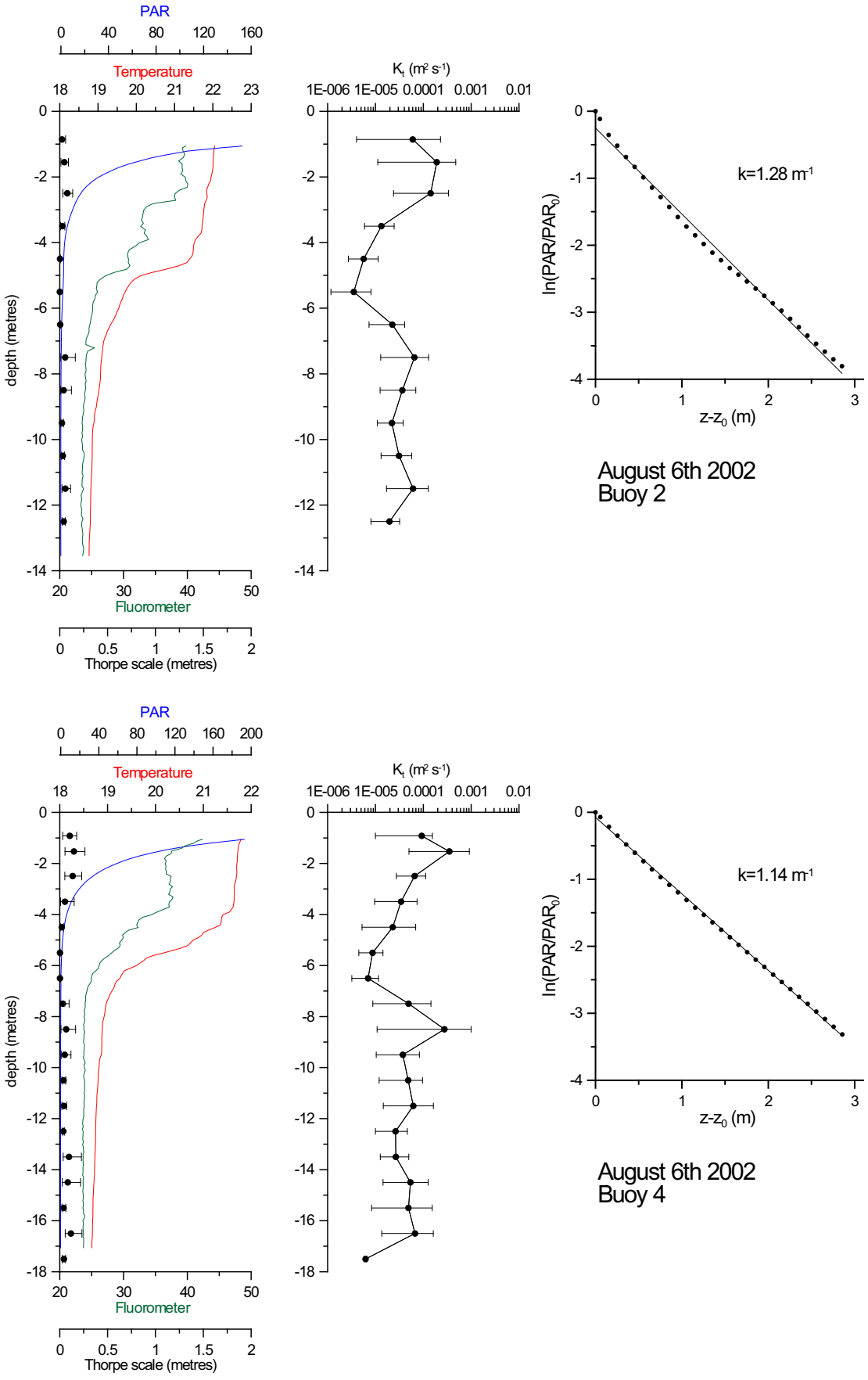

Figure B.3: SCAMP profiles for 6 August 2002 at Buoys 2 (top) and 4 (bottom).

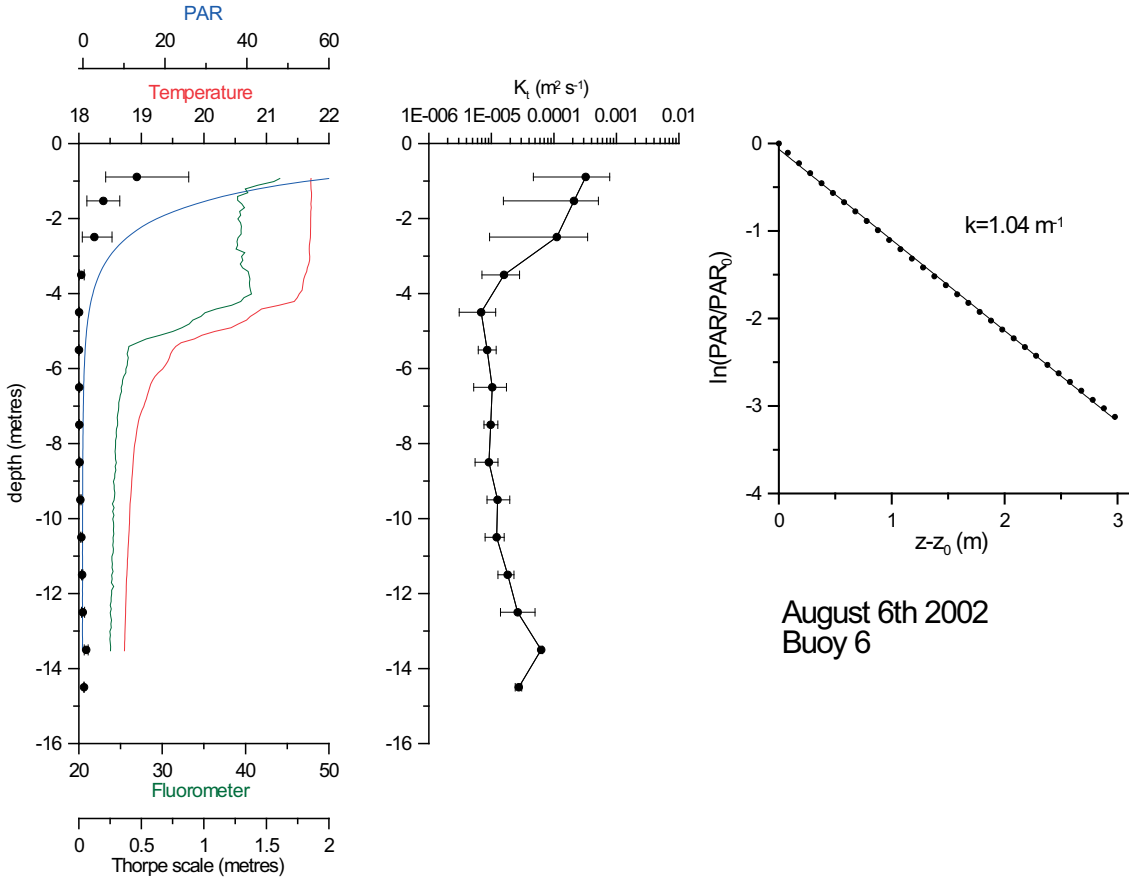

Figure B.4: SCAMP profiles for 5 August 2002 at Buoy 6.

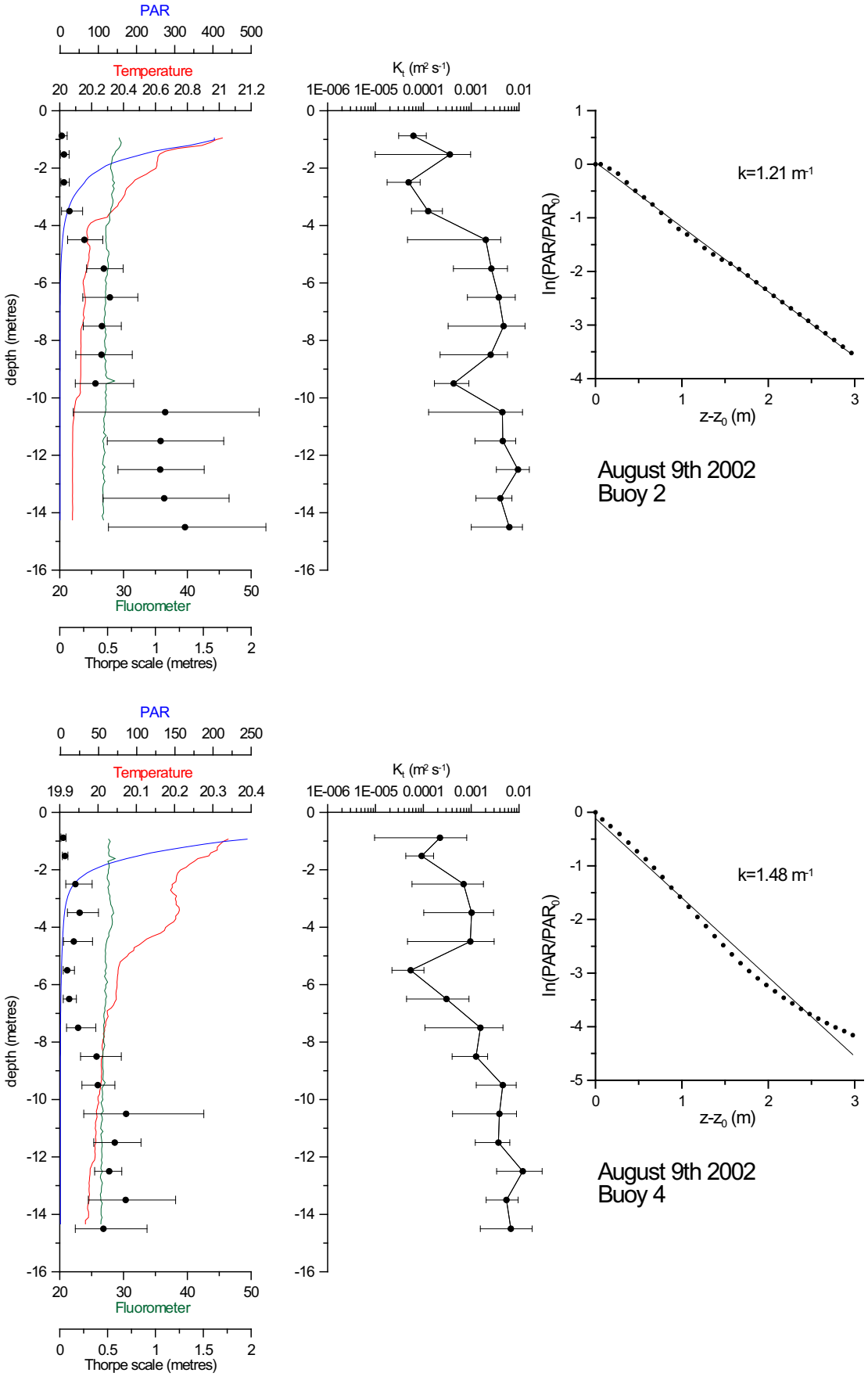

Figure B.5: SCAMP profiles for 9 August 2002 at Buoys 2 (top) and 4 (bottom).

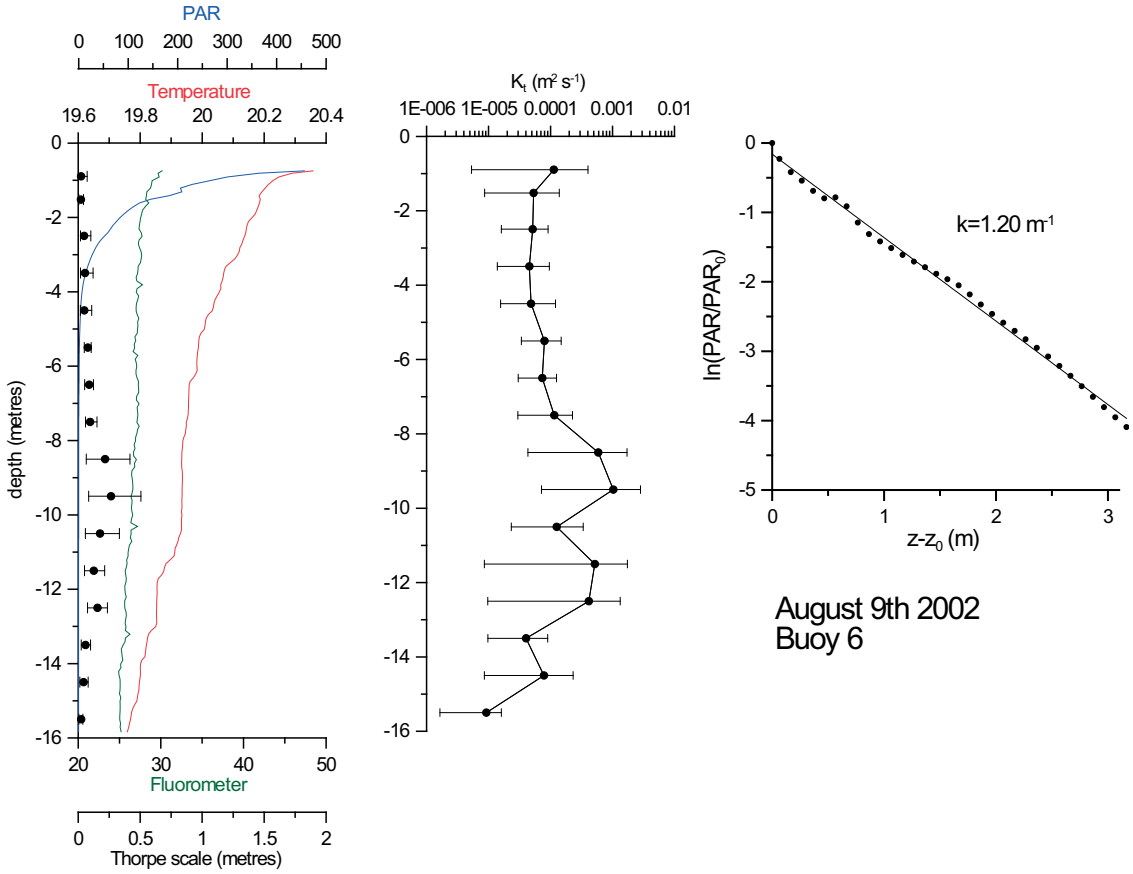

Figure B.6: SCAMP profiles for 9 August 2002 at Buoy 6.

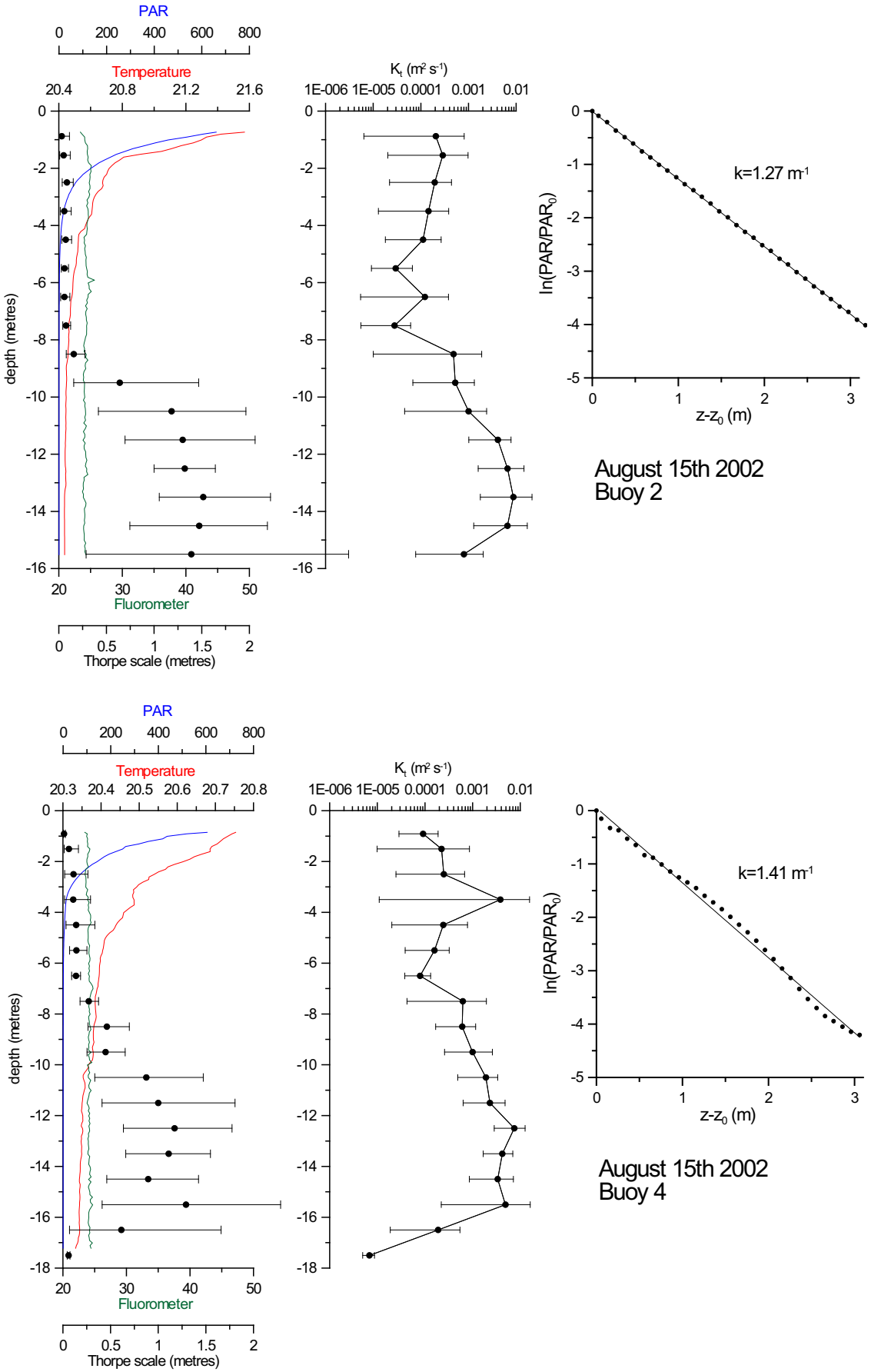

Figure B.7: SCAMP profiles for 15 August 2002 at Buoys 2 (top) and 4 (bottom).

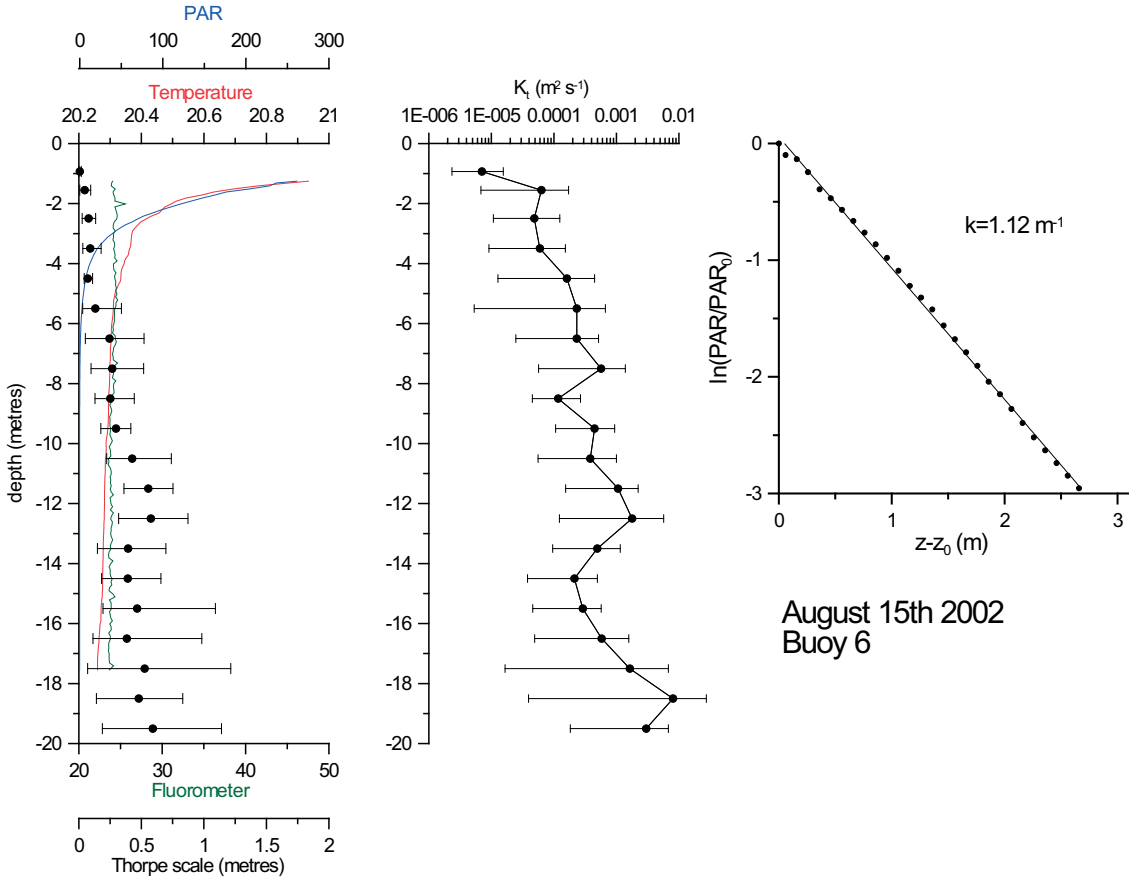

Figure B.8: SCAMP profiles for 15 August 2002 at Buoy 6.

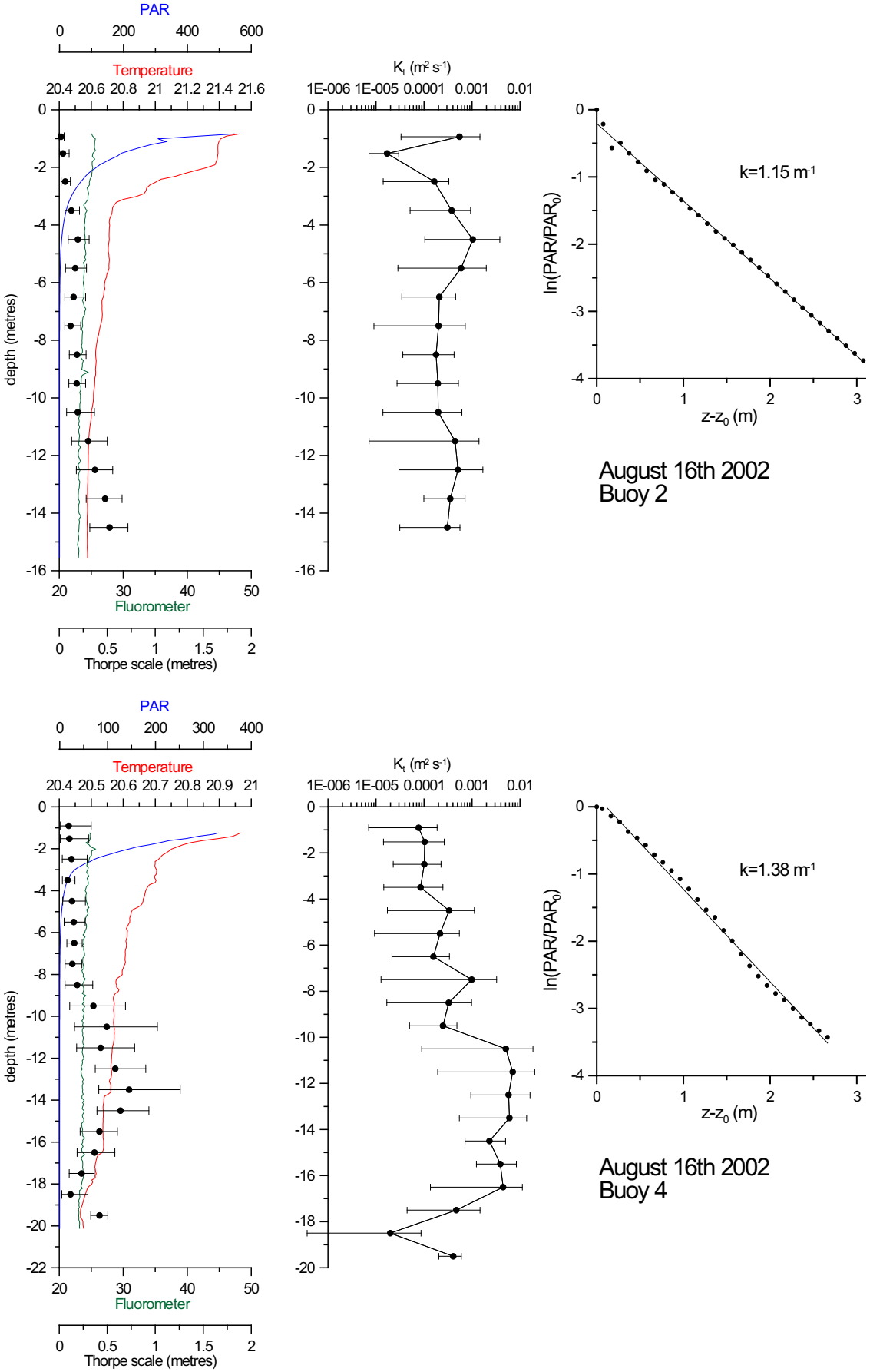

Figure B.9: SCAMP profiles for 16 August 2002 at Buoys 2 (top) and 4 (bottom).

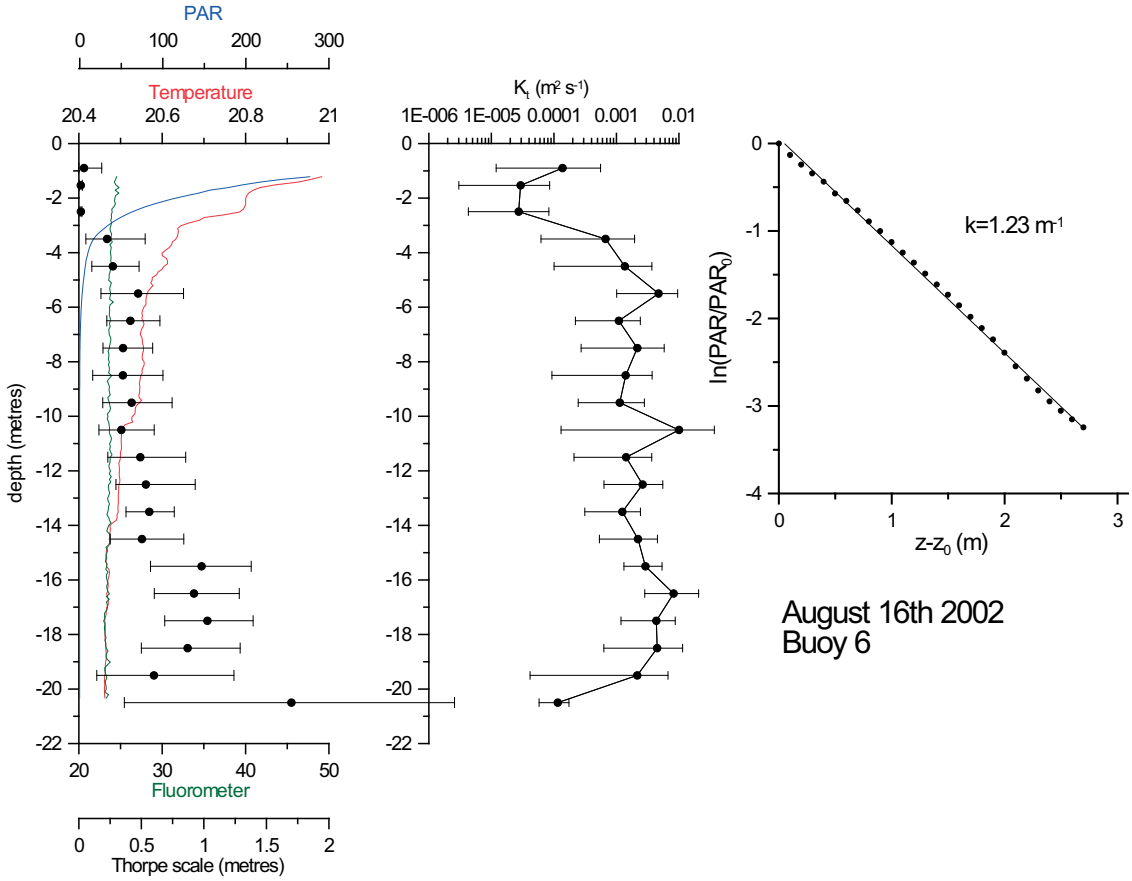

Figure B.10: SCAMP profiles for 16 August 2002 at Buoy 6.

Bibliography

Abarbanel, H., D. Holm, J. Marsden, and T. Ratiu. Richardson number criterion for the non-linear stability of 3D stratified flow. *Physical Review Letters*, 52:2352–2355, 1984.

Ali, E. M. *Processes and Conditions Influencing Phytoplankton Growth and Bloom Initiation in a Macrotidal Estuary, Southampton Water*. Ph.D. thesis, School of Ocean and Earth Science, University of Southampton, 2003.

Anderson, D. M. and K. D. Stolzenbach. Selective retention of two dinoflagellates in a well-mixed estuarine embayment: The importance of diel vertical migration and surface avoidance. *Marine Ecology Progress Series*, 25:39–50, 1985.

Antai, E. E. *Seasonal Trophodynamics of Bacterioplankton and Heterotrophic Microflagellates in Southampton Water*. Ph.D. thesis, Department of Oceanography, University of Southampton, 1989.

Barkmann, W. and J. D. Woods. On using a Lagrangian model to calibrate primary production determined from *in vitro* incubation measurements. *Journal of Plankton Research*, 18(5):767–788, 1996.

Batchelor, G. Small-scale variation of convected quantities like temperature in turbulent fluid. *Journal of Fluid Mechanics*, 5:113–133, 1959.

Berdalet, E. and M. Estrada. Effects of turbulence on several dinoflagellate species. In T. J. Smayda and Y. Shimizu (eds.), *Toxic phytoplankton blooms in the sea*, Proceedings of the 5th International Conference on Toxic Marine Phytoplankton, pp. 737–740. Elsevier, 1993.

Berg, H. C. and E. M. Purcell. Physics of chemoreception. *Biophysical Journal*, 20:193–215, 1977.

Berman, T. and B. Shteinman. Phytoplankton development and turbulent mixing in Lake Kinneret (1992-1996). *Journal of Plankton Research*, 20(4):709–726, 1998.

Brand, L. E. and R. R. L. Guillard. The effects of continuous light and light intensity on the reproduction rates of 22 species of marine phytoplankton. *Journal of Experimental Marine Biology and Ecology*, 50:119–132, 1981.

Broekhuizen, N. Simulating motile algae using a mixed Eulerian-Lagrangian approach: Does motility promote dinoflagellate persistence or co-existence with diatoms? *Journal of Plankton Research*, 21(7):1191–1216, 1999.

Burchard, H. and H. Baumert. On the performance of a mixed-layer model based on the $k-\epsilon$ turbulence closure. *Journal of Geophysical Research*, 100(C5):8523–8540, 1995.

Burchard, H. and K. Bolding. Comparative analysis of four second-moment turbulence closure models for the oceanic mixed layer. *Journal of Physical Oceanography*, 31:1943–1968, 2001.

Burchard, H., K. Bolding, and M. Villarreal. GOTM, a general ocean turbulence model. Theory, applications and test cases. Tech. Rep. EUR 18745 EN, European Commision, 1999.

Burchard, H. and E. Deleersnijder. Stability of algebraic non-equilibrium second-order closure models. *Ocean Modelling*, 3:33–50, 2001.

Burchard, H., O. Petersen, and T. P. Rippeth. Comparing the performance of the Mellor-Yamada and the k-ε two-equation turbulence models. *Journal of Geophysical Research*, 103(C5):10 543–10 554, 1998.

Canuto, V. M., A. Howard, Y. Cheng, and M. S. Dubovikov. Ocean turbulence. part I. one-point closure model – momentum and heat vertical diffusivities. *Journal of Physical Oceanography*, 31:1413–1426, 2001.

Carr, J. F., C. M. de Turville, R. T. Jarman, and J. F. Spencer. Water temperatures in the Solent estuarine system. In J. D. Burton (ed.), *The Solent Estuarine System: An Assessment of Present Knowledge*, NERC Publication Series C No. 22, pp. 36–43. 1980.

Craig, P. and M. Banner. Modelling wave-enhanced turbulence in the ocean surface layer. *Journal of Physical Oceanography*, 24:2546–2559, 1994.

Crawford, D. and T. Lindholm. Some observations on vertical distribution and migration of the phototrophic ciliate *Mesodinium rubrum* (=*Myrionecta rubra*) in a stratified brackish inlet. *Aquatic Microbial Ecology*, 13:267–274, 1997.

Crawford, D. W. and D. A. Purdie. Evidence for avoidance of flushing from an estuary by planktonic, phototrophic ciliate. *Marine Ecology Progress Series*, 79:259–265, 1992.

Csanady, G. Mass transfer to and from small particles in the sea. *Limnology and Oceanography*, 31:237–248, 1986.

Csanady, G. T. Turbulent diffusion of heavy particles in the atmosphere. *Journal of Atmospheric Science*, 20:201–208, 1963.

Cullen, J. J. and M. R. Lewis. The kinetics of algal photoadaptation in the context of vertical mixing. *Journal of Plankton Research*, 10(5):1039–1063, 1988.

D'Alessio, S. J. D., K. Abdella, and N. A. McFarlane. A new second-order turbulence closure scheme for modelling the oceanic mixed layer. *Journal of Physical Oceanography*, 28(8):1624–1641, 1998.

de Boor, C. *A Practical Guide to Splines*, vol. 27 of *Applied Mathematical Sciences*, chap. 14. Springer, Berlin, 1978.

Denman, K. and J. Marra. Modelling the time dependent photoadaptation of phytoplankton to fluctuating light. In J. Nihoul (ed.), *Marine Interface Ecohydrodynamics*, pp. 341–359. Elsevier, Amsterdam, 1986.

Dimou, K. and E. Adams. A random walk, particle tracking model for well-mixed estuaries and coastal waters. *Estuarine, Coastal and Shelf Science*, 37:99–110, 1993.

Dyer, K. R. Sedimentation and sediment transport. In J. D. Burton (ed.), *The Solent Estuarine System: An Assessment of Present Knowledge*, NERC Publication Series C No. 22, pp. 20–24. 1980.

Emery, W. J. and R. E. Thomson. *Data Analysis Methods in Physical Oceanography*, chap. 5.5, pp. 392–404. Pergamon, 1998.

Eppley, R. W., R. W. Holmes, and J. D. H. Strickland. Sinking rates of marine phytoplankton measured with a fluorometer. *Journal of Experimental Biology and Ecology*, 1:191–208, 1967.

Eppley, R. W. and B. J. Peterson. Particulate organic matter flux and planktonic new production in the deep ocean. *Nature*, 282:677–680, 1979.

Estrada, M. and E. Berdalet. Effects of turbulence of phytoplankton. In D. M. Anderson, A. D. Cembella, and G. M. Hallegraef (eds.), *Physiological Ecology of Harmful Algal Blooms*, NATO ASI Series, Vol. G 41, pp. 601–618. Springer, Berlin, 1998.

Falkowski, P. G. Light-shade adaptation and vertical mixing of marine phytoplankton: A comparative field study. *Journal of Marine Research*, 41(2):215–237, 1983.

Falkowski, P. G. Physiological responses of phytoplankton to natural light regimes. *Journal of Plankton Research*, 6(2):295–307, 1984.

Falkowski, P. G. Ironing out what controls primary production in the nutrient rich waters of the open ocean. *Global Change in Biology*, 1:161–163, 1995.

Falkowski, P. G. and J. A. Raven. *Aquatic Photosynthesis*. Blackwell, 1997.

Farmer, D. and C. McNeil. Photoadaptation in a convective layer. *Deep-Sea Research II*, 46:2433–2446, 1999.

Fung, J. C. H. Gravitational settling of particles and bubbles in homogeneous turbulence. *Journal of Geophysical Research*, 98:20 287–20 297, 1993.

Galperin, B., L. Kantha, S. Hassid, and A. Rosati. A quasi-equilibrium turbulent energy model for geophysical flows. *Journal of Atmospheric Sciences*, 45(1):55–62, 1988.

Gargett, A. E. Eddy diffusivity in the ocean interior. *Journal of Marine Research*, 42:359–395, 1984.

Gavis, J. Munk and Riley revisited: nutrient diffusion transport and rates of phytoplankton growth. *Journal of Marine Research*, 34:161–179, 1976.

Geider, R. J., H. L. MacIntyre, and T. M. Kana. A dynamic model of phytoplankton growth and acclimation: Responses of the balanced growth rate and chlorophyll a:carbon ratio to light, nutrient-limitation and temperature. *Marine Ecology Progress Series*, 148:187–200, 1997.

Gerz, T., U. Schumann, and S. Elghobashi. Direct numerical simulation of stratified, homogeneous turbulent shear flows. *Journal of Fluid Mechanics*, 200:563–594, 1989.

Gouesbet, G. and A. Berlemont. Eulerian and Lagrangian approaches for predicting the behaviour of discrete particles in turbulent flow. *Progress in Energy and Combustion Science*, 25:133–159, 1999.

Graham, D. I. and P. W. James. Turbulent dispersion of particles using eddy interaction models. *International Journal of Multiphase Flow*, 22(1):157–175, 1996.

Hansen, D. V. and M. Rattray. Gravitational circulation in straits and estuaries. *Journal of Marine Research*, 23:104–122, 1965.

Hasle, G. R. and E. E. Syvertsen. Marine diatoms. In C. R. Thomas (ed.), *Identifying Marine Diatoms and Dinoflagellates*. Academic Press, San Diego, 1996.

Hinze, J. O. *Turbulence*, chap. 5.7, pp. 460–471. McGraw-Hill, 2nd edn., 1975.

Horstmann, U. Observations on the peculiar diurnal migration of a red tide dinoflagellate in tropical shallow waters. *Journal of Phycology*, 16:481–485, 1980.

Howard, L. Note on a paper by J.W. Miles. *Journal of Fluid Mechanics*, 10:509–512, 1961.

Huisman, J., R. Jonker, C. Zonneveld, and F. J. Weissing. Competition for light between phytoplankton species: Experimental tests of mechanistic theory. *Ecology*, 80:211–222, 1999.

Huisman, J., J. Sharples, J. M. Stroom, P. M. Visser, W. E. A. Kardinaal, J. M. H. Verspagen, and B. Sommeijer. Changes in turbulent mixing shift competition for light between phytoplankton species. *Ecology*, 85(11):2960–2970, 2004.

Huisman, J. and B. Sommeijer. Maximal sustainable sinking velocity of phytoplankton. *Marine Ecology Progress Series*, 244:39–48, 2002.

Hunter, J. R., P. D. Craig, and H. E. Phillips. On the use of random walk models with spatially variable diffusivity. *Journal of Computational Physics*, 106:366–376, 1993.

Hydrographic Office, U. K. Southampton water and approaches. Chart No. 1905, Admiralty Charts & Publications, 1997.

Ibelings, B. W., L. R. Mur, and A. E. Walsby. Diurnal changes in buoyancy and vertical distribution in populations of *Microcystis* in two shallow lakes. *Journal of Plankton Research*, 13(2):419–436, 1991.

Jassby, A. D. and T. Platt. Mathematical formulation of the relationship between photosynthesis and light for phytoplankton. *Limnology and Oceanography*, 21:540–547, 1976.

Jonsson, P. R. and P. Tiselius. Feeding behaviour, prey detection and capture efficiency of the copepod *Acartia tonsa* feeding on planktonic ciliates. *Marine Ecology Progress Series*, 60:35–44, 1990.

Jungo, E., P. Visser, J. Stroom, and L. Mur. Artificial mixing to reduce growth of the blue-green alga *Microcystis* in Lake Nieuwe Meer, Amsterdam: An evaluation of 7 years of experience. *Water Science and Technology*, Water Supply Vol 1(1):17–23, 2001.

Kalnay, E., M. Kanamitsu, R. Kistler, W. Collins, D. Deaven, L. Gandin, M. Iredell, S. Saha, G. White, J. Woollen, Y. Zhu, M. Chelliah, W. Ebisuzaki, W. Higgins, J. Janowiak, K. Mao, C. Ropolewski, J. Wang, A. Leetmaa, R. Reynolds, R. Jenne, and D. Joseph. The NCEP/NCAR 40-year Reanalysis Project. *Bulletin of the American Meteorological Society*, 3(77):437–471, 1996. Data available at http://www.cdc.noaa.gov/.

Kamykowski, D. Trajectories of autotrophic marine dinoflagellates. *Journal of Phycology*, 31:200–208, 1995.

Kamykowski, D., G. Janowitz, G. Kirkpatrick, and R. Reed. A study of time dependent primary productivity in a natural upper-ocean mixed layer using a biophysical model. *Journal of Plankton Research*, 18(8):1295–1322, 1996.

Kamykowski, D. and A. S. McCollum. The temperature acclimatised swimming speed of selected marine dinoflagellates. *Journal of Plankton Research*, 8(2):275–287, 1986.

Kamykowski, D., R. Reed, and G. Kirkpatrick. Comparison of sinking velocity, swimming velocity, rotation and path characteristics among six marine dinoflagellate species. *Marine Biology*, 113:319–328, 1992.

Kamykowski, D. and A. K. Yamazaki. A study of metabolism-influenced orientation in the diel vertical migration of marine dinoflagellates. *Limnology and Oceanography*, 42:1189–1202, 1997.

Kamykowski, D. and S.-J. Zentara. The diurnal vertical migration of motile phytoplankton through temperature gradients. *Limnology and Oceanography*, 22:148–151, 1977.

Kantha, L. and C. Clayson. An improved mixed layer model for geophysical applications. *Journal of Geophysical Research*, 99(C12):25 235–25 266, 1994.

Kantha, L. H. and C. A. Clayson. *Small Scale Processes in Geophysical Fluid Flows*, vol. 67 of *International Geophysics Series*. Academic Press, San Diego, 2000.

Karp-Boss, L., E. Boss, and P. A. Jumars. Motion of dinoflagellates in a simple shear flow. *Limnology and Oceanography*, 45(7):1594–1602, 2000.

Kato, H. and O. Phillips. On the penetration of a turbulent layer into stratified fluid. *Journal of Fluid Mechanics*, 37(4):643–655, 1969.

Kessler, J. O. Hydrodynamic focusing of motile algal cells. *Nature*, 313:218–220, 1985.

Kifle, D. *Seasonal and Spatial Variation in Species Composition, Abundance, Biomass and Primary Production of Phytoplankton in Southampton Water, U.K.* Ph.D. thesis, Department of Oceanography, University of Southampton, 1992.

Kim, Y., S. Kang, I. Seo, and B. Oh. Far-field transport of effluent plumes discharged from Masan Sea outfall plumes. *Ocean Research*, 22:69–80, 2000.

Klausmeier, C. A. and E. Lichtmann. Algal games: The vertical distribution of phytoplankton in poorly mixed water columns. *Limnology and Oceanography*, 46(8):1998–2007, 2001.

Köhler, J. Influence of turbulent mixing on growth and primary production of *Microcystis aeruginosa* in the hypertrophic Bautzen Reservoir. *Archiv für Hydrobiologie*, 123:413–429, 1992.

Kolmogoroff, A. The local structure of turbulence in incompressible viscous fluids at very large Reynolds numbers. *Dokl. Nauk. SSR*, 30:301–305, 1941.

Kromkamp, J. C. and L. R. Mur. Buoyant density changes in the cyanobacterium *Microcystis aeruginosa* due to changes in the cellular carbohydrate content. *FEMS Microbiological Letters*, 25:105–109, 1984.

Kundu, P. and I. Cohen. *Fluid Mechanics*. Academic Press, San Diego, second edn., 2002.

Kuylenstierna, M. and B. Karlson. Plankton database. http://www.marbot.gu.se/, 2000.

Lalli, C. M. and T. R. Parsons. *Biological Oceanography: An Introduction*. The Open University. Butterworth Heinemann, Oxford, 2002.

Lande, R. and A. M. Wood. Suspension times of particles in the upper ocean. *Deep-Sea Research I*, 34(1):61–72, 1987.

Lauria, M. L. *Physical Constraints on Phytoplankton in Estuaries and Shallow Coastal Waters*. Ph.D. thesis, School of Ocean and Earth Science, University of Southampton, 1998.

Lauria, M. L., D. A. Purdie, and J. Sharples. Contrasting phytoplankton distributions controlled by tidal turbulence in an estuary. *Journal of Marine Systems*, 21:189–197, 1999.

Lazier, J. R. N. and K. H. Mann. Turbulence and diffusive layers around small organisms. *Deep-Sea Research I*, 36:1721–1733, 1989.

Leakey, R. J. G. *The Ecology of Planktonic Ciliates in Southampton Water*. Ph.D. thesis, School of Biological Sciences, University of Southampton, 1989.

Levandowski, M. and P. J. Kaneta. Behaviour in dinoflagellates. In F. J. R. Taylor (ed.), *The biology of dinoflagellates*, pp. 360–397. Blackwell Scientific Publications, 1987.

Lewis, M. R., J. J. Cullen, and T. Platt. Relationships between vertical mixing and photoadaptation of phytoplankton: similarity criteria. *Marine Ecology Progress Series*, 15:141–149, 1984*a*.

Lewis, M. R., E. P. W. Horne, J. J. Cullen, N. S. Oakey, and T. Platt. Turbulent motions may control phytoplankton photosynthesis in the upper ocean. *Nature*, 311:49–50, 1984*b*.

Lizon, F., L. Seuront, and Y. Lagadeuc. Photoadaptation and primary production study in tidally mixed coastal waters using a Lagrangian model. *Marine Ecology Progress Series*, 169:43–54, 1998.

Lombardi, E. H. and B. Capon. Observations on the tidepool ecology and behaviour of *Peridinium gregarium*. *Journal of Phycology*, 7:188–194, 1971.

MacIntyre, H. L., T. M. Kana, and R. J. Geider. The effect of water motion on short-term rates of photosynthesis by marine phytoplankton. *Trends in Plant Science*, 5(1):12–17, 2000.

MacIntyre, S., A. Alldredge, and C. Gotschalk. Accumulation of marine snow at density discontinuities in the water column. *Limnology and Oceanography*, 40:449–468, 1995.

Malone, T. C. Algal size. In I. Morris (ed.), *The Physiological Ecology of Phytoplankton*, pp. 433–463. Blackwell, 1980.

Malone, T. C., C. Garside, R. Anderson, and O. A. Roels. The possible occurrence of photosynthetic microorganisms in deep sea sediments of the North Atlantic. *Journal of Phycology*, 9:482–488, 1973.

Mann, K. H. and J. R. N. Lazier. *Dynamics of Marine Ecosystems*. Blackwell, Cambridge, 2nd edn., 1996.

Maranon, E., M. Behrenfeld, N. Gonzalez, B. Mourino, and M. Zubkov. High variability of primary production in oligotrophic waters of the Atlantic Ocean: Uncoupling from phytoplankton biomass and size structure. *Marine Ecology Progress Series*, 257:1–11, 2003.

Margalef, R. Life-forms of phytoplankton as survival alternatives in an unstable environment. *Oceanologica Acta*, 1(4):493–509, 1978.

Marra, J. Effect of short-term variations in light intensity on photosynthesis of a marine phytoplankter: A laboratory simulation study. *Marine Biology*, 46:191–202, 1978*a*.

Marra, J. Phytoplankton photosynthetic response to vertical movement in a mixed layer. *Marine Biology*, 46:203–208, 1978*b*.

Martin, J. H., K. Coale, K. Johnson, and S. Fitzwater. Testing the iron hypothesis in ecosystems of the equatorial Pacific Ocean. *Nature*, 371:123–129, 1994.

Martin, P. Simulation of the mixed layer at OWS November and Papa with several models. *Journal of Geophysical Research*, 90(C1):903–916, 1985.

McAndrew, D., S. Coppen, and C. Rogers. Measurements of fluid turbulence along the path of a heavy particle in a backward-facing step flow. 1998. Third International Conference on Multiphase Flow (ICMF'98), Lyon, France.

Mellor, G. L. One-dimensional ocean surface modelling: A problem and a solution. *Journal of Physical Oceanography*, 31(4):790–809, 2001.

Mellor, G. L. and T. Yamada. A hierarchy of turbulence closure models for planetary boundary layers. *Journal of the Atmospheric Sciences*, 31(7):1791–1806, 1974.

Mellor, G. L. and T. Yamada. Development of a turbulence closure model for geophysical fluid problems. *Reviews of Geophysics and Space Physics*, 20(4):851–875, 1982.

Metaxas, A. Behaviour in flow: Perspectives on the distribution and dispersion of meroplanktonic larvae in the water column. *Canadian Journal of Fisheries and Aquatic Science*, 58:86–98, 2001.

Miles, J. On the stability of heterogeneous shear flow. *Journal of Fluid Mechanics*, 10:496–508, 1961.

Morel, A. and R. Smith. Relation between total quanta and total energy for aquatic photosynthesis. *Limnology and Oceanography*, 19:591–600, 1974.

Munk, W. and G. A. Riley. Absorption of nutrients by aquatic plants. *Journal of Marine Research*, 11:215–240, 1952.

Nagai, T., H. Yamazaki, and D. Kamykowski. A Lagrangian photoresponse model coupled with 2nd-order turbulence closure. *Marine Ecology Progress Series*, 265:17–30, 2003.

Neale, P. and J. Marra. Short-term variation of P_{max} under natural irradiance conditions: A model and its implications. *Marine Ecology Progress Series*, 26:113–124, 1985.

Neale, P. J. and P. J. Richerson. Photoinhibition and the diurnal variation of phytoplankton photosynthesis I. development of a photosynthesis-irradiance model from studies of *in situ* responses. *Journal of Marine Research*, 9:167–193, 1987.

Oakey, N. S. and J. A. Elliot. Dissipation in the mixed layer near Emeral Basin. In J. C. L. Nihoul (ed.), *Marine Turbulence*, pp. 123–133. Elsevier, Amsterdam, 1980.

O'Brien, K. R., G. N. Ivey, D. P. Hamilton, and A. M. Waite. Simple mixing criteria for the growth of negatively buoyant phytoplankton. *Limnology and Oceanography*, 48(3):1326–1337, 2003.

Okubo, A. Fantastic voyage into the deep: Marine biofluid mechanics. In E. Teromoto and M. Yamaguti (eds.), *Mathematical Topics in Population Biology, Morphogenesis and Neuroscience*, pp. 32–47. Springer Verlag, New York, 1987.

Olesen, M. Comparison of the sedimentation of a spring diatom bloom and of a subsurface chlorophyll maximum. *Marine Biology*, 121:541–547, 1995.

Osborn, T. R. Measurements of energy dissipation adjacent to an island. *Journal of Geophysical Research*, 83:2939–2957, 1978.

Pasciak, W. and J. Gavis. Transport limitation of nutrient uptake in phytoplankton. *Limnology and Oceanography*, 19(6):881–888, 1974.

Passow, U. Vertical migration of *Gonyaulax catenata* and *Mesodinium rubrum*. *Marine Biology*, 110:455–463, 1991.

Perry, M., M. Talbot, and R. Alberte. Photoadaptation in marine phytoplankton: Response of the photosynthetic unit. *Marine Biology*, 62:91–101, 1981.

Phillips, A. J. Distribution of chemical species. In J. D. Burton (ed.), *The Solent Estuarine System: An Assessment of Present Knowledge*, NERC Publication Series C No. 22, pp. 44–59. 1980.

Platt, T., C. Gallegos, and W. Harrison. Photoinhibition of photosynthesis in natural assemblages of marine phytoplankton. *Journal of Marine Research*, 38(4):687–701, 1980.

Pollingher, U. and E. Zemal. *In situ* and experimental evidence of the influence of turbulence on cell division processes of *Peridinium cinctum* forma *westii* (Lemm.) Lefevre. *British Phycological Journal*, 16:281–287, 1981.

Prandtl, L. Über die ausgebildete Turbulenz. *Zeitschrift für angewandte Mathematik und Mechanik*, 5:136, 1925.

Pufahl, A. G., B. A. Kagan, and W. Eifler. Spikes and jittering in the numerical solution of the planetary boundary layer problem: causes and effects. *International Journal for Numerical Methods in Fluids*, 25(1):105–121, 1997.

Purcell, E. M. Life at low Reynolds number. *American Journal of Physics*, 43:3–11, 1977.

Reynolds, C., J. Thompson, and A. Ferguson. Growth- and loss-rate responses of phytoplankton to intermittent artificial mixing and their potential application to the control of planktonic algal biomass. *Journal of Applied Ecology*, 21:11–39, 1984.

Ribeiro, C. H. A., J. J. Waniek, and J. Sharples. Observations of the spring-neap modulation of the gravitational circulation in a partially mixed estuary. *Ocean Dynamics*, 54:299–306, 2004.

Richardson, K., A. W. Visser, and F. Bo Pedersen. Subsurface phytoplankton blooms fuel pelagic production in the North Sea. *Journal of Plankton Research*, 22(9):1663–1671, 2000.

Rodi, W. Examples of calculation methods for flow and mixing in stratified fluids. *Journal of Geophysical Research*, 92(C5):5305–5328, 1987.

Rodi, W. *Turbulence Models and Their Application in Hydraulics*. IAHR Monograph. A.A. Balkema, Rotterdam, 3rd edn., 2000.

Rohr, J., J. Losee, and J. Hoyt. Stimulation of bioluminescence by turbulent pipe flow. *Deep-Sea Research I*, 37(10):1639–1646, 1990.

Ross, O. N. and J. Sharples. Recipe for 1-d Lagrangian particle tracking models in space-varying diffusivity. *Limnology and Oceanography: Methods*, 2:289–302, 2004. Http://www.aslo.org/lomethods/free/2004/0289.pdf.

Ruiz, J. The role of turbulence in the sedimentation loss of pelagic aggregates from the mixed layer. *Journal of Marine Research*, 54:385–406, 1996.

Ruiz, J., M. García, and J. Rodríguez. Sedimentation loss of phytoplankton cells from the mixed layer: effects of turbulence levels. *Journal of Plankton Research*, 18(9):1727–1734, 1996.

Saiz, E., A. Calbert, and E. Broglio. Effects of small-scale turbulence on copepods: The case of *Oithona davisae*. *Limnology and Oceanography*, 48(3):1304–1311, 2003.

Sharples, J. Investigating the seasonal vertical structure of phytoplankton in shelf seas. *Marine Models Online*, 1:3–38, 1999.

Sharples, J., C. M. Moore, T. R. Rippeth, P. M. Holligan, D. J. Hydes, N. R. Fisher, and J. Simpson. Phytoplankton distribution and survival in the thermocline. *Limnology and Oceanography*, 46(3):486–496, 2001.

Sharples, J., J. H. Simpson, and J. Brubaker. Observations and modelling of periodic stratification in the Upper York River Estuary, Virginia. *Estuarine, Coastal and Shelf Science*, 38:301–312, 1994.

Sieburth, J. M., J. Smetacek, and J. Lenz. Pelagic ecosystem structure: Heterotrophic compartments of the plankton and their relationship to plankton size fractions. *Limnology and Oceanography*, 23(6):1256–1263, 1978.

Simpson, J. H. and D. G. Bowers. Models of stratification and frontal movement in shelf seas. *Deep-Sea Research I*, 28A(7):727–738, 1981.

Simpson, J. H., W. R. Crawford, T. P. Rippeth, A. R. Campbell, and J. V. S. Cheok. The vertical structure of turbulent dissipation in shelf seas. *Journal of Physical Oceanography*, 26:1579–1590, 1996.

Simpson, J. H. and J. R. Hunter. Fronts in the Irish Sea. *Nature*, 250:404–406, 1974.

Smayda, T. J. Harmful algal blooms: Their ecophysiology and general relevance to phytoplankton blooms in the sea. *Limnology and Oceanography*, 42(5, part 2):1137–1153, 1997.

Smith, W. O. and R. T. Barber. A carbon budget for the autotrophic ciliate *Mesodinium rubrum*. *Journal of Phycology*, 15:27–33, 1979.

Snyder, W. H. and J. L. Lumley. Some measurements of particle velocity autocorrelation functions in a turbulent flow. *Journal of Fluid Mechanics*, 48(1):41–71, 1971.

Sommer, U. Sedimentation of principal phytoplankton species in Lake Constance. *Journal of Plankton Research*, 6(1):1–14, 1984.

Sommer, U. Some size relationships in phytoflagellate motility. *Hydrobiologia*, 161:125–131, 1988.

Spagnol, S., E. Wolanski, E. Deleersnijder, R. Brinkman, F. McAllister, B. Cushman-Roisin, and E. Hanert. An error frequently made in the evaluation of advective transport in two-dimensional Lagrangian models of advection-diffusion in coral reef waters. *Marine Ecology Progress Series*, 235:299–302, 2002.

Spigel, R. and J. Imberger. Mixing processes relevant to phytoplankton dynamics in lakes. *New Zealand Journal of Marine and Freshwater Research*, 21:361–377, 1987.

Strang, E. J. and H. J. S. Fernando. Vertical mixing and transports through a stratified shear layer. *Journal of Physical Oceanography*, 31:2026–2048, 2001.

Sverdrup, H. U. On conditions for the vernal blooming of phytoplankton. *Journal du Conseil Permanent International pour l'Exploration de la Mer*, 18:287–295, 1953.

Taylor, F. J. R. (ed.). *The Biology of Dinoflagellates*. Blackwell, 1987.

Taylor, G. and T. von Kármán. *Journal of the Royal Aeronautical Society*, 41:1109, 1937.

Tennekes, H. and J. L. Lumley. *A first course in turbulence*. MIT Press, 1972.

Therriault, J.-C., D. Booth, L. Legendre, and S. Demers. Phytoplankton photoadaptation to vertical excursion as estimated by an *in vivo* fluorescence ratio. *Marine Ecology Progress Series*, 60:97–111, 1990.

Thomas, W. H. and C. H. Gibson. Quantified small-scale turbulence inhibits a red tide dinoflagellate *Gonyaulax polyedra* Stein. *Deep-Sea Research I*, 37:1583–1593, 1990.

Thomson, D. J. Random walk modelling of diffusion in inhomogeneous turbulence. *Quarterly Journal of the Royal Meteorological Society*, 110:1107–1120, 1984.

Toetz, D. Effects of whole lake mixing on water quality and phytoplankton. *Water Research*, 15:1205–1210, 1981.

Van der Veer, B., J. Koedood, and P. M. Visser. Artificial mixing: A therapy measure combating cyanobacteria in Lake Nieuwe Meer. *Water Science and Technology*, 31(8):245–248, 1995.

Visser, A. W. Using random walk models to simulate the vertical distribution of particles in a turbulent water column. *Marine Ecology Progress Series*, 158:275–281, 1997.

Visser, P. M., B. W. Ibelings, and L. R. Mur. Autumnal sedimentation of *Microcystis spp.* as a result of an increase in carbohydrate ballast at reduced temperature. *Journal of Plankton Research*, 17(5):919–933, 1995*a*.

Visser, P. M., B. W. Ibelings, B. Van der Veer, J. Koedood, and L. R. Mur. Artificial mixing prevents nuisance blooms of the cyanobacterium *Microcystis* in Lake Nieuwe Meer, The Netherlands. *Freshwater Biology*, 36:435–450, 1996.

Visser, P. M., H. A. Ketelaars, and L. R. Mur. Reduced growth of the cyanobacterium *Microcystis* in an artificially mixed lake and reservoir. *Water Science and Technology*, 32(4):53–54, 1995*b*.

Visser, P. M., J. Passarge, and L. R. Mur. Modelling vertical migration of the cyanobacterium *Microcystis*. *Hydrobiologia*, 349:99–109, 1997.

Walsh, J. J. Marine photosynthesis and the global carbon cycle. In P. G. Falkowski (ed.), *Primary Productivity in the Sea*, pp. 497–506. Plenum Press, 1980.

Wang, D., W. Large, and J. McWilliams. Large eddy simulation of the equatorial ocean boundary layer: Diurnal cycle, eddy viscosity and horizontal rotation. *Journal of Geophysical Research*, 101(C2):3649–3662, 1996.

Wang, L.-P. and M. R. Maxey. Settling velocity and concentration distribution of heavy particles in homogeneous isotropic turbulence. *Journal of Fluid Mechanics*, 256:27–68, 1993.

Wang, L.-P. and D. E. Stock. Dispersion of heavy particles in turbulent motion. *Jorunal of the Atmospheric Sciences*, 50(13):1897–1913, 1993.

Webber, N. B. Hydrography and water circulation in the Solent. In J. D. Burton (ed.), *The Solent Estuarine System: An Assessment of Present Knowledge*, NERC Publication Series C No. 22, pp. 25–35. 1980.

Wells, M. R. and D. E. Stock. The effects of crossing trajectories on the dispersion of particles in a turbulent flow. *Journal of Fluid Mechanics*, 136:31–62, 1983.

Westwood, I. J. and N. B. Webber. A tidal exchange experiment at the entrance to Southampton Water. In *Proceedings of the 17th Congress, Int. Assoc. for Hydr. Res.*, vol. 3, pp. 85–92. Baden-Baden, 1977.

Williams, P. J. L. Phytoplankton in Southampton Water. In J. D. Burton (ed.), *The Solent Estuarine System: An Assessment of Present Knowledge*, NERC Publication Series C No. 22, pp. 73–75. 1980.

Wolf, K. U. and J. D. Woods. Lagrangian simulation of primary production in the physical environment – the deep chlorophyll maximum and nutricline. In B. J. Rothschild (ed.), *Toward a Theory in Biological-Physical Interactions in the World Ocean*, NATO ASI Series C, pp. 51–70. Kluwer Academic Publishers, Doderecht, 1988.

Woods, J. D. and R. Onken. Diurnal variation and primary production in the ocean – preliminary results of a Lagrangian ensemble model. *Journal of Plankton Research*, 4:735–756, 1982.

Yamazaki, H. and D. Kamykowski. The vertical trajectories of motile phytoplankton in a wind-mixed water column. *Deep-Sea Research I*, 38:219–241, 1991.

Yudine, M. I. Physical considerations on heavy-particle diffusion. *Advances in Geophysics*, 6:185–191, 1959.